INTRACRYSTALLINE DEFORMATION OF CALCITE

JOHANNES H.P. DE BRESSER

INTRACRYSTALLINE DEFORMATION OF CALCITE

JOHANNES H.P. DE BRESSER

INTRACRYSTALLINE DEFORMATION OF CALCITE

Intrakristallijne deformatie van calciet

(met een samenvatting in het Nederlands)

PROEFSCHRIFT

TER VERKRIJGING VAN DE GRAAD VAN DOCTOR AAN DE
RIJKSUNIVERSITEIT TE UTRECHT, OP GEZAG VAN DE
RECTOR MAGNIFICUS, PROF.DR. J.A. VAN GINKEL,
INGEVOLGE HET BESLUIT VAN HET COLLEGE VAN DEKANEN
IN HET OPENBAAR TE VERDEDIGEN OP MAANDAG
8 APRIL 1991 DES NAMIDDAGS TE 14.30 UUR

DOOR

JOHANNES HUBERTUS PETRUS DE BRESSER

GEBOREN OP 21 MEI 1959 TE BOXTEL

PROMOTOR: PROF.DR. H.J. ZWART
CO-PROMOTOR: DR. C.J. SPIERS

VOORWOORD

Tijdens het onderzoek beschreven in dit proefschrift heb ik dankbaar de hulp aanvaard van veel mensen. Mijn promotor, prof. Henk Zwart, gaf me de kans en vrijheid met allerlei aspekten van de strukturele geologie kennis te maken. De bijdrage van co-promotor Chris Spiers in het werk was essentieel; zonder de vele suggesties, lange diskussies en schier eindeloze rij korrekties van het manuscript was het resultaat aanzienlijk minder geweest. Reinoud Vissers las kritisch door vier hoofdstukken heen, individuele hoofdstukken werden gelezen door Bas den Brok, Herman van Roermund en Brad Smith. Ook Mervyn Paterson (ANU, Canberra) en Jim Boland (CSIRO, Victoria), 'reviewed' delen van de text. Diskussies tenslotte met Hans-Rudolf Wenk (UC Berkeley) en Neville Carter (Texas A&M University) waren nuttig voor me.

Voor de experimenten in het HPT-laboratorium werd ik op weg geholpen door Raymond Franssen, later was er altijd hulp beschikbaar van Gert Kastelein en Colin Peach. Elektronen Mikroskopie was mogelijk door de hulp van Herman van Roermund, Martyn Drury, Anton-Jan Bons, Brad Smith en, door de jaren heen, van Joop Pieters (Moleculaire Celbiologie). Duizend-en-één praktische probleempjes werden verholpen door Magda Mathot-Martens en ook Hans Schiet, Fred Trappenburg en Fred Quint (Audiovisuele dienst), Otto Stiekema (gesteente preparatie) en Paul Anten (ICP-analyses) deden goed werk voor me.

Veel tips en vooral ook gesteentemonsters kwamen van Janos Urai, Daan den Hartog Jager ging mee kalken verzamelen in Wales. Het samenwerken met de collega-promovendi, met name met Bas den Brok, Peter Schutjens, Eilard Strating en Ronald Bakker, alsook met Lourdes Miralles Ferrer was zeer prettig en gelukkig ook relativerend. Ook de overige collaga's van de vakgroep (strukturele) geologie bedank ik voor de plezierige tijd op Het Instituut (en in Italië, Kees!). Morele steun kwam er van mijn oude Pyreneeën makkers Folkert Majoor en Maarten Ploegsma.

De laatste alinea van een voorwoord als dit betreft traditioneel het thuisfront, maar eigenlijk zou dit natuurlijk de eerste alinea moeten zijn. Lucy, jouw steun en opoffering, en het laatste 3/4 jaar ook nog de zorg voor Steven, waren verbazingwekkend en geweldig! En daarbij kwam veel hulp van Maria Moonen.

Allen bedankt!

CONTENTS

ABSTRACT

It is well established from observations on natural calcite tectonites that intracrystalline plastic mechanisms are important during the deformation of calcite rocks in nature. In this thesis, new data are presented on fundamental aspects of deformation behaviour of calcite under conditions where 'dislocation creep' mechanisms dominate. The data provide a better understanding of the rheological behaviour of calcite rocks, and provide a basis for meaningful texture (crystallographic preferred orientation) modelling for calcite polycrystals.

In chapter 1, previous work on intracrystalline plastic mechanisms in calcite is summarized. Aspects of deformation behaviour hitherto insufficiently understood are highlighted, thus defining the scope for the present study.

Chapter 2 describes uniaxial compression experiments performed on optical quality calcite single crystals at temperatures and constant strain rates in the range 400 to 800 °C and $3x10^{-4}$ to $3x10^{-8}$ sec^{-1} respectively (mostly under controlled CO_2 pressure). The tests were carried out with the compression direction parallel to [$40\bar{4}1$], i.e. parallel to the intersection of two cleavage rhombs. At temperatures below ~600 °C, the crystals deformed largely by e-twinning. At higher temperatures, deformation occurred by slip on a single r<$\bar{2}021$> system plus a single f system in the so-called positive sense, as identified by slip line analysis. The effective slip direction within the active f-plane was of <$10\bar{1}1$> type rather than the <$02\bar{2}1$> type reported previously. In the slip dominated regime, the samples exhibited steady state flow behaviour. The flow stresses were found to be relatively insensitive to strain rate and can be empirically described by a power law creep equation with a stress exponent ranging from ~13 at 550-600 °C to ~9.5 at 700-800 °C. Irregular dislocation networks, observed in TEM, are prominent features of the dislocation substructure. These networks may have developed from dislocation interactions involving double cross slip. A related network recovery mechanism is implied by the steady state flow behaviour of the single crystals.

In chapter 3, results are presented for uniaxial compression experiments on calcite single crystals in a second orientation, namely with the compression direction at 30° to the c-axis and 23° to the pole on a cleavage rhomb (i.e. subparallel to [$22\bar{4}3$]). The tests were performed at temperatures in the range 300-800 °C, mostly at a constant strain rate of $3x10^{-5}$ sec^{-1}. The stress-strain curves exhibited multistage hardening behaviour, steady state only being approached at higher temperatures and/or high strains (>10%). The active glide systems were found to be two r<$\bar{2}021$> systems and one single f<$10\bar{1}1$> system, all in the so-called negative sense. In addition, at T≥600 °C, definitive evidence was found for slip on the basal plane. The observed work hardening behaviour is attributed to the absence of a network-related recovery mechanism.

Chapter 4 compares the strength characteristics of the r, f and c glide systems in

calcite. Based on yield data obtained from multi-stage stress-strain curves, it is shown that no significant difference exists in strength between positive and negative glide on the r<$20\bar{2}1$> and f<$10\bar{1}1$> systems. Considering present results as well as previous data, it is also concluded that two regimes of slip system activity exist: 1) a low temperature regime involving e-twinning, r<$20\bar{2}1$> glide and f<$02\bar{2}1$> glide, and 2) a higher temperature regime characterized by r<$20\bar{2}1$>, f<$10\bar{1}1$> and c<a> slip. A major texture transition is to be expected passing between these regimes

In chapter 5, the stress (σ) vs. dislocation density (ρ) relation for calcite single crystals is experimentally determined. The relationship obtained is found to be in good agreement with the well-known theoretical relation, $\sigma \propto \rho^{0.5}$, based on theory of dislocation interaction. Data on calcite polycrystals, however, deviate from this. Using a concept of non-homogeneous deformation related to grain size, a simple model is put forward to account for this.

In chapter 6, the flow data obtained for single crystals compressed in the [$40\bar{4}1$] orientation (chapter 2) are fitted to various microphysical models of dislocation creep. By considering the fitting results and microstructural observations, and comparing these with existing data on other materials, it is proposed that the steady state deformation of single crystals is best explained by a dislocation cross slip controlled creep mechanism. Mechanical behaviour and microstructures characteristic of calcite polycrystals, deformed at roughly identical conditions, show various similarities with the single crystals, and their creep behaviour may well be rate-controlled by the same mechanism.

Finally, chapter 7 reports observations on deformed limestones from a small scale shear zone in SW Wales, U.K., where maximum PT conditions were 130 MPa, and 200 °C respectively. Flattened, strained calcite grains, high dislocation densities and a weak but distinct crystallographic preferred orientation indicate that deformation occurred predominantly by intracrystalline mechanisms. Using conventional paleopiezometers (dislocation density, recrystallized grain size, twinning frequency) and failure criteria, a paleostress within the range 70-410 MPa was inferred for the shear zone. Values computed by extrapolating various experimentally determined flow equations for calcite materials show a far wider range of stresses. Notably, power laws are unsuccesful in reliably predicting paleostresses in deformed calcite rocks at low metamorphic grade. In contrast, the cross slip controlled creep equation established for single crystals in the [$40\bar{4}1$] orientation may offer a method for estimating minimum flow stresses in limestones deformed at low temperature.

SAMENVATTING

Op grond van waarnemingen aan natuurlijke calciet-tektonieten is algemeen vastgesteld dat intrakristallijne mechanismen belangrijk zijn tijdens vervorming van calciet-gesteenten. In dit proefschrift worden nieuwe gegevens gepresenteerd met betrekking tot fundamentele aspekten van het deformatiegedrag van calciet onder kondities waarbij 'dislokatie kruip' mechanismen domineren. Deze gegevens leiden tot een beter begrip van het rheologisch gedrag van calciet-gesteenten, en vergemakkelijken betekenisvolle modellering van kristallografische voorkeursmaaksels in calciet polykristallen.

In hoofdstuk 1 wordt bestaand werk aan intrakristallijne mechanismen in calciet samengevat. Aspekten van het deformatiegedrag die nog onvoldoende begrepen worden zijn aangegeven, waardoor een kader ontstaat waarbinnen nieuwe gegevens gepresenteerd kunnen worden in de volgende hoofdstukken.

Hoofdstuk 2 beschrijft uniaxiale kompressie experimenten op calciet enkelkristallen van optische kwaliteit, uitgevoerd bij temperaturen tussen 400 en 800 °C en vervormingssnelheden in het bereik 3×10^{-4} tot 3×10^{-8} sec^{-1}. De richting van kompressie in deze testen was parallel aan [40$\overline{4}$1], wat de snijlijn is van twee rhomboëdrische (splijt-)vlakken. Bij een temperatuur beneden 600 °C vervormden de kristallen voornamelijk door middel van **e**-vertweelinging. Bij hogere temperatuur vond deformatie plaats via dislokatieglij op een enkel **r**<$\overline{2}$021> slip-systeem plus een enkel **f**-systeem, beide systemen in de zogenaamde positieve richting. Dit werd bepaald door middel van sliplijn analyse. De effektieve glijrichting voor het aktieve **f**-systeem bleek parallel te zijn aan <10$\overline{1}$1>, in plaats van parallel aan de in eerdere literatuur gerapporteerde <02$\overline{2}$1> richting. In het door glij gedomineerde bereik vertoonden de kristallen 'steady state' vloeigedrag. De bijbehorende vloeispanningen bleken relatief ongevoelig te zijn voor veranderingen in de vervormingssnelheid en konden empirisch beschreven worden door middel van 'power law' kruipvergelijkingen met spannings-exponenten variërend van ~13 bij 550-600 °C tot ~9.5 bij 700-800 °C. Onregelmatige dislokatie-netwerken, waargenomen met behulp van Transmissie Elektronen Mikroskopie (TEM) vormen karakteristieke elementen van de dislokatie substruktuur. Deze netwerken zijn mogelijk ontstaan door dislokatie interaktie waarbij 'cross slip' (dwarsglij) optrad op nieuwe, anders georiënteerde kristallografische vlakken. Het steady state vloeigedrag van de enkelkristallen impliceert een hieraan gerelateerd netwerk-'recovery' mechanisme.

In hoofdstuk 3 worden de resultaten gepresenteerd van uniaxiale kompressie experimenten in een tweede oriëntatie, nu met de kompressierichting in een hoek van 30° met de c-as en 23° met een splijtvlaknormaal. Deze kompressierichting is subparallel aan [22$\overline{4}$3]. De testen werden uitgevoerd bij temperaturen tussen 300 en 800 °C, in het algemeen bij een konstante vervormingssnelheid van 3×10^{-5} sec^{-1}. De spanning-vervormingskurves vertoonden meer-fase 'hardening' (verharding) gedrag,

waarbij steady state alleen benaderd werd bij hogere temperaturen en/of hoge strains (>10%). Twee r<$\bar{2}$021> systemen en een enkel f<10$\bar{1}$1> systeem vormden de aktieve glijsystemen, allen in de zogenaamde negatieve richting. Bovendien werden ondubbelzinnige aanwijzingen gevonden voor aktieve glij op het basale vlak. De waargenomen hardening wordt toegeschreven aan de afwezigheid van een dislokatie-netwerk recovery mechanisme.

Hoofdstuk 4 vergelijkt de sterkte-karakteristieken van de r, f en c-glijsystemen in calciet. Gebruikmakend van 'yield' (bezwijk) data verkregen uit de meer-fase spanning-vervormingskurves wordt aangetoond dat er geen signifikante sterkte-verschillen bestaan tussen positieve en negatieve glij op de r<$\bar{2}$021> en f<10$\bar{1}$1> systemen. Op basis van zowel de huidige resultaten als reeds bekende gegevens wordt ook gekonkludeerd dat er twee verschillende regimes van glijsysteem aktiviteit bestaan, namelijk 1) een lage temperatuur regime met e-vertweelinging, r<$\bar{2}$021> glij en f<02$\bar{2}$1> glij, en 2) een hoge temperatuur regime gekarakteriseerd door r<$\bar{2}$021>, f<10$\bar{1}$1> en c<a> glij. Een belangrijke transitie in type kristallografische voorkeurs-oriëntatie is te verwachten bij de overgang van het ene regime naar het andere.

In hoofdstuk 5 wordt de relatie tussen vloeispanning (σ) en dislokatiedichtheid (ρ) voor calciet-enkelkristallen experimenteel bepaald. De gevonden relatie komt goed overeen met de algemeen bekende theoretische relatie $\sigma \propto \rho^{0.5}$, die gebaseerd is op dislokatie-interaktie theorie. Echter, gegevens met betrekking tot calciet-polykristallen wijken hiervan af. Gebruikmakend van een koncept van inhomogene vervorming gerelateerd aan korrelgrootte wordt een eenvoudig model gepresenteerd dat dit afwijkend gedrag verklaard.

In hoofdstuk 6 worden de kruip-data voor de in de [40$\bar{4}$1] richting gedeformeerde kristallen (hoofdstuk 2) ingepast in verschillende mikrofysische modellen voor dislokatiekruip. Op basis van zowel een kritische beschouwing van de 'fitting' resultaten en mikrostrukturele observaties, als een vergelijking met bestaande gegevens met betrekking to andere materialen wordt beargumenteerd dat de steady state vervorming van de enkelkristallen het best kan worden verklaard via een dislokatie-kruip mechanisme gekontroleerd door cross slip. Het mechanisch gedrag en de mikrostrukturele karakteristieken van calciet-polykristallen vertonen, bij vergelijkbare deformatie kondities, diverse overeenkomsten met die van de enkelkristallen. Het lijkt dan ook aannemelijk dat het kruipgedrag van polykristallen bij deze kondities gekontroleerd wordt door een zelfde cross slip mechanisme.

In hoofdstuk 7 tenslotte worden de resultaten gepresenteerd van een studie van een gedeformeerde kalk uit een kleinschalige natuurlijke schuifzone in Zuid-Wales, Groot Brittanië, waar de maximum temperatuur-druk kondities respectievelijk 200 °C en 130 MPa waren. Afgeplatte vervormde calcietkorrels, hoge dislokatiedichtheden en een zwakke maar evidente kristallografische voorkeursoriëntatie geven aan dat deformatie grotendeels plaatsvond via intrakristallijne mechanismen. Gebruikmakend van konventionele paleospannings-indicatoren (dislokatiedichtheid, gerekristalliseerde korrelgrootte en tweelingfrekwentie) en breukkriteria wordt de paleospanning

verondersteld te liggen binnen het bereik 70-410 MPa. Waardes die berekend zijn via extrapolatie van verschillende experimenteel bepaalde vloeiwetten voor calciet-materialen vertonen een groter spanningsbereik. Met name 'power laws' falen bij het betrouwbaar voorspellen van paleospanningen in gedeformeerde calciet-gesteenten bij lage metamorfe graad. De cross slip gekontroleerde kruipvergelijking opgesteld voor enkelkristallen in de [40$\overline{4}$1] richting lijkt echter een methode te leveren voor het bepalen van minimum vloeispanningen in kalken die zijn gedeformeerd bij lage temperatuur.

CHAPTER 1

INTRACRYSTALLINE DEFORMATION OF CALCITE: PREVIOUS WORK AND SCOPE OF THE PRESENT STUDY

1.1 INTRODUCTION

Calcite is an important rock-forming mineral, being the principal constituent of carbonate rocks such as limestone and marble. Carbonates almost invariably accumulate in marine sedimentary basins and, due to lithospheric plate motion, are often subject to complex deformation during orogeny. It has long been recognized that intracrystalline plastic mechanisms are important in this. An understanding of deformation behaviour of calcite rocks by such mechanisms offers constraints on the geological conditions prevailing during natural deformation and permits evaluation of geophysical models for the rheology of crustal rocks. For this reason, a great deal of work has been done on the identification of glide systems in calcite, on the rheological behaviour of calcite rocks, and on the development of microstructures and textures (crystallographic preferred orientations) under conditions where 'dislocation creep' mechanisms dominate. In this first chapter, previous work on intracrystalline plastic mechanisms in calcite will be summarized. It will be shown that while a great deal of data has been obtained, fundamental aspects of the deformation behaviour of calcite are insufficiently understood to adequately address geological and geophysical problems. A framework is thus established for the presentation of new fundamental data on this in the subsequent chapters.

1.2 CRYSTALLOGRAPHY OF CALCITE

Calcite is a trigonal polymorph of calcium-carbonate ($CaCO_3$), with point group $\bar{3}$ $2/m$ (also referred to as $\bar{3}m$, e.g. McKie and McKie 1986) and space group $R\bar{3}c$. Its crystal structure can be described as a face-centered rhombohedron (Phillips 1962, Deer et al. 1962) containing four $CaCO_3$ molecules. It thus corresponds to a

distorted face-centered cubic cell analogous to that of halite (NaCl). The CO_3 groups in calcite form planar triangles of oxygens with a carbon atom in the centre. The triangles are oriented normal to the three-fold inversion axis and are rotated by 180° about this axis in successive planes (Paterson 1979, 1985 - see Fig. 1.1a). Because of this alternation of CO_3 orientations, the four-$CaCO_3$ cell is not a true unit cell but a *pseudo* face-centered rhombohedral cell. Either a smaller, *primitive* rhombohedral cell (the 'structural' cell), containing two $CaCO_3$ (Fig. 1.1a), or a larger *true* face-centered rhombohedral cell (the 'morphological' cell), containing 32 $CaCO_3$, must be chosen to describe the lattice. These three rhombohedral cells can be indexed with reference to rhombohedral axes (i.e. the rhomb edges) or hexagonal axes (with the c-axis parallel to the inversion axis). A somewhat confusing set of possible cells results, complicating the comparison of results of different authors in the literature.

In Table 1.1, the most important planes and directions in calcite are given, with the rhombohedral *and* hexagonal indices for both the structural and the morphological cell. Note the letter notations commonly used in the literature. In this thesis, use is
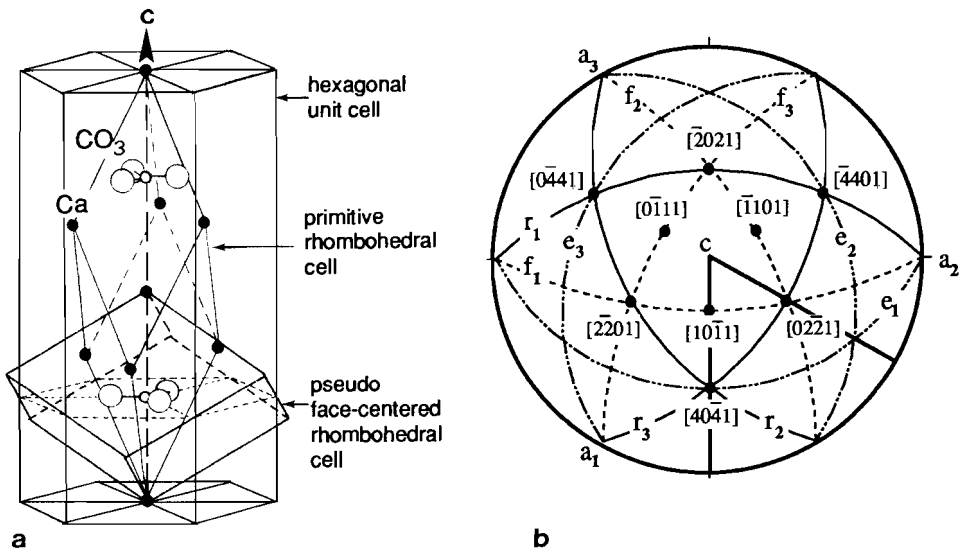
Figure 1.1
a) The structure of calcite (after Fig. 47 in Deer et al. 1962).
Shown are the elongated primitive rhombohedral cell (the structural cell, containing two $CaCO_3$) and the pseudo face-centered rhombohedral cell in relation to the hexagonal unit cell. Note the CO_3 triangles normal to the vertical trigonal axis.
b) Stereographic (upper hemisphere) Wulff projection of calcite showing the important planes and directions, using four-digit Miller Bravais indices based on the structural hexagonal cell.

made of the structural hexagonal unit cell (as advised by Paterson 1979) with a=4.99 Å and c=17.06 Å, employing four-digit Miller-Bravais indices (hkil), where i=—(h+k). The disposition of the important planes and directions in a stereographic projection is shown in Fig. 1.1b.

(planes)	hexagonal structural cell	hexagonal morphological cell	rhombohedral structural cell	rhombohedral morphological cell
c	0001	0001	111	111
e_1	$\bar{1}018$	$\bar{1}012$	233	011
e_2	$1\bar{1}08$	$1\bar{1}02$	323	101
e_3	$01\bar{1}8$	$01\bar{1}2$	332	110
f_1	$\bar{1}012$	$\bar{2}021$	011	$\bar{1}11$
f_2	$1\bar{1}02$	$2\bar{2}01$	101	$1\bar{1}1$
f_3	$01\bar{1}2$	$02\bar{2}1$	110	$11\bar{1}$
r_1	$10\bar{1}4$	$10\bar{1}1$	211	100
r_2	$\bar{1}104$	$\bar{1}101$	121	010
r_3	$0\bar{1}14$	$0\bar{1}11$	112	001
m_1	$10\bar{1}0$	$10\bar{1}0$	$2\bar{1}\bar{1}$	$2\bar{1}\bar{1}$
m_2	$\bar{1}100$	$\bar{1}100$	$\bar{1}2\bar{1}$	$\bar{1}2\bar{1}$
m_3	$0\bar{1}10$	$0\bar{1}10$	$\bar{1}\bar{1}2$	$\bar{1}\bar{1}2$
a_1	$2\bar{1}\bar{1}0$	$2\bar{1}\bar{1}0$	$1\bar{1}0$	$1\bar{1}0$
a_2	$\bar{1}2\bar{1}0$	$\bar{1}2\bar{1}0$	$01\bar{1}$	$01\bar{1}$
a_3	$\bar{1}\bar{1}20$	$\bar{1}\bar{1}20$	$\bar{1}01$	$\bar{1}01$

[intersections]

$r_1{:}r_2$	$0\bar{4}41$	$0\bar{1}11$	$\bar{1}\bar{1}3$	001
$r_2{:}r_3$	$40\bar{4}1$	$10\bar{1}1$	$3\bar{1}\bar{1}$	100
$r_1{:}r_3$	$\bar{4}401$	$\bar{1}101$	$\bar{1}3\bar{1}$	010
$f_1{:}f_2$	$02\bar{2}1$	$01\bar{1}2$	$11\bar{1}$	110
$f_2{:}f_3$	$\bar{2}021$	$\bar{1}012$	$\bar{1}11$	011
$f_1{:}f_3$	$2\bar{2}01$	$1\bar{1}02$	$1\bar{1}1$	101
$a_1{:}f_3$	$0\bar{1}11$	$0\bar{1}14$	001	112
$a_2{:}f_1$	$10\bar{1}1$	$10\bar{1}4$	100	211
$a_3{:}f_2$	$\bar{1}101$	$\bar{1}104$	010	121

cell parameters:
  hexagonal structural cell: a = 4.99 Å, c =17.06 Å
  hexagonal morphological cell: a =19.96 Å, c =17.06 Å
  rhombohedral structural cell: a_{RH}= 6.37 Å, α = 46.05°
  rhombohedral morphological cell: a_{RH}=12.85 Å, α =101.55°

Table 1.1
Indices of the most important planes and directions in calcite, employing different unit cells. Indices for c and a axes as for planes, cell parameters after Deer et al. (1962).

1.3 EXPERIMENTAL DEFORMATION OF CALCITE SINGLE CRYSTALS

1.3.1 Observed slip systems

As early as the last century, mechanical twinning was recognized as an important deformation mechanism in calcite. Amongst others, Baumhauer (1879) showed that twins can be easily introduced into a calcite crystal at room temperature and atmospheric pressure. However, it was realized that twinning can only account for a limited amount of strain, with other mechanisms being required for substantial plastic deformation. Basic insight into the nature of such mechanisms was first provided by the work of F.J. Turner, D.T. Griggs and H.C. Heard in the nineteen-fifties and early sixties. In one of their earliest papers, Turner et al. (1954) described compression and extension experiments performed on calcite crystals in various crystallographic orientations, at temperatures in the range 20 to 400 °C and at confining pressures in the range 500 to 1000 MPa. Identification of the glide systems activated was attempted using a petrographic method (see Turner and Weiss 1963). In this method, thin sections of the heterogeneously deformed crystals were inspected for domains of more or less homogeneous strain (e.g. kink bands). The analyses of both *external* rotations of such domains (i.e. rotation of crystal axes with respect to the loading direction) and *internal* rotations of passive markers within the domains (e.g. early twins rotated with respect to crystal axes) can lead to identification of the dominant glide plane and glide direction. Along with twinning on e $\{\bar{1}018\}<40\bar{4}1>$ (3 systems), Turner et al. (1954) found slip on r $\{10\bar{1}4\}<\bar{2}021>$ (3 systems) to be an important glide mechanism. Subsequent experiments (Griggs et al. 1960), performed at temperatures between 300 and 800 °C, suggested slip on f $\{\bar{1}012\}<02\bar{2}1>$ (6 systems) to be an additional, mainly high temperature mechanism of plastic deformation.

Twinning on e occurs in the so-called positive sense, defined by Turner et al. (1954 - see Fig. 1.2) as the relative displacement of upper layers of the lattice upward toward the (positive) c-axis. Although slip on r and f was believed to be possible in both the negative and positive senses, the chosen orientations of the loading direction with respect to the crystal axes (in the studies quoted) were such that only negative slip was observed. Note that here and henceforth the notation (hkil)[UVTW]$^{\pm}$ is used to specify individual slip systems (i.e. slip plane + slip direction). The superscripts indicate slip sense.

Following the early work described above, increasingly sophisticated experiments by Keith and Gilman (1960), Turner and Heard (1965a), Borg and Handin (1967), Paterson and Turner (1970) and Braillon et al. (1972, 1978) confirmed the importance of e$^+$ twinning and r and f slip in the negative sense in calcite single crystals. In addition, Weiss and Turner (1972) and Braillon and Serughetti (1976) activated slip on r in the positive sense. Spiers and Wenk (1980) also investigated
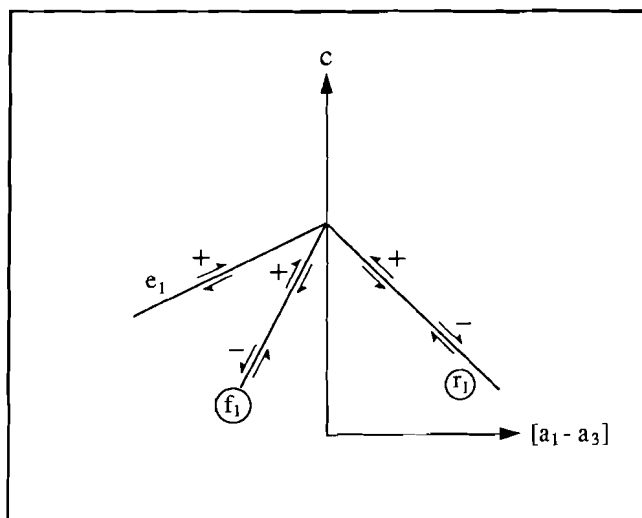
Figure 1.2
Definition of sense of gliding on the e_1, r_1 and f_1 planes
in calcite, after Turner et al. (1954 - cf. Fig. 1.1b).

r^+ slip, at temperatures in the range 350 to 650 °C, and observed a transition towards dominant f-slip in the positive sense at the higher temperatures. Aside from the above, various glide systems of relatively minor importance have been reported. These include r^+ twinning (Borg and Handin 1967), f^- twinning (Paterson and Turner 1970), slip on **a** (Turner and Heard 1965a, Paterson and Turner 1970), slip on **m** (Thomas and Renshaw 1967) and basal slip (Turner and Orozco 1976). Table 1.2 summarizes the glide mechanisms reported for calcite to date, and the experimental conditions under which they were observed.

1.3.2 Effect of temperature

In the most extensively studied temperature range of 100 to 550 °C, calcite single crystals almost invariably exhibit work hardening flow. The stress-strain curves obtained often show multistage behaviour (Fig. 1.3), characteristic of slip system interactions (Alexander and Haasen 1968). The macroscopic yield stresses (σ_Y - see Fig. 1.3) have been used to calculate critical resolved shear stresses (CRSS) for the e^+, r^- and f^- systems, following common practice in the early metallurgical literature. These CRSS values decrease with increasing temperature, and while differing considerably at low temperature, the values for the main glide systems appear to converge at higher temperature (see chapter 4 or Fig. 2 in Wenk 1985).

At temperatures above 600 °C, the stress-strain curves change in character

previous work and current scope

	experimental conditions			
twinning systems:	temperature [°C]	strain rate [sec⁻¹]	pressure [MPa]	reference
e⁺ {$\bar{1}$018}<40$\bar{4}$1>	20-300	2.5x10⁻⁴	500-1000	Turner et al. 1954
	300-800	2.5x10⁻⁴	500	Griggs et al. 1960
r⁺ {10$\bar{1}$4}<$\bar{2}$021> *	20	torsion tests	300	Borg and Handin 1967
	300	?	500	Weiss and Turner 1972
f⁻ {$\bar{1}$012}<$\bar{1}$01$\bar{1}$> *	300 ?	?	500	Paterson and Turner 1970

slip systems:				
r⁻ {10$\bar{1}$4}<20$\bar{2}\bar{1}$>	20-400	2.5x10⁻⁴	300-1000	Turner et al. 1954
	300-600	2.5x10⁻⁴	500	Griggs et al. 1960
	25-500	4x10⁻¹, 3x10⁻⁷	500	Turner and Heard 1965
r⁺ {10$\bar{1}$4}<$\bar{2}$021>	300	?	500	Weiss and Turner 1972
	460-550	1x10⁻⁴	unconf.	Braillon & Serughetti 1976
	350-650	2.5x10⁻⁵	unconf.	Spiers and Wenk 1980
f⁻ {$\bar{1}$012}<$\bar{2}$20$\bar{1}$><0$\bar{2}$2$\bar{1}$>	20, (300?)	2.5x10⁻⁴	500	Turner et al. 1954
	600-800	2.5x10⁻⁴	500	Griggs et al. 1960
f⁺ {$\bar{1}$012}<2$\bar{2}$01><02$\bar{2}$1>	575-650	2.5x10⁻⁵	unconf.	Spiers and Wenk 1980
a {$\bar{1}$2$\bar{1}$0}<$\bar{2}$021> *	300, 500	?	500	Paterson and Turner 1970
	300	3.3x10⁻⁷	500	Turner and Heard 1965a
c {0001}<$\bar{1}$2$\bar{1}$0> *	800	2.5x10⁻⁴	500	Griggs et al. 1960
	300	2.5x10⁻⁴	500	Turner and Orozco 1976
m {10$\bar{1}$0}<$\bar{1}$2$\bar{1}$0> *	550	?	?	Thomas and Renshaw 1967

Table 1.2
*Previously reported glide mechanisms in calcite plus corresponding experimental conditions. Compare with Fig. 1.1b. * indicates system of relatively minor importance. The a, c and m systems have a neutral sense of gliding. Unconf. means unconfined, i.e. at atmospheric pressure.*

(Griggs et al. 1960) from multistage behaviour to smooth curves without a clear yield point but with continuously decreasing work hardening rate finally reaching steady state (Fig. 1.3). This change was attributed to a change in dominating slip system, f-slip becoming increasingly important at the cost of r-slip towards higher temperatures.
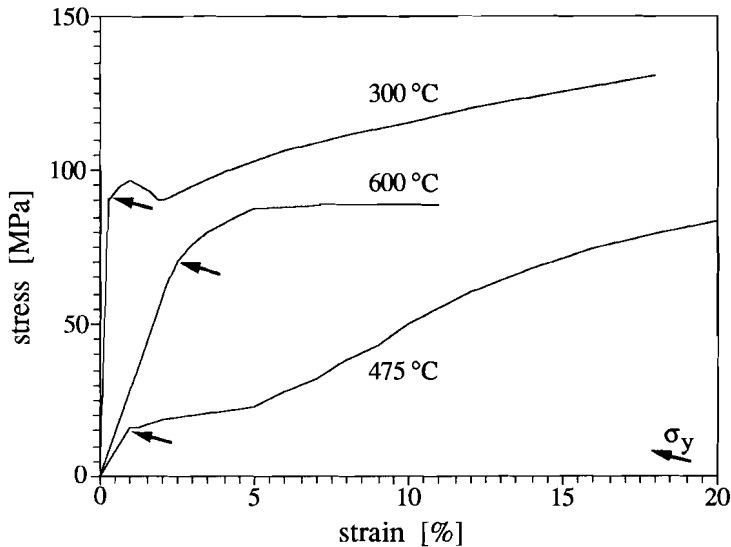
Figure 1.3
Examples of stress-strain curves for single crystals of calcite. 300 °C curve from Turner et al. (1954); extension parallel the intersection of two cleavage planes. 475 °C curve from Braillon et al. (1972); compression parallel c-axis. 600 °C curve from Griggs et al. (1960); compression at 30° to the c-axis and 75° to an r-plane. The curves at relatively low temperature (300 and 475 °C) show typical multistage behaviour, which disappears towards higher temperature (600 °C curve). σ_y denotes the yield stress.

1.3.3 Effect of strain rate

Very limited attention has been paid to the influence of strain rate on the plastic deformation of calcite single crystals. Turner and Heard (1965a) describe 19 experiments at two widely differing extension rates, respectively 4×10^{-1} and 3.3×10^{-7} sec^{-1}, at temperatures between 25 and 500 °C. Their results suggest hardly any sensitivity of the differential stress to the rate of straining. However, the crystals did not show steady state behaviour, reproducibility was poor, and the results are not consistent with those from the earlier experiments of Turner et al. (1954) and Griggs et al. (1960) at an intermediate strain rate.

In contrast to the above, a high sensitivity of flow stress to strain rate was claimed by Braillon et al. (1978), who investigated calcite single crystals experimentally compressed parallel to the c-axis at strain rates $(\dot{\varepsilon})$ between 3.5×10^{-4} and 1.1×10^{-5} sec^{-1}, and temperatures (T) in the range 100 to 550 °C. Based on activation energies calculated on the basis of stress relaxation and strain rate change experiments, they obtained for T>300 °C a creep equation of the form $\dot{\varepsilon} \propto \sigma^{3.5}$. This result, however, seems meaningless in view of the non-steady state character of the

deformation behaviour in the regular constant strain rate tests (see stress-strain curves in Braillon et al. 1972), and also conflicts with the higher power law stress exponent (~13 for T=300-550 °C) which can be estimated from the 'flow' stress data (probably yield stresses) presented by Braillon et al. (1978).

Rutter et al. (1978) also performed limited stress relaxation tests on single crystals of calcite. Their results (at T=20 °C) showed a sensitivity of the applied stress to the strain rate which varies as a function of pre-relaxation strain, but in general is very low, with power law stress exponents above 20.

1.3.4 Effect of orientation

With regard to effects of the orientation of the loading direction in relation to the crystal axes, there has been frequent discussion whether slip on r and slip on f operate with equal ease in opposite senses. From a theoretical point of view, the critical shear stresses for these slip systems need not to be the same (Paterson 1985). Weiss and Turner (1972) suggest that r slip in the positive sense is easier than r⁻, but Spiers and Wenk (1980) conclude the opposite.

1.4 EXPERIMENTAL DEFORMATION OF CALCITE ROCKS

Because of the relative ease with which calcite crystals and rocks can be deformed under laboratory conditions, numerous studies have been performed on plastic deformation of limestones and marbles, at T=20-1050 °C, confining pressures in the range 300 to 500 MPa and $\dot{\varepsilon}=10^{-1}$-$10^{-8}$ sec⁻¹. The classical work of Griggs and co-workers on Yule marble (e.g. Griggs and Miller 1951, Griggs et al. 1951, 1953, 1960) yielded a considerable amount of information on mechanical behaviour and on the development of textures and microstructures. Later work on Yule marble (Heard 1963, Turner and Heard 1965b, Heard and Raleigh 1972) and on other, now almost 'classical' calcite materials (Solnhofen limestone, Carrara marble) contributed greatly in these areas (Rutter 1974, Schmid 1976, Schmid et al. 1977, 1980, 1987).

It has been found that at laboratory strain rates, both limestone and marble deform in steady state flow provided that temperatures exceed 400 °C. However, a unique flow law holding at all conditions of T, σ and $\dot{\varepsilon}$ has not been established either for calcite aggregates in general or for a single calcite rock (see Fig. 1.4). Rather a subdivision into deformation *regimes* has been proposed, each regime having its own constitutive flow equation describing the mechanical behaviour (Table 1.3). From microstructural observations, it was attempted to relate these flow regimes to specific mechanisms of deformation. Intracrystalline plastic mechanisms were found to

predominate in most regimes (Table 1.3) and geometrical analysis of lattice bending confirmed the importance of the **e, r** and, to a lesser extent, **f** glide systems which were known from the single crystal studies. The coarse-grained Yule and Carrara marbles and the fine-grained Solnhofen limestone exhibit somewhat different characteristics and will be treated seperately below.

In the high stress, exponential flow regimes for Yule and Carrara marble (Heard and Raleigh 1972, Schmid et al. 1980), twinning on **e** dominates, with additional evidence for substantial dislocation glide, mainly on **r**. Locally, subgrains and recrystallized grains developed. In the lower stress power law flow regimes, the importance of twinning diminishes rapidly. Also, subgrain and recrystallization structures become more pronounced, possibly demonstrating an increasing importance of (diffusion-assisted) dislocation climb.

In the exponential flow regime for Solnhofen limestone (regime 1, Schmid et al. 1977), twinning is insignificant and the microstructure of flattened grains and subgrains is thought to indicate that creep is controlled by dislocation climb. The microstructures in the high stress power law regime (regime 2) are not dissimilar from those in the exponential regime, but the equiaxed, polygonal grain structure in regime 3 (see Table 1.3) is claimed to result from a grain boundary sliding (GBS) mechanism of deformation (see also Olgaard 1985).
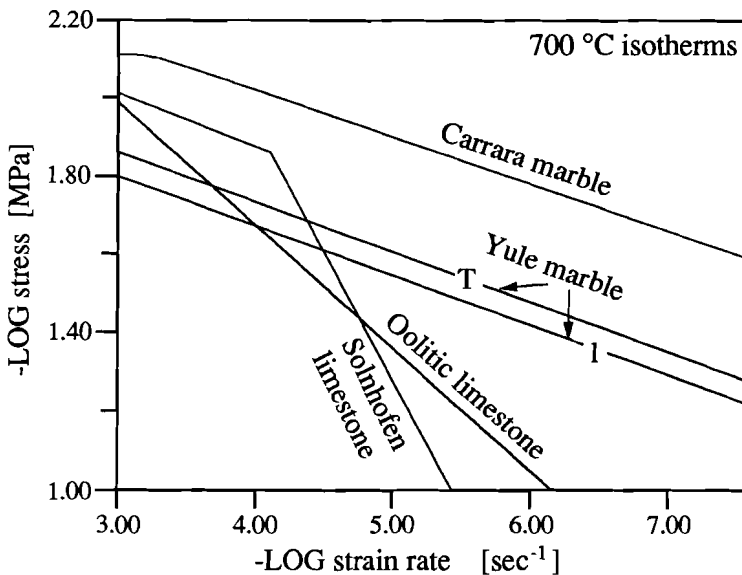
Figure 1.4
Log-log plot of strain rate vs. differential stress showing 700 °C isotherms plotted using best fit creep laws for various calcite materials (see Table 1.3). Carrara marble isotherm after Schmid et al. (1980), Yule marble after Heard and Raleigh (1972), Solnhofen limestone after Schmid et al. (1977). Isotherm for oolitic limestone (Schmid and Paterson 1977) determined graphically.

used empirical flow equations:

exponential: $\dot{\varepsilon} = A' \cdot \exp(-Q/RT) \cdot \exp(\sigma/\sigma_0)$

power law: $\dot{\varepsilon} = A \cdot \exp(-Q/RT) \cdot \sigma^n$

A, A', n and σ_0 are empirical constants, $\dot{\varepsilon}$ is strain rate [sec^{-1}],
σ is the flow stress [MPa], Q the apparent activation energy [kJ/mol],
R the gas constant and T the absolute temperature.

material, refer.	LOG A'	σ_0	Q	LOG A	n	
Yule marble, a)						
I orientation:	7.8	9.1	260			at σ > 110 MPa
I orientation:			260	-3.9	8.3	at σ < 110 Mpa
T orientation:	7.0	13.8	239			at σ > 140 MPa
T orientation:			256	-3.6	7.7	at σ < 140 MPa
Carrara marble						
regime 1, b):	5.8	11.4	260			at σ > 100 Mpa
regime 2, c):			420	3.1	7.6	at σ = 20-100 MPa
regime 3, c):			428	8.1	4.2	at σ < 20 MPa
Solnhofen lmst						
regime 1, d):	-0.12	16.0	197			at σ > 190 MPa
regime 2, e):			298	3.4	4.7	at σ < 190 MPa
regime 3, e):			214	4.4	1.7	at σ < 100-40 MPa

Yule marble, exponential regime: twinning, r-glide,
no subgrains, no polygonization
power law regime: polygonization, inter- and
intragranular recrystallization

Carrara marble, regime 1: predominant twinning, considerable slip movement, local
subgrain development and recrystallization, limited GBS
regime 2: absence or paucity of twinning, strong but variable sub-
grain development (core- and mantle structures)
regime 3: complete recrystallization by subgrain rotation mechanism,
exaggerated grain growth, more significant GBS

Solnhofen limestone, regime 1: flattened grains, unulose extinction, subgrains,
twinning insignificant
regime 2: as regime 1
regime 3: equiaxed grains, straight grain boundaries,
polygonal structure

Table 1.3
Empirical flow laws describing the mechanical behaviour of various experimentally deformed calcite rocks, and microstructural observations.
a) Heard 1963, Heard and Raleigh 1972, see also Rutter 1974: extension tests at temperatures 25-800 °C, confining pressure 500 MPa strain rates 10^{-1} to 10^{-8} sec^{-1}. I orientation: normal to foliation, T orientation: parallel to foliation.
b) Rutter 1974: compression tests at temperatures 20-500 °C, confining pressure 150 MPa and strain rates 6×10^{-4} to 5×10^{-8} sec^{-1}.
c) Schmid et al. 1980: compression tests at temperatures 600-1050 °C, confining pressure 300 MPa and strain rates 6×10^{-3} to 10^{-6} sec^{-1}.
d) as b)
e) Schmid 1976, Schmid et al. 1977: compression tests at 600-900 °C, confining pressure 300 MPa and strain rates 7×10^{-3} to 10^{-6} sec^{-1}.

Although the studies quoted above have added considerable information to our knowledge on mechanical behaviour of calcite materials, they remain, in some degree, *empirical* studies, lacking a comparison with theoretical creep models and a critical evaluation of the fitting parameters.

1.5 DEVELOPMENT OF TEXTURES

1.5.1 Experiments

Because of interest in interpreting natural textures, extensive investigations of the development of crystallographic preferred orientations (textures) in calcite rocks followed the experimental, axi-symmetric tests on Yule marble (e.g. Griggs et al. 1953, Turner et al. 1956). Later, X-ray goniometry gave information on the full nature of textures in samples deformed in axi-symmetric geometry (Casey et al. 1978), as well as in pure shear and simple shear (Wagner et al. 1982, Kern and Wenk 1983, Schmid et al. 1987). Although a variety of textures was found as a function of conditions of deformation (temperature, geometry/deformation path) and type of material (limestone vs. marble), basically two types of texture have been distinguished (see Fig. 1.5):

[1] Marbles deformed in the exponential flow regimes (dominant twinning - see Table 1.3) show preferred orientations of c-axes on a small circle making a small angle (~20-30°) to the compression axis (effectively yielding a broad maximum), or a large angle to the extension axis. Such patterns can also be found in limestones deformed at very high stresses and low temperatures, i.e. at the upper limits of the exponential field (Rutter 1974).

[2] Within its exponential flow regime and upper power law regime (regimes 1 and 2), Solnhofen limestone shows c-axis patterns with split maxima (refer Fig. 1.5). Limited results published on textures in marbles deformed in the power law field (e.g. Schmid et al. 1987) show comparable patterns.

For details, the reader is referred to Wenk (1985).

A third type of pattern, exhibiting weak concentrations of c-axis perpendicular to the compression axis, was found in samples of Solnhofen limestone deformed in the grain boundary sliding regime (Casey et al. 1978), but may well have been inherited from the initial texture of the rock.

1.5.2 Computer modelling

Computer simulations of texture development have been carried out by Lister (1978), Wenk et al. (1986) and Takeshita et al. (1987), using the Taylor method
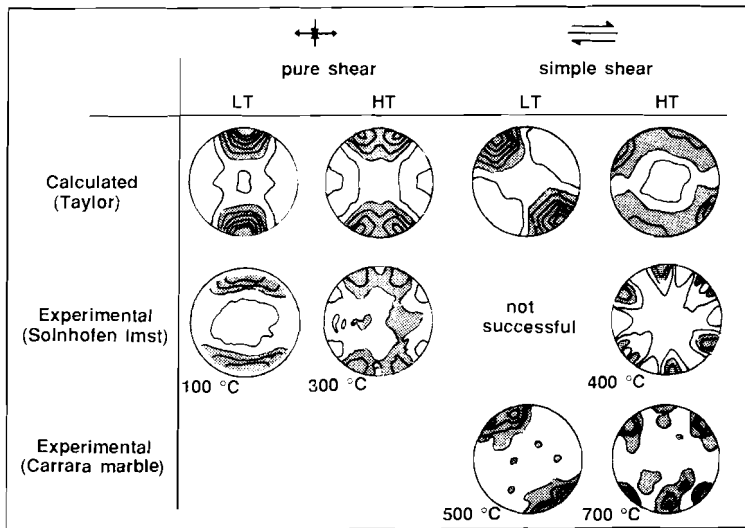
Figure 1.5
Calculated (Taylor) and experimentally produced c-axis pole figures for calcite rocks. Equal area projections. Taylor and experimental data on Solnhofen limestone after Wenk et al. (1987), contourinterval 0.5 of a uniform distribution, shade above 1. Experimental data on Carrara marble after Schmid et al. (1987), contourinterval 2.0 of a uniform distribution, lowest contour 1.0. All experimental textures obtained for samples deformed at exponential regime conditions (Table 1.3), except 700 °C pattern for Carrara marble (power law regime). Figure adopted from De Bresser (1989).

(Taylor 1938) or related techniques. A distinction can be made between low temperature (LT) and high temperature (HT) calculated preferred orientations. For LT pure shear, the c-axes are concentrated in a broad maximum parallel to the main compression direction. At higher temperature, this maximum is split into two maxima that are symmetrically oriented at an angle of about 30° to the main compression direction. LT simple shear pole figures show the same broad maximum as the pure shear equivalents, but its orientation is rotated against the sense of shear.

The results of the modelling can be compared with experimentally produced textures (see Wenk et al. 1987, and Fig. 1.5). From Fig. 1.5, it is clear that the calculated and experimentally produced LT-HT pure shear and LT simple shear textures correspond reasonably well with each other, while this is not obvious for the HT simple shear textures. The latter nevertheless agree in the slight asymmetry of the pattern with respect to the shear plane and the splitting of the maximum, in comparison with the HT pure shear textures.

1.5.3 Natural textures

Natural calcite textures reported so far (e.g. Trommsdorff 1964, Schmid et al. 1981, Behrmann 1983) are in general monotonous, showing only a single point maximum of c-axes, comparable with the LT texture type (Fig. 1.5). However, c-axis patterns in calcite rocks from the Pyrenean Gavarnie thrust zone (De Bresser 1988) show characteristics of both low temperature and high temperature textures, i.e. broad concentrations of c-axes as well as split maxima, illustrating more variation in natural calcite textures than previously demonstrated.

1.6 OBSERVATIONS ON LATTICE DEFECTS

The use of the Transmission Electron Microscope (TEM) as an analytical tool in the study of materials has made it possible to investigate intracrystalline deformation in calcite on the scale of lattice defects. Primary goals in this have been to correlate the observed linear defects (dislocations) to the macroscopically identified glide

Burgers vector direction	associated dislocations	material	reference
$<2\bar{1}\bar{1}0>$ b_1	dipoles on r-plane	single crystal	Braillon et al. 1974, Braillon and Serughetti 1976b
$<\bar{2}021>$ b_3	dipoles dipoles on r free dislocs, dipoles, loops dislocation arrays // r	single crystal single crystal Solnhofen lmst Carrara marble	Braillon and Serughetti 1976b Braillon et al. 1978 Schmid et al. 1977 Schmid et al. 1980
$<2\bar{1}\bar{1}0>$ b_1 $<10\bar{1}1>$ b_2 $<\bar{2}021>$ b_3	dislocation-reactions, nodes	Yule marble	Goetze and Kohlstedt 1977
$<\bar{1}100>$ b_4	dislocations limiting planar (growth?) defects // c	single crystal	Braillon and Serughetti 1976a
$<40\bar{4}1>$ b_8	dislocations in e-twin boundaries	single crystal	Braillon and Serughetti 1976b

Table 1.4
Directions of Burgers vectors in calcite reported in the literature. Number codes b_x after Goetze and Kohlstedt (1977).

systems, and to determine the orientation and length of the associated displacement vectors, i.e. the Burgers vectors.

Experimentally deformed calcite single crystals have been studied in TEM by Braillon et al. (1974, 1978), Braillon and Serughetti (1976a, 1976b), and Barber and Wenk (1976), experimentally deformed calcite polycrystals by Barber and Wenk (1979a), Schmid et al. (1977, 1980), Goetze and Kohlstedt (1977) and Briegel and Goetze (1978), and naturally deformed calcite rocks by Barber and Wenk (op. cit. and 1979b) and Briegel and Goetze (op. cit.). All found dipole and loop structures, and complex patterns of curved dislocations which interact with each other and seldomly lie in well-defined planes. Burgers vector analyses (by contrast experiments) appeared to be difficult, mainly because of the relatively rapid radiation damage of calcite in the electron beam. Table 1.4 summarizes the, unfortunately rarely well-evidenced, Burgers vector directions presented in the above literature. From this table, it can be seen that a Burgers vector parallel to $<\bar{2}021>$, associated with dislocations on the **r** plane, is often observed. This Burgers vector orientation corresponds to the macroscopically determined slip direction for **r**-slip (cf. Table 1.2). Other Burgers vectors are found, but cannot easily be related to specific glide mechanisms.

1.7 APPLICATION OF EXPERIMENTAL RESULTS TO NATURAL CALCITE DEFORMATION

The principal aim of experimental rock deformation in geology is to provide constraints on rheological behaviour and stress states under *natural* conditions. The results of experimental studies on calcite polycrystals, however, are not often incorporated in analyses of naturally deformed calcite rocks, in contrast for example to work on olivine. Exceptions are formed by the work of Schmid (1982) and Pfiffner (1982), who present studies of deformed limestones from the Helvetic zone of the Alps, attempting to bridge the gap between experiment and (field, optical and TEM) observations on naturally deformed material. They conclude that the observed microstructures can satisfactory be explained by either (experimentally calibrated) power law creep, at stresses up to 100 MPa, or by grain boundary sliding controlled creep, at stresses below 10 MPa. In general however, most studies are concentrated on specific aspects of deformation, such as microstructures (e.g. Vernon 1981, Heitzmann 1987) or textures (e.g. Dietrich and Song 1984, Dietrich 1986). The main reasons for the modest application of experimental results to studies of naturally deformed calcite rocks probably lie in the lack of reproducibility of laboratory data (refer Fig. 1.4) and the associated problems with extrapolation to natural conditions (e.g. Paterson 1985) plus the generally more complex histories of natural rocks.

1.8 PROBLEM DEFINITION AND SCOPE OF THE PRESENT WORK

The above review of the literature illustrates the extensive work already done on plastic deformation of calcite, but also shows remaining gaps. These are highlighted below.

The generally accepted set of main glide systems (**e**, **r**, **f**) has been used in all studies directed at modelling texture development in calcite aggregates. Such modelling requires detailed specification of the single crystal glide systems and their relative strenghts. However, while slip on **r** and **f** in the negative sense is widely reported, only very limited and contradictory data are available for **r** and **f** slip in the positive sense. Furthermore, there are insufficient data on the temperature and strain rate dependence of the absolute strengths (critical resolved shear stresses) of the **e**, **r** and **f** systems to allow their *relative strengths* to be estimated with confidence, particularly under geological conditions. The present study aims to present further fundamental data on the active glide systems in calcite, particularly on slip on **r** and **f** in the positive sense, in order to help facilitate meaningful texture modelling for calcite rocks. To obtain such data, compression experiments have been performed on calcite single crystals in two crystallographic orientations, one orientation aiming to activate slip on **r** and **f** in the positive sense, the other orientation directed to activate negative slip on these systems, thus enabling a comparison of slip behaviour in opposite senses.

Laboratory experiments have provided insight into the mechanical behaviour and the development of microstructures in calcite rocks, but the inherent complexity of polycrystals hampered an unambiguous identification of the specific mechanism(s) controlling the rate of deformation. In the present study, observations on the creep behaviour of calcite *single* crystals are reported, that is, on the influence of strain rate on the plastic deformation of single crystals. Such data offer a basis for developing a better understanding of the dislocation plastic behaviour of calcite *poly*crystals, in particular since single crystal data provide information on intracrystalline processes independently of grain boundary (i.e. grain size) effects. Emphasis is laid on deformation at relatively high temperatures (550 to 800 °C), because this links up with existing work on polycrystals, and has received less attention than low temperature (20-550 °C, see Table 1.2) plastic deformation. An attempt will be made to relate the macroscopically observed creep behaviour to microphysical models for intracrystalline deformation by dislocation mechanisms. In order to do this in a meaningful way, transmission electron microscopy of dislocations in deformed crystals is incorporated.

It is hoped that new fundamental data on plastic deformation of calcite single crystals will find applications in future modelling of creep behaviour and texture development, providing enhanced insight into deformation mechanisms and conditions in natural calcite tectonites.

1.9 ORGANIZATION OF THIS THESIS

In the following chapters of this thesis (chapters 2 and 3), the experimental method and results of compression experiments on single crystals of calcite in two orientations will be given, reporting mechanical data and observations on glide systems and lattice defect microstructures. The results of the experiments will be used to determine relative strengths of the calcite glide systems in chapter 4, discussing the significance for texture modelling. In chapter 5, the defect substructure observed in experimentally deformed samples will be related quantitatively to the flow behaviour of the single crystals. The observed behaviour is then compared with microphysical models for intracrystalline deformation in chapter 6, in an attempt to identify the rate controlling creep process. Finally, a naturally deformed calcite rock is described in chapter 7, and the experimental results on single crystals are applied, along with other data, in an attempt to assess the paleostress associated with deformation.

CHAPTER 2

EXPERIMENTAL COMPRESSION OF CALCITE SINGLE CRYSTALS - Part 1: deformation by r^+ and f^+ slip

2.1 INTRODUCTION

This chapter reports a series of 67 deformation experiments performed on calcite single crystals at strain rates in the range 3×10^{-4} to 3×10^{-8} sec^{-1} and at temperatures (T) between 400 and 800 °C (i.e. $0.4 T_m$ to $0.7\ T_m$, where T_m is the incongruent melting temperature of calcite in the system CaO-CO$_2$ at 100 MPa pressure - see Wyllie and Tuttle 1960). The crystals were uniaxially compressed in the $[40\bar{4}1]$ direction following Spiers and Wenk (1980), and were found to deform by e-twinning (T<600 °C) and by slip on r and f in the positive sense. The effective slip direction on the active f-plane was found to be of $<10\bar{1}1>$ type rather than the $<2\bar{2}01>$ type reported previously for f-slip. At strains above 1-2%, steady state flow was observed at T≥550-600 °C. Flow stresses were rather insensitive to strain rate and can be empirically described by power law creep equations with stress exponents ranging from ~13 at 550-600 °C to ~9.5 at 700-800 °C. TEM study of deformed crystals revealed dislocations predominantly of mixed character, with widely distributed line orientations. The dislocations frequently form loose irregular networks oriented oblique to the active slip systems.

2.2 THE SAMPLES: Preparation and Orientation

The present experiments were performed on cleaved calcite 'prisms' compressed in the $[40\bar{4}1]$ direction, i.e. parallel to the intersection of two rhombohedral (r) cleavage planes (arbitrarily denoted r_2 and r_3 here). The morphology and dimensions of the samples are illustrated in Fig. 2.1a, while the orientation of the compression axis with respect to the crystal axes is shown in the stereographic projection of Fig. 2.1b. The samples were prepared from elongated rhombs of calcite cleaved from four large parent crystals of optical quality 'iceland spar' (total trace element content <
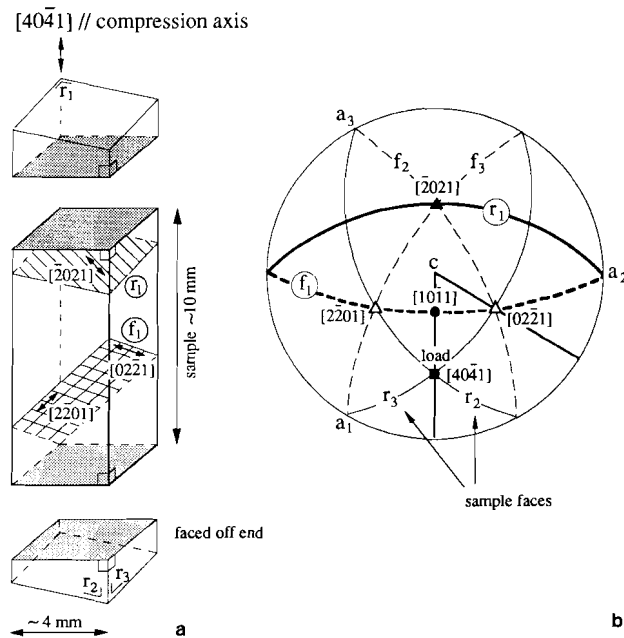
Figure 2.1
a) Morphology, dimensions and crystallographic orientation of the samples used in the present study. Stippled areas denote the loaded ends of the cleaved and trimmed sample (cleavage rhombs).
b) Stereographic (upper hemisphere) Wulff projection of calcite showing relevant planes and directions. Compare with Fig. 2.1a and Table 2.2.

400 ppm, individual trace elements ≤ 100 ppm - Table 2.1). The ends of the cleaved rhombs were trimmed using a diamond saw, thus producing the final geometry shown in Fig. 2.1a (aspect ratio ~2.5). The cleaved (vertical) faces of the samples were of high optical quality with only occasional cleavage steps being present. Prior to deformation, all samples were annealed at 500 °C for a period of 24 hours to remove dislocation damage. TEM analysis of the annealed samples showed the residual dislocation density to be less than ~10^6 cm^{-2}.

As described above, the samples were compressed parallel to their length, i.e. in the [40$\bar{4}$1] direction (Fig. 2.1a,b). The corresponding Schmid factors for the **e**, **r** and **f** glide systems generally reported in the literature, are listed in Table 2.2. From this table it is clear that the chosen orientation is unfavourable for e-twinning. However, it is relatively favourable for slip on the r_1 (10$\bar{1}$4)[$\bar{2}$021]⁺ system (S=0.31), on the two symmetrically disposed f_1 ($\bar{1}$012)[$\bar{2}\bar{2}$01]⁺ and f_1 ($\bar{1}$012)[02$\bar{2}$1]⁺ systems (S=0.38), and on f_2 (1$\bar{1}$02)[02$\bar{2}$1]⁻ and f_3 (01$\bar{1}$2)[$\bar{2}\bar{2}$01]⁻ (S=0.38; refer Table 2.2 and Figs 2.1a,b).

	Parent P1			Parent P2			Parent P3			Parent P9		
Ce	100.4	±2.1	(6)	98.6	±3.6	(6)	96.6	±4.1	(6)	98.6	±5.3	(6)
Mg	75.6	±1.2	(6)	49.8	±3.5	(6)	73.1	±1.8	(6)	100.1	±1.5	(6)
Sr	11.4	±0.2	(8)	11.7	±0.3	(9)	16.9	±0.2	(8)	21.8	±0.4	(8)
Zn	4.2	±3.3	(6)	2.4	±1.0	(6)	16.8	±3.0	(5)	69.0	±0.6	(8)
Ti	8.2	±1.0	(7)	7.5	±1.5	(9)	8.0	±0.9	(8)	8.2	±1.1	(7)
V	7.1	±0.4	(6)	6.9	±0.4	(6)	6.5	±0.5	(6)	6.6	±0.6	(6)
P	< 6		(6)	< 6		(6)	13.5	±1.2	(6)	< 6		(6)
Cu	4.0	±0.4	(8)	4.1	±2.0	(9)	3.3	±0.4	(8)	3.4	±0.2	(8)
Cr	2.3	±0.8	(8)	2.1	±1.1	(9)	1.9	±0.6	(8)	2.3	±0.6	(7)
Zr	1.3	±0.3	(6)	1.0	±0.2	(6)	1.5	±0.5	(6)	1.2	±0.3	(6)
Y	0.26	±0.09	(8)	0.15	±0.04	(9)	6.8	±0.1	(8)	2.1	±0.1	(8)
Mn	0.44	±0.08	(8)	≤0.17	±0.07	(8)	0.26	±0.13	(8)	0.25	±0.03	(7)
Be	0.06	±0.02	(8)	≤0.05	±0.02	(9)	0.28	±0.01	(8)	0.59	±0.03	(8)

Table 2.1
Trace element content (in ppm) of calcite parent crystals, analyzed by Inductively Coupled Plasma (ICP) emission spectrofotomtry. Table shows analytical mean, standard deviation and number of analyses (in brackets). The following elements fell below the corresponding detection limit: K (< 30 ppm), Pb (< 20 ppm), Ni (< 3 ppm), S (< 2.4 ppm), Co (< 2 ppm) and Li (≤ 0.4 ppm). Analyses for Na, Fe, Al, Ba, Si and B were found too inaccurate for presentation, but were not likely to exceed a few ppm.

e-twinning:
e_1 $(\bar{1}018)[40\bar{4}1]$ S=0
e_2 $(1\bar{1}08)[\bar{4}401]^+$ S=0.12 positive sense
e_3 $(01\bar{1}8)[0\bar{4}41]^+$ S=0.12 positive sense

r-slip:
r_1 $(10\bar{1}4)[\bar{2}021]^+$ S=0.31 positive sense
r_2 $(\bar{1}104)[2\bar{2}01]$ S=0
r_3 $(0\bar{1}14)[02\bar{2}1]$ S=0

f-slip:
f_1 $(\bar{1}012)[2\bar{2}01]^+[02\bar{2}1]^+$ S=0.38, 0.38 positive sense both
f_2 $(1\bar{1}02)[\bar{2}021]^+[0\bar{2}\bar{2}1]^-$ S=0.20, 0.38 positive and negative sense resp.
f_3 $(01\bar{1}2)[\bar{2}021]^+[\bar{2}20\bar{1}]^-$ S=0.20, 0.38 positive and negative sense resp.

Table 2.2
Schmid factor S for the main twinning and glide systems generally quoted for calcite, as calculated for loading in the $[40\bar{4}1]$ direction. Slip directions after Wenk (1985). All indices refer to the hexagonal cell with a=4.99 Å and c=17.06 Å, upper hemisphere coordinates.

2.3 EXPERIMENTAL METHOD

2.3.1 Apparatus

The samples were deformed in uniaxial compression using an Instron 1193 testing machine equipped with an externally heated, controlled atmosphere cell (Fig. 2.2). The tests were carried out at temperatures in the range 400 to 800 °C, making use

↓ LOAD

movable cross head

water cooling

cylindrical piston, made of Rene 41 (Ni) super alloy

controlling thermocouple

CO_2 outlet

O-ring seal

ceramic furnace, Kanthal A windings

controlled atmosphere cell (two halfs)

platinum seal between two halfs of the atmosphere cell

sample

lower piston

CO_2 inlet

O-ring seal

measuring thermocouple

water cooling

10 cm

5 kN load cell

a)

Figure 2.2
a) diagram of the experimental apparatus used in the present tests.
b), c) (right page), details from Fig. 2.2a.

b)

water cooling

CO_2-outlet

controlled atmosphere cell

5 kN load cell

top half of atmosphere cell

platinum seal

sample

lower piston

thermocouple

platinum wire to hold sample

c)
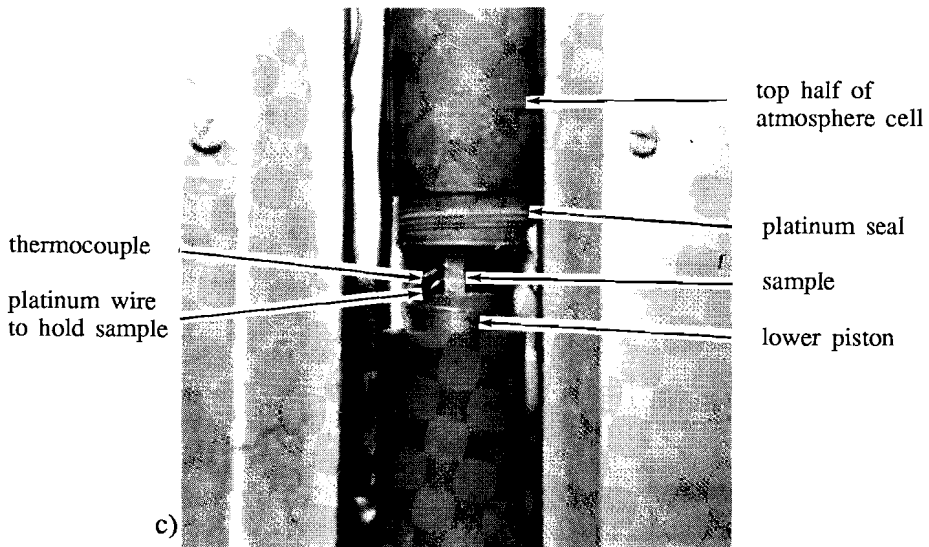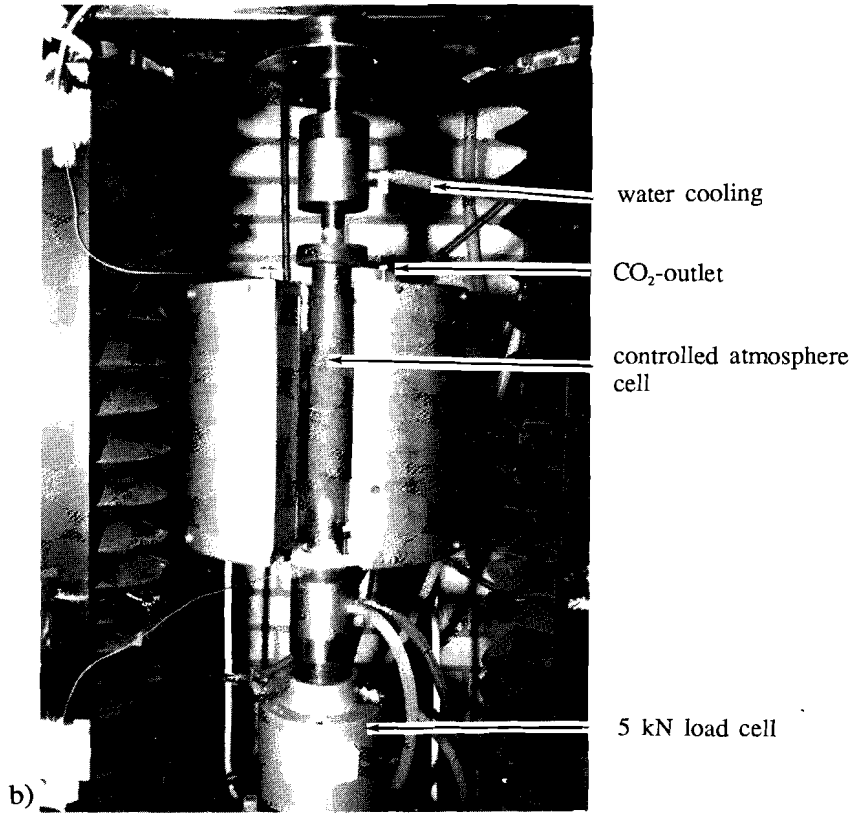
of a two zone furnace. Temperature was controlled using a Eurotherm (type 093) controller connected to a Chromel-Alumel (Cr-Al) thermocouple positioned at the furnace outside the specimen cell. One other thermocouple was used for temperature measurement adjacent to the sample. The experimental apparatus allowed temperatures to be kept constant within ~3 °C. The temperature drop between the centre of the sample and the contacts with loading the pistons was ~4 °C.

The first 20 samples were deformed in air at atmospheric pressure. All other tests were carried out using a CO_2 atmosphere maintained at 0.25 MPa overpressure. The purpose of this was to suppress decomposition of the samples. The controlled atmosphere cell was isolated from the laboratory atmosphere using O-ring seals and a platinum gasket between the two halves of the tube assembly (see Fig. 2.2c). The O-rings caused a constant resistance against movement of the pistons, varying between 10 and 25 N.

2.3.2 Procedure

Three types of experiments were performed:

1) Most experiments were conducted at fixed displacement rate, i.e. fixed cross head speed (accuracy better than 0.1% of the set speed). At low strains, this gives approximately constant strain rate; between 2 and 10% shortening the strain rate increases less than 1% per % strain (e.g. see Fig 2.7a further on). Strain rates ranged from 3×10^{-4} to 3×10^{-7} sec^{-1}.

2) A number of tests were performed in strain rate stepping mode, in which the displacement rate was instantaneously increased or decreased one order of magnitude per step (slowest step 3×10^{-8} sec^{-1}).

3) Two test were carried out in strain rate cycling mode, stepping the displacement rate succesively down and up and vice versa (one order of magnitude per step).

In all experiments, the sample was first located between the loading pistons. In controlled atmosphere tests, the sealed tube was flushed with CO_2 before closing the outlet (see Fig. 2.2) and gradually setting the small overpressure. In all tests, the sample was then heated to the desired temperature, leaving the apparatus until thermal equilibrium was reached. Before actually deforming a sample, the loading piston was advanced freely until a constant level of O-ring resistance was reached. All tests were terminated by rapidly unloading the sample, with immediate quenching using a blast of cold CO_2 gas (i.e. directly from a CO_2 bottle with the pressure regulator set at 0.25 MPa), followed by removing the specimen from the furnace.

2.3.3 Data acquisition and processing

Axial load was measured with an external Instron load cell with an absolute error $\leq$ 0.5% of the measured load. The raw load signal was recorded versus time using a chart recorder. After digitizing the curves, the accuracy of the recorded load was around 2%. The load-time data were processed to produce stress-strain curves, calculating displacement from cross-head velocity and elapsed time, and applying appropriate corrections for apparatus stiffness, thermal expansion of the crystal and change in cross-sectional area of the sample assuming homogeneous deformation and constant volume. Taking into account the individual errors of measured sample dimensions (length accurate within 0.25%; volume within 1.30%), calculated displacement (absolute accuracy ~4 μm), and changing cross-sectional area during deformation (accurate within 1.30%), errors in strain were less than 0.0035 (i.e. 0.35%) and errors in stress <~2.4% were found. In practice, single crystals do not deform homogeneously, but rather evolve as shown in Fig. 2.3. This reduces the accuracy of the computed cross-sectional area, yielding a maximum error of ~5%.

a)   b)
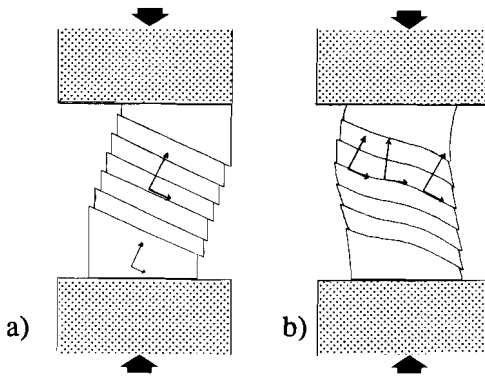
Figure 2.3
Deformation of a single crystal between two solid pistons by glide on a single system, with (b) and without (a) friction on the contact surface. Note the heterogeneous straining, with rotation of the glide plane (b).

2.4 MECHANICAL DATA

2.4.1 Stress-strain behaviour

The complete set of 67 tests reported here is listed in Table 2.3, where samples originating from a specific parent crystal (P1, P2, P3 and P9, cf. Table 2.1) are grouped together. Figures 2.4 to 2.8 show a representative selection of the stress-strain curves obtained for the experiments. Note that in the initial pseudo-elastic part of the curves, almost all of the measured strain was permanent.

Table 2.3

experiment	parent crystal		temperature [°C]	strain rate [sec⁻¹]	flow stress at 5% strain [Mpa]
54sc31	P1		400	3.0×10^{-5}	~105 *
53sc29	P1		450	3.0×10^{-5}	~115 *
11sc03	P1	Air	500	1.7×10^{-5}	93.3
02sc04	P1	Air	500	2.0×10^{-5}	failed
07sc12	P1	Air	550	3.2×10^{-4}	114.2
12sc17	P1	Air	550	1.6×10^{-3}	failed
13sc18	P1	Air	550	3.0×10^{-5}	failed
19sc26	P1	Air	550	3.1×10^{-5}	85.5 *
\ step			550	3.5×10^{-6}	75.6
\ step			550	3.2×10^{-7}	67.4 *
05sc16	P1	Air	550	3.1×10^{-5}	86.2
03sc01	P1	Air	550	3.2×10^{-5}	73.7
01sc05	P1	Air	550	3.1×10^{-5}	70.7
04sc02	P1	Air	550	1.6×10^{-5}	68.9
06sc13	P1	Air	550	3.1×10^{-6}	68.6
16sc19	P1	Air	600	3.0×10^{-4}	failed
17sc23	P1	Air	600	3.0×10^{-4}	78.8
14sc15	P1	Air	600	3.1×10^{-5}	59.2
55sc32	P1		600	3.2×10^{-5}	53.7
20sc33	P1	Air	600	1.0×10^{-5}	49.4
\ step			600	1.1×10^{-6}	43.5 *
\ step			600	1.1×10^{-7}	36.0 *
15sc20	P1	Air	600	3.1×10^{-6}	50.3
18sc24	P1	Air	600	3.0×10^{-6}	65.3 *
\ step			600	3.2×10^{-7}	54.5
\ step			600	3.2×10^{-6}	40.5 *
10sc10	P1	Air/D	650	3.2×10^{-4}	61.0
08sc09	P1	Air/D	650	3.2×10^{-5}	39.3
09sc11	P1	Air/D	650	3.2×10^{-6}	28.9
36sc22	P1		650	3.1×10^{-5}	53.0
35sc28	P1		650	3.1×10^{-6}	41.6
\ step			650	3.1×10^{-7}	37.7 *
23sc14	P1		800	3.0×10^{-5}	20.1
29sc61	P2		550	2.1×10^{-5}	stopped at 1.8%
30sc52	P2		550	2.9×10^{-5}	94.2
31sc61	P2		550	3.0×10^{-5}	failed
46sc69	P2		550	2.8×10^{-6}	93.1
40sc42	P2		550	2.9×10^{-7}	88.3 *
\ step			550	2.9×10^{-6}	89.0
51sc68	P2		600	2.9×10^{-4}	85.9
34sc46	P2		600	3.1×10^{-5}	68.3
48sc75	P2		600	2.9×10^{-5}	67.5
42sc37	P2		600	2.8×10^{-6}	54.3
32sc39	P2		600	3.0×10^{-6}	58.7 *
\ step			600	3.0×10^{-7}	46.9 *
49sc63	P2		600	2.9×10^{-7}	46.5
\ step			600	3.2×10^{-8}	42 *
44sc62	P2		650	2.9×10^{-4}	55.3
45sc67	P2		650	2.9×10^{-5}	52.5
41sc43	P2		650	3.1×10^{-6}	37.3

Table 2.3 continued

experiment	parent crystal	temperature [°C]	strain rate [sec^{-1}]	flow stress at 5% strain [Mpa]	
27sc41	P2	650	2.9x10^{-5}	54.3 *	
\ step		650	2.9x10^{-6}	44.6	
\ step		650	3.0x10^{-7}	36 *	
43sc49	P2	700	2.9x10^{-4}	49.0	
21sc45	P2	700	3.1x10^{-5}	42.2	
38sc47	P2	700	2.9x10^{-5}	44.9	
39sc50	P2	700	3.0x10^{-6}	34.0	
26sc36	P2	700	2.7x10^{-6}	32.4 *	
\ step		700	2.8x10^{-7}	26.5	
37sc51	P2	700	3.0x10^{-7}	22.5	
52sc66	P2	800	2.9x10^{-4}	40.8	
22sc44	P2	800	1.7x10^{-5}	30.5	
24sc34	P2	800	2.7x10^{-6}	25.4	
25sc40	P2	800	2.8x10^{-6}	26.8	
28sc38	P2	800	3.0x10^{-7}	19.6	
					final stress [MPa] and strain (%)
60sc89	P3	650	3.0x10^{-5}	39	39.3 (7.1%)
61sc90	P3	650	3.0x10^{-5}	39.5	39.5 (5.4%)
62sc91	P3	650	3.0x10^{-5}		38.1 (4.0%)
63sc92	P3	650	3.0x10^{-5}		39.7 (3.0%)
64sc93	P3	650	3.0x10^{-5}		39.9 (1.1%)
65sc94	P3	650	3.0x10^{-5}		34.4 (1.2%)
66sc95	P3	650	3.0x10^{-5}		19.6 (0.4%)
47sc74	P9	550	3.0x10^{-5}	70.3	
33sc73	P9	600	3.1x10^{-5}	53.1	
59sc78	P9	650	3.1x10^{-4}	60.5	
50sc72	P9	650	3.1x10^{-5}	38.8	
58sc70	P9	650	3.1x10^{-6}	28.7	
67sc79	P9	650	3.1x10^{-7}	28.7 #	
\ step		650	3.2x10^{-6}	33.3	
\ step		650	3.2x10^{-5}	40.9 #	
\ step		650	3.4x10^{-4}	55.7 #	
\ step		650	3.5x10^{-5}	44.4 #	
\ step		650	3.6x10^{-6}	35.7 #	
\ step		650	3.7x10^{-7}	30.6 #	
56sc77	P9	700	3.1x10^{-5}	30.3	
57sc76	P9	800	3.1x10^{-5}	22.9	

Table 2.3
List of experiments on crystals cleaved from parent crystal P1, P2, P3 and P9. All tests performed in a CO_2 atmosphere, except those denoted 'Air'. 'D' indicates samples which desintegrated after the test due to (incipient) decomposition (P1, 650 °C, air). Star (*) indicates flow stresses obtained by (linear) extrapolation of the steady state portion of the stress-strain curve to 5% strain. In five experiments, the crystals failed after pervasive twinning, before enough strain was reached to allow accurate extrapolation to 5%. Experiments 27sc41 and 67sc79 were strain rate cycling experiments, flow stresses denoted # were determined just before a step in strain rate.
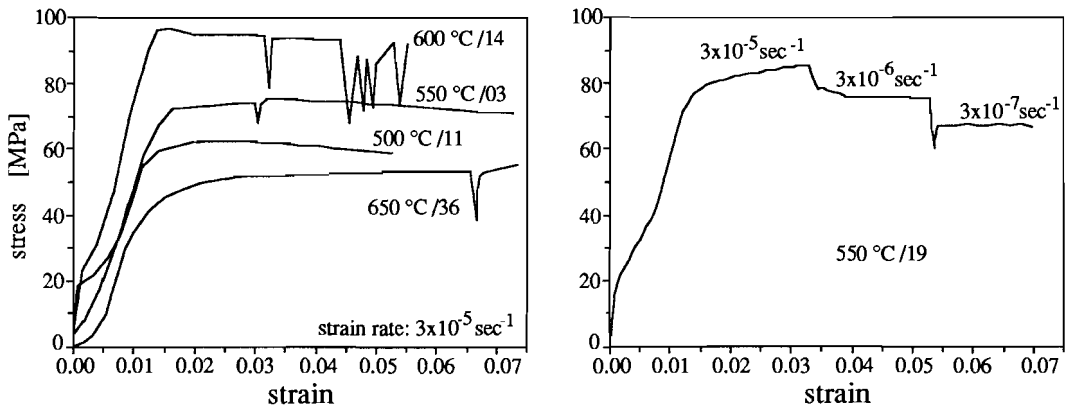
Figure 2.4
*Typical stress strain curves obtained for calcite single crystals from parent crystal
P1. Each curve is labelled with test temperature and test no. (cf. Table 2.3).*
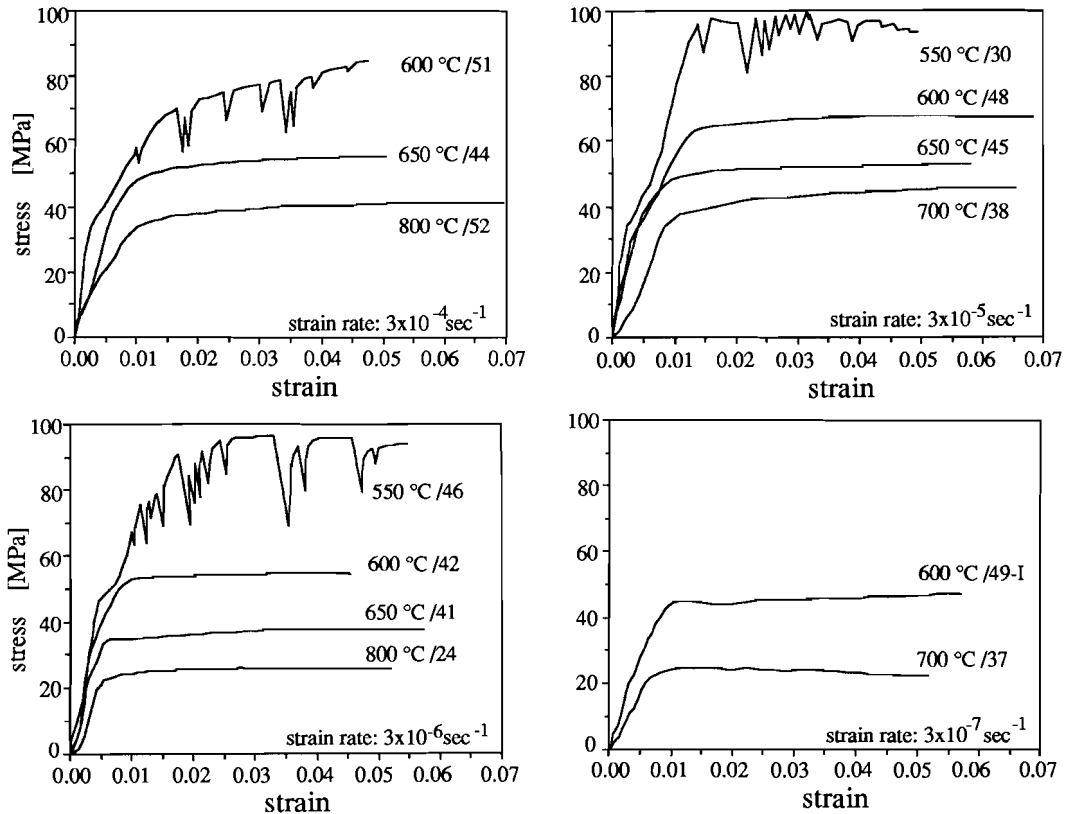
Figure 2.5
*Typical stress strain curves obtained for calcite single crystals from parent crystal
P2. Each curve is labelled with test temperature and test no. (cf. Table 2.3).*
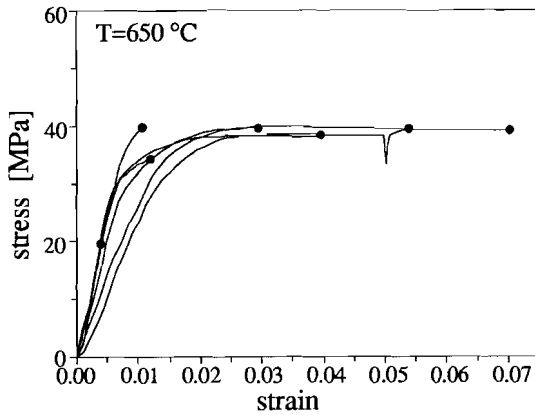
Figure 2.6
Stress-strain curves obtained
for calcite single crystals from
parent crystal P3. Temperature
650 °C, strain rate 3x10⁻⁵ sec⁻¹.
Dots indicate end points of
curves.
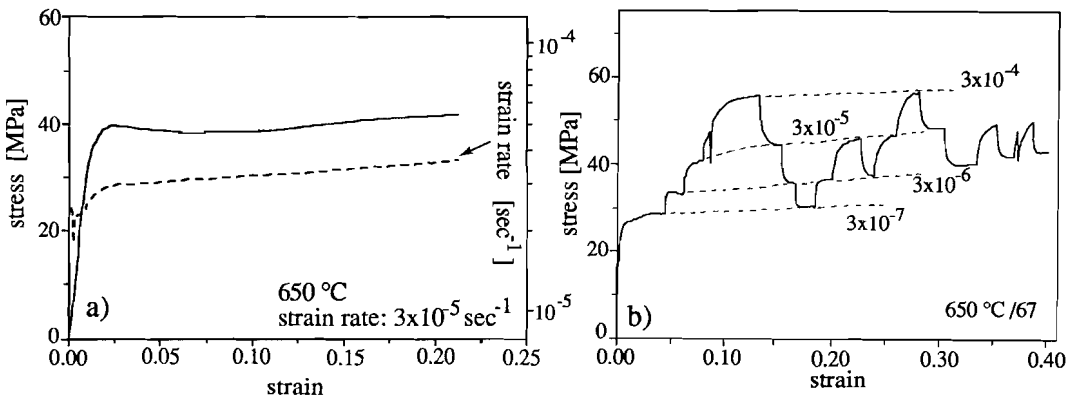
Figure 2.7
Stress-strain curves obtained for calcite crystals from parent crystal P9. Dashed line
in a) indicates dependence of strain rate on strain. The curve in b) is an example
of a strain rate cycling test, at four different rates of straining. Note the high strains
achieved in these compression tests.
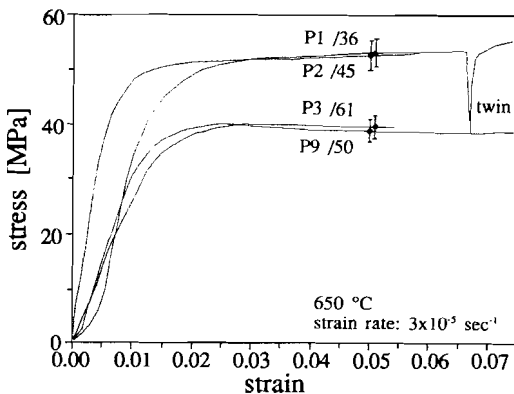
Figure 2.8
Stress strain curves obtained
for samples from four different
parent crystals, at identical
experimental conditions.
5% error bars indicated.

The stress-strain curves show two broad types of behaviour:

1) Discontinuous stress-strain behaviour with frequent instantaneous load drops. This was seen in all tests performed at T≤500 °C, in several tests at 550 °C for samples from parent crystal P1, and in tests at 550 °C and the fastest test at 600 °C for samples from parent crystal P2 (Figs. 2.4 and 2.5). As in many metals (Reed-Hill et al. 1964), the load drop behaviour was found to be associated with deformation twinning (see section 2.5). Occasional twins sometimes developed at T>600 °C (e.g. Figs. 2.4, 2.6) but were found to be associated with anomalous stress concentrations at the corners of the sample.

2) Smooth stress-strain behaviour, with more or less steady state flow being achieved at strains of 1-2%. This was seen in all tests not showing twinning, i.e. in almost all tests at T≥550-600 °C. Minor hardening was sometimes observed at strains above 5%, as illustrated in Fig. 2.7a, but this was shown to be not significantly greater than apparent hardening effects expected as a result of sample shortening (increasing strain rate at constant piston displacement rate) and crystallographic rotation (Fig. 2.3) during deformation.

In the case of repeated experiments, that is, tested under identical experimental conditions, samples taken from individual parent crystals (e.g. P3, Fig. 2.6) yielded flow stresses (or upper bound stresses in case of twinned samples) in the 'steady state' region which deviate not more than 5% (average value of 11 duplicate tests, one standard deviation 4%) from the mean flow stress at those conditions. This value is comparable to the estimated error in individual stress levels (see section 2.3), implying that repeated experiments did not show *significant* differences in steady state flow stress, though considerable variability was seen at low strains (below 1% - e.g. Fig. 2.6). In contrast, samples taken from *different* parent crystals did show significant differences in steady state flow stress (Fig. 2.8), forcing separate treatment of the data sets obtained from each parent.

In strain rate stepping and cycling experiments, performed across the temperature range 550-700 °C (refer Table 2.2), steady state flow stresses were re-established within 0.4% strain (Figs. 2.4b, 2.7b) and were found to be independent of stepping history (see Fig. 2.7b). When extrapolated linearly to 5% strain, flow stresses obtained from the stepping and cycling tests were closely similar to values obtained from corresponding constant strain rate tests.

2.4.2 Stress vs. strain rate data

The steady state flow stresses (or upper bound stresses in the case of twinned samples), arbitrarily measured at 5% strain (see Table 2.3), are plotted in standard log-log plots of strain rate versus stress in Figs. 2.9-2.11. These figures show the complete set of strain rate vs. stress data obtained, and correspond to parent

crystals P1, P2 and P9 respectively. In all cases, the flow stresses (σ) are clearly rather insensitive to strain rate ($\dot{\epsilon}$). Individual isotherms, fitted assuming a power law relationship of the type $\dot{\epsilon} \propto \sigma^n$, yield stress exponents (n) in the range 12-16 at T$\approx$600 °C, decreasing to ~9.5 at 700-800 °C (Table 2.4). Note the two different 650 °C isotherms for crystals cleaved from parent P1 (Fig. 2.9). Here, the flat lying isotherm (n~14) describes deformation behaviour in a CO_2 atmosphere under slight overpressure, while the steeper isotherm (n~6) corresponds to crystals deformed in air. The latter samples showed evidence of minor decomposition and tended to disintegrate after the experiment, particularly in the case of longer term tests. For this reason, the mechanical data obtained for samples tested in air at 650 °C are not considered further.

The dependence of (steady state) flow stress on temperature is illustrated in the log stress versus 1/T plots given in Figs. 2.12-2.14. The lines of constant strain rate in these plots show an increase in slope at temperatures rising from 400 to 550 °C (Fig. 2.12), followed by a decrease in slope towards 800 °C (Figs. 2.13 and 2.14), suggesting a change in apparent activation energy for creep with changing temperature.
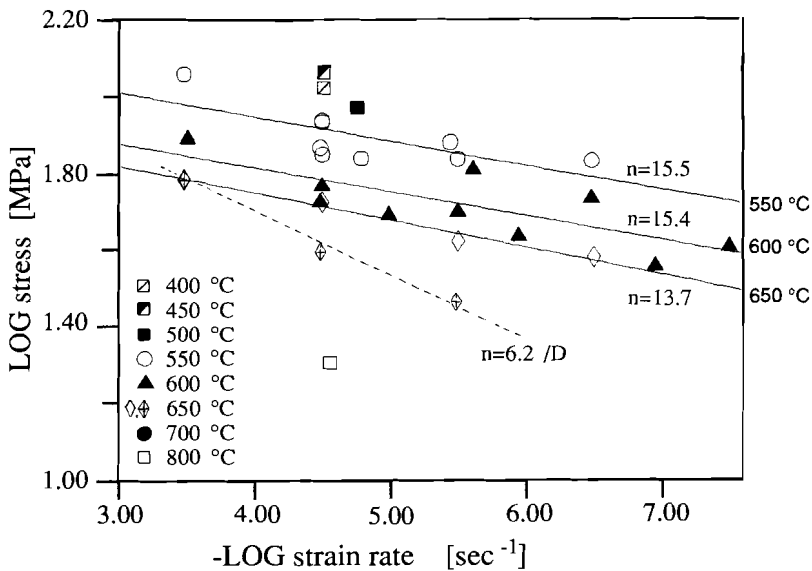
Figure 2.9
Log-log plot of strain rate vs. differential stress, constructed using the flow stresses (or upper bound stresses in case of twinned samples) supported at 5% strain, parent crystal P1 - see Table 2.3. Strain rate stepping data are incorporated. Best fit isotherms have been drawn assuming individual power law relationships (see Table 2.4). Dashed isotherm is based on mechanical data from samples deformed in air, which samples tended to disintegrate after the experiment.
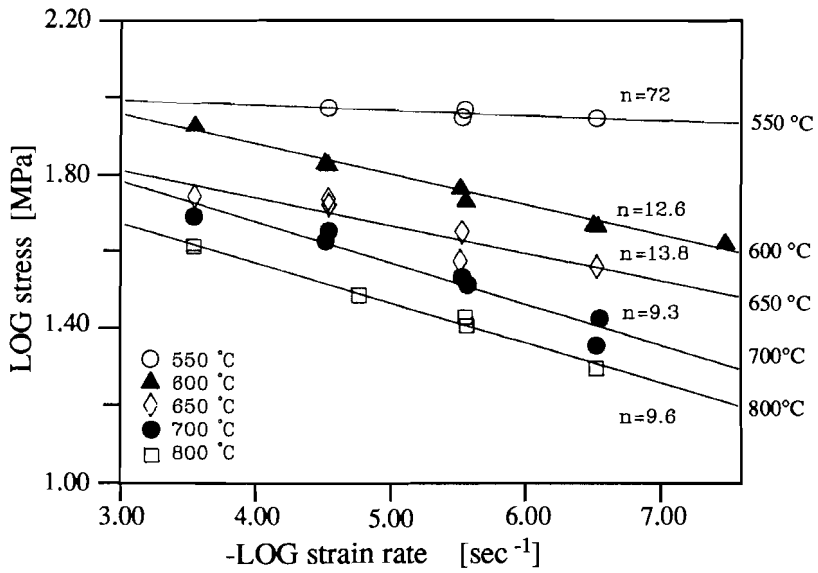
Figure 2.10
Log-log plot of strain rate vs. differential stress (as Fig. 2.9), parent crystal P2. See
Table 2.3.
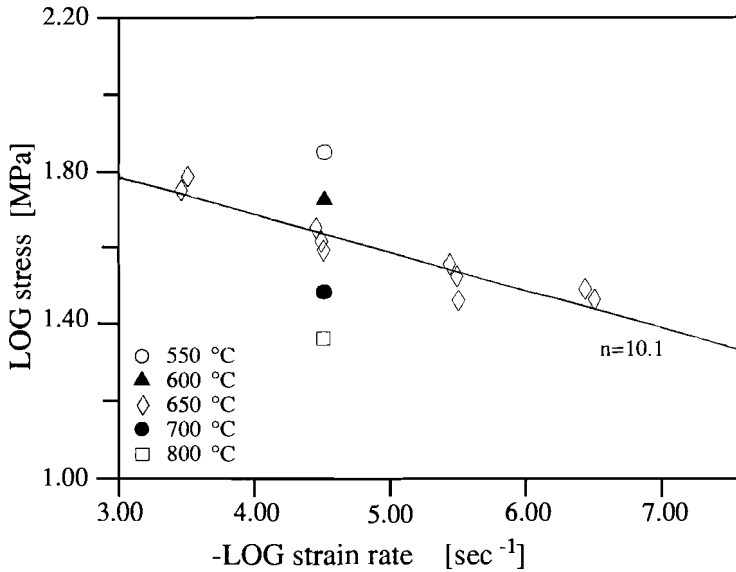
Figure 2.11
Log-log plot of strain rate vs. differential stress (as Figs 2.9 and 2.10), parent
crystal P9. See Table 2.3.

isotherm [°C]		n	error	corr.	data
P1	550	15.5	±5.3	0.746	9
	600	15.4	±4.3	0.789	10
	650	13.7	±1.5	0.988	4
	650 D	6.2	±0.6	0.995	3
P2	550	71.7	±37.2	0.808	4
	600	12.6	±0.8	0.990	8
	650	13.8	±3.2	0.907	6
	700	9.3	±1.1	0.967	7
	800	9.6	±0.6	0.994	5
P9	650	10.1	±1.3	0.940	10

Table 2.4
Stress exponents for individually fitted isotherms assuming a power law relationship between stress and strain rate, $\dot{\varepsilon} \propto \sigma^n$, obtained by linear regression in logaritmic space. Indicated are standard error, correlation coefficient (corr.) and number of data points used in regression. 'D' refers to samples which tended to disintegrate after the experiments. The flow stress value at $\dot{\varepsilon}=3 \times 10^{-4}$ sec^{-1} and T=650 °C (see Fig. 2.9) was included in the linear regressions for both 650 °C isotherms.
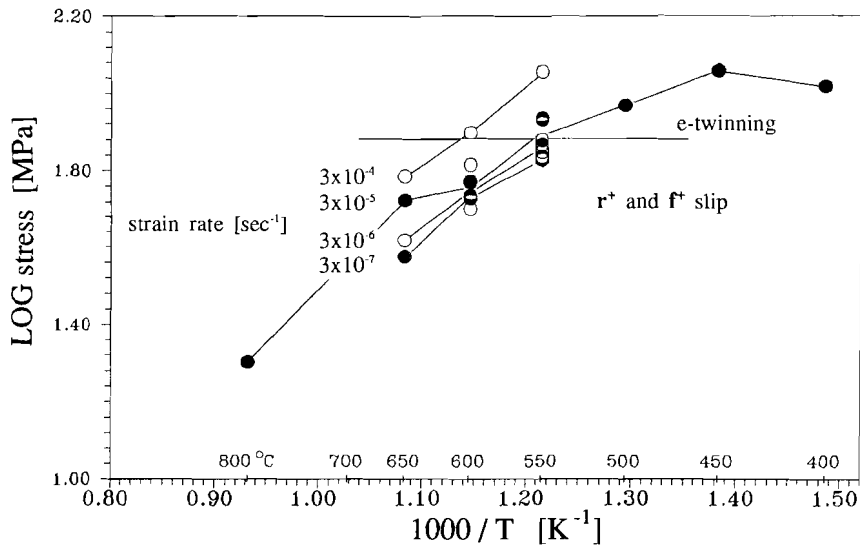
Figure 2.12
Log flow stress vs. reciprocal temperature for samples from parent P1. Twinning and slip regimes are based on data presented in Fig. 2.19a.
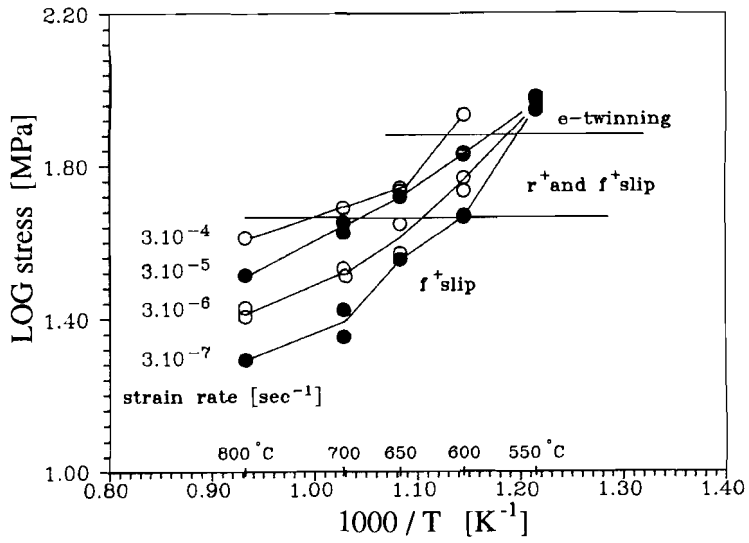
Figure 2.13
Log flow stress vs. reciprocal temperature for samples from parent P2. Twinning and slip regimes are based on data presented in Fig. 2.19b.
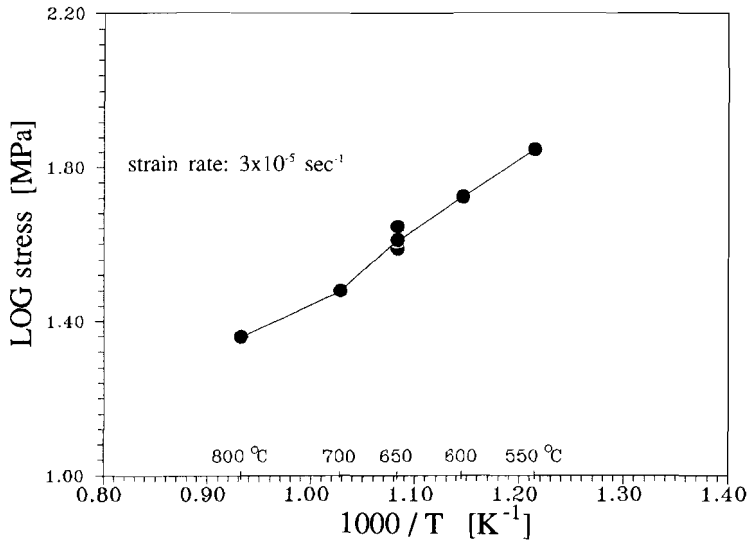
Figure 2.14
Log flow stress vs. reciprocal temperature for samples from parent P9.

2.4.3 Influence of starting composition

As mentioned previously, samples cleaved from different parent crystals, prepared following the same technique and tested under identical conditions of temperature and strain rate, show a significant difference in flow strength (see Fig. 2.8). This effect does not correlate with the use of air vs. CO_2 in the controlled atmosphere cell (see Table 2.3). The observed difference in strength must therefore be related to differences in starting material, such as the impurity and defect content or structure. Heat treatment and Electron Microscope analysis suggest the dislocation structure to be the same in all samples. No data are available on vacancy distribution, however, trace element analyses have been carried out on all parent crystals (Table 2.1). In Fig. 2.15, the results of these analyses are plotted against the (steady state) flow stress (averaged for individual parent crystals) for samples deformed at 600 and 650 °C at $\dot{\varepsilon}=3\times10^{-5}$ sec⁻¹. The diagrams are scaled such that the error in the analytical mean is comparable between individual plots. For almost all elements whose impurity content differs significantly (i.e. more than the error in the analytical mean) between parents, a *decrease* is observed in flow stress with *increasing* trace element concentration. An exception is the Mn-content at (T=650 °C), which shows a weak positive correlation with stress.
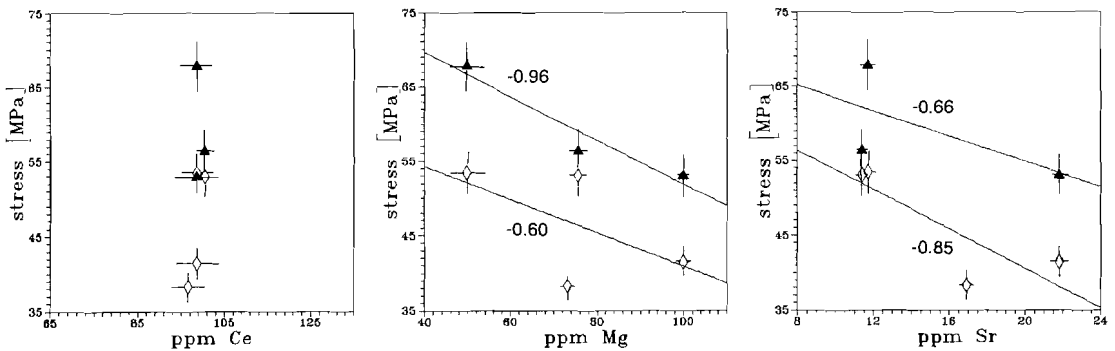
Figure 2.15
Flow stress vs. impurity content for calcite single crystals cleaved from four different parent crystals (refer Table 2.1). All flow stresses obtained at a strain rate of 3x10⁻⁵ sec⁻¹, temperatures 600 °C (closed triangles) and 650 °C (open lozenges). Best fit lines with correlation coefficient, determined by linear regression method.
Figure continued overleaf.
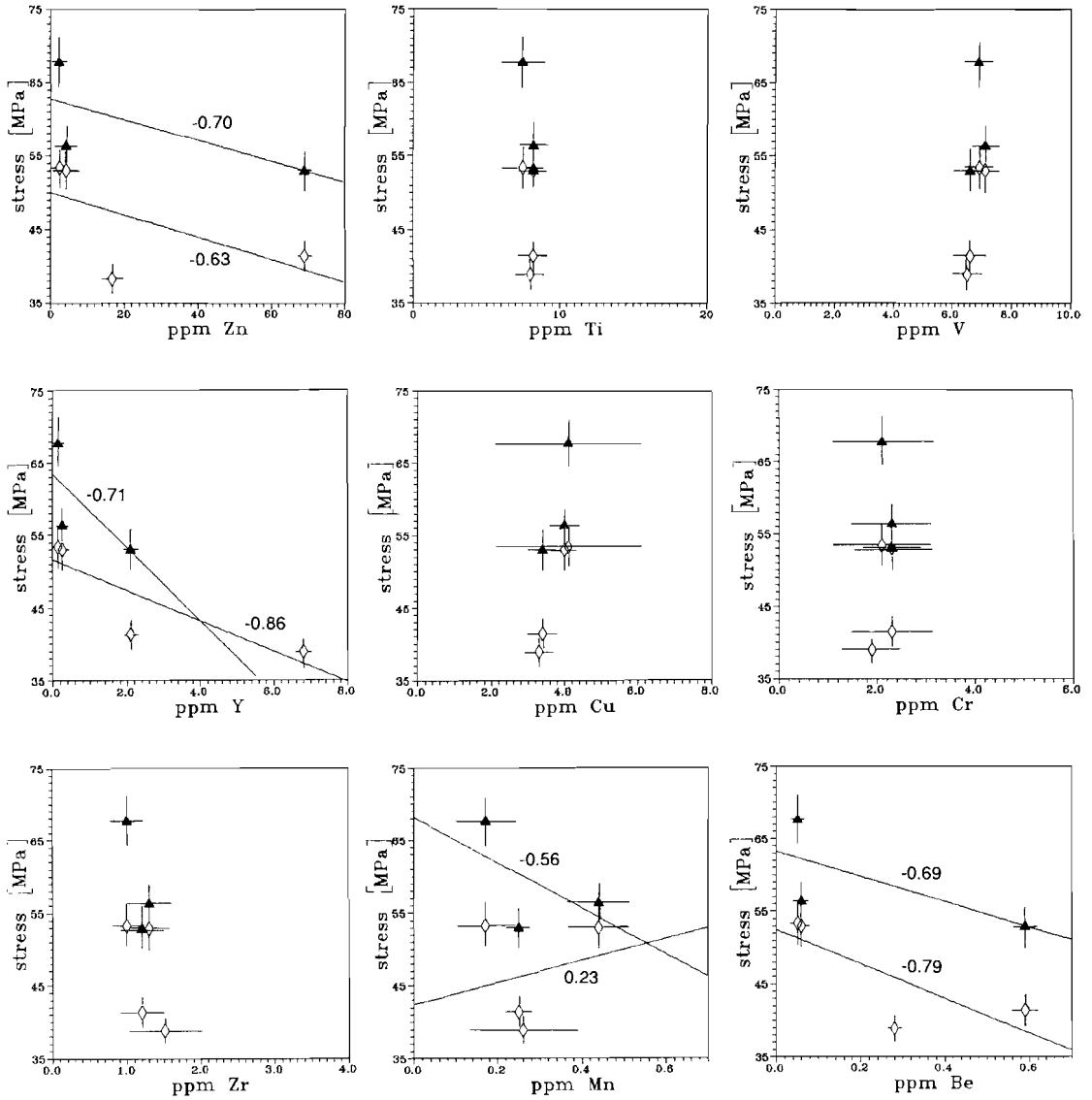
Figure 2.15 continued

2.5 GLIDE SYSTEMS AND OPTICAL / SEM MICROSTRUCTURES

The deformed crystals were studied using a number of techniques, including optical and scanning electron microscopy (SEM). Both were used to carry out 'slip line analysis', of the type frequently used in metallurgy to identify glide systems (Haasen et al. 1980). This technique, coupled with morphological observations, revealed that twinning on the e_2 and e_3 systems is important in all tests at $T \leq 500$ °C, in the tests performed at 550 °C on crystals cleaved from parent P2, and in the fastest tests at 550 and 600 °C for samples from P1 and P2 respectively. Occasional twins seen at higher temperatures were associated with anomalous stress concentrations at the corners of the sample. All samples showing load drop behaviour were found to contain twins.

In accordance with the above, little or no twinning was observed at $T > 600$ °C, i.e. in samples supporting flow stresses below 75 MPa. Examination of these samples revealed numerous slip lines, glide bands and kink bands (Figs 2.16-2.18), proving intense slip activity. Slip-line analysis, coupled with orientation analysis of glide bands seen in thin section, showed that the operative slip planes were r_1 and f_1 (refer Fig. 2.1a,b) with slip occurring in the positive sense on both. No evidence was found for slip on f_2 or f_3 (see Fig. 2.1b, Table 2.2) in any of the samples tested. In the case of the r_1 and f_1 planes, the observed slip lines could be traced continuously around the entire (cleaved) surface of the deformed samples (Figs 2.16d and 2.17), indicating that the operative slip directions did not lie in the r_2 and r_3 planes making up the sample surface (refer Fig. 2.1a,b). Taking the observed sense of shear on the r_1 and f_1 slip bands into account, and assuming that slip is confined to rational, low-index directions, this implies that slip occurred in the $[\bar{2}021]^+$ direction on r_1 and in the $[10\bar{1}1]^+$ direction on f_1 (see Fig. 2.1a,b). Geometric analysis of kink bands (Figs 2.16a,b and 2.17) and c-axis rotations associated with intense f_1 slip (carried out using the method of Turner et al. 1954) yielded rotation axes parallel to the a_2 direction (Fig. 2.1b), thus confirming that slip on f_1 occurred in the $[10\bar{1}1]$ direction.

The above indicates that the main *slip* systems activated in the present experiments were the $r_1(10\bar{1}4)[\bar{2}021]^+$ system and the $f_1(\bar{1}012)[10\bar{1}1]^+$ system. However, these two systems were not of equal importance under all conditions. Optical examination of the entire suite of samples revealed a transition from $r_1(10\bar{1}4)[\bar{2}021]^+$ slip plus minor f_1^+ slip (accompanying dominant twinning) at the higher strain rates and lowest temperature (550 °C), to dominant $f_1(\bar{1}012)[10\bar{1}1]^+$ slip at the lower strain rates and higher temperatures. This transition is illustrated with a series of optical micrographs in Fig. 2.18, and is mapped as a function of stress, temperature and strain rate in Fig. 2.19. Note that r_1^+ slip was observed to be important only at flow stresses above ~60 MPa. The absence of significant twinning at stresses below 75 MPa is also indicated in Fig. 2.19.

Observations on slip band morphology are now reported. Firstly, the r_1 and f_1 slip
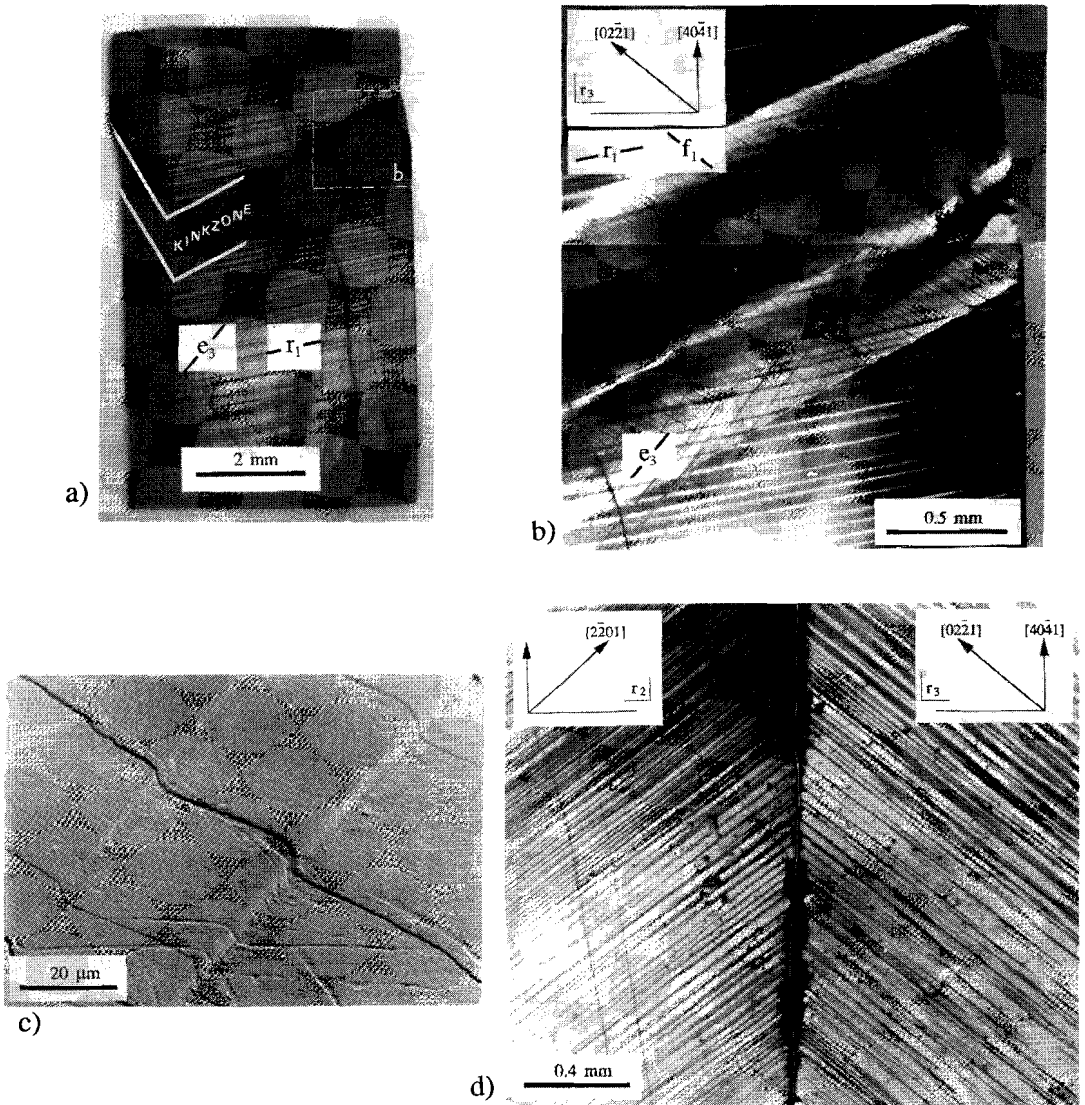
Figure 2.16
a) Deformed single crystal of calcite with r_1-slip traces, local e_3-twinning and a kink band dominated by f_1-slip (outlined area refers to Fig. 2.16b). Load direction vertical, sample 06sc13 (T=550 °C, $\dot{\varepsilon}$=3x10^{-6} sec^{-1}). See also Fig. 2.17
b) Detail of Fig. 2.16a showing part of the kink zone,
c) SEM (secondary electrons) micrograph of f_1-slip lines on a sample face,
d) f_1 slip lines traceable from the r_2 to the r_3 face in a sample deformed at T=650 °C and strain rate 3x10^{-5} sec^{-1}.

a)

b)
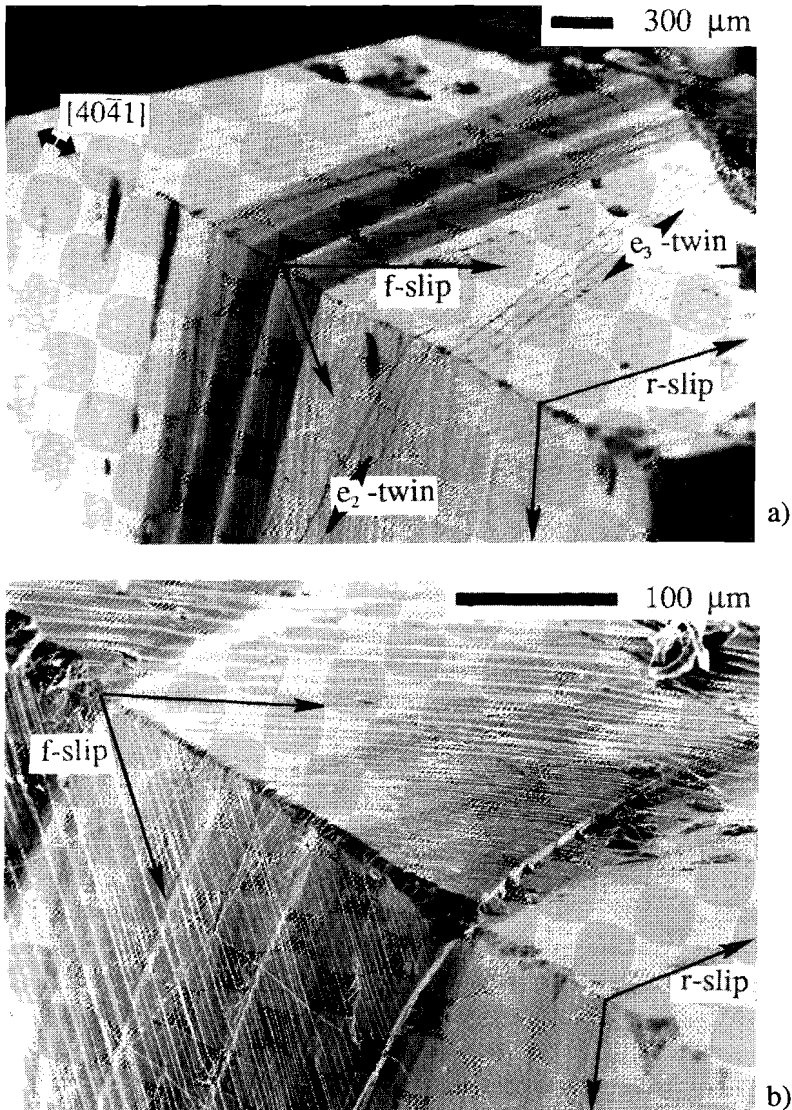
Figure 2.17
SEM (secondary electrons) micrographs of sample 06sc13 (T=550 °C, ἐ=3x10⁻⁶
sec⁻¹), see also Figs 2.16a,b.
a) r- and f-slip lines traceable from one sample face to the other, indicating a slip
direction oblique to both faces. e-twin surface phenomena are only visible on one
sample (r-)face, implying a twinning direction parallel to the other. The central dark
band denotes an f-slip dominated kink zone.
b) Detail from kinkzone in Fig. 2.17a.
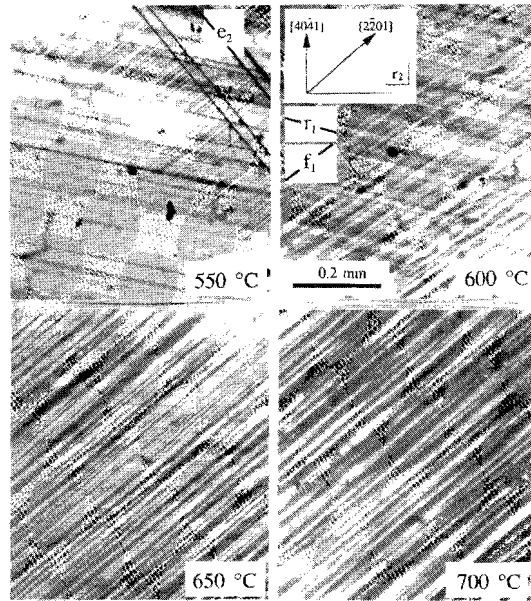
Figure 2.18
Optical micrographs showing the transition from r⁺ slip plus minor f⁺ slip
(accompanying twinning) at low temperature to pure f⁺ slip at high temperature,
seen on an r₂ cleavage plane (load direction vertical). parent crystal P2, strain rate
3x10⁵ sec⁻¹, compare with Fig. 2.19b.

bands tended to be straight. However, the f-slip bands were often seen to terminate in the body of the crystal, transferring their displacement to a neighbouring band in the manner illustrated in Fig. 2.20a. This type of feature will be referred to henceforth as 'slip band shift'. Locally, f-slip lines were found to be arranged in 'en echelon' packets, making a small angle with the f-plane (Fig. 2.20b), separated by regions of slip band shift. On a given sample face, both s- and z-asymmetry of the shift structure can be found. Very rarely, displaced slip bands are visibly interconnected by an oblique slip band (Fig. 2.20c).

Estimates of the total displacement accumulated across slip bands indicated that slip activity within these bands was responsable for the bulk of the imposed strain. These estimates were obtained from offsets observed in SEM micrographs. In addition, changes in the external shape of the crystals were found to be consistent with the observed slip systems.

Finally it is noted that all samples showed evidence of micro-cracking. Careful examination of samples during the quenching stage of the tests showed that these cracks were always introduced by the quench treatment.
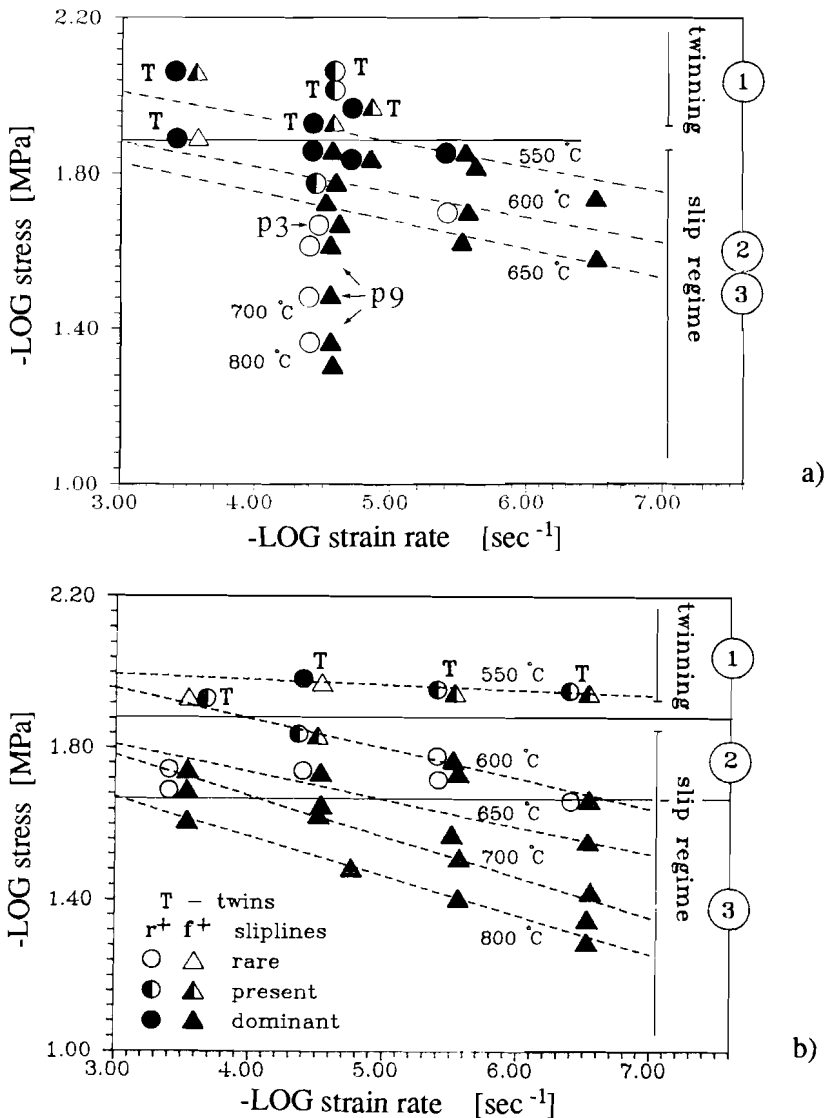
Figure 2.19
Log-log plots of strain rate vs. differential stress summarizing microstructural observations on twinning and slip activity:
a) For parent crystal P1, P3 and P9.
  (1): regime with dominant e-twinning, significant r_1^+ slip and minor f_1^+ slip,
  (2)/(3): regime with f_1^+ slip and minor r_1^+ slip
b) For parent crystal P2
  (1): twinnig regime as in a)
  (2): slip regime as 2/3 in a)
  (3): regime of pure f_1^+ slip.
Note that within the slip regime (2+3) f-slip dominates overall. Isotherms taken from Figs. 2.9 and 2.10.
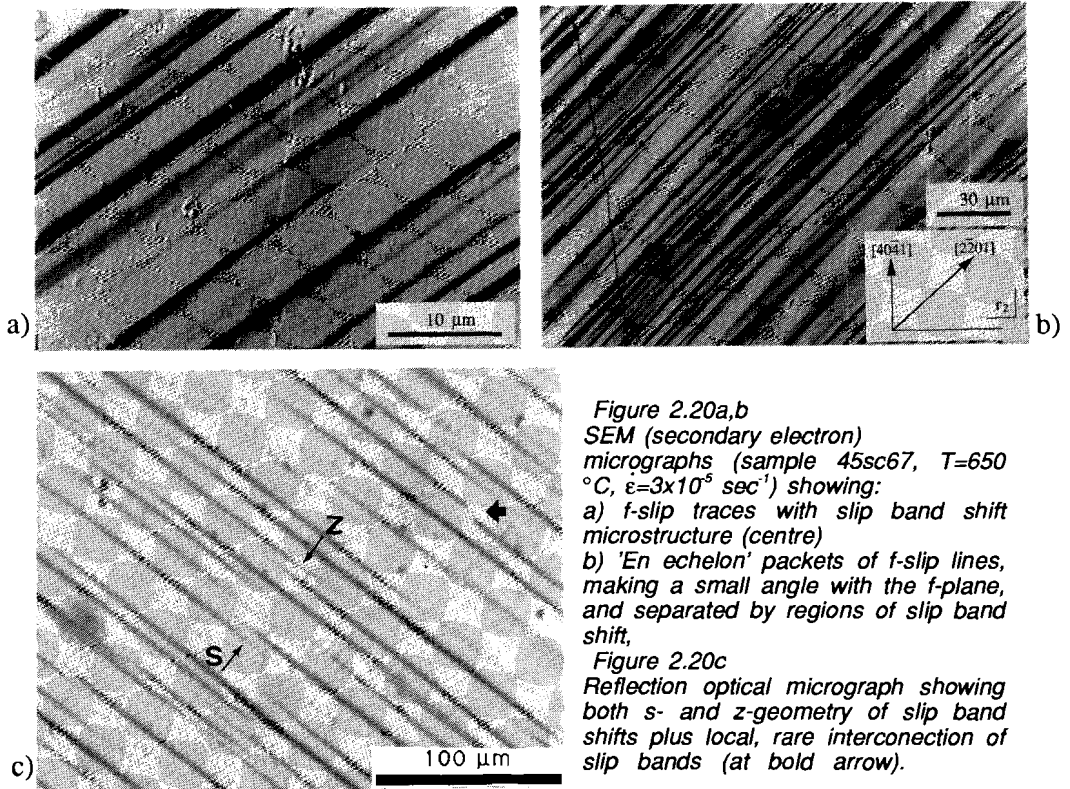
Figure 2.20a,b
SEM (secondary electron)
micrographs (sample 45sc67, T=650
°C, ε̇=3x10⁻⁵ sec⁻¹) showing:
a) f-slip traces with slip band shift
microstructure (centre)
b) 'En echelon' packets of f-slip lines,
making a small angle with the f-plane,
and separated by regions of slip band
shift,
Figure 2.20c
Reflection optical micrograph showing
both s- and z-geometry of slip band
shifts plus local, rare interconection of
slip bands (at bold arrow).

2.6 TEM MICROSTRUCTURES

2.6.1 Methods and aims

In the framework of the experiments reported in this chapter, one undeformed and 22 deformed crystals were selected for Transmission Electron Microscopy (TEM) study. In preparing the samples for TEM work, optical thin sections were first cut parallel to one of the cleavage planes (i.e. parallel to the loading direction in case of deformed samples). Grid-mounted TEM specimens ('foils') of 3 mm diameter were then prepared from the thin sections using standard methods. Conventional ion-milling techniques were used to create electron-transparent areas. A few specimens were made by simply glueing thin cleavage fragments directly onto support grids. These fragments came from a limited number of crystals which disintegrated after the deformation experiment (section 2.4.1). The edges of the fragments were found

thin enough for TEM study.

Transmission Electron Microscopy was performed using a JEOL 200C microscope with a side-entry double tilt goniometer stage, operating at 200 kV.

The aims of the TEM work were:

a) qualitative characterization of the dislocation substructure and its dependence upon deformation conditions;

b) analysis of dislocation line orientations in relation to the calcite crystallography and loading geometry;

c) determination of the Burgers vector of dislocations related to the active slip systems as identified by slip line analysis;

d) quantitative determination of the dependence of dislocation density on flow stress, to be treated seperately in chapter 5.

2.6.2 Characterization of the dislocation substructure

As mentioned in the description of the initial samples, undeformed annealed material showed only a few dispersed, slightly curved dislocations, with a density below $\sim 10^6$ cm^{-2}. The dislocation substructure of the deformed crystals, on the other hand, was found to be characterized by both straight and curved, locally helical dislocations suggesting active dislocation climb, and by irregular pseudo-hexagonal dislocation networks (Fig. 2.21). Kinks, jogs, loops, dipoles and dislocation debris were common. No tendency was observed for dislocations to be concentrated in bands. Well-defined tilt boundary configurations or subgrains were rare, and no evidence was found for dislocation dissociation.

Qualitatively speaking, the general nature of the dislocation microstructure of the deformed samples did not vary substantially with experimental conditions, although it changed in detail. Firstly, crystals deformed at the highest stresses showed, of course, numerous twin lammellae, but their boundaries rarely contained significant densities of twinning dislocations. More importantly, a clear decrease in density of dislocations was observed with decreasing flow stress (chapter 5). Towards lower flow stresses, the presence of the pseudo-hexagonal dislocation networks became more conspicuous, and they more closely approached an equilibrium polygonal configuration. Alongside these trends, the relative importance of curved dislocations in the total population appeared to decrease, as did the importance of helical dislocations and dipoles. At flow stresses below 35 Mpa no dipoles were observed.

Aside from the above, the samples deformed at 700-800 °C sometimes showed scattered rectangular voids ($\sim$0.1 μm diameter), locally developed on dislocations. Most dislocations however were free of these voids. No evidence was found for any correlation between the quenching cracks reported above and the observed dislocation substructure and/or density.
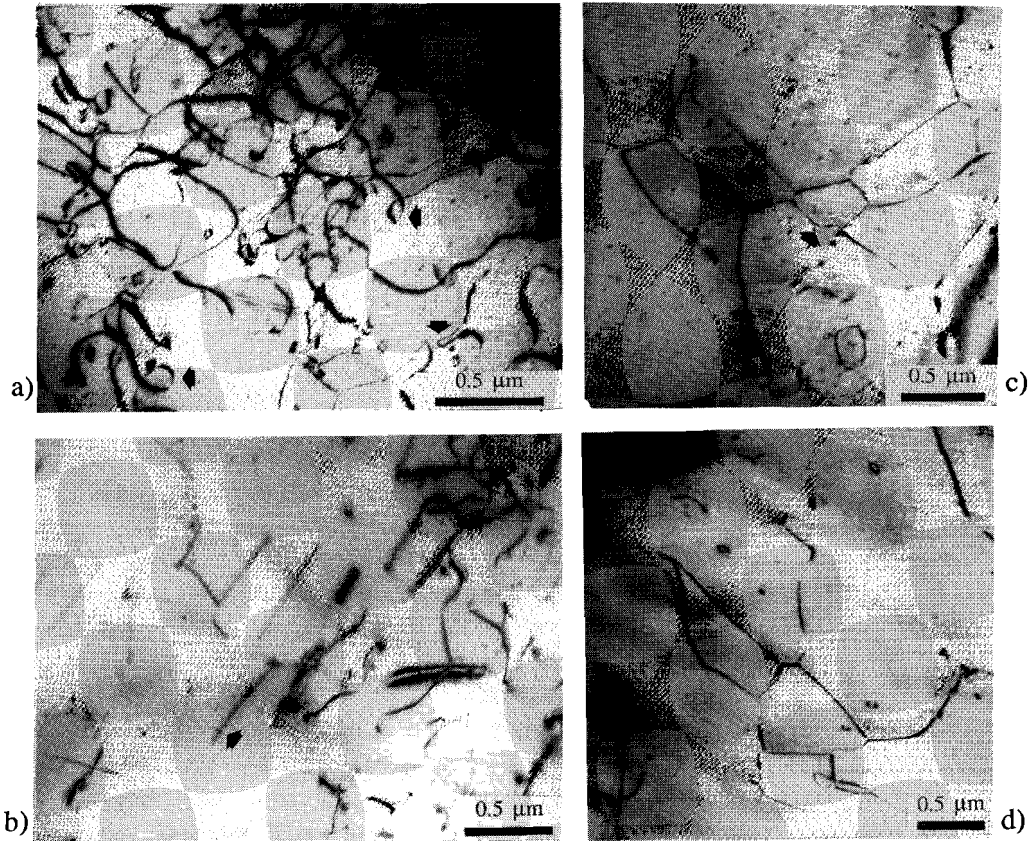
Figure 2.21
Bright field (multi-beam conditions) TEM micrographs showing typical dislocation microstructure in the deformed calcite single crystals;
a) dense configuration of dominantly curved, locally helical (horizontal arrows) dislocations and dislocation dipoles (vertical arrow). Sample 07sc12; T=550 °C, flow stress 114 Mpa.
b) straight individual dislocations, directions determined parallel [2̄021] (refer Fig. 2.1). Sample as in a)
c) and d) characteristic irregular dislocation network, with dislocation jog (arrow). Samples respectively 60sc89 (T=650 °C, flow stress 39 MPa) and 01sc05 (T=550 °C, flow stress 71 MPa).

2.6.3 Dislocation line orientations

The orientations of straight (segments of) dislocation lines were measured in TEM foils of three samples deformed under conditions where $f[10\bar{1}1]^+$ slip was the only active slip system as identified by slip line analysis (section 2.5), i.e. at low flow stresses and T=700-800 °C. For these measurements, fully oriented TEM foils were studied under various but controlled electron beam directions, making use of indexed diffraction patterns. Geometrical manipulations using the stereographic projection for calcite (Fig. 2.1) then allowed determination of dislocation line orientations to within 5°. As indicated above, all TEM foils were prepared (sub)parallel to one of the compression parallel cleavage planes, r_2 or r_3. Since r_2 and r_3 are symmetrically indistinguishable, the foil plane was arbitrarily designated as r_3.

Both individual dislocations and dislocation network segments were analysed for line orientation. The complete set of results is given in the stereographic projection of Fig. 2.22a. This shows the dislocation line orientations to be widely distributed with no clear tendency to lie in well-defined planes. Fig. 2.22b depicts the data obtained for network dislocations only. Data corresponding to dislocations interacting in a common node are linked with great circles. The network dislocations form both planar and three-dimensional structures in scattered crystallographic orientations, although a weak concentration of networks exists subparallel to $(0\bar{1}11)$.

Now, since the foil planes r_2 and r_3 (designated r_3) are symmetrically equivalent,
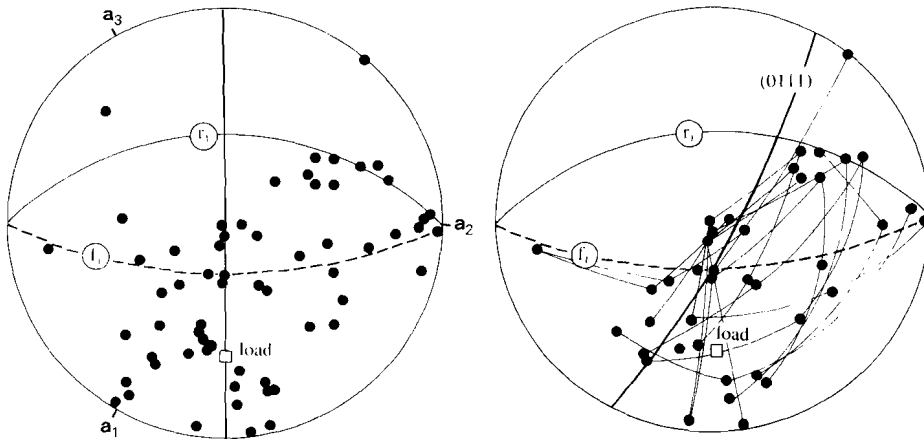
Figure 2.22
Measured orientations of dislocation lines in calcite single crystals deformed dominantly by f_1 slip at T=700-800 °C, given in a (Wulff) stereographic projection. In the diagram on the right, measured dislocations which join in network nodes are interconnected. See text for further discussion.

and since the loading direction lies in the a_2 plane bisecting the angle between r_2 and r_3 (see Fig. 2.1), the a_2 plane may be used as a mirror plane in a symmetry operation on all dislocation directions, in order to obtain a symmetrically homogenized picture of the line distribution. The resulting orientations are plotted and contoured on an equal area projection in Fig. 2.23. This shows a weak but clear concentration in the macroscopically active slip plane f_1, with maxima developed in the [10$\bar{1}$1] and [$\bar{1}$2$\bar{1}$0] directions, i.e. respectively parallel and perpendicular to the macroscopic slip direction. Other concentrations exist subparallel to the c-axis and the [$\bar{4}$401] and [0$\bar{4}$41] directions, and in a zone between a_1 and the loading axis [40$\bar{4}$1]. The concentrations denoted I (subparallel [$\bar{4}$401]), II (the f_1 plane) and III (a_1 to [40$\bar{4}$1]) in Fig. 2.23b comprise the three main groups of dislocations interacting in network nodes (compare with 2.22b).

The rigorous method of measuring dislocation line orientations employed above is a time consuming procedure. An impression of the dislocation arrangement in a large number of samples can be obtained more rapidly by measuring *projected* directions of dislocation lines on oriented TEM-images. Fig. 2.24 shows rose diagrams of randomly selected dislocation line segments projected on the foil plane r_3 (using the foil plane normal), in five samples covering most of the temperature range investigated. For comparison, a rose diagram is added of the data presented in Fig. 2.22a, also projected onto r_3.
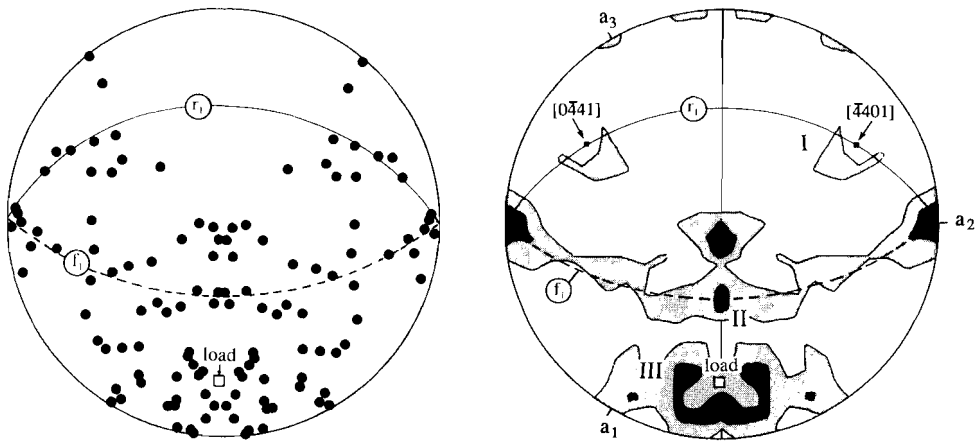
Figure 2.23
Measured orientations of dislocation lines from Fig. 2.22 after symmetry operation using a_2 as a mirror plane, contoured on the diagram on the right. Contour levels 1.5 and 3% per 1% area, 124 data points, equal area projection.
I, II and III denote preferent orientations for dislocations forming networks (cf. Fig. 2.22).

07sc12
T = 550 °C
σ = 114 Mpa
n = 198

01sc05
T = 550 °C
σ = 71 MPa
n = 150

62sc91
T = 650 °C
σ = 38 MPa
n = 168

24sc34
T = 800 °C
σ = 25 MPa
n = 142

23sc14
T = 800 °C
σ = 20 Mpa
n = 172

LOAD

after
Fig. 2.22a
T = 700-800 °C
σ = 20-25 MPa
n = 62

III $[2\bar{2}01]$

a_1

$[\bar{2}021]$

I
a_2

$[\bar{1}101]$

$[02\bar{2}1]$
$[0\bar{1}11]$

II

a_3 $[10\bar{1}1]$
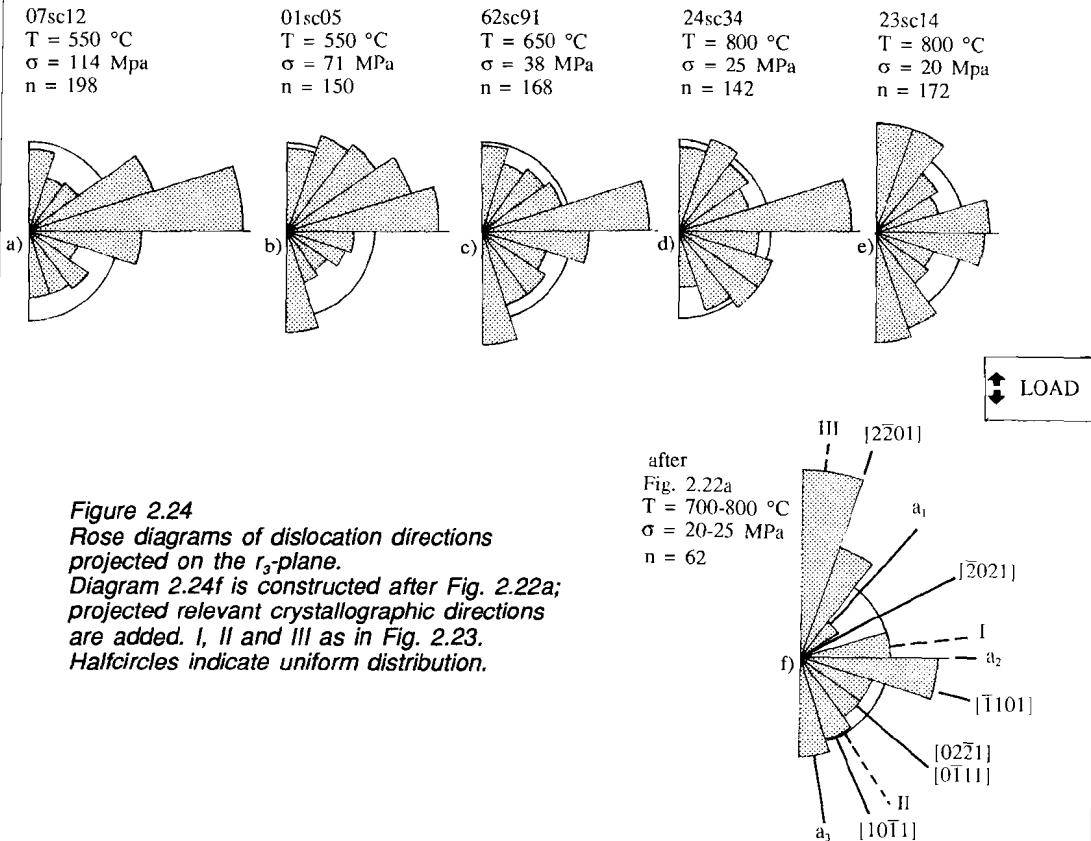
Figure 2.24
Rose diagrams of dislocation directions
projected on the r₃-plane.
Diagram 2.24f is constructed after Fig. 2.22a;
projected relevant crystallographic directions
are added. I, II and III as in Fig. 2.23.
Halfcircles indicate uniform distribution.

The following points emerge from Fig. 2.24:
a) the dislocations chosen for full orientation determination (Fig. 2.22a, projected in
   2.24f) form a reasonable reflection of the total population of dislocations measured
   in samples deformed at 700-800 °C (compare with Fig. 2.24d,e);
b) the rose diagrams show a substantial spread of dislocation orientations under all
   experimental conditions. Preferred orientation intensities are generally below two
   times uniform distribition, i.e. are relatively weak;
c) across the entire range of temperatures investigated, projected orientations
   parallel to the a_2 axis are dominant. At low temperature and high flow stress,
   projected dislocations parallel to $[\bar{2}021]$ are markedly present as well (Figs.
   2.24a,b), but towards higher temperatures and lower flow stresses, projected
   dislocations parallel to $[10\bar{1}1]$ become more important (Fig. 2.24d,e). This most
   likely represents the change in active slip system, from dominant $r[\bar{2}021]^+$ at LT-

high stress conditions towards pure f[10$\bar{1}$1]$^+$ slip at HT-low stress (cf. Fig. 2.18);
d) projected dislocation lines parallel to the I, II and III directions, which represent
   the preferred orientations forming the dislocation networks (Figs 2.22b and 2.23b),
   become more conspicuous at high temperatures and low flow stresses. This is
   consistent with the qualitative observation (section 2.6.2) that networks become
   better developed towards these conditions.

2.6.4 Burgers vector analysis of network dislocations

Experimental determination of Burgers vectors of dislocations can be done by
means of tilting experiments with contrast analyses in TEM (e.g. Christie and Ardell
1976). This is generally done by applying the dynamical theory of diffraction contrast
for two-beam conditions in an elastically isotropic crystal (e.g. Edington 1975). In this
theory, dislocations show no contrast (are 'invisible') for specific sets of diffracting
crystal planes. For a pure *screw* dislocation, there will be no contrast when $\bar{g} \cdot \bar{b} = 0$,
where $\bar{b}$ is the Burgers vector and $\bar{g}$ is the reciprocal lattice vector normal to the set
of diffracting planes. Thus, for all conditions where $\bar{g}$ is perpendicular to $\bar{b}$, screw
dislocations are expected to be out-of-contrast. In addition to $\bar{g} \cdot \bar{b} = 0$, an extra
condition must be fulfilled for invisibility of a pure *edge* dislocation; now also $\bar{g} \cdot \bar{b} \times \bar{u}$
must equal zero, $\bar{u}$ being a vector parallel to the dislocation line. Only one set of
diffracting planes, perpendicular to the edge dislocation, then results in invisibility.
For mixed dislocations, invisibility requires $\bar{g} \cdot \bar{b} = 0$, $\bar{g} \cdot \bar{b} \times \bar{u} = 0$ *and* $\bar{g} \cdot b_e = 0$, where b_e is
the edge component of the Burgers vector (Head et al. 1973, Edington 1975).

Strictly taken, the above only holds for elastically *isotropic* crystals - which do not
exist. However, it has been found, notably for metals (Christie and Ardell 1976), that
edge and mixed dislocations often only show faint ('residual') contrast when $\bar{g} \cdot \bar{b} = 0$
even if $\bar{g} \cdot \bar{b} \times \bar{u}$ and $\bar{g} \cdot b_e$ are not equal to zero. Thus, in practice the direction of a
Burgers vector is often determined using the $\bar{g} \cdot \bar{b} = 0$ criterion alone, interpreting
residual contrast as 'effective invisibility'. This method gives acceptable but not
always unambiguous results for Burgers vector directions. Dislocation image
matching by computer simulation (e.g. Head et al. 1973) is a powerful tool in further
analysis of thus-determined Burgers vectors, but requires elaborate knowledge on
the exact diffraction conditions, dislocation directions and foil orientation and
thickness.

Calcite is an elastically strongly anisotropic mineral (Heinisch et al. 1975), and it
damages quickly under the electron beam allowing little time for study. The present
orientation analysis (section 2.6.3) has also shown a scattered distribution of
dislocation lines in the single crystal samples, implying that these dislocations are
dominantly of mixed character. Referring to the above part of this section, accurate

Burgers vector analysis in materials with these characteristics is complicated. However, TEM analyses using the 'effective invisibility' criterion can be carried out with reasonable confidence (refer Table 1.4). This method was employed here.

For each two-beam condition producing effective invisibility of a dislocation segment, the product $\bar{g}\cdot\bar{b}$ was tested against the eight shortest Burgers vectors in calcite (see Table 2.8) in an attempt to locate $\bar{b}$ for which $\bar{g}\cdot\bar{b}=0$. This seldomly resulted in unambiguous determination of the Burgers vector for individual dislocations. For this reason, further analysis was focussed on dislocations interacting at three-fold nodes, since these are subject to additional constraints which assist determination of $\bar{b}$. Nodal dislocations have three different Burgers vectors, the sum of which must be zero (Hirth 1983). In addition, the line tension of the dislocations at each node, resulting from the elastic line *energies* (proportional to the square of the Burgers vector length), must also have a zero vector sum, provided that the nodal configuration is an equilibrium configuration (Goetze and Kohlstedt 1977). The angles between the dislocation lines x, y and z then are related to the line energies by

$$c \,/\, \sin(\hat{xy}) = b \,/\, \sin(\hat{xz}) = a \,/\, \sin(\hat{yz}) \qquad (2.1)$$

where a, b and c are proportional to the line energies (see Table 2.8) of dislocations x, y and z, and $\hat{yz}$, $\hat{xz}$ and $\hat{xy}$ are the corresponding angles between the dislocations.

Figs 2.25 and 2.26 and Table 2.9 give the diffraction conditions and contrast

Burgers vector		length	energy ratio	planes
b_1 1/3	$<2\bar{1}\bar{1}0>$	4.98 Å	1	r, f, e, c, a
b_2 1/3	$<10\bar{1}1>$	6.37 Å	1.6	f, a
b_3 1/3	$<2\bar{2}01>$	8.09 Å	2.6	r, f, a
b_4	$<01\bar{1}0>$	8.64 Å	3.0	c, a
b_5 1/3	$<1\bar{3}21>$	9.50 Å	3.6	r
b_6 1/3	$<\bar{1}012>$	11.50 Å	5.3	a
b_7 1/3	$<4\bar{3}\bar{1}1>$	11.80 Å	5.6	f
b_8 1/3	$<40\bar{4}1>$	12.80 Å	6.6	r, e, a

Table 2.8
Eight shortest possible Burgers vectors in calcite (after Goetze and Kohlstedt 1977). The line energy of a dislocation, in a first approach, can be regarded as proportional to the square of the Burgers vector length, resulting in the indicated energy ratios.
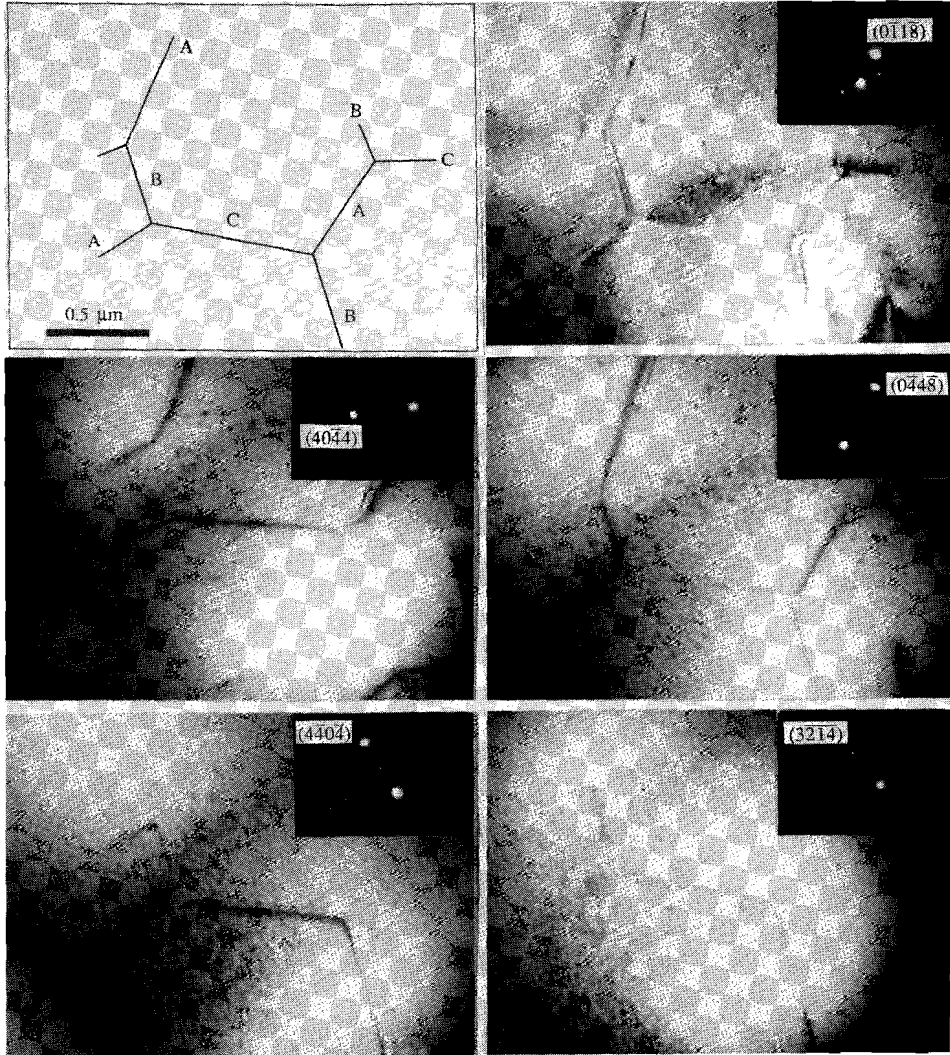
Figure 2.25
TEM contrast experiments on dislocation network ABC, Sample 37sc51 (T=700 °C, ε̇=3x10⁻⁷ sec⁻¹, dominant f⁺ slip). Refer Table 2.8.
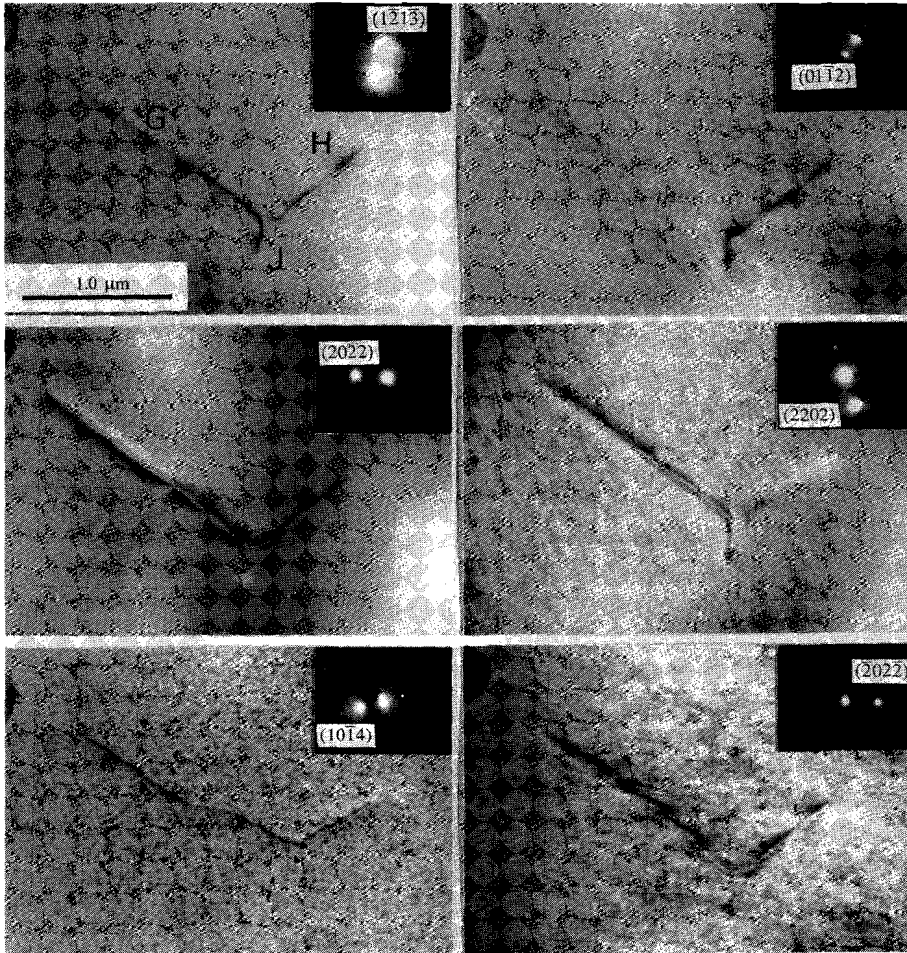
Figure 2.26
TEM contrast experiments on dislocation network GHJ, sample 24sc34 (T=800 °C, $\dot{\varepsilon}=3 \times 10^{-6}$ sec^{-1}, dominant f_1 slip). Refer Table 2.8).

operating diffraction condition	A	B	C	D	E	F	G	H	J	K
(01̄1̄8)	+	+	-							
(404̄4)	+	-	+							
(202̄2)							+	+	-	
(04̄4̄8)	+	+	-							
(011̄2)							-	+	+	
(4̄404̄)	-	+	+							
(2̄202)							+	-	+	
(32̄1̄4)	-	+	+							
(21̄1̄3)				-	+	+				
(2̄11̄3)				+	-	+				
(12̄1̄3)							+	+	+	
(101̄4)							+	+	-	
(2̄110)										+
(04̄48)										-
additional requirement	Σ b̄ = 0			Σ b̄ = 0			Σ b̄ = 0			
ratios of dislocation line energies	1.2	: 1.1	: 1	1.3	: 1.0	: 1	1.1	: 1	: 1.0	
resulting b̄:	[101̄1]	[1̄1̄01̄]	[2̄110]	[101̄1]	[1̄1̄01̄]	[2̄110]	[2̄110]	[112̄0]	[12̄10]	[2̄110]
		Fig. 2.25						Fig. 2.26		

Table 2.9
Results of contrast experiments on selected dislocations A to K (refer Fig. 2.27) from calcite crystals deformed at relatively high temperature and low flow stress. Strong contrast is indicated by +, residual or no contrast by a - sign. ABC, DEF and GHJ join in a network node, requiring Σb=0. Ratios of dislocation line energies are calculated using equation 2.2 and measured (mean) angles between dislocation lines. Length of the Burgers vector in all cases is ⅓[HKIL] (Table 2.8).

observations for three sets of network dislocations (plus one additional free dislocation) in samples deformed at high temperature and low flow stress, i.e. under conditions of pure f[101̄1]⁺ slip (cf section 2.6.3). The line orientations of the dislocations are depicted in Fig. 2.27. After measuring the angles between the dislocations interacting in nodes, energy ratios can be calculated and compared with ratios determined from predicted energies (Table 2.8). Combining the results from

contrast observations with the additional requirements at dislocation nodes (Table 2.9), two types of dislocation networks can be identified:

1) for one type (ABC, DEF, Fig. 2.25 and Table 2.9), conditions are found consistent with Burgers vectors parallel [10$\bar{1}$1], [1$\bar{1}$0$\bar{1}$] and [$\bar{2}$110]. With the exception of F, the dislocation lines of ABC and DEF make a relatively small angle (between 5 and 50°) with their corresponding Burgers vectors and therefore tend to lie in the (0$\bar{1}$11) plane. Note the presence of the [10$\bar{1}$1] Burgers vector here (cf. the inferred slip direction for f_1^+ slip);

2) for the second type (GHJ, Fig. 2.26), Burgers vectors were determined parallel to the a_1 , a_2 and a_3 axes. Again, the dislocation lines are oriented at a small angle (10-35°) to their corresponding Burgers vectors, hence lie subparallel to the basal plane.

Both type 1 and type 2 network dislocations are of mixed character, but with a dominant screw component. Networks oriented roughly parallel to (0$\bar{1}$11) were observed to be by far the most common type, as apparent from the line orientations in Fig. 2.22a. In addition, the contrast behaviour of these networks, tested for a limited number of two beam conditions, was found consistent with the Burgers vecotrs determined for the type 1 network.
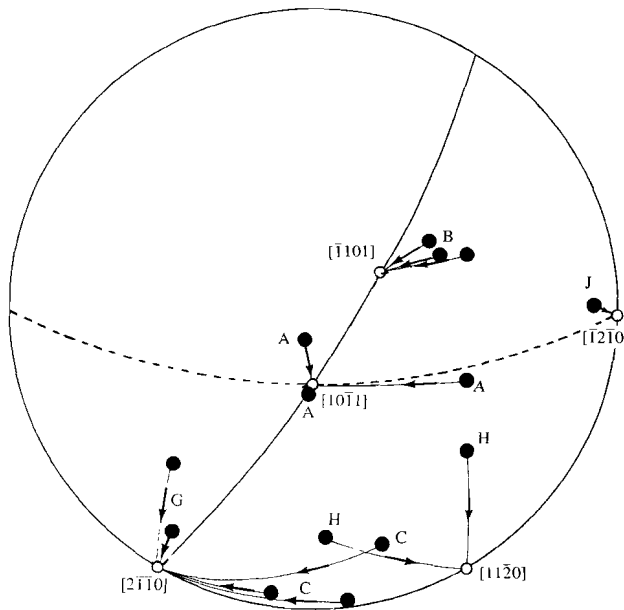
Figure 2.27
Dislocation line orientations and corresponding Burgers vectors for networks ABC and GHJ. Compare with Table 2.9 and Figs. 2.25-2.26.

2.7 DISCUSSION

2.7.1 Solid solution softening

The correlation between increasing impurity content and decreasing flow strength found in the deformed calcite samples (section 2.4.3) suggests that the presence of cations other than Ca^{2+} reduces the creep strength of calcite at T=600 and 650 °C, i.e. under conditions favouring slip. In most materials, cation impurities are found to produce a *hardening* effect (solid solution hardening - e.g. salt: Heard and Ryerson 1986, galena: Cox 1986) and various theories of work hardening involving interactions of dislocations with solute atoms have been proposed (see Nabarro 1985). An important aspect in these theories involves the elastic misfit straining of the region with the point defect (i.e the impurity cation) with respect to the matrix. Such strain fields may impede the *motion* of dislocations. On the other hand, stress concentrations at local lattice distortions may also favour the *formation* of dislocation loops, which may then act as dislocation multiplication sources (Morrison-Smith et al. 1976). For example in quartz, clusters of molecular water are proposed to form easy nucleation sites for glissile dislocations (McLaren et al. 1983, 1989). The relatively high strength of dry quartz with respect to 'wet' crystals has been thus explained by the lack of these easy nucleation sites in dry crystals. The present data on calcite suggest a comparable role for impurity cations, particularly since the effect seems to be independent of cation type.

2.7.2 Slip on f in the [10$\bar{1}$1] direction (a new slip direction?)

The f_1 slip line and kink analyses reported in this chapter indicate an effective slip direction on f_1 of [10$\bar{1}$1], i.e. precisely intermediate between the [2$\bar{2}$01] and [02$\bar{2}$1] directions expected for f (i.e. f_1) on the basis of previous literature. This implies either that a truly new f-slip direction has been activated in our tests, or it implies coupled activity in two coplanar <2$\bar{2}$01> directions. In the latter case, any strongly heterogeneous deformation should favour one of the two slip directions relative to the other, at least locally (see Davidge and Pratt 1964). Slip line domains would then develop on opposite faces of the sample, but not on adjacent faces. However, additional deformation experiments performed using samples with aspect ratios (length:width:width) varying between 3:1:1 and 3.5:2:1 (c.f. normal ratios 2.5:1:1, Fig.2.1), in order to enhance heterogeneous deformation, did not show development of slip line domains on opposite faces. On the contrary, domains of f-lines could be followed around the crystals in all cases.

In addition, TEM contrast analysis of dislocations oriented subparallel to the f_1 plane (Fig. 2.27) strongly suggest a Burgers vector parallel to [10$\bar{1}$1], that is, parallel

to the effective slip direction on f_1 deduced from slip line and kink analyses. Contrast conditions consistent with Burgers vectors parallel $<2\bar{2}01>$ were only found for dislocations lying well outside the f_1 plane. Dislocation lines tend to be not only concentrated within f_1 but they also show preferred orientations parallel and perpendicular to $[10\bar{1}1]$ direction (Fig. 2.23b) This is convincingly consistent with dislocations of repectively pure screw and pure edge character in the $f[10\bar{1}1]^+$ system.

On this basis the hypothesis of coupled activity involving two $<2\bar{2}01>$ directions is rejected, and a true slip direction $[10\bar{1}1]^+$ for f-slip in the present tests is inferred.
The existence of this new slip direction is strongly supported by dislocation line energy considerations (Heinisch et al. 1975, Motohashi et al. 1976, Paterson 1985), since the length of the Burgers vector parallel to $<10\bar{1}1>$ is only 6.37 Å (i.e. $1/3<10\bar{1}1>$ - see Table 2.9) compared with a value of 8.09 Å for that parallel to $<2\bar{2}01>$.

2.7.3 The role of dislocation networks in deformation

It has been shown above that irregular pseudo-hexagonal dislocation networks (Fig. 2.21) are prominent features of the dislocation substructure in the deformed crystals, particularly at the higher temperatures and lower flow stresses. In metals and semiconductors, networks are commonly thought to result from the interaction of glissile dislocations with other dislocations which thread the slip plane (e.g. Hirth 1983). The latter are called *forest* dislocations, which can be provided by glide on secondary slip systems or by a variety of other mechanisms (e.g. see Hirth 1983). If the forest dislocations have some mobility, they may combine with glissile dislocations to form a third set of dislocation segments (Weertman and Weertman 1983), resulting in a network structure with attractive junctions of dislocations in nodes.

In the present experiments, two types of dislocation networks have been identified (section 2.6.4): type 1 networks lying roughly parallel to $(0\bar{1}11)$, with Burgers vectors parallel to $[10\bar{1}1]$, $[1\bar{1}0\bar{1}]$ and $[\bar{2}110]$ (e.g. Fig. 2.25), and type 2 subbasal networks, with Burgers vectors parallel to the three a-axes (Fig. 2.26). These two types are treated seperately below, in an attempt to analyse their development in terms of dislocation interactions. Type 1 networks will continue to be discussed using the Burgers vector indices implied by the fact that the plane of all TEM foils was arbitrary designated parallel to the r_3 cleavage plane (refer section 2.6.3). Note however that, for symmetry reasons, these networks are indistinguishable from the symmetrically equivalent networks parallel to $(1\bar{1}01)$, with Burgers vectors parallel to $[10\bar{1}1]$, $[01\bar{1}\bar{1}]$ and $[\bar{1}\bar{1}20]$.

In the first, most common type of network, one of the member dislocation types has a Burgers vector parallel to $[10\bar{1}1]$ and generally lies in the macroscopically identified active $f[10\bar{1}1]^+$ slip plane, whereas the others make angles with the f_1 plane, i.e. are 'forest' dislocations with respect to f_1 (refer Fig. 2.27). Assuming the dislocations with $\bar{b}=1/3[10\bar{1}1]$ to be primary slip dislocations, two types of interactions with dislocations having Burgers vectors parallel to $[1\bar{1}0\bar{1}]$ or $[\bar{2}110]$ are possible, given by the reactions:

$$1/3[10\bar{1}1] + 1/3[1\bar{1}0\bar{1}] = 1/3[2\bar{1}\bar{1}0] \qquad (2.2)$$
$$\text{or} \quad 1/3[10\bar{1}1] + 1/3[\bar{2}110] = 1/3[\bar{1}101] \qquad (2.3)$$

Both reactions lead to a new configuration of lower energy, hence are energetically favourable reactions (recalling that dislocation line energies are proportional to b^2, see Table 2.8). Now, let the dislocations which reacted with dislocations having $\bar{b}=1/3[10\bar{1}1]$ (equations 2.3 and 2.4) form part of a secondary slip system. If is assumed that this secondary slip system is a known gliding mechanism in calcite (Table 1.2 and section 2.7.1), three slip systems are eligible (i.e have $\bar{b}$ parallel $[1\bar{1}0\bar{1}]$ or $[\bar{2}110]$), namely $f_2[\bar{1}101]$, $m_3[\bar{2}110]$ and $c[\bar{2}110]$. These slip systems have Schmid factors of respectively 0.12, 0.35 and 0.34. The much lower Schmid factor for the $f_2[\bar{1}101]$ system (S=0.12) with respect to the operating $f_1[10\bar{1}1]^+$ system (S=0.48) makes it rather unlikely for f_2 to be active. In view of the present author, the published evidence for active slip on m (Thomas and Renshaw 1967) is too limited to allow further consideration, leaving basal slip as the potential secondary slip system.

The second type of network identified has Burgers vectors parallel to <a>, and the specific network analysed (GHJ, Figs 2.26, 2.27) was oriented only slightly obliquely (~20°) to the calcite basal plane. In view of the above discussion, this once more suggests basal slip as a potential secondary slip system. Dislocations moving on the two symmetrically disposed coplanar $c[2\bar{1}\bar{1}0]$ and $c[\bar{1}\bar{1}20]$ slip systems (S=0.34, third system $c[1\bar{2}10]$ has S=0) may have interacted with each other, according to the Burgers vector reaction

$$1/3[2\bar{1}\bar{1}0] + 1/3[\bar{1}\bar{1}20] = 1/3[1\bar{2}10] \qquad (2.4)$$

From the above, type 1 dislocation networks thus can be explained assuming reactions between dislocations of the demonstrably active $f_1[10\bar{1}1]$ system and the $c[\bar{2}110]$ system (eq. 2.3), while reactions between dislocations of the two coplanar $c[2\bar{1}\bar{1}0]$ and $c[\bar{1}\bar{1}20]$ basal slip systems explain type 2 networks (eq. 2.4). These reactions are illustrated in Fig. 2.28. The figure shows that after development of a type 1 network, dislocations initially lying within a specific f- or c-plane have shifted position to a new f- or c-plane respectively, while a new dislocation segment is
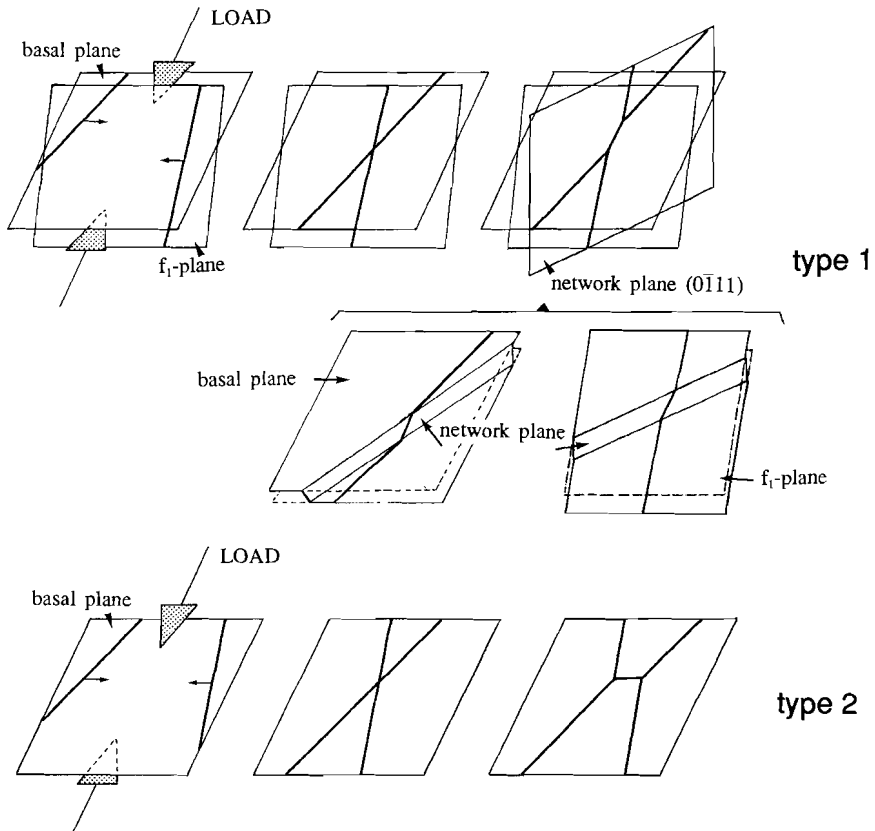
Figure 2.28
Illustration of dislocation interactions proposed in equations 2.3 and 2.4, to explain the development of dislocation networks parallel to the basal and (0$\bar{1}$11) planes in calcite (cf. Figs. 2.25-2.26). Note the double cross slip of dislocations in development of the type 1 networks.

created oriented oblique to both **f** and **c**. This would involve double cross slip of the f[10$\bar{1}$1] dislocations coupled with double cross slip of the c[$\bar{2}$110] dislocations, the cross slip plane being (0$\bar{1}$11). It must be noted here that slip line analysis (section 2.5) has not shown evidence for active basal slip, implying that *if* the c-system was active, it was not very important in accumulating strain.

Recalling that the dislocations of type 1 networks are of mixed character with a dominant screw component (section 2.6.4), it follows that the (0$\bar{1}$11) networks (and the symmmetrically equivalent (1$\bar{1}$01) networks) can be regarded as 'distributed' twist boundaries of interacting screw dislocations (e.g. Hirth and Lothe 1968). The intersections of these twist boundaries with the sample faces r_2 and r_3 (cf. Fig. 2.1) coincide in orientation with the ill-defined boundaries of the shift features seen in the
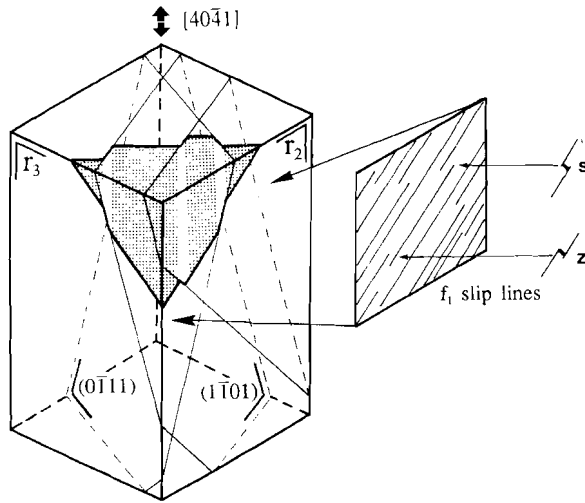
Figure 2.29
Simplified drawing of a calcite single crystal, explaining the s- and z-shape f₁-slip
band shift features (section 2.5) by means of a translation parallel (0̄111) and the
symmetrically equivalent (1̄101) plane, i.e. parallel the plane containing the Burgers
vectors of the type 1 dislocation networks.

f₁-slip bands (Fig. 2.20). A shift of f₁-slip lines along the (0̄111)- and (1̄1̄01) network planes offers an explanation for both the s- and z-symmetrical shift geometries (Fig. 2.29, cf. Fig 2.20). Thus, it is suggested here that the prominent (0̄111)-type dislocation networks in the deformed calcite crystals are combined cross slip planes and twist boundaries which interconnect separated f-slip bands.

Since steady state deformation is attained under most conditions investigated (T≥600 °C), the development of the networks does not seem to harden the crystals. On the contrary, the network-related cross slip process might serve as a recovery mechanism (refer Poirier 1976).

2.8 SUMMARY / CONCLUSIONS

1) Uniaxial compression experiments have been performed on optical quality calcite single crystals at temperatures in the range 400-800 °C and at constant strain rates in the range 3×10^{-4} to 3×10^{-8} sec^{-1}. Early tests were carried out in air, but the majority were performed in a controlled atmosphere cell using a CO_2 overpressure of 0.25 MPa to suppress decomposition. The crystals were loaded in the [404̄1] direction (i.e. parallel to the intersection of two r cleavage rhombs, r₂ and

r_3) following earlier experiments of Spiers and Wenk (1980). This orientation was chosen with the intention of activating slip in the (so-called) positive sense on the previously reported $r\{10\overline{1}4\}<\overline{2}021>$ and $f\{\overline{1}012\}<02\overline{2}1>$ systems.

2) At temperatures below ~600 °C, the samples deformed largely by e-twinning. At higher temperatures, the samples exhibited steady state flow behaviour, with deformation occurring by slip on $r_1(10\overline{1}4)[\overline{2}021]$ and $f_1(\overline{1}012)[10\overline{1}1]$ in the positive sense, the f_1 system dominating. Thus, slip on f did not occur in the previously reported direction, and the existence of a new set of slip systems, namely $f\{\overline{1}012\}<10\overline{1}1>$ is implied. This possibility is supported by dislocation line energy considerations, and is consistent with the findings of TEM contrast experiments.

3) In the slip-dominated, steady-state flow regime (T≥550-600 °C) the flow stresses supported at 5% strain were found to be relatively insensitive to strain rate, with empirical power law fits to the data yielding a conventional stress exponent n ranging from ~13 at 550-600 °C to ~9.5 at 700-800 °C.

4) The dislocation substructure is characterized by both straight and curved, locally helical dislocations, and by irregular dislocation networks. Many dislocations are oriented oblique to the active r or f slip planes. These observations suggest active dislocation climb. The main dislocation networks were found to be oriented subparallel to $(0\overline{1}11)$. These probably developed from interactions of f_1 dislocations with dislocations from secondary slip systems, notably c<a>, and simultaneously may have accomodated cross slip between individual f-slip bands.

CHAPTER 3

EXPERIMENTAL COMPRESSION OF CALCITE SINGLE CRYSTALS - Part 2: deformation by r⁻, f⁻ and c slip

3.1 INTRODUCTION

Following the extensive set of experiments reported in chapter 2 for calcite single crystals compressed in the $[40\bar{4}1]$ direction, the present chapter documents a series of 14 tests carried out with the loading direction oriented nominally parallel to $[22\bar{4}3]$. Whereas the crystals compressed along $[40\bar{4}1]$ were found to deform by r and f slip in the positive sense, the new experiments were performed with the aim of activating slip on r and f in the *negative* sense, thus enabling a comparison of slip behaviour in opposite senses. In addition, the new compression direction was chosen such that the basal (c<a>) systems would also be favourably stressed for slip. Limited evidence for basal slip has been reported previously for calcite (Griggs et al. 1960, Turner and Orozco 1976), but it is usually considered to be unimportant in terms of relative activity (Wenk et al. 1983). Nonetheless, basal slip has been put forward to account for crystallographic preferred orientations developed in experimentally sheared marbles at high temperatures (Schmid et al. 1987). In addition, the observations on dislocation interaction in samples compressed parallel to $[40\bar{4}1]$ (section 2.7.3) suggest active c slip is essential in the development of the observed dislocation configuration. Thus new data on basal slip in calcite are clearly desirable.

In the present tests, the single crystals were compressed subparallel to $[22\bar{4}3]$ at temperatures in the range 300-800 °C. Slip on r in the negative sense was found to be the main deformation system throughout the entire temperature range investigated, with minor slip on a secondary r⁻ system up to T=700 °C. Evidence was also found for c-slip at temperatures above 600 °C, and for f-slip in the negative sense at T≥650 °C. The present samples showed work hardening flow rather than the steady state behaviour seen in samples compressed parallel to $[40\bar{4}1]$. This is attributed to the absence of a network recovery mechanism. orientation.

3.2 THE SAMPLES: Preparation and Orientation

The present experiments were performed on calcite single crystals compressed in a direction making an angle of ~30° with the c-axis and ~23° with the pole to r_1 (see Fig. 3.1). This direction is parallel to $[22\overline{4}3]$ within 1°, and will be referred to henceforth (in a nominal manner) using these indices.

All samples were prepared from two large parent crystals of optical quality 'iceland spar' as follows. First, slices of ~4 mm thickness were cut from the parent crystals, parallel to the plane containing the r_1 and r_2 poles. This was done using a metallurgical preparation saw equipped with a diamond-coated blade. Rectangular samples measuring 4x4x8 mm were then sawn from the slices with their long axes making angles of 23° and 52° respectively with the poles to the r_1 and r_2 cleavage planes. Finally, the sample faces were carefully polished to high optical quality, using 0.25 μm diamond spray. Prior to deformation, all samples were annealed at 500 °C for a period of 24 hours to remove dislocation damage.

The Schmid factors for the main twinning and glide systems in calcite, for compression parallel to the length of the present samples (i.e. subparallel to $[22\overline{4}3]$), are listed in Table 3.1. Following the observation of $f<10\overline{1}1>^+$ slip reported in chapter 2, slip on $f<10\overline{1}1>$ in the negative sense is included in Table 3.1, in addition to the
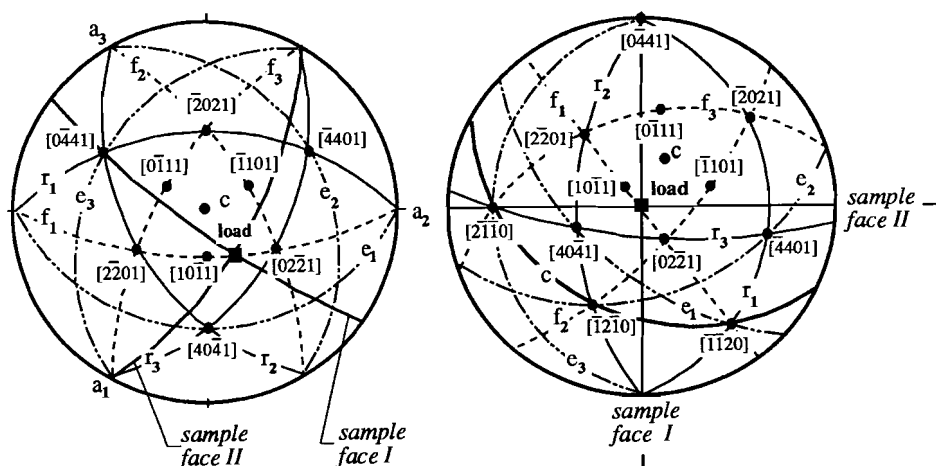
Figure 3.1
Stereographic projection of calcite showing relevant planes and directions. Compare with Table 3.1.
a) normal upper hemisphere projection,
b) rotated projection, with load vertical and sample faces I and II oriented NS and EW respectively.

e-twinning:
e_1 $(\bar{1}018)[\bar{4}04\bar{1}]^-$ S=0.45   negative sense
e_2 $(1\bar{1}08)[4\bar{4}0\bar{1}]^-$ S=0.30   negative sense
e_3 $(01\bar{1}8)[0\bar{4}41]^+$ S=0.01   positive sense

r-slip:
r_1 $(10\bar{1}4)[20\bar{2}\bar{1}]^-$ S=0.28   negative sense
r_2 $(\bar{1}104)[\bar{2}20\bar{1}]^-$ S=0.38   negative sense
r_3 $(0\bar{1}14)[0\bar{2}2\bar{1}]^-$ S=0.29   negative sense

f-slip:
f_1 $(\bar{1}012)[\bar{2}20\bar{1}]\,[0\bar{2}2\bar{1}]^-$ S=0.01, 0.01   negative sense both
       $(\bar{1}012)[\bar{1}01\bar{1}]^-$ S=0.01   negative sense
f_2 $(1\bar{1}02)[20\bar{2}\bar{1}]\,[0\bar{2}2\bar{1}]^-$ S=0.12, 0.36   negative sense both
       $(1\bar{1}02)[1\bar{1}0\bar{1}]^-$ S=0.31   negative sense
f_3 $(01\bar{1}2)[20\bar{2}\bar{1}]\,[\bar{2}20\bar{1}]^-$ S=0.24, 0.47   negative sense both
       $(01\bar{1}2)[01\bar{1}\bar{1}]$ S=0.45   negative sense

c-slip:
       $(0001)[\bar{1}\bar{1}20]$ S=0.43
       $(0001)[1\bar{2}\bar{1}0]$ S=0.21
       $(0001)[2\bar{1}\bar{1}0]$ S=0.21

Table 3.1
Schmid factors S for the main twinning and glide systems generally quoted for calcite, for loading in the [22$\bar{4}$3] direction: slip directions after Wenk (1985), except for f<10$\bar{1}$1> (this study). The c-system has neutral sense of gliding. All indices refer to the hexagonal cell with a=4.99 Å and c=17.06 Å, upper hemisphere coordinates.

frequently quoted f$^-$<$\bar{2}$20$\bar{1}$> systems (refer Table 2.1). From the table it is clear that the chosen orientation is relatively favourable for slip on the r_2 (1$\bar{1}$04)[$\bar{2}$20$\bar{1}$]$^-$ system (S=0.38), on f_3 (01$\bar{1}$2) in the [$\bar{2}$20$\bar{1}$]$^-$ or [01$\bar{1}\bar{1}$]$^-$ directions (S=0.47, 0.45 resp.), and on c[$\bar{1}\bar{1}$20] (S=0.43). The chosen orientation is unfavourable for twinning on **e**, since **e**-twinning only occurs in the positive sense (see Table 1.2).

3.3 EXPERIMENTAL METHOD

The samples were deformed in uniaxial compression using the same experimental apparatus and technique as described in section 2.3. The tests were carried out in a CO_2 atmosphere (overpressure ~0.25 MPa) at temperatures in the range 500-800 °C and at an approximately constant strain rate of 2.8×10^{-5} sec^{-1}. One test was performed in strain rate cycling mode, varying the strain rate between 2.8×10^{-4} and 2.8×10^{-7} sec^{-1}. In addition to the present tests (T≥500 °C), this chapter includes earlier, unpublished results obtained by C.J. Spiers (at UC Berkeley, USA) in experiments performed at T=300-500 °C. These latter tests were carried out in air but were otherwise more or less identical to those described here.

3.4 MECHANICAL DATA

The complete set of 14 tests reported here is listed in Table 3.2, and a representative selection of stress-strain curves is shown in Fig. 3.2. All curves exhibit a comparable sequence of hardening stages. After a first stage of almost linear hardening (stage I), in which almost all of the measured strain is permanent, the stress-strain curves show a sharp yield point at 0.3-0.8% strain. At low temperatures (300 °C - Fig. 3.2a), a distinct stress drop follows yield. This stress drop becomes less significant towards higher temperature (400 °C - Fig. 3.2b) and disappeares entirely at T≥500 °C (Fig. 3.2c-f). The post-yield portion of the stress-strain curves (stage II) exhibits gradual hardening with an increase in hardening coefficient

a)

sample	P	T	$\dot{\varepsilon}$x10^5	flow stress [MPa] at x% strain:				final strain
				3%	4%	5%	6%	
spx21	I	300 °C	2.86	101.0	113.4	123.8	130.0	7.6%
spx18	I	400 °C	2.86	54.4	60.4	64.7	73.9*	5.8%
spx16	I	500 °C	2.85	48.6	63.8	75.8	83.9*	5.7%
spx17	I	500 °C	2.85	44.6	57.5	70.9	79.6	13.4%
b9x35	II	500 °C	2.74	49.3	66.0	76.9	85.1*	5.6%
b6x32	II	600 °C	2.85	38.1	51.6	59.4	63.5	6.3%
b1x19	I	650 °C	2.86	37.5	40.4	42.4	43.8	10.2%
b10x36	II	650 °C	2.64	- cycling test; see below		55.5*	57.3*	16.3%
b8x34	II	700 °C	2.77	- test stopped at 2.2% strain, final stress: 25.5 Mpa				
b5x31	II	700 °C	2.87	34.7	40.7	44.2	46.6*	5.8%
b4x30	II	700 °C	2.66	35.4	42.4	46.5	50.3*	5.0%
b7x33	II	800 °C	2.86	24.4	26.9	28.5	29.7	6.2%
b2x20	I	800 °C	2.87	25.1	25.8	26.5	27.0	10.6%
b3x23	I	800 °C	2.89	19.8	21.1	21.7	22.1	6.1%

b) T=650 °C
strain rate cycling
test b10x36

strain rate [sec^{-1}]	stress [MPa]		strain
2.6x10^{-7}	42.3*	at	5.0%
2.6x10^{-6}	47.6	at	5.0%
2.6x10^{-5}	55.5*	at	5.0%
2.6x10^{-4}	56.6*	at	5.0%
2.8x10^{-4}	68.3	at	9.1%
2.9x10^{-5}	64.0	at	11.2%
3.1x10^{-6}	60.1	at	14.0%
3.2x10^{-7}	54.1	at	16.3%

Table 3.2
List of experiments reported in this chapter. P denotes the parent crystal, T the temperature and ε̇ the strain rate [sec⁻¹]. All stress values denoted with an asterix (*) were obtained by extrapolation of the stress strain curve using a power law relation between stress and strain. a) constant strain rate experiments, b) strain rate cycling test, see Fig. 3.3. 'sp'-denoted experiments were performed by C.J. Spiers at UC Berkeley, USA.
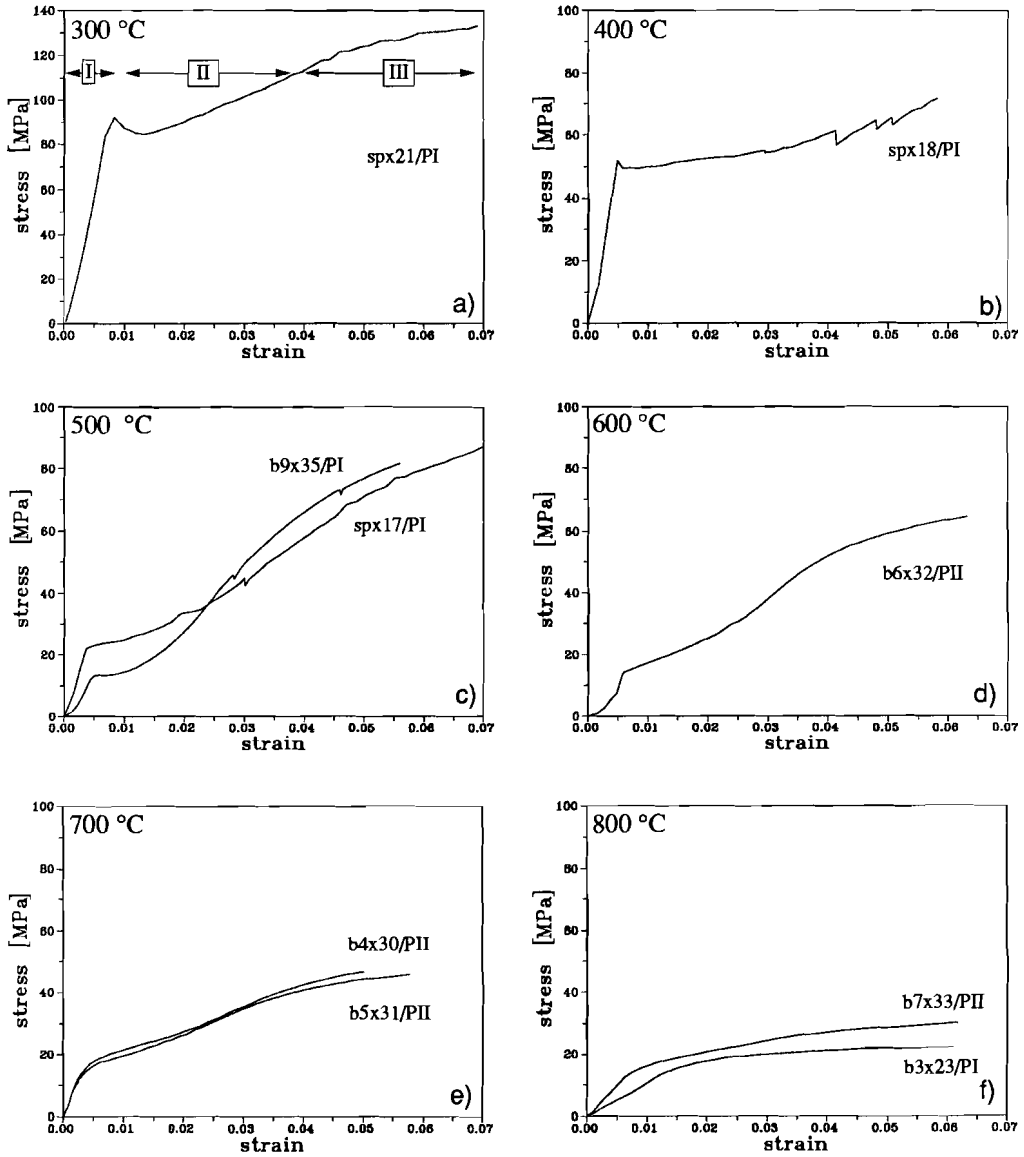
Figure 3.2
Selected stress-strain curves obtained for calcite crystals compressed parallel to
[2243]. Each curve is labelled with the test no. and no. of parent crystal. Typical
hardening stages I, II and III (see text) indicated for the 300 °C curve.

towards higher strains. A weakly defined inflection point at 3-4% strain marks the beginning of a final stage (III). This stage is characterised by a continuously decreasing hardening rate, producing a roughly parabolic portion in the stress-strain curve. Steady state is not reached in any of the tests performed at T≤700 °C. However, steady state was closely approached at strains above 3% in two tests at 800 °C (Table 3.2, Fig. 3.2f-lower curve). At T≤500 °C and strains above 3%, small instantaneous load drops were observed in most experiments. These were found to be associated with deformation twinning, as seen in samples deformed parallel [40$\bar{4}$1] (chapter 2).

The stress-strain curves obtained for samples prepared from the same parent crystal were found to be closely reproducible (see curves at 700 °C - Fig.3.2e). However, as in the experiments performed in the [40$\bar{4}$1] orientation (section 2.4.2), differences in behaviour were observed between samples from *different* parent crystals (see curves at 500 and 800 °C - Fig. 3.2c and f).

The results of the single strain rate cycling experiment performed at T=650 °C are presented in Fig. 3.3 (refer Table 3.2). Steady state flow is approached in each step above ~9% strain. The corresponding flow stresses, arbitrarily taken at the ends of the individual constant strain rate periods (Table 3.2b), are plotted against strain rate in Fig. 3.4, together with the flow stresses supported at 5% strain. The latter were obtained by extrapolation of the relevant parts of the stress-strain curve using a power law relation ($\sigma = K \cdot \varepsilon^p$) between stress ($\sigma$) and strain ($\varepsilon$) to mathematically describe the curve (after Taylor 1934). Fitting of the strain rate ($\dot{\varepsilon}$) and stress data to a conventional power law of the form

$$\dot{\varepsilon} = A \cdot \sigma^n \cdot \exp(-Q/RT), \qquad\qquad (3.1)$$

(where A and n are constants, Q represents the apparent activation energy, R the gas constant and T the absolute temperature, see chapter 6) yielded stress exponents (Fig. 3.4) of n=22±4 at 5% strain and n=30±3 at quasi steady state (above 9% strain).

The dependence of flow stress on temperature for various amounts of strain is illustrated in the log stress versus 1/T plots given separately for parent crystals I and II (Fig. 3.5). The lines of constant strain appearing in this plot show an increase in slope with increasing temperature. Applying equation 3.1 with the stress exponent n=22, obtained at 5% strain and 650 °C, yields an apparent activation energy of about 400 kJ/mole at 500-650 °C increasing to ~740 kJ/mole at 650-800 °C. Note that these values are estimates only, since they do not correspond to *steady state* flow. They are also physically meaningless unless equation 3.1 can be shown to correctly represent the active microscale mechanism.
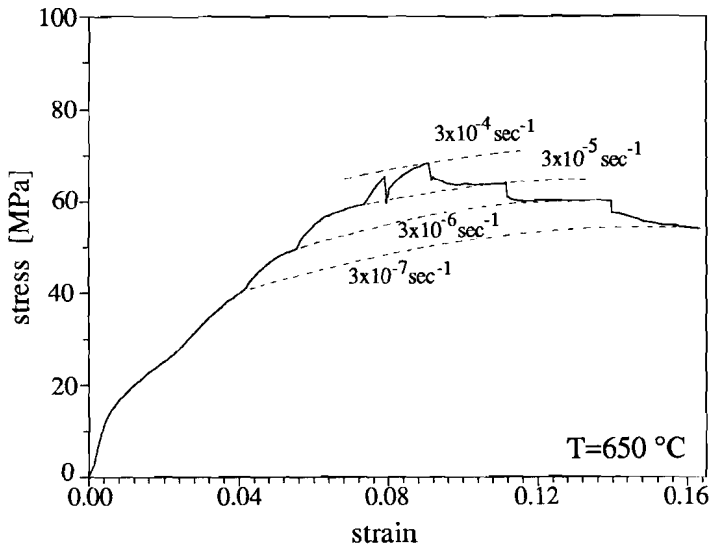
Figure 3.3
Stress-strain curve obtained from a strain rate cycling test, compression subparallel [2243]. Dashed lines are graphical interpolations.
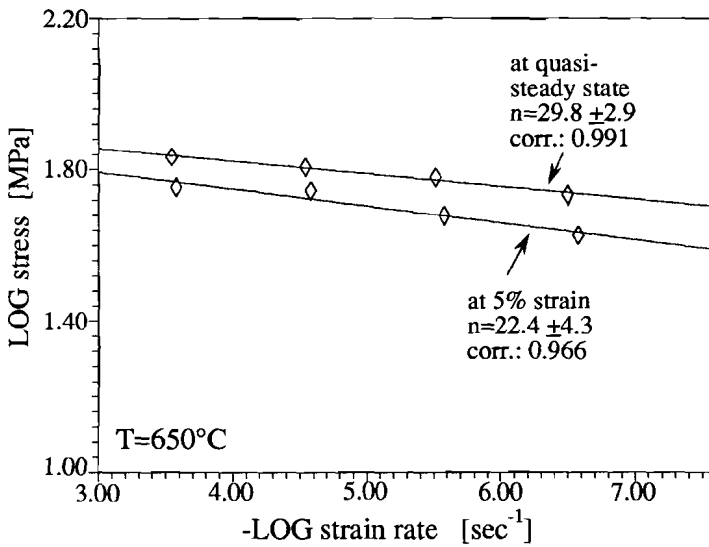
Figure 3.4
Log-log plot of strain rate vs. flow stress as obtained from the single strain rate cycling test reported in this chapter (Fig. 3.3, Table 3.2). Best fit isotherms and stress exponents n determined using individual power law fits (equation 3.1). 'Corr.' indicates correlation coefficent of best fit.
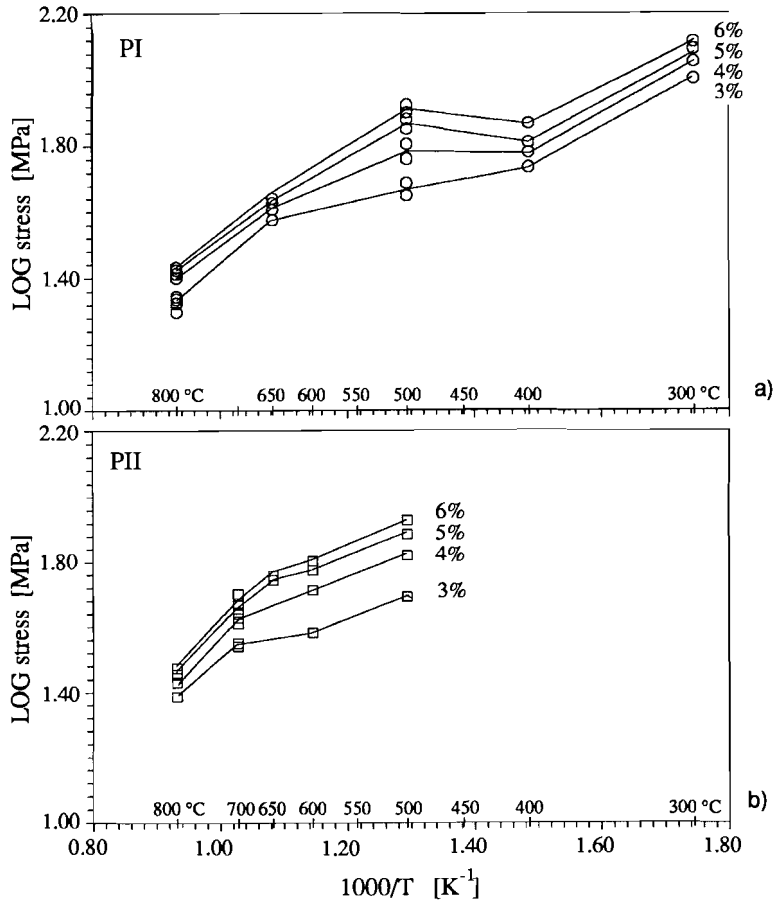
Figure 3.5
Log flow stress (at 3 to 6% strain) vs. reciprocal temperature for samples from parent crystals PI (a) and PII (b). All data at strain rate 3x10⁻⁵ sec⁻¹.

3.5 GLIDE SYSTEMS AND OPTICAL MICROSTRUCTURES

3.5.1 Methods and general observations

Transmission and reflection optical microscopy were used to carry out slip line analysis on the deformed crystals in order to identify the active glide systems (compare section 2.5). Fig. 3.6 shows the predicted orientations on the sample faces of slip lines corresponding to the **e**-twinning and **r**, **f** and **c** glide systems given in Table 3.1. Slip lines on deformed crystals were identified by measuring their orientation and, where possible, by tracing them from one sample face to the other. The results were compared with Fig. 3.6. It can be seen from this figure that the **f**, **c**
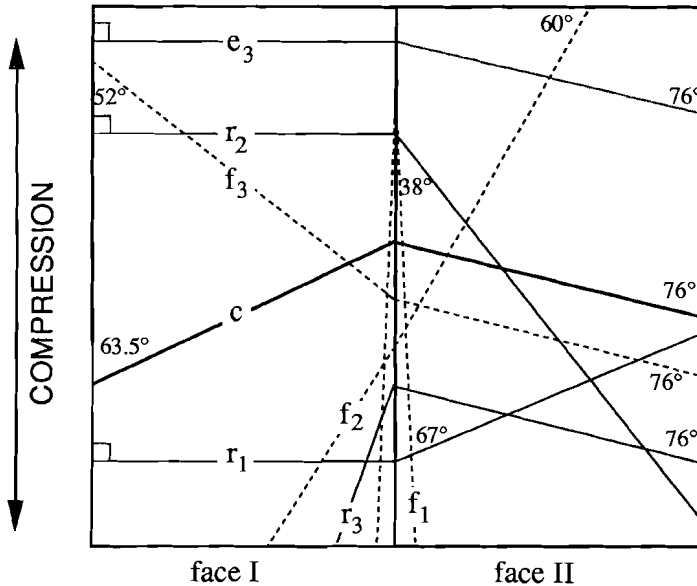
Figure 3.6
Predicted intersections of the main glide systems with sample faces I and II in the
present loading orientation (compare with Fig. 3.1 and Table 3.1).

and **r** systems are easily distinguished on sample face I, while the r_1^- and r_2^-
systems can be identified on sample face II. Twins on **e** were usually observed as
sharp lamellae showing abrupt extinction in plane-polarized light. They were in all
cases traceable around the compressed crystal and immediately identifiable from Fig.
3.6.

The measured slip line orientations and other relevant observations are
summarized in Table 3.3. From this data it is clear that the active deformation
systems were twinning on **e** at T≤600 °C, **r** slip across the entire range of
temperatures, and **f** and basal slip at T≥600 °C. These observations will be
discussed in more detail below.

3.5.2 e-twinning

Notwithstanding the low Schmid factor for the e_3-twinning system (Table 3.1), e_3-
twins were found in all samples deformed at T≤600 °C. With the exception of the
crystal compressed at T=300 °C, twins were observed exclusively in the end regions
of the samples, suggesting activation at local stress concentrations near the pistons
(cf. Wenk 1985). The small instantaneous load drops seen in some low temperature
tests (Fig. 3.2) are inferred to have been associated with twinning.

⌐--------experiment--------⌐				⌐-twin-⌐	⌐----observed slip lines----⌐		⌐-(inferred) glide planes-⌐				⌐----notes----⌐
sample	P	T	%ε	e_3	on face I	on face II	r_2^-	r_1^-	f_3^-	c	
spx21	I	300	7.6	TT	86-90° → 125-131°	138-144° 57-63° ~105°	●	○	△		kinks ~⊥ r_2
spx16	I	500	5.7	TT	87-90° →	136-142° 59-73°	●	○			kinks ~⊥ r_2
b9x35	II	500	5.6	TT	82-90° →	138-148° ~68°	●	○			kinks ~⊥ r_2
b6x32	II	600	6.3	TT	84-90° → 117-127° 59-63°	137-147 67-70° 104-110° idem	●	○	△	□	
b1x19	I	650	10.2		81-90° 54-60°	131-141° 60° 100-102°	●	○		□	kinks ~⊥ r_2
b10x36	II	650	16.3		86-90° 114-126° → 49-64°	127-144° 99-109° idem	●		◭	□	strain rate cycling test
b8x34	II	700	2.2		90-97° →	134-141° 68°	●	○			test stopped early
b5x31	II	700	5.8		90-94° 110-120° 60-61°	134-139° 103-118° idem	●		▲	◧	
b4x30	II	700	5.0		90-99° 113-120° 60-62°	137-144° 108-115° idem	●		▲	◧	
b7x33	II	800	6.2		90-96° 113-122° → 63-64°	~135° 108-120° idem	◑		▲	□	
b2x20	I	800	10.6		90-113° 63-78° →	137-141° 106-114°	◑			■	subgrains: walls ~⊥r_2
b3x23	I	800	6.1		90-104° 63-74°	127-139° 102-103°	●			□	subgrains: walls ~⊥r_2

Table 3.3
Observed slip lines and inferred glide planes for calcite crystals compressed subparallel [2243]. P indicates the parent crystal, T the temperature in °C and %ε the percentage final strain. The presence of e_3 twins in the sample is indicated with TT. The orientations of the slip lines are given as angles from the loading axis, measured clockwise on the sample faces labelled I and II (refer Fig. 3.6). The arrow (→) joins slip lines traceable from sample face I to II. Relative importance of observed slip lines is indicated as follows: open symbols = slip lines rare; half-open symbols = slip lines present; closed symbols = slip lines dominant. Deformed crystals from experiments spx17 and spx18 were not available for study.

3.5.3 The r-systems

For the entire temperature range investigated, slip line evidence showed the r_2^- system to be an important glide system. In numerous cases, the r_2^- slip lines could be traced continuously around the surface of the deformed sample (Fig. 3.7). Kink structures oriented perpendicular to the r_2-plane were observed in several samples at T≤650 °C (Fig. 3.8, Table 3.3). At the highest temperature investigated (800 °C), elongated subgrains were found, with slightly wavy boundaries. These were developed in the same crystallographic orientation as the (low T) kink walls. The presence of kinks and subgrains points to heterogeneous straining. Further however, their boundaries are generally expected to be oriented subnormal to the glide direction of the dominant slip system (Turner and Weiss 1963, see also Spiers 1979, 1982 and Fig. 2.3). As can be seen from Fig. 3.9, this confirms [$2\bar{2}01$] as the slip direction for the r_2^- system. In addition to the dominant r_2 [$2\bar{2}01$]$^-$ system, minor activity on r_1 was observed at temperatures below 700 °C. However, no evidence was found for slip on r_3.
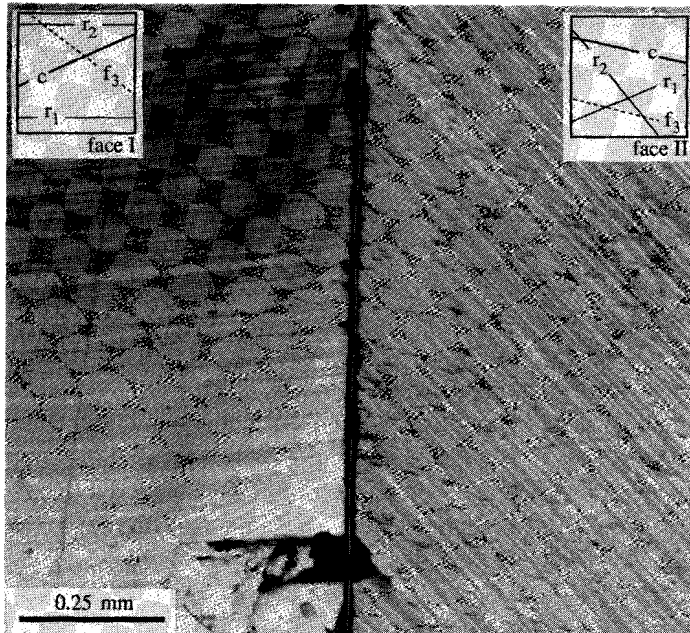
Figure 3.7
r_2^- slip lines traceable from sample face I to sample face II (cf. Fig. 3.6). Note faint dark bands on face I, representing r_2^- related kink zones. Sample spx16 (deformed at T=500 °C), reflected light. Compression direction is vertical.
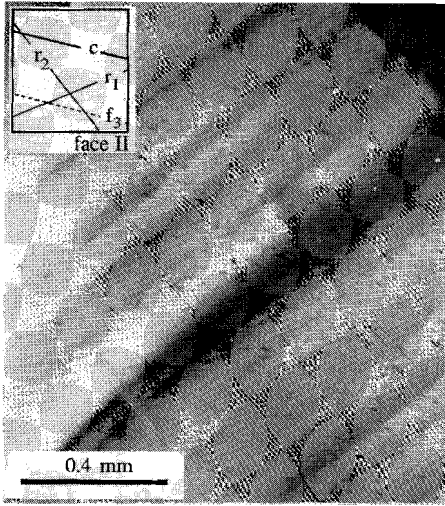
Figure 3.8
Narrow kink zones oriented perpendicular to the r_2^- glide plane. Sample spx16 (T= 500 °C), transmitted light.
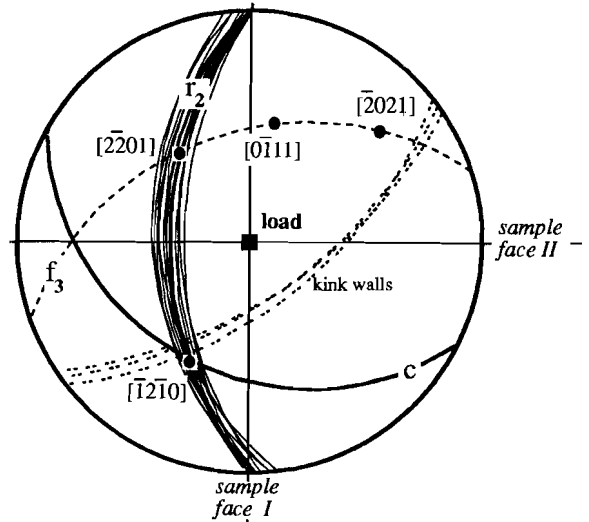
Figure 3.9
Stereographic (equal angle) projection of calcite showing relevant planes and directions (cf. Fig. 3.1b), and measured orientations (thin plain lines) of glide planes identified as r_2^- (cf. Figs. 3.7, 3.8). Note orientation of [2̄201] normal to the kink walls, confirming this direction as the r_2^- slip direction.

3.5.4 The f-system

Out of twelve crystals studied, type I faces of six samples showed sharply defined, wavy slip lines oriented at angles of 100-120° (measured clockwise) to the compression axis (Table 3.3, refer Fig. 3.6). These suggest minor active slip on f_3 in the negative direction at T=300 °C and 600 °C, becoming increasingly important at T≥650 °C. However, no evidence was found for slip on f_3 at the intermediate temperature investigated (T=500 °C). Also, only one sample deformed at T=800 °C (b7x33 - see Table 3.3) exhibited dominant f-slip lines, while two others (b2x20, b3x23) showed no clear evidence for f-slip.

In a few cases, f_3 slip lines were found to be traceable from sample face I to II. Highly localized slip bands in one particular sample (b10x36, T=650 °C) showed shear displacement in the plane of face I, with clear steps developed on face II (Fig. 3.10). This indicates an f_3 slip direction nearly parallel to sample face I, implying
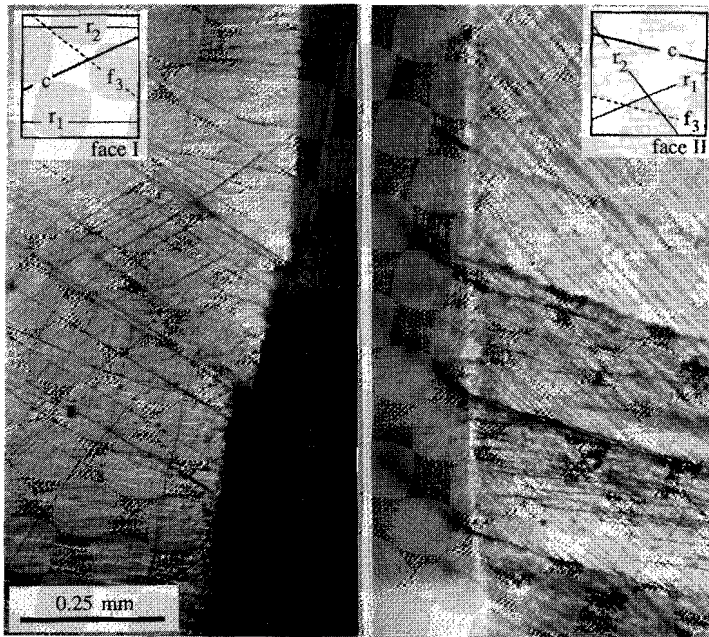
Figure 3.10
f_3^- slip lines traceable from sample face I (left) to sample face II (right). Also visible are slip lines developed due to glide on r_2^- and c (cf. Figs. 3.7 resp. 3.12). Localized slip_on f_3^- planes resulted in clear steps developing on face II only. This implies a [01$\overline{1}$1] slip direction (see Fig. 3.11). Sample b10x36 (T-650 °C), reflected light.

[01$\overline{1}$1] rather than [$\overline{2}$20$\overline{1}$] as the active glide direction (see Fig. 3.11, cf. Table 3.1). Slip band shift features of the type associated with f-slip in crystals compressed parallel [40$\overline{4}$1] (section 2.5), were not observed in the present orientation.

The orientations of f_3-planes inferred from slip lines on the sample surfaces, are slightly rotated away from the initial f_3 orientation with respect to the load axis (Fig. 3.11, Table 3.3). This is interpreted as indicating heterogeneous straining of the sample. The rotation axis is expected to be oriented perpendicular to the slip direction of the dominant active system (Turner and Weiss 1963), but cannot simply be related to the f_3-slip direction in the current samples, since the same samples also show significant r_2^- slip (Table 3.3). However, the axis of rotation determined from Fig. 3.11 makes a relatively large angle (58°) with [0$\overline{1}$11] as opposed to the small angle of 21° with [2$\overline{2}$01]. The orientation of the rotation axis for f_3-planes thus best agrees with a glide direction parallel [0$\overline{1}$11], supporting the conclusion drawn from Fig. 3.10.
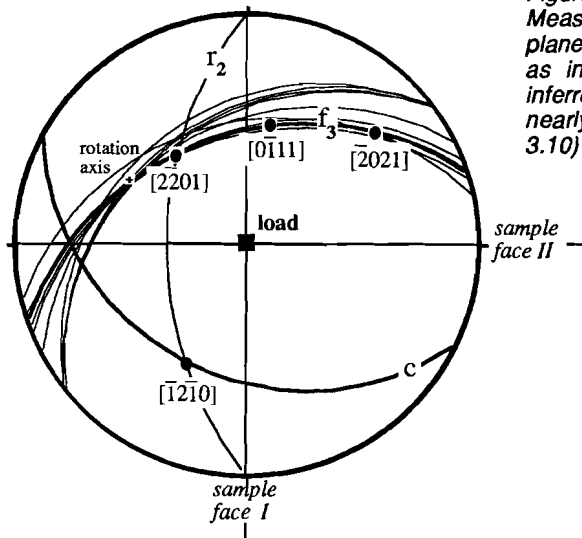
Figure 3.11
Measured orientations of glide planes identified as f_3^-. Projection as in Fig. 3.9. Note orientation of inferred slip direction $[0\bar{1}11]$ lies nearly within sample face I (cf. Fig. 3.10)

3.5.5 The c-system

The crystals deformed at T≥600 °C show slip lines on face I making angles of 49-64° with the loading axis (Fig. 3.12, Table 3.3). These slip lines are oriented subparallel to the intersection of the basal plane with the sample face, suggesting active c-slip. Slip lines found traceable from sample face I to II on sample b2x20 (T=800 °C, Fig. 3.12a,b) provide further evidence for significant c-slip at high temperature. In many crystals showing c-slip, the slip lines are often seen to terminate in the body of the crystal (Fig. 3.12c). This microstructure is similar to the shift features seen in the f-slip bands in samples compressed parallel to $[40\bar{4}1]$ (compare with Fig. 2.20). The importance of c-slip in sample b3x23 was markedly less than that in sample b2x20, deformed at identical experimental conditions (T=800 °C, Tables 3.2 and 3.3). However, the latter crystal was compressed to a higher strain (10,6% cf. 6.1% for b2x20), suggesting that the relative importance of c-glide increases with increasing strain.

Determined orientations of the c-slip planes are rotated with respect to the initial orientation of the c-plane (Fig. 3.12d). As mentioned above for the case of f_3-slip in samples compressed parallel to $[22\bar{4}3]$, the orientation of the rotation axis cannot be related to heterogeneous straining due to c-slip alone, since the same samples also show important slip on r_2. The present observations thus allow no direct identification of the direction of slip.
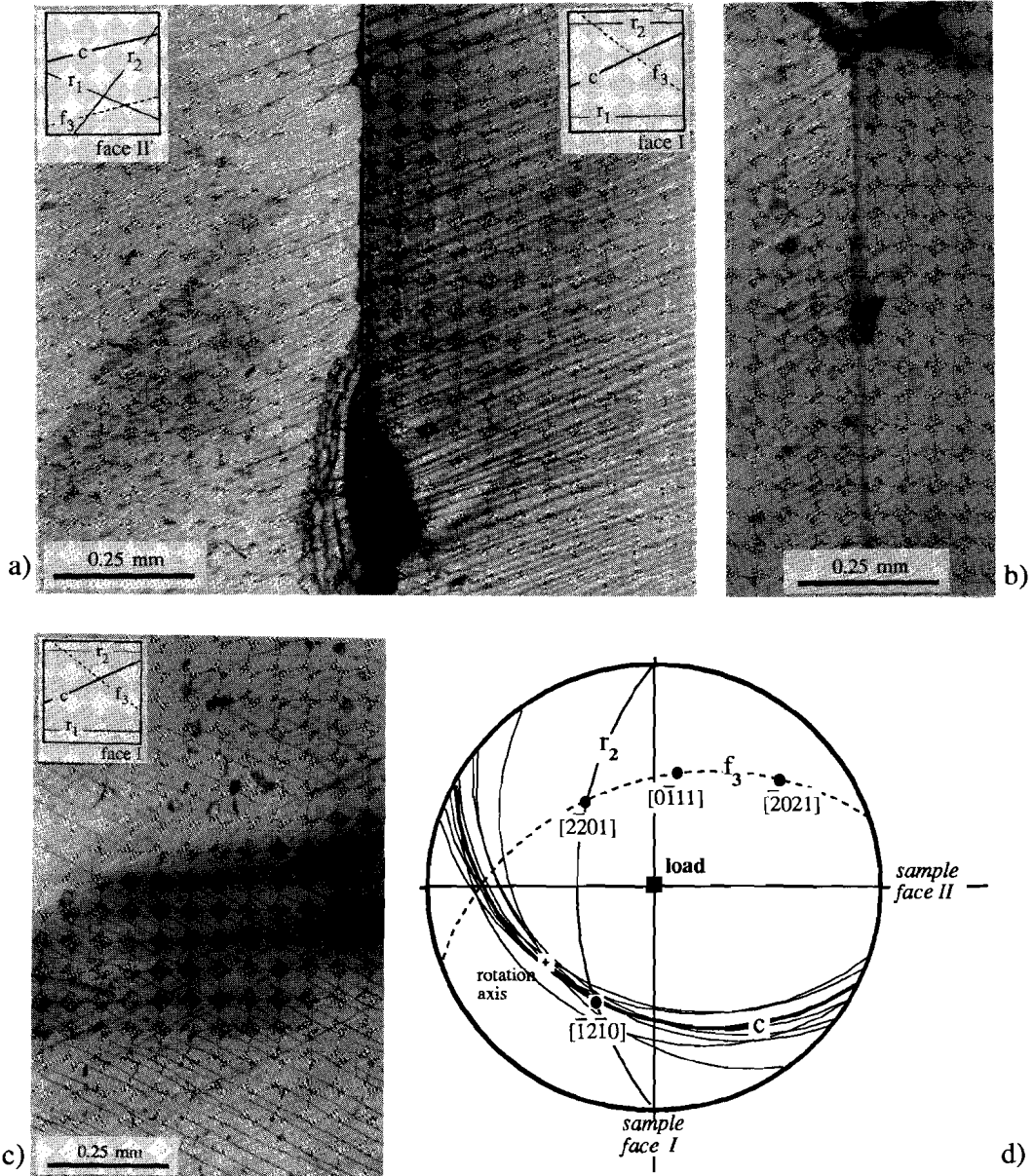
Figure 3.12
Optical micrographs showing slip lines of the c-glide system:
a) c-slip lines traceable from sample face I to sample face II. Sample b2x20 (T=800 °C), reflected light.
b) as micrograph a); deformed crystal now viewed on edge,
c) c-slip lines showing shift microstructures, and sharply defined wavy slip lines related to f_3^-. Sample b5x31 (T=700 °C), transmitted light.
d) measured orientations of glide planes identified as **c**. Projection as in Fig. 3.9.

3.6 **DISCUSSION**

3.6.1 Introductory remarks

The remainder of this chapter consists of a discussion of the following points:
1) the difference in importance of the r-systems in the [40$\bar{4}$1] and [22$\bar{4}$3] loading orientations;
2) the previously unreported <10$\bar{1}$1> slip direction for glide on **f**;
3) the evidence presented for slip on **c**;
4) the difference in stress-strain behaviour seen in crystals deformed parallel to [40$\bar{4}$1] and to [22$\bar{4}$3].

The *strengths* of the observed glide systems in both positive and negative senses will be treated in chapter 4.

3.6.2 r⁻ slip versus r⁺ slip

In the present [22$\bar{4}$3] orientation, slip on the r<$\bar{2}$021> system, in the negative sense, was found to be important at flow stresses down to 20 MPa, across the entire temperature range investigated (300-800 °C). In the [40$\bar{4}$1] orientation, however, r<$\bar{2}$021> slip in the *positive* sense (chapter 2), was found important only at T≤600 °C and at steady state flow stresses above ~60 MPa (see Fig. 2.19). The difference in Schmid factors for the r-systems in the two loading orientations (S=0.31 for loading parallel to [40$\bar{4}$1] and S=0.38 for loading parallel to [22$\bar{4}$3]) is too small to account for this strong difference in the importance of r-slip at the observed flow stresses. This implies that either the r⁻ and r⁺ systems are not of equal strength, or that the flow behaviour of the calcite crystals is not determined by the strength of the r-system, but by one or more of the other glide mechanisms (**f**, **c**) active in both orientations. This point will be returned to in chapter 4.

3.6.3 f⁻ slip versus f⁺slip

The present observations on f⁻ slip ([22$\bar{4}$3] orientation) strongly suggest the active slip direction to be <10$\bar{1}$1>, which is the same direction as inferred for slip on **f** in the opposite (positive) sense ([40$\bar{4}$1] orientation, section 2.7.2). However, the slip direction generally quoted for f⁻ glide and used in texture simulations is <2$\bar{2}$01> (e.g. Lister 1978, Wenk 1985, Takeshita et al. 1987). This is based on the work of Turner et al. (1954) and Griggs et al. (1960). Their evidence for f⁻<2$\bar{2}$01> slip is re-examined here.

Turner et al. (1954) performed deformation experiments on cylinders cut from

calcite single crystals in a wide range of crystallographic orientations. The experiments were done at 500 and 1000 MPa confining pressure and temperatures in the range 20 to 400 °C ($\dot{\varepsilon}$=2.5x10^{-4} sec^{-1}). Twinning on **e** and **r**$^{-}$<$\bar{2}$021> slip were found to be the main deformation systems in most orientations. However, **f**-slip was also identified, in four low temperature tests in orientations which have high Schmid factors for **f**-slip and relatively low values for slip on **r**. In two samples compressed perpendicular to **r**, at T=20 °C, a broad kink band was developed for which the orientation and rotation axis were consistent with gliding on **f**, with slip direction <$\bar{2}\bar{2}$01> rather than <10$\bar{1}$1>. A third experiment in the same orientation, now at higher temperature (300 °C) showed only subordinate local glide on **f** in the end regions of the sample. In one experiment performed in a compression orientation at 30° to the c-axis and 75° to the **r**, plane (T=20 °C), the shape of the specimen after deformation also favoured **f**<$\bar{2}\bar{2}$01> slip. However, samples deformed at 150, 300 and 400 °C in the same orientation did not show any evidence for active **f**-slip. At higher temperatures, above 500-600 °C, Griggs et al. (1960) reported evidence for important **f**$^{-}$ slip in samples *extended* parallel to [40$\bar{4}$1], but they did not unambiguously identify the direction of slip.

In summary, the <$\bar{2}\bar{2}$01> slip direction generally quoted for **f**-slip in calcite is only corroborated by Turner et al's (1954) experimental evidence based on three crystals which were deformed at room temperature. Above 20 °C, **f**-slip disappears as an important glide mechanism, but reappears at T>500-600 °C (Griggs et al. 1960). At these higher temperatures, no direction of slip was previously demonstrated, but the present results indicate glide parallel to <10$\bar{1}$1>, both in the positive and negative senses. It thus appears that we are dealing with two different **f**-systems: a room temperature **f**<$\bar{2}\bar{2}$01> mechanism (after Turner et al. 1954 - only negative sense observed) and a high temperature **f**<10$\bar{1}$1> mechanism (this study, both senses).

3.6.4 Slip on c

The present slip line observations have clearly demonstated active **c**-glide in several samples compressed subparallel to [22$\bar{4}$3] at T≥600 °C. However, the slip direction could not be identified. In contrast, no slip line evidence was found for active **c**-slip under compression parallel to [40$\bar{4}$1]. However, TEM observations on samples deformed in the [40$\bar{4}$1] orientation did show dislocation networks lying more or less parallel to the basal plane, with Burgers vectors parallel to the three a-axes (type 2 networks; section 2.6.4). A model was presented in section 2.7.3 explaining the development of these networks on the basis of interactions of mobile dislocations in the *c*-plane. Combining the model with the slip line evidence for **c**-slip in the [22$\bar{4}$3]-compressed crystals, a **c**<a> glide system seems likely. A **c**-slip direction parallel to <a> is further supported by dislocation line energy considerations (e.g.

Paterson 1985), since the Burgers vector 1/3<a> is the shortest possible direction of translation in the basal plane which leads to perfect lattice restoration (refer Table 2.8). Hence, it is a favourable glide direction.

Indications for active c<a> slip were previously given by Griggs et al. (1960) and Turner and Orozco (1976). The first authors proposed simultaneous activity of c-plus r-glide to explain rotational effects observed in one of their samples deformed at 800 °C. Turner and Orozco (1976) concluded active c-slip from the geometry of a subsidiary kink near the margins of a sample compressed at 30° to the c-axis and 75° to the r_1 plane at 300 °C. This indirect and rather limited evidence for c-slip now appears to be substantiated by direct observations of activity on c.

3.6.5 Stress-strain behaviour

In chapter 2, calcite crystals compressed parallel to [40$\overline{4}$1] at $\dot{\varepsilon}$=3x10^{-4}-3x10^{-7} sec^{-1} were found to deform largely by e-twinning at temperatures below 600 °C. These crystals exhibited discontinuous stress-strain behaviour. At higher temperatures (T≥600 °C), the samples showed smooth steady state flow, achieved at 1-2% strain. Deformation under these conditions predominantly occurred by positive slip on f<10$\overline{1}$1> and r<$\overline{2}$021>, the relative importance of the latter system gradually decreasing towards T=800 °C. Further, subordinate slip on c<a> was suggested on the basis of TEM-observations on network dislocations. Minor inflections resembling yield points were observed in the first part (ε<1%) of the stress-strain curves at T≤600 °C.

The crystals compressed in the [22$\overline{4}$3] orientation also showed e-twinning at T≤600 °C (Table 3.3). However, the smooth stress-strain curves obtained at higher temperature did not show steady state flow (Fig. 3.2, Table 3.2), but rather a sequence of hardening stages, now with pronounced yield points and inflections in the curves. Slip occurred on r<$\overline{2}$021>⁻ across the entire temperature range investigated (300-800 °C), competing with f<10$\overline{1}$1>⁻ and/or c<a> at T≥650 °C.

It appears that while f<10$\overline{1}$1>⁺ slip with subordinate r<$\overline{2}$021>⁻ and/or, possibly, c<a> slip is capable of producing steady state flow in compression parallel to [40$\overline{4}$1], simultaneous activity of r<$\overline{2}$021>⁻ with f<10$\overline{1}$1>⁻ and/or c<a> in compression parallel to [22$\overline{4}$3] is not. This must be related to the way the different slip systems interfere with each other during deformation, i.e. the way mobile dislocations of the different glide systems interact. This will be discussed in some detail.

Based on TEM-observations, it was suggested in section 2.7.3 that in crystals deformed parallel to [40$\overline{4}$1], the interaction of dislocations gliding in the dominant f-glide system ($\overline{b}$=1/3<10$\overline{1}$1>) with mobile dislocations from subordinate c-systems ($\overline{b}$=1/3<$\overline{2}$110>) resulted in the formation of networks consisting of dislocations dominantly of screw character with three coplanar Burgers vectors. The plane

containing these Burgers vectors is oriented oblique to both **f** and **c**. As mentioned, steady state deformation is almost always attained in the [40$\bar{4}$1] orientation, hence the development of the oblique networks does not seem to harden the crystals. It was hypothesized (section 2.7.3) that networks play an essential role in bringing about the steady state mechanical behaviour, notably by network-related recovery involving dislocation cross slip. The question now arises whether or not interaction of dislocations in crystals compressed parallel to [22$\bar{4}$3] can produce similar network planes. Since no TEM-observations are yet available on this, possible dislocation reactions can only be considered theoretically. All feasible reactions, represented by the sums of the Burgers vectors of the identified **r**, **f** and **c**-systems, are given in Table 3.4 and are discussed below.

Out of the six hypothetical reactions, two produce new dislocations of lower energy (reduced b^2) and thus are favourable reactions. The first of these (reaction 3.2 in Table 3.4) involves Burgers vectors corresponding to the f$_3^-$ and c-systems, and would result in (screw dislocation) network planes oblique to both **f** and **c**. Such planes might account for the 'shift' features observed in c-slip lines (Fig. 3.12c), analogous to the way proposed for the f-slip band shifts found in crystals compressed parallel [40$\bar{4}$1] (cf. Fig. 2.29). However, the (dominant) r$_2^-$ slip system in the [22$\bar{4}$3] orientation is not involved, hence these networks would not be expected to play a key-role in the mechanical behaviour. The second favourable reaction (3.5 in Table 3.4) does include dislocations of the r$_2^-$ system. The three Burgers vectors which participate in this reaction are coplanar, the plane being oriented oblique to r$_2$,

involved slip-systems	Burgers vector sum	type of junction	b^2	
f$_3^-$ and c	1/3 [01$\bar{1}\bar{1}$] + 1/3 [$\bar{1}\bar{1}$20] = 1/3 [$\bar{1}$01$\bar{1}$]	repulsive	<u>40.6+24.8>40.6</u>	(3.2)
	1/3 [01$\bar{1}\bar{1}$] - 1/3 [$\bar{1}\bar{1}$20] = 1/3 [12$\bar{3}\bar{1}$]	attractive	40.6+24.8<90.3	(3.3)
r$_2^-$ and f$_3^-$	1/3 [$\bar{2}$20$\bar{1}$] + 1/3 [01$\bar{1}\bar{1}$] = 1/3 [$\bar{2}$3$\bar{1}\bar{2}$]	repulsive	65.5+40.6<187.6	(3.4)
	1/3 [$\bar{2}$20$\bar{1}$] - 1/3 [01$\bar{1}\bar{1}$] = 1/3 [$\bar{2}$110]	attractive	<u>65.5+40.6>24.8</u>	(3.5)
r$_2^-$ and c	1/3 [$\bar{2}$20$\bar{1}$] + 1/3 [$\bar{1}\bar{1}$20] = 1/3 [$\bar{3}$12$\bar{1}$]	repulsive	65.5+24.8=90.3	(3.6)
	1/3 [$\bar{2}$20$\bar{1}$] - 1/3 [$\bar{1}\bar{1}$20] = 1/3 [$\bar{1}$3$\bar{2}\bar{1}$]	attractive	65.5+24.8=90.3	(3.7)

Table 3.4
Hypothetical Burgers vector reactions in calcite crystals compressed parallel [22$\bar{4}$3], involving the slip systems r$_2$[$\bar{2}$20$\bar{1}$]$^-$, f$_3$[01$\bar{1}\bar{1}$]$^-$ and c[2$\bar{1}\bar{1}$0] (compare with Table 3.1). Indices of the Burgers vectors are given such that the corresponding screw dislocations all have the same (right-handed) sign and correct gliding sense with respect to the positive c-axis and [22$\bar{4}$3] loading axis. Values for b^2 are calculated from Burgers vector lengths given in Table 2.8, and are proportional to the (screw) dislocation line energies (e.g. Motohashi et al. 1976, Goetze and Kohlstedt 1977). Only those reactions which result into new dislocations of lower energy (underlined) are energetically favourable.

but parallel to f_3 (compare Fig. 3.1). Since parallel to f_3, this plane cannot serve as a cross slip plane for f_3-dislocations. Network-related recovery of f-dislocations involving cross slip, as inferred for crystals compressed parallel to [40$\overline{4}$1] thus appears impossible. In addition, cross slip of r_2-dislocations onto the f_3 network planes seems unlikely, since this effectively requires f-slip in the [$\overline{2}$20$\overline{1}$] direction rather than the [01$\overline{1}\overline{1}$] direction observed under the present conditions. Furthermore, shift features of the type apparently related to oblique dislocation networks in the case of f- and c-glide (Figs. 2.29 resp. 3.12c) have not been observed in r_2^- glide bands, so that there is no microstructural support for dislocation reaction 3.5 (Table 3.4).

In conclusion, if the hypothesis is accepted that the development of oblique dislocation networks influences the mechanical behaviour of single crystals, the differences in stress-strain curves between crystals compressed parallel to [40$\overline{4}$1] and [22$\overline{4}$3] (respectively showing steady state and hardening characteristics) can be explained by a difference in interactions of the main slip systems. While oblique networks developed via cross slip in crystals deformed in the [40$\overline{4}$1] orientation, cross slip involved development of such networks was unlikely in the [22$\overline{4}$3] orientation. Network related cross slip recovery thus did not occur, so steady state flow could not be attained.

3.7 SUMMARY AND CONCLUSIONS

1) Uniaxial compression tests have been performed on calcite single crystals at temperatures in the range 300-800 °C and a constant strain rate of 3×10^{-5} sec^{-1}. In addition, one strain rate cycling test was carried out. The crystals were compressed in a direction oriented 30° to the c-axis and 23° to the pole to r_1. This orientation was chosen with the aim of activating slip on **r** and **f** in the negative sense, and on the **c**-plane.

2) Across the entire range of temperatures investigated, slip on r_2 ($\overline{1}$104)[$\overline{2}$20$\overline{1}$]$^-$ was found to be the main deformation system. Significant glide on f_3 (01$\overline{1}$2) in the [01$\overline{1}\overline{1}$]$^-$ direction was observed above 650 °C. Limited activity on this slip system already occurred at T=300 and T=600 °C, but not at temperatures in between. The direction of slip on f_3^- was identical to that seen in compression tests parallel to [40$\overline{4}$1] but in the opposite sense. This confirms the existence of a set of new slip systems in calcite, namely the f<10$\overline{1}$1>$^\pm$ systems. At T≥600 °C, clear evidence was also found for slip on the basal plane. On the basis of TEM work in samples compressed parallel to [40$\overline{4}$1] and from dislocation line energy considerations, the slip direction for the c-systen was argued to be parallel <a>. The observed c-slip verifies previous indirect evidence for basal slip in calcite.

3) The stress-strain curves exhibited multistage hardening behaviour and steady state was approached only at higher temperature and strains mostly above 10%. Flow stresses were found to be rather insensitive to strain rate (as observed in a strain rate cycling test), with empirical power law fits to the data yielding stress exponents of ~22 at 5% strain or ~30 at quasi-steady state.

4) The mechanical behaviour of the crystals, notably the continuous hardening usually up to 10% strain, is markedly different from that of calcite crystals compressed parallel to [40$\overline{4}$1], which show steady state flow from ~2% strain. This is thought to be related to differences in the way the active slip systems interact in the two loading orientations. It is suggested that a dislocation-network related mechanism of cross slip recovery plays a role in promoting steady state flow in the [40$\overline{4}$1] orientation, but cannot operate in the [22$\overline{4}$3] orientation.

CHAPTER 4

STRENGTH CHARACTERISTICS OF THE r, f, AND c SLIP SYSTEMS IN CALCITE

4.1 INTRODUCTION

The experiments on calcite single crystals reported in the preceding chapters showed twinning on **e** and slip on $r\{10\bar{1}4\}<\bar{2}021>^{\pm}$, $f\{\bar{1}012\}<10\bar{1}1>^{\pm}$ and **c**<a> to be important deformation mechanisms. The samples tested became weaker both with increasing temperature and decreasing strain rate, and the observed glide systems showed clear changes in relative importance. It follows that with changing experimental conditions, the *strengths* of the individual glide systems change not only in an *absolute* sense, but also *relative* to each other. In this chapter, the experimental and microstructural data obtained from the tests reported in chapter 2 and 3 are used to quantitatively determine the strength properties of the **r**, **f** and **c** glide systems. The main body of data concerns the dependence of strength on temperature, but limited data on the influence of strain rate (notably for r^+ and f^+ slip) are also reported. Particular attention will be paid to the relative strengths of the **r** and **f** slip systems in opposite senses, since previous workers have suggested that the positive and negative systems are not equivalent (Weiss and Turner 1972, Spiers and Wenk 1980) .

The principal application of the data considered in the present chapter lies in the area of numerical modelling of texture development in calcite rocks. Such modelling requires detailed specification of the single crystal slip and twinning systems and their relative strengths. Previous texture computations carried out for calcite polycrystals have assumed the principal glide systems to be $e\{\bar{1}018\}<40\bar{4}1>$, $r\{10\bar{1}4\}<\bar{2}021>$ and $f\{\bar{1}012\}<2\bar{2}01>$ (e.g. Lister 1978, Takeshita et al. 1987, Wenk et al. 1987 - cf. present findings) with relatively limited experimental data available to constrain their relative strengths (Turner et al. 1954, Griggs et al. 1960, Braillon et al. 1972). The present chapter is intended to help provide the data needed to allow more effective texture modelling work to be carried out for calcite in future.

4.2 MULTI-STAGE STRESS-STRAIN BEHAVIOUR IN RELATION TO ACTIVE SLIP SYSTEMS

4.2.1 Samples deformed parallel to [22$\bar{4}$3]

Figure 4.1a shows typical stress-strain curves reported in chapter 3 for calcite crystals compressed parallel to [22$\bar{4}$3] (refer Fig. 3.2, Table 3.2). As described, the curves exhibit a characteristic sequence of hardening stages, with a relatively clear first yield point (A) at 0.3-0.8% strain, and a less clearly defined inflection or quasi-yield point (B) at about 3% strain (refer Fig. 3.2). A selected test was terminated after the first yield point, but before the second. The resulting stress-strain curve is given in Fig. 4.1b, together with the corresponding curve obtained under identical experimental conditions, but extending to a larger strain.

Optical examination of the faces of the sample deformed beyond the first yield point only, revealed that substantial slip took place on r_2^- but not on the other (**f, c**) glide systems (see Fig. 4.1c). However, the crystals which were deformed beyond point B (the second 'yield' point) showed clear evidence for activity on f_3^- and/or **c**, in addition to **r** (Fig. 4.1d, refer section 3.5).

4.2.2 Samples deformed parallel to [40$\bar{4}$1]

Typical stress-strain curves obtained for single crystals compressed parallel to [40$\bar{4}$1] are given in Fig. 4.2a (see also Figs 2.4-2.5, Table 2.3). On close inspection, many stress-strain curves show a sequence of yield and hardening stages roughly comparable to that observed in curves for crystals deformed in [22$\bar{4}$3] orientation, particularly at the lower temperatures. The first 'yield' point (A*) now appears as a minor inflection or 'kink' in the curve (generally at 0.1-0.6% strain), while a second, very marked one (B*) occurs at a strain of ~1%. Beyond the first yield, the stress-strain curves exhibit considerable hardening, while steady state flow is achieved beyond the second yield point. Curves obtained for samples deformed at relatively high temperature often lack a well-defined first yield point (see Fig. 4.1a). As in the case of the [22$\bar{4}$3] loading orientation, selected tests were terminated after the first yield point, before B*. The stress-strain curve of one such test is given in Fig. 4.2b, together with the corresponding curve extending to higher strain, beyond B*.

The crystals deformed beyond the first yield only showed evidence for r_1^+ slip, but not for slip on the **f** system (Fig. 4.2c). The f_1^+ system was clearly identified in all test extended beyond the second yield point (Fig. 4.2d, see also section 2.5). High temperature samples showing second yield but no first yield, generaly showed f_1^+
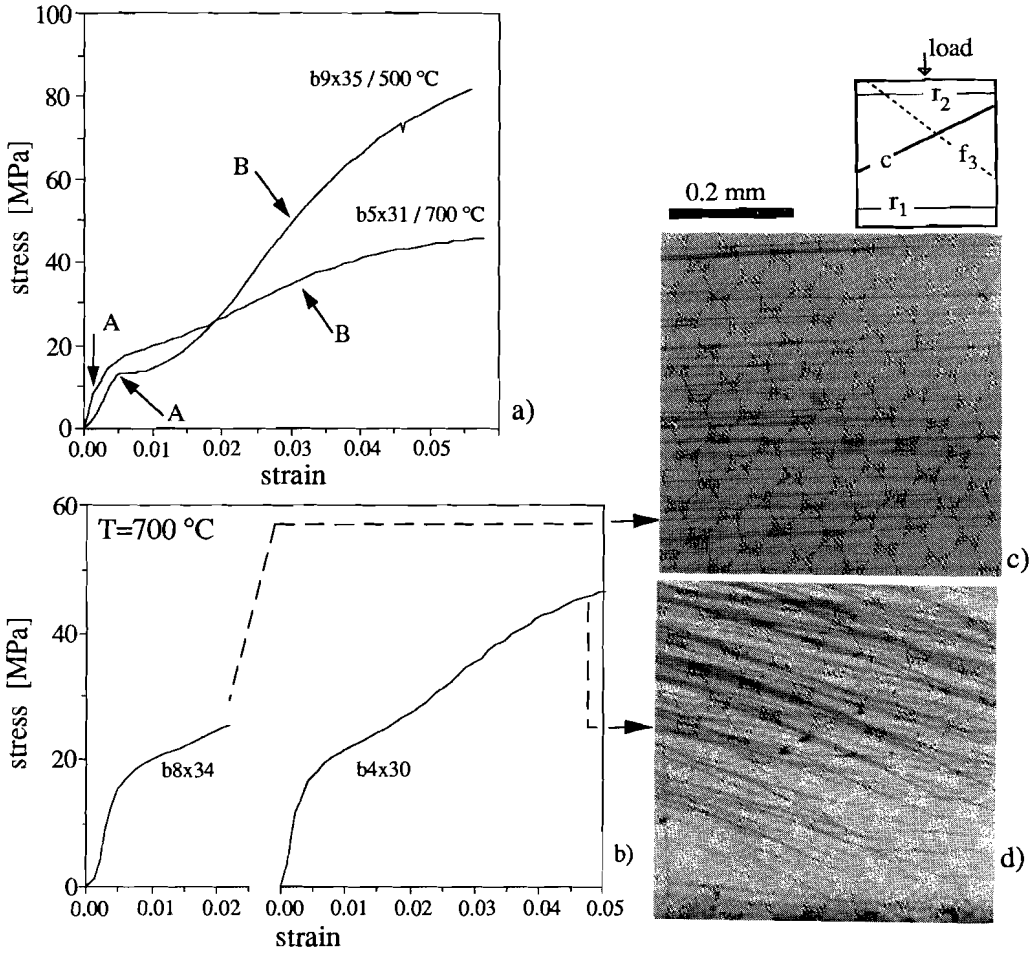
Figure 4.1
a) typical stress-strain curves for calcite crystals compressed parallel to [22$\bar{4}$3].
A and B indicate first and second 'yield' points in the curve, i.e. points of inflection or marked decrease in hardening rate.
b) stress-strain curves resulting from tests terminated after first yield (left) respectively second yield (right). [22$\bar{4}$3] orientation, $\dot{\epsilon}$=3x10 $^{-5}$ sec^{-1}. Corresponding microstructures (reflected light) are given in c) resp. d)
c) microstructure showing development of r$_2$ lines only,
d) microstructure showing both r$_2$ and f$_3$ slip lines.

slip only. The series of optical micrographs in Fig. 4.3 illustrates the gradual development of f-slip lines on the face of a series of samples compressed parallel to [40$\bar{4}$1], at increasing strains beyond the point corresponding to second yield (see also Fig. 2.6, Table 2.3).
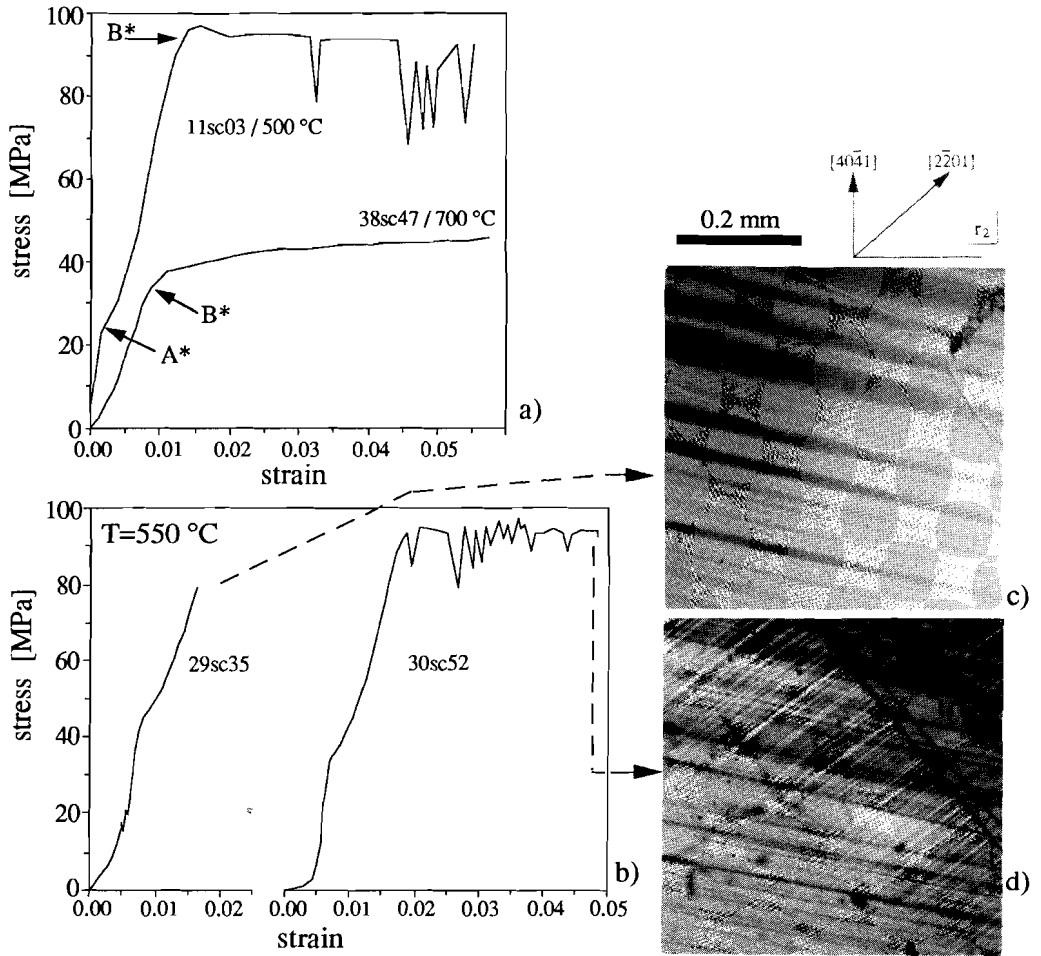
Figure 4.2
a) typical stress-strain curves for calcite crystals compressed parallel to [40$\bar{4}$1].
A* and B* indicate first and second 'yield' points in the curve, i.e. points of inflection
or marked decrease in hardening rate.
b) stress-strain curves resulting from tests terminated after first yield (left)
respectively second yield (right). [40$\bar{4}$1] orientation, $\dot{\epsilon}$=2-3x10^{-5} sec^{-1}. Corresponding
microstructures (reflected light) are given in c) resp. d)
c) microstructure showing development of r_1^+ lines only,
d) microstructure showing both r_1^+ and f_1^+ slip lines, as well as a few *e*-twins.
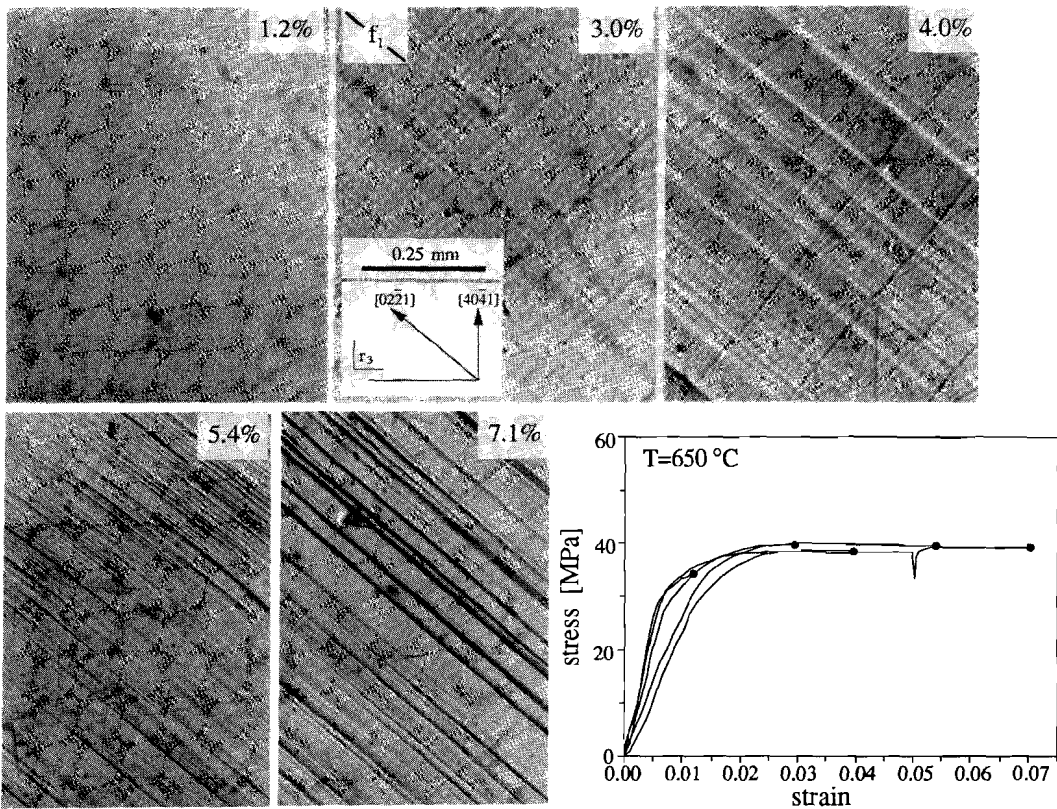
Figure 4.3
Gradual development of f-slip lines at increasing strain. Micrographs (reflected light) taken from samples represented by their stress-strain curves. Compression parallel [40$\overline{4}$1], $\dot{\varepsilon}$ = 3x10^5 sec^{-1}, parent P3. First yields hardly visible.

4.2.3 Yield stresses

The stresses corresponding to the yield points A, B and A*, B* for all crystals tested are given in Table 4.1. In all cases, the positions of the yield points were determined by visually inspecting the raw load-time curves for points of inflection or marked decrease in hardening rate. Repeated inspection of individual curves showed these points to be relocatable to within 2-10% of the initially determined load, dependent on the sharpness of the yield point. After processing the load-time data in order to obtain stress-strain curves (section 2.3), the total error in determining yield points lay between 5 and 11%. Average accuracies for first and second yield were estimated to be 7.5 and 6.5% respectively.

From the data in Table 4.1, a good correlation can be seen between the presence

Table 4.1

sample	T [°C]	first yield [MPa]	ε at yield	ε̇ at yield [sec⁻¹]	second yield [MPa]	ε at yield	ε̇ at yield [sec⁻¹]	slip-systems
Parent crystal P1:								
54sc31	400	65	1.1%	1.9×10^{-5}	obscured by twinning			r_1^+
53sc29	450	49	0.9%	2.0×10^{-5}	obscured by twinning			r_1^+
11sc03	500	23.2	0.2%	0.8×10^{-5}	93.5	1.3%	1.3×10^{-5}	r_1^+ f_1^+
02sc04	500	57.6	0.8%	1.8×10^{-5}	obscured by twinning			r_1^+ f_1^+
07sc12	550	26.9	0.1%	1.1×10^{-4}	86.7	1.3%	2.4×10^{-4}	r_1^+ f_1^+
19sc26	550	19.4	0.1%	1.9×10^{-5}	71.1	1.2%	2.3×10^{-5}	r_1^+ f_1^+
05sc16	550	27.6	0.3%	1.3×10^{-5}	obscured by twinning			r_1^+ f_1^+
03sc01	550	22.7	0.5%	1.7×10^{-5}	60.4	1.2%	2.1×10^{-5}	r_1^+ f_1^+
01sc05	550	14.9	0.1%	1.5×10^{-5}	60.8	1.0%	1.8×10^{-5}	r_1^+ f_1^+
04sc02	550	20.9	0.5%	0.9×10^{-5}	59.2	1.2%	1.0×10^{-5}	r_1^+ f_1^+
06sc13	550	20.1	0.2%	1.4×10^{-6}	64.4	1.5%	2.2×10^{-6}	r_1^+ f_1^+
17sc23	600	18.1	0.2%	0.7×10^{-4}	50.0	0.7%	1.8×10^{-4}	r_1^+ f_1^+
14sc15	600	18.4	0.1%	1.0×10^{-5}	57.8	1.2%	2.3×10^{-5}	r_1^+ f_1^+
55sc32	600	not well-defined			43.5	2.0%	2.4×10^{-5}	r_1^+ f_1^+
20sc33	600	not observed			41.2	1.8%	0.8×10^{-5}	no data
15sc20	600	16.5	0.2%	1.5×10^{-6}	44.2	0.8%	2.0×10^{-6}	r_1^+ f_1^+
18sc24	600	not observed			obscured by twinning			f_1^+
36sc22	650	not observed			34.1	1.0%	2.4×10^{-5}	f_1^+
35sc28	650	not observed			36.8	0.6%	2.7×10^{-6}	f_1^+
23sc14	800	not observed			not well-defined			f_1^+
Parent crystal P2:								
29sc35	550	41.4	0.9%	1.3×10^{-5}	not reached			r_1^+
30sc52	550	34.1	0.7%	1.3×10^{-5}	95.2	2.1%	2.0×10^{-5}	r_1^+ f_1^+
46sc49	550	46.3	0.5%	1.5×10^{-6}	obscured by twinning			r_1^+ ?
40sc42	550	44.2	0.2%	1.5×10^{-7}	obscured by twinning			r_1^+ f_1^+
51sc68	600	33.7	0.3%	1.6×10^{-4}	62.1	1.2%	2.3×10^{-4}	r_1^+ f_1^+
34sc46	600	30.8	0.5%	1.6×10^{-5}	61.2	1.3%	2.3×10^{-5}	r_1^+ f_1^+
48sc75	600	29.1	0.3%	1.5×10^{-5}	61.7	1.2%	2.5×10^{-5}	r_1^+ f_1^+
42sc37	600	26.7	0.3%	1.1×10^{-6}	46.2	0.7%	2.1×10^{-6}	r_1^+ f_1^+
32sc39	600	23.0	0.5%	1.3×10^{-6}	40	0.7%	1.7×10^{-6}	r_1^+ f_1^+
49sc63	600	19.2	0.3%	1.8×10^{-7}	39.8	0.8%	2.3×10^{-7}	r_1^+ f_1^+
44sc62	650	not observed			36.2	0.6%	2.0×10^{-4}	r_1^+ f_1^+
45sc67	650	dubious			40.5	0.6%	2.1×10^{-5}	f_1^+
41sc43	650	not observed			33.0	0.5%	1.9×10^{-6}	f_1^+
27sc41	650	not observed			33.4	0.5%	1.1×10^{-5}	r_1^+ f_1^+
43sc49	700	13.3	0.1%	0.7×10^{-4}	28.7	0.4%	1.9×10^{-4}	r_1^+ f_1^+
21sc45	700	not observed			30.9	0.7%	1.7×10^{-5}	f_1^+
38sc47	700	not observed			33.4	0.8%	2.1×10^{-5}	f_1^+
39sc50	700	not observed			30.6	0.7%	2.4×10^{-5}	f_1^+
26sc36	700	not observed			25.8	0.6%	1.8×10^{-6}	f_1^+
37sc51	700	11.1	0.3%	2.2×10^{-7}	18.3	0.5%	2.0×10^{-7}	f_1^+
52sc66	800	not observed			31.0	0.9%	2.4×10^{-4}	f_1^+
22sc44	800	not observed			not well-defined			f_1^+
24sc34	800	not observed			19.5	0.4%	1.5×10^{-6}	f_1^+
25sc40	800	not observed			not well-defined			f_1^+
28sc38	800	not observed			19.9	0.6%	1.7×10^{-7}	f_1^+

Table 4.1 continued

sample	T [°C]	first yield [MPa]	ε at yield	$\dot{\varepsilon}$ at yield [sec⁻¹]	second yield [MPa]	ε at yield	$\dot{\varepsilon}$ at yield [sec⁻¹]	slip-systems
Parent crystal P3:								
60sc89	650	5.8	0.3%	2.3×10^{-5}	26.7	1.1%	2.4×10^{-5}	r_1^+ f_1^+
61sc90	650	6.2	0.2%	2.0×10^{-5}	30.8	1.2%	2.5×10^{-5}	r_1^+ f_1^+
62sc91	650	6.1	0.1%	1.9×10^{-5}	27.8	0.6%	2.0×10^{-5}	r_1^+ f_1^+
63sc92	650	6.5	0.2%	1.9×10^{-5}	26.9	0.7%	2.2×10^{-5}	r_1^+ f_1^+
64sc93	650	5.7	0.2%	1.8×10^{-5}	33.9	0.8%	2.3×10^{-5}	r_1^+ f_1^+
65sc94	650	5.9	0.1%	2.0×10^{-5}	27.9	0.5%	2.1×10^{-5}	r_1^+ f_1^+?
66sc95	650	4.0	0.1%	1.9×10^{-5}	not reached			r_1^+
Parent crystal P9:								
47sc74	550	not observed			59.1	1.3%	1.8×10^{-5}	r_1^+ f_1^+
33sc73	600	not observed			41.5	1.1%	2.2×10^{-5}	r_1^+ f_1^+
59sc78	650	not observed			not well-defined			f_1^+
50sc72	650	not observed			28.2	0.9%	2.4×10^{-4}	r_1^+ f_1^+
58sc70	650	12.9	0.2%	2.3×10^{-6}	24.2	0.6%	2.4×10^{-6}	r_1^+ f_1^+
67sc79	650	7.1	0.1%	$\sim 10^{-7}$	20.3	0.3%	2.0×10^{-7}	no data
56sc77	700	6.4	0.3%	2.3×10^{-5}	18.2	0.6%	2.3×10^{-5}	r_1^+ f_1^+
57sc76	800	3.3?	0.1%	1.8×10^{-5}	13.7	0.8%	2.5×10^{-5}	r_1^+ f_1^+
Parent crystal PI:								
spx21	300	91.9	0.8%	2.7×10^{-5}	~118	4.3%	2.8×10^{-5}	r_2^- r_1^- f_3^-
spx18	400	51.7	0.5%	2.7×10^{-5}	not observed			no data
spx16	500	18.4	0.3%	2.7×10^{-5}	~49	3.0%	2.8×10^{-5}	r_2^- r_1^-
spx17	500	22.1	0.4%	2.7×10^{-5}	~62	4.3%	2.8×10^{-5}	no data
b1x19	650	7.5	0.4%	1.7×10^{-5}	19.1	1.3%	2.5×10^{-5}	r_2^- r_1^- c
b2x20	800	dubious			16.3	0.6%	2.6×10^{-5}	r_2^- c
b3x23	800	5.5	0.5%	2.4×10^{-5}	11.4	1.1%	2.5×10^{-5}	r_2^- c
Parent crystal PII:								
b9x35	500	13.3	0.5%	2.6×10^{-5}	50.4	3.1%	2.4×10^{-5}	r_2^- r_1^-
b6x32	600	14.1	0.6%	1.8×10^{-5}	48.8	3.7%	2.7×10^{-5}	r_2^- r_1^- f_3^- c
b10x36	650	12.3	0.5%	2.1×10^{-7}	33.7	3.1%	2.5×10^{-7}	r_2^- f_3^- c
b8x34	700	12.8	0.4%	2.0×10^{-5}	not reached			r_2^- r_1^-
b5x31	700	11.8	0.3%	1.6×10^{-5}	34.4	2.9%	2.7×10^{-5}	r_2^- f_3^- c
b4x30	700	13.5	0.3%	2.0×10^{-5}	39.0	3.5%	2.5×10^{-5}	r_2^- f_3^- c
b7x33	800	11.7	0.6%	2.3×10^{-5}	25.6	3.4%	2.7×10^{-5}	r_2^- f_3^- c

Table 4.1
First and secondary yield stresses observed in stress-strain curves of experimentally deformed calcite single crystals. Samples from parent crystals P1, P2, P3 and P9 are compressed parallel to [4041] (refer chapter 2), samples from PI and PII are compressed parallel to [2243] (refer chapter 3). Average accuracies for first and second yield stresses are 7.5 respectively 6.5%. Note that the strain rate increases from first to second yield point (compare also with the rates at 5% strain, Tables 2.3-2.6 and 3.2). This is due to the use of a non-perfectly stiff testing machine. Macroscopically observed slip systems taken from Fig. 2.19 and Table 3.3.

of first yield points in stress-strain curves and observations of r-slip lines on the faces of the correponding samples. Those crystals which show clear evidence for glide on r ([22$\bar{4}$3] and [40$\bar{4}$1] samples) generally show first yields in the stress-strain curve, while absence of first yields largely corresponds with absence of r-slip line evidence but abundant f-slip ([40$\bar{4}$1] samples).

4.2.4 Interpretation

For both loading orientations [22$\bar{4}$3] and [40$\bar{4}$1] it has been shown that samples deformed beyond the point of first yield (A, A*) but not beyond second yield (B, B*) show macroscopic slip on r only. Also, a good correlation was noted between the presence of first yields in stress-strain curves and observations of r-slip lines on corresponding samples. From this, it is inferred that the first yield point represents the onset of macroscopic slip on the r-system.

For crystals deformed beyond the second yield point, samples compressed parallel to [40$\bar{4}$1] show no additional macroscopic glide system other than $f_1[10\bar{1}1]^+$, that is besides $r_1{}^+$. It thus seems justified to relate the second yield point (B*) to the onset of macroscopic slip on $f_1{}^+$.

Interpretation of the second yield for samples compressed in the [22$\bar{4}$3] orientation is more complicated. Potentially, three different glide systems can be related to the second yield point (i.e. the inflection point in the curves), namely $r_1{}^-$, $f_3{}^-$ and c (refer Tables 4.1 and 3.3). However, a relation between second yield and onset of macroscopic $r_1{}^-$ glide can be excluded since minor $r_1{}^-$ slip lines were already observed on the faces of the sample compressed beyond the first yield only (Fig. 4.2a, Table 3.3). The second yield can thus be related to the onset of macroscopic slip c in those cases where this system was the only active system besides $r_2{}^-$ and $r_1{}^-$. In cases where $f_3{}^-$ and c were active simultaneously (five samples; Table 4.1), the stress at second yield is assumed to be linked to the macroscopically most pronounced (i.e. relatively dominant) glide system. This is $f_3{}^-$ in all samples showing mixed activity on f and c (Table 3.3).

In summary, stress-strain curves obtained for calcite single crystals compressed in [40$\bar{4}$1] and [22$\bar{4}$3] direction show first and second yield points which can be related to the onset of macroscopic slip on specific glide planes. Initial macroscopic yield is linked to the onset of significant activity on the r<$\bar{2}$021> system. Secondary yield is related to initiation of significant f<10$\bar{1}$1>$^+$ slip in the [40$\bar{4}$1] samples, and f<0$\bar{1}$11>$^-$ or c<a> slip in the [22$\bar{4}$3] samples.

4.3 CRITICAL RESOLVED SHEAR STRESSES

4.3.1 Definitions and slip systems considered

The strength of a slip system is conventionally expressed in terms of the Critical Resolved Shear Stress (CRSS or τ_c) for the system (e.g. Reed-Hill 1973). This is the shear stress resolved on the slip plane, in the slip direction, which must be reached in order to produce *significant* plastic deformation. In other words, τ_c is the critical shear stress at which large numbers of dislocations are caused to move such that *macroscopic* slip becomes observable. Such behaviour is generally associated with the development of a yield point in the single crystal stress-strain curve (e.g. Alexander and Haasen 1968). Thus, values for the CRSS for a given slip system are generally determined from yield behaviour seen in the stress-strain curves of deformed single crystals. The CRSS is obtained from the recorded yield stress (σ_Y) via the relation

$$\tau_c = \sigma_Y \cdot S \qquad\qquad (4.1)$$

where S is the Schmid factor for the active slip systems.

On the basis of numerous experimental and theoretical studies, the CRSS for a specific glide system is generally considered to be independent of the orientation of the deforming crystal.

Using the above definitions, the critical resolved shear stresses for the $r<\bar{2}021>^{\pm}$, $f<10\bar{1}1>^{\pm}$ and c<a> glide systems in calcite can now be determined from the first and second yield stress data obtained for these systems (Table 4.1). The temperature range considered is 300-800 °C. Table 4.2 summarizes the slip systems activated in the various tests reported in chapters 2 and 3, together with the corresponding Schmid factors and the yield point to which activation is related.

Compression parallel [40$\bar{4}$1]:

r<$\bar{2}$021>, positive glide sense, S=0.31,   related to first yield point A$^{\bullet}$
f<10$\bar{1}$1>, positive glide sense, S=0.48,   related to second yield point B$^{\bullet}$

Compression parallel [22$\bar{4}$3]:

r<$\bar{2}$021>, negative glide sense, S=0.38,   related to first yield point A
f<10$\bar{1}$1>, negative glide sense, S=0.45,   related to second yield point B
c<2$\bar{1}\bar{1}$0>, neutral glide sense, S=0.43,   related to second yield point B if
                                            f<10$\bar{1}$1>$^{-}$ was not active

Table 4.2
Summary of the active glide systems observed in the two loading orientations shown (chapters 2 and 3), with Schmid factors S and inferred yield point (refer table 4.1).

4.3.2 CRSS data for slip on r

Critical resolved shear stresses $\tau_c^{(r)}$ for slip on the r<$\bar{2}$021> system in the present two loading orientations, calculated from first yields (A, A*) at strain rates in the range 10^{-5} to 3×10^{-5} sec^{-1} (Table 4.1), are presented as a function of temperature in Figs 4.4a,b. The following points emerge from these figures.

1) For r<$\bar{2}$021> slip in the positive and negative directions, the CRSS decreases rapidly with increasing temperature up to T≈600 °C. However, little change is observed at higher temperature.

2) CRSS values for samples taken from the *same* parent crystal van vary
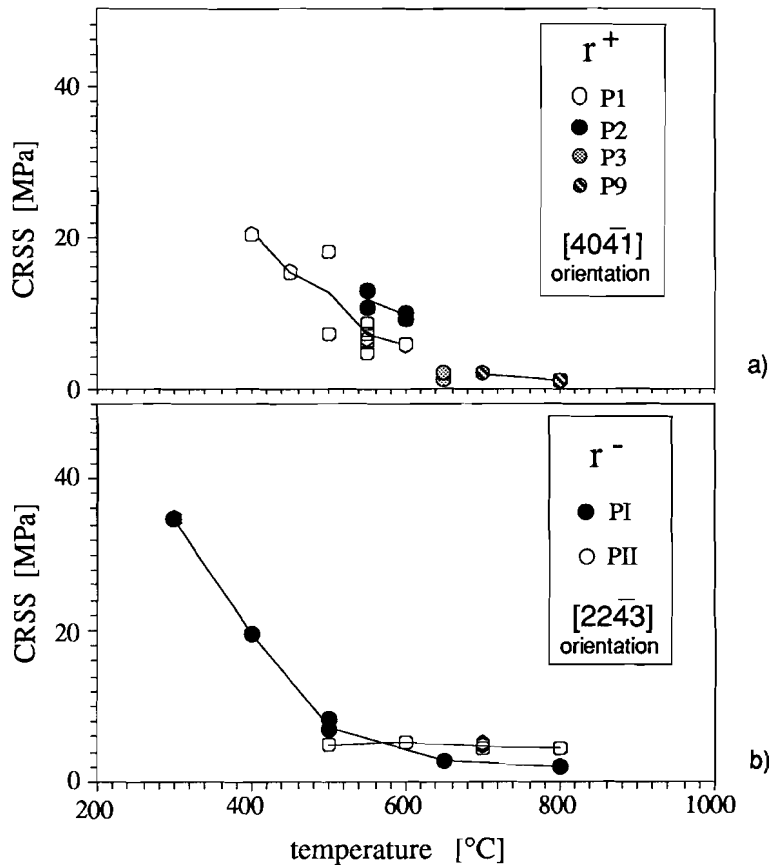
Figure 4.4
Critical Resolved Shear Stresses as a function of temperature for r<$\bar{2}$021> slip in positive and negative direction, calculated from first yield stresses at ε̇ = 1-3x10^{-5} sec^{-1} (see Table 4.1). Values for samples from the same parent crystal are plotted using identical symbols, and (average values) are interconnected. From data obtained from parent P3, only the extremes are indicated (refer Table 4.1).

significantly under otherwise identical experimental conditions (e.g. parent P1 at 550 and 600 °C, Fig. 4.4a).

3) Data obtained for samples taken from *different* parent crystals vary considerably. Note for example the difference in average CRSS for r⁺-slip between samples from parent crystals P1 and P2 at T=550 and 600 °C (Fig. 4.2a).

4) Taking the above mentioned variability into account, there is no evidence for any significant difference in strength between r<$\bar{2}$021> slip in the positive and negative senses.

4.3.3 CRSS data for slip on f

Fig. 4.5 shows the critical resolved shear stress values $\tau_c^{(f)}$ obtained for slip on the positive and negative f<10$\bar{1}$1> systems, as determined from second yields points (B, B*) at strain rates in the range 10^{-5} to 3×10^{-5} sec^{-1} (Table 4.1). The main points which emerge from Figs 4.5a,b are similar to those noted above for r-slip:

1) the CRSS decreases rapidly with increasing temperature;

2) data obtained for samples from different parent crystals show considerable variability;

3) CRSS values for samples prepared from the same parent crystal and tested under identical conditions can vary significantly;

4) taking the above variations into account, there is no real evidence for a significant difference in strength between f<10$\bar{1}$1> slip in the positive and in the negative senses, in the temperature range 600-800 °C. The one data point for f⁻-slip at T=300 °C (Fig. 4.5b) does lie well below the trend in CRSS for f⁺. Noting that no f⁻ slip has been observed between 300 and 600 °C (Table 3.3), this particular data point might represent the low temperature f<2$\bar{2}$01> slip system (after Turner et al. 1954 - see discussion in section 3.6.3) rather than the higher temperature f<10$\bar{1}$1> system.

4.3.4 CRSS data for slip on c

The results of three compression experiments in the [22$\bar{4}$3] orientation allowed determination of critical resolved shear stresses $\tau_c^{(c)}$ for slip on **c** in the a-direction (Table 4.1). These are added to Fig. 4.5b. In the temperature range 650-800 °C, the **c**<a> system is weaker initially than the f<10$\bar{1}$1> system, but stronger than r<$\bar{2}$021>. Using the relevant Schmid factor for **c**<a> slip in the [40$\bar{4}$1] direction (S=0.34), the flow stresses required for activation of c-slip in this loading orientation can be
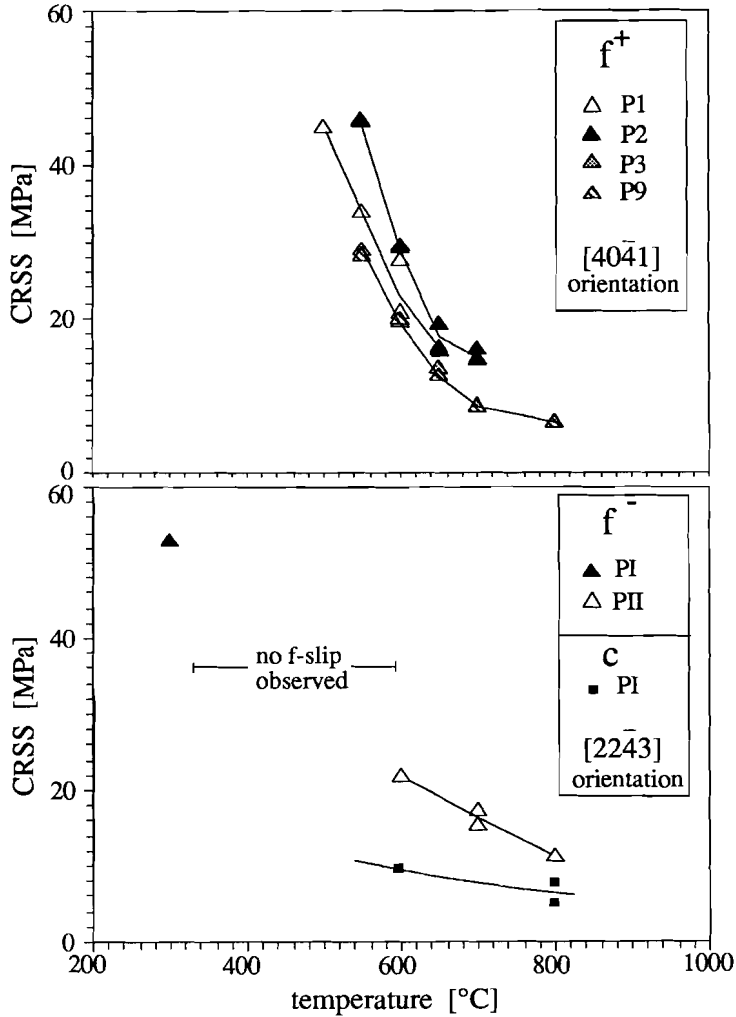
Figure 4.5
Critical Resolved Shear Stresses as a function of temperature for f<10$\bar{1}$1> slip in positive and negative direction and for c<a> slip ([22$\bar{4}$3] orientation only), calculated from second yield stresses at $\dot{\varepsilon}$ = 1-3x10^{-5} sec^{-1} (see Table 4.1). From data obtained from parent P3 only the average value is given (refer Table 4.1).

determined. For T=650 and 800 °C this yields ~24 and ~18 MPa respectively. These values are lower than the second yield stresses (B* - see Table 4.1), implying that c-slip is expected to have been activated. This is consistent with the minor basal slip suggested to have occurred in the [40$\bar{4}$1] orientation on the basis of TEM-observations (section 2.7.3), though no slip line evidence for c-slip was found.

4.3.5 Strain rate dependence of CRSS for slip on r^+ and f^+

The data presented in Table 4.1 show the strain rate dependence of the stress supported at onset of macroscopic slip on the $r<20\bar{2}1>^+$ and $f<10\bar{1}1>^+$ systems in the [$40\bar{4}1$] loading orientation. To illustrate this dependence, first and second yield stresses are graphed as a function of strain rate in standard log-log plots in Fig. 4.6, together with (near steady state) flow stresses supported at 5% strain (cf. Figs. 2.9-2.11). Best fit isotherms obtained assuming a power law relation between (yield) stress and strain rate are characterised by widely varying but generally high stress exponents (Table 4.3), illustrating a low strain rate sensitivity. Errors in the yield stress exponents (n) are large, especially in comparison with the better constrained n-values for isotherms at steady state (cf. Table 2.7). Since the scatter in flow and yield stress values are not significantly different (~5 and ~7% resp., at fixed conditions), these large errors in n may indicate that, in addition to variables such as temperature, deformation rate and parent crystal (i.e. composition), unknown (i.e. uncontrolled) factors are important in determining the critical stress level for onset of macroscopically observable slip.

In Fig. 4.6, the close correspondence of isotherms for second yield with the steady state isotherms illustrates that in samples compressed parallel to [$40\bar{4}1$] steady state cannot be achieved until slip on the $f,[10\bar{1}1]^+$ system becomes macroscopically significant. This is also apparent from the stress-strain curves obtained in the [$40\bar{4}1$]

isotherm [°C]		first yield / CRSS r^+				second yield / CRSS f^+		
		n error	corr.	data		n error	corr.	data
P1	550	15.2 ± 7.7	0.894	3 [*1]		14.0 ± 6.4	0.742	6
	600	40.9 ±32.5	0.786	3		27.3 ±18.7	0.720	4 [*2]
	650	not observed				-28.7		2
P2	550	-22.4 ±17.8	0.666	4		not observed		
	600	12.5 ± 2.3	0.939	6		12.4 ± 2.8	0.913	6
	650	not observed				42.6 ±55.1	0.484	4
	700	31.7		2		15.1 ± 7.2	0.726	6
	800	not observed				15.1 ± 5.3	0.944	3
P9	650	5.3		2		14.5 ± 0.3	0.999	3

Table 4.3
Stress exponents n for individually fitted isotherms assuming a power law relationship between yield stress (or CRSS by means of eq. 4.1) and strain rate of data for r^+ and f^+ slip (parents P1, P2 and P9), obtained by linear regression in logarthimic space. Indicated are standard error, correlation coefficient (corr.) and number of data points used in regression. Compare with Table 2.7. [*1] *of five data points at $\dot{\varepsilon}\approx2\times10^{-5}$ sec^{-1} only the average value was used in regression (see Fig. 4.6a).* [*2] *of two data points at $\dot{\varepsilon}\approx3\times10^{-5}$ sec^{-1} only the average value is used (Fig. 4.6b).*
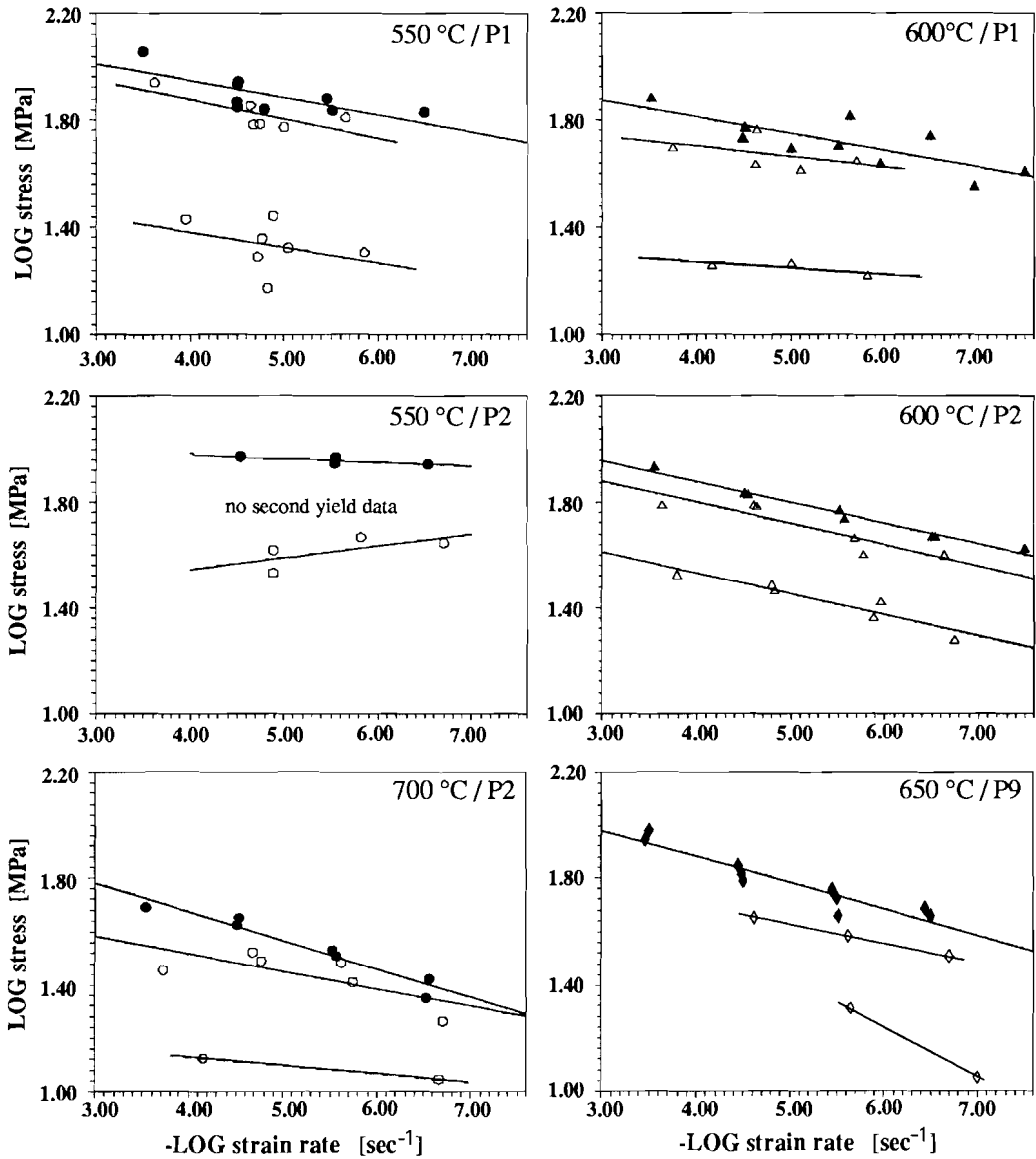
Figure 4.6
Selected Log-Log plots of strain rate vs. stress, constucted using first and second
yield stresses and flow stresses supported at 5% strain (compare Table 4.1 and
Figs. 2.9-2.11), in the [40$\overline{4}$1] loading orientation. Temperature and parent crystal
indicated, best fit isotherms calculated assuming a power law relationship between
strain rate and stress (see Tables 4.3 and 2.7); lowermost isotherms - first yield
stresses (onset of r$^+$ slip), middle ones - second yield stresses (f$^+$ slip), upper
isotherms - flow stresses at 5% strain (closed symbols).

orientation (Fig. 4.2). Whatever mechanism controls the rate of steady state creep in these crystals, it must depend in some way on the mobility of dislocations in the f<10$\bar{1}$1>$^+$ system.

4.3.6 Summary and comparison of CRSS values for r, f and c-slip

With the intention of giving a unified picture of the present data set on CRSS's, all values obtained (at $\dot{\epsilon}\approx$2x10^{-5} sec^{-1}) are compiled in Fig. 4.7. The dependence on temperature of the CRSS for **f** and **r** appears reasonably well described by empirical power law relationships. Best fit regression analyses yielded:

$$\tau_c^{(r)} = 10^{14.58 \pm 1.78} \cdot T_{ABS}^{-4.71 \pm 0.61} \qquad \text{N=31, corr.=-0.821} \qquad (4.2)$$

$$\tau_c^{(f)} = 10^{16.22 \pm 1.47} \cdot T_{ABS}^{-5.05 \pm 0.50} \qquad \text{N=27, corr.=-0.897} \qquad (4.3)$$

$$\tau_c^{(c)} = 10^{7.54 \pm 6.17} \cdot T_{ABS}^{-2.24 \pm 2.05} \qquad \text{N= 3, corr.=-0.737} \qquad (4.4)$$

with τ_c given in MPa, T_{ABS} in K and N and corr. being respectively the number of data points and the correlation coefficient of best fit. Note that no distinction has been made between positive and negative slip on **r** and **f**. From equations (4.2) and
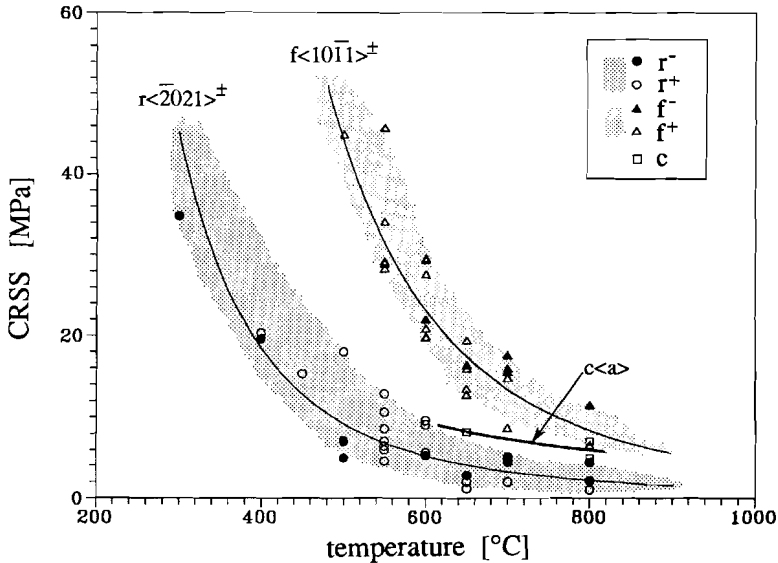
Figure 4.7
*Summary of CRSSs for r-slip (after Fig. 4.4), f-slip (after Fig. 4.5) and c-slip (section 4.3.4). Best fit lines for **r**, **f** and **c** given by equations 4.2-4.4.*

(4.3) it follows that at strain rates of ~2×10^{-5} sec^{-1} the ratio of CRSS for **f** and **r** is

$$\tau_c^{(f)}/\tau_c^{(r)} = 43.7 \cdot T_{ABS}^{-0.34} \tag{4.5}$$

At temperatures increasing from 500 to 800 °C, the *average* ratio of CRSS for **f** and **r** thus decreases only slightly from 4.6 to 4.1. Taking the observed strain rate insensitivity of CRSS into account (Fig. 4.6), these ratios are not expected to depend strongly on rate of deformation.

Omitted from the above analysis is the single CRSS for f$^-$-slip obtained at 300 °C (see Fig. 4.5b). As noted previously, this data point does not lie on the general trend for $\tau_c^{(f)}$ vs. T, and the value of 1.5 calculated for $\tau_c^{(f)}/\tau_c^{(r)}$ for this particular data point is significantly lower than expected on the basis of eq. 4.4. This further supports the suggestion that f-slip in the sample concerned occurred in the low temperature <$2\bar{2}01$> direction rather than in the higher temperature <$10\bar{1}1$> direction (refer section 3.6.3).

In numerical modelling of texture development, the relative strengths of the feasible glide systems form essential input. In this respect, equation 4.5 can be used to calculate average $\tau_c^{(f)}/\tau_c^{(r)}$ ratios. However, the yield data given in Table 4.1 can also be used to calculate ratios of CRSS's for **r**, **f** and **c** slip for *individual* crystals. Values obtained for $\tau_c^{(c)}/\tau_c^{(r)}$ are 2.8 (±0.3) at T=650 °C and 2.4 (±0.2) at T=800 °C. Ratios $\tau_c^{(f)}/\tau_c^{(r)}$ vary considerably, yet fall in the range 2.5-9.1. At fixed temperature or strain rate, the number of $\tau_c^{(f)}/\tau_c^{(r)}$ data available is rather limited. Nonetheless, the following observations can be made:

1) Under otherwise identical experimental conditions, the ratio R=$\tau_c^{(f)}/\tau_c^{(r)}$ varies with changing parent crystal. For example, R=3.2 (±0.3), 4.1 (±0.4) and 4.8 (±0.5) respectively for samples from parents P2, P1 (both f$^+$/r$^+$) and PII (f$^-$/r$^-$). N.B. T=600 °C and $\dot{\varepsilon}\approx2\times10^{-5}$ sec^{-1}.

2) With increasing temperature, $\tau_c^{(f)}/\tau_c^{(r)}$ ratios decrease (cf. eq. 4.5). For example R decreases from 6.2 (±0.6) at 500 °C to 4.8 (±0.5) at 600 °C for samples from parent P1 (f$^+$/r$^+$, $\dot{\varepsilon}\approx2\times10^{-5}$ sec^{-1}), and from 4.1 (±0.4) at 600 °C to 2.6 (±0.3) at 800 °C for samples from parent PII (f$^-$/r$^-$, $\dot{\varepsilon}\approx2\times10^{-5}$ sec^{-1}).

4.4 DISCUSSION

4.4.1 Comparison with previous data

In previous deformation experiments on calcite single crystals, the range of testing conditions investigated and the crystallographic directions chosen for compression or extension were such that deformation predominantly occurred by twinning on **e** or

slip on **r** (Turner et al. 1954, Griggs et al. 1960, Weiss and Turner 1972, Braillon et al. 1972). From yield point observations, values for the CRSS for r-slip in the negative sense were calculated for temperatures ranging from 20 to 600 °C (at $\dot{\varepsilon} \approx 2.5 \times 10^{-4}$ sec^{-1}, references given above). The data obtained are plotted in Fig. 4.8, together with the present results for both negative and positive r-slip at somewhat higher temperature (300-800 °C). At any given temperature, the data are rather dispersed, notably at 20 °C. In general however, the results of earlier workers ($\dot{\varepsilon} \approx 2.5 \times 10^{-4}$ sec^{-1}) link up reasonably well with the new data ($\dot{\varepsilon} \approx 2 \times 10^{-5}$ sec^{-1}), and there seems to be no reason to distinguish between positive and negative r-slip over the entire temperature range.

In contrast to the numerous data for r-slip, only three CRSS values for f-slip are presented in the literature, as far as the present author is aware. These data apply to the f$<2\bar{2}01>^{-}$ system at room temperature (Fig. 4.8, refer section 3.6.3), and are henceforth denoted $\tau_c^{(f\text{-}LT)}$. At this temperature, the average value for $\tau_c^{(f\text{-}LT)}$ is 1.4 times the average value for r-slip. This matches very well with a $\tau_c^{(f)}/\tau_c^{(r)}$ ratio of 1.6 which results at 300 °C if f-glide follows the $<2\bar{2}01>$ direction, as suggested in section 4.3.6. Tentatively, two lines of best (power law) fit are given in Fig. 4.8. One shows the temperature dependence of the CRSS for f$<2\bar{2}01>$ at T=20-300 °C (ratio $\tau_c^{(f\text{-}LT)}/\tau_c^{(r)}$ ~1.5). The other shows the CRSS for f$<10\bar{1}1>$ slip at T≥500 °C (ratio $\tau_c^{(f)}/\tau_c^{(r)}$ ~4).

In the experiments reported in chapters 2 and 3, twinning on **e** was only an important deformation mechanism at the lower temperatures (T<550-600 °C). Attention was not focussed on e-twinning, but it was noted that, in samples compressed parallel to [40$\bar{4}$1] (chapter 2), no pervasive twinning occurred at flow stresses below 75 MPa. Taking into account the appropiate Schmid factor, (Table 2.1), this yields a lower limit of 9 MPa for the CRSS for e-twinning at T~575 °C. This is in reasonable agreement with the value of 12 MPa reported by Spiers and Wenk (1980) for the CRSS for e-twinning at T=500 °C. However, values given by Turner et al. (1954 - Fig. 4.8), at lower temperatures, are a factor of 3-4 less. Clearly, twinning is an important, low strength mechanism at low temperature. However, taking into account the importance of stress-concentration effects in nucleating twins, it is probably not useful to attach too much significance to CRSS values (Spiers 1982).

4.4.2 Consequences for texture modelling

Published studies on simulations of texture development in calcite polycrystals use the Taylor method (after Taylor 1938, expandend by Bishop and Hill 1951a,b) or the Calnan and Clews (1950) method. In the Taylor method, it is assumed that deformation (i.e. strain) is homogeneous throughout the polycrystal, while the Calnan

Legend:
1) r$<2021>^{\pm}$
4)
5) r$<2021>^{-}$
6)
2) f$<1011>^{\pm}$
3) f$<2201>^{-}$
7)
8) e-twinning

$$\tau_C^{(f\text{-}LT)} = 10^{7.56+1.78}\, T_{ABS}^{-2.12+0.11}$$

↑ equations not reported
↓ before in the text

$$\tau_C^{(r)} = 10^{10.36+0.36}\, T_{ABS}^{-3.27+0.13}$$

$$\tau_C^{(f)} = 10^{16.22+1.47}\, T_{ABS}^{-5.05+0.50}$$

equation 4.3

$$\tau_C^{(c)} = 10^{7.54+6.17}\, T_{ABS}^{-2.24+2.05}$$

equation 4.4

CRSS [MPa] vs temperature [K]
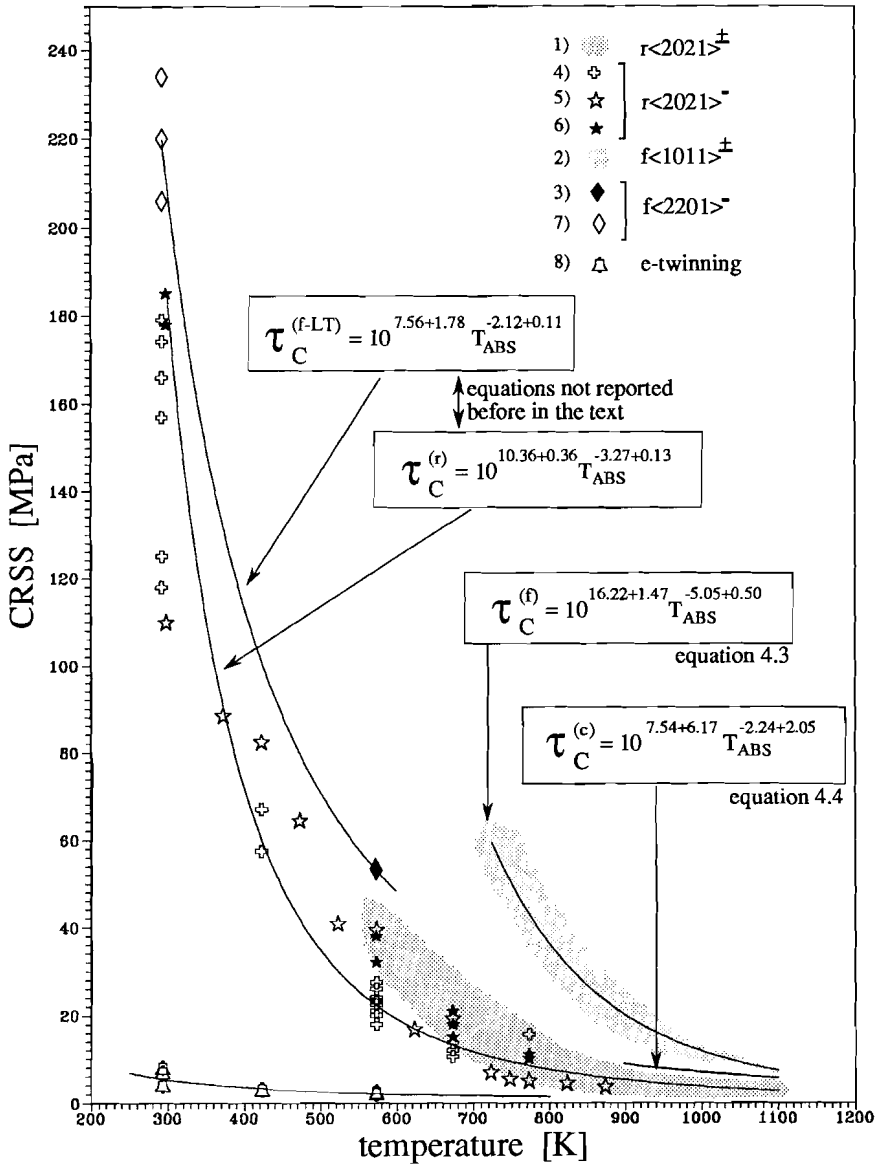
Figure 4.8
Compilation of CRSS-data from the literature, and comparison with the present data. Shaded areas taken from Fig. 4.7. Note modified best fit line for temperature dependence of $\tau_C^{(r)}$ with respect to eq. 4.2: now all data from the literature are included in regression analysis. Sources: 1) 2) 3) this study, 4) 7) 8) after Turner et al. (1954), 5) after Griggs et al. (1960), 6) after Braillon et al. (1972).

and Clews model is an expansion of the assumption that the stress is homogeneously distributed (e.g. see Spiers 1982, Wenk 1985).

Wenk et al. (1973) apply the Calnan and Clews method to calcite, but the majority of published studies on calcite polycrystals is based on the Taylor(-Bishop-Hill) method (Lister 1978, Van Houtte and Wagner 1985, Wenk et al. 1986, 1987, Takeshita et al. 1987). The latter method is concentrated upon here. In the Taylor method, homogeneous deformation is assumed to be accomodated by slip and mechanical twinning on five independent systems with low strain rate sensitivity (i.e. rigid-plastic behaviour). A survey of possible texture types can be undertaken by exploring the so-called Single Crystal Yield Surface (SCYS), which is a polyhedron describing the yield behaviour of the crystal in five-dimensional stress-space (e.g. Takeshita et al. 1987). Each facet of the polyhedron represents the yielding condition corresponding to a particular slip or twinning system and its distance to the origin of the SCYS is proportional to the critical resolved shear stress (CRSS). Relative changes of the CRSS's (hence, changes in relative activity of different slip systems), result in new configurations (topologies) of the SCYS. For each configuration, the set of five independent slip systems necessary to accomodate an arbitrary imposed increment of strain can be found, and the associated stress state and lattice rotation can be calculated. Doing this for each grain in a model polycrystal thus enables texture development to be calculated for any desired path.

It follows from the above description that knowledge of all potential slip and twinning systems and their critical resolved shear stresses is required in order to define a SCYS and to compute texture development. In this respect, the single crystal data obtained in the present study supply important new information.

Firstly, the present results demonstrate the existence of an important set of high temperature slip systems not reported previously, namely $f<10\bar{1}1>$. It has also been shown that c-slip is likely to be of far greater importance in calcite than previously thought, again at high temperatures. Neither the $f<10\bar{1}1>$ or c<a> glide systems have been included in texture modelling to date.

Secondly, contrary to earlier suggestions and assumptions, there seems to be no quantitative basis for a distinction in strength between positive and negative slip on r and f, irrespective of the absolute values of the CRSS's.

Finally, the low strain rate sensitivity observed for the CRSS's on r^+ and f^+ (section 4.3.5) supports the applicability of the Taylor approach to texture modelling in calcite polycrystals. Note however that the assumption of homogeneous strain is of questionable applicability except when all systems have similar strengths (Spiers 1979, Van Houtte and Wagner 1985).

A generalized overview of the critical resolved shear stresses *at onset of macroscopic slip* on the main calcite deformation systems is presented in Fig. 4.9. The diagram combines both previous and newly presented data, and shows that,
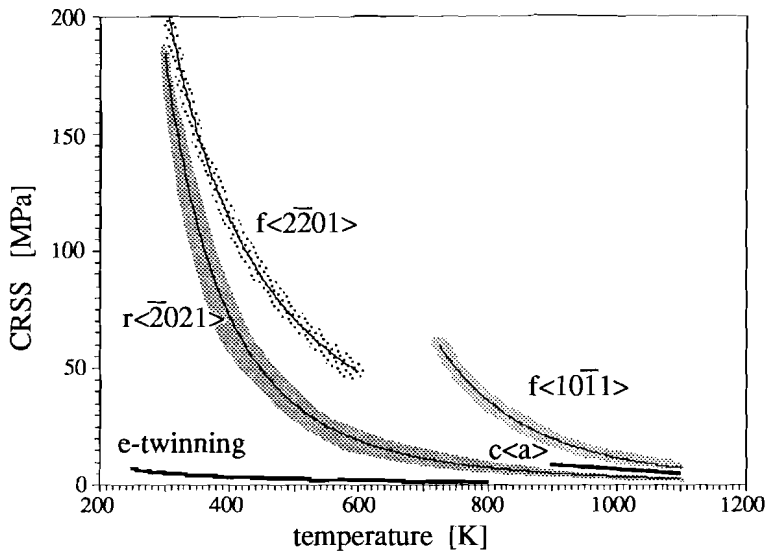
Figure 4.9
Simplified diagram showing temperature dependence of CRSSs fo the main calcite glide and twinning systems, constructed after Figs. 4.4-4.8.

assuming slip onset data apply, a transition in SCYS configuration and hence texture type is expected at T$\approx$300-500 °C ($\sim$570-770 K), due to a major change in slip direction for f-slip and the conformably changing $\tau_c^{(f)}/\tau_c^{(r)}$ ratios. The increasing importance of c-slip at T$\sim$600 °C ($\sim$870 K) may also bring about a texture transition. Since neither f<10$\bar{1}$1> nor c<a> slip have been incorporated in existing texture simulations, the high temperature textures predicted to date cannot apply to either natural or experimentally produced textures, and any apparent agreement must be fortuitous (see section 1.5). The poor agreement noted between c-axis pole figures calculated for high temperature simple shear and measured c-axes textures in experimentally sheared marbles (Schmid et al. 1987 - see Fig. 1.5) and in naturally deformed limestones from a Pyrenean thrust zone (De Bresser 1989) is consistent with this.

As mentioned previously, the shape of the SCYS is determined by the relative strengths of the various slip systems. For simplicity, critical resolved shear stresses at onset of macroscopic slip are usually used to represent the strength of the slip systems. In general, however, the various CRSS values (hence SCYS configuration) depend not only on temperature and strain rate but also on strain (Wenk et al. 1986). For example, work hardening on an active glide system represents an increase in the CRSS of the system with increasing strain. Such effects are clearly apparent in the present tests on calcite single crystals, where, after a first yield related to the onset of r-slip, considerable hardening occurs until a second system (f

or **c**) is activated (e.g. Figs 4.1, 4.2). In other words, the stress resolved on the r-plane increases with increasing strain in order to continue macroscopic glide on **r**. At the second yield point, the newly activated slip system starts accumulating part of the strain or may even take over completely if hardening on the new system occurs at a lower rate than on the initial r-plane. Taking these considerations into account, CRSS ratios determined at the *onset* of slip (as given in section 4.3 and Fig. 4.9) become meaningless for texture modelling, since the ratios change continuously with increasing strain, in a manner dependent on the orientation of individual crystals. This problem can be partly circumvented by systematically exploring the SCYS for various ratios of CRSS's, thereby identifying major SCYS configurations and texture transitions. Nonetheless, some information regarding the 'harder' and 'softer' systems is still required to model texture development to a first approximation. CRSS-ratios determined at onset of slip thus form a reasonable starting point, and their use for calcite appears justified by broad agreement found between calculated and observed textures at low temperatures (Wenk et al. 1986, 1987). It is hoped that a comparable agreement can be obtained for the higher temperatures by incorporating the $f<10\bar{1}1>$ and $c<a>$ slip systems and their corresponding (relative) stengths in future texture modelling. In this context, it is important to note that the work hardening of the $r<\bar{2}021>$ systems seen in the present experiments implies that at strains above 2% the SCYS will be dominated by the $f<10\bar{1}1>$ and $c<a>$ systems. Thus, high temperature texture development should be dominated by these systems, with the approximate (near steady state) strengths (or relative strengths) reported here applying.

4.5 SUMMARY AND CONCLUSIONS

Stress-strain curves obtained for calcite crystals compressed in both the $[40\bar{4}1]$ or $[22\bar{4}3]$ directions mostly show two yield points. From microstructural evidence, it was inferred that these yield points can be related to the onset of macroscopically observable slip, first on an $r<\bar{2}021>^{\pm}$ system and then on an $f<10\bar{1}1>^{\pm}$ or $c<a>$ system. Using the appropriate Schmid factors, critical resolved shear stresses (CRSS) were calculated for onset of slip on the various systems over the temperature range of 300-800 °C. At any given temperature, the CRSS values often vary considerably. Nonetheless, clear trends are apparent in the data. With increasing (absolute) temperature (T_{ABS}) the CRSS values (τ_c) decrease in a manner which can be described by empirical laws of the type $\tau_c = A \cdot T_{ABS}^{b}$, where b<0. Over the temperature range investigated, CRSS's for the f-system are higher than those for the r-system, while values obtained for c-slip lie in between. No evidence was found for a difference in strength between positive and negative glide on **r** and **f**.

Yield stresses for r^+ and f^+ slip were observed to be rather insensitive to strain rate, with empirical power law fits resulting in conventional stress exponents generally above 12.

Comparing the present results with previous data, it was concluded that two regimes of slip system activity exist, namely a low temperature regime involving e-twinning, slip on $r<\bar{2}021>^{\pm}$ and on $f<2\bar{2}01>^-$ (positive direction not reported), and a high temperature regime with $r<\bar{2}021>^{\pm}$, $f<10\bar{1}1>^{\pm}$ and $c<a>$ slip, the two latter systems dominating at strains above a few percent. This low-high temperature transition in slip systems occurs at ~400 °C, and is expected to be associated with major changes in SCYS configuration and with one or more texture transitions. Since the $f<10\bar{1}1>$ and $c<a>$ systems have not previously been taken into account in texture modelling, high temperature texture predictions carried out to date cannot be correct, and any apparent agreement with natural or experimental textures must be fortuitous. Further texture modelling is needed for the high temperature regime, taking the f and c systems observed here into full account as the dominant high temperature mechanisms.

CHAPTER 5

DISLOCATION DENSITY vs. STRESS RELATION FOR CALCITE

5.1 INTRODUCTION

The migration of linear defects or dislocations under the action of an applied stress forms the basic mechanism of intracrystalline plastic flow in solids. During flow by this type of mechanism, the total line length of dislocations present in unit volume, i.e. the dislocation density ρ, can be theoretically linked to the applied (differential) stress σ by a relation of the type $\sigma \propto \rho^{0.5}$ (e.g. Kohlstedt and Weathers 1980). In steady state deformation, a constant density of dislocations is therefore expected, independently of strain. This theoretical relationship forms the basis of many microphysical models for dislocation dynamics and creep (e.g. Alexander and Haasen 1969, Frost and Ashby 1980), and offers a possible method of estimating paleo-stresses during natural deformation (Twiss 1977).

Aside from theoretical developments, the dependence of dislocation density on stress has been experimentally determined for many metals and ionic materials (reviewed by Takeuchi and Argon 1976), and for a number of geological materials, such as olivine (Durham et al. 1977) and quartz (McCormick 1977). The experimental results show that the density of dislocations indeed increases with differential stress, but the empirical relationships often deviate somewhat from the theoretical predictions.

In this chapter, the stress vs. dislocation density relation for calcite single crystals will be determined, in order to test the validity of the theoretical relation for calcite. The result is used to assess whether it is justified to compare the dislocation creep behaviour of calcite with microphysical models based on the theoretical relation.

The method employed involved the measurement of dislocation densities in experimentally deformed single crystals of calcite, using Transmission Electron Microscopy (TEM). The crystals were uniaxially compressed parallel to [40$\bar{4}$1], at constant strain rate and at temperatures in the range 550-800 °C, and were found to exhibit steady state flow behaviour with flow stresses between 20 and 115 MPa (refer chapter 2). It is shown that a steady state dislocation density ρ is established

after ~2% strain, and that the ρ-σ relation agrees well with theory. The single crystal data are compared with existing and newly obtained data from experimentally deformed calcite rocks. The latter deviate from the single crystal results at low stresses. On the basis of a simple model, this is explained in terms of the influence of grain size.

5.2 THEORETICAL RELATIONSHIP BETWEEN DISLOCATION DENSITY AND STRESS

The background theory for the commonly quoted dependence of dislocation density on applied stress, $\sigma \propto \rho^{0.5}$, is treated in many textbooks (e.g. Honeycombe 1968, Nicolas and Poirier 1976, Poirier 1985) and papers (e.g. Twiss 1977, Kohlstedt and Weathers 1980, Weertman and Weertman 1983a). It is briefly repeated below.

In the neighbourhood of a dislocation, the lattice of the host is elastically strained, resulting in an internal stress field σ_i. From elastic theory (e.g. Hirth 1983), it can be shown that σ_i varies with the distance L to the dislocation line as

$$\sigma_i \propto \mu b / L \tag{5.1}$$

where μ is the mean shear modulus of the crystal and b is the length of the Burgers vector. Equation 5.1 holds for all stress components. Various models have been proposed to relate the average internal stress field ($\bar{\sigma}_i$) over the entire crystal to the distribution of dislocations (e.g. see Kohlstedt and Weathers 1980). They are all of the type

$$\bar{\sigma}_i = \alpha \mu b / L \tag{5.2}$$

where L is now the spacing between dislocations and α is a constant dependent on the type of dislocation (edge vs. screw) and the geometry of the dislocation configuration. For example, a configuration of edge dislocations passing each other on parallel slip planes, separated a distance L, predicts a value of 0.6 for α (Taylor 1934). Usually however, a random distribution of dislocations is assumed, in which the dislocations are essentially in equilibrium with the stress fields of their neighbours at an average separation L (e.g. Weertman and Weertman 1983a). The total density of dislocations ρ_t is then related to L according to the equation

$$\rho_t = 1 / L^2 \tag{5.3}$$

Noting now that for creep to proceed at steady state the applied stress σ has to be

just equal to the internal stress ($\bar{\sigma}_i = \sigma$, Poirier 1985), equations 5.2 and 5.3 can be combined to

$$\sigma = \alpha \mu b \cdot \rho_t^{0.5} \qquad (5.4)$$

where the constant α is often quoted to be of the order of 1 (Kohlstedt and Weathers 1980). As given here, the relation between dislocation density and applied stress is independent of strain rate and strain, and only slightly dependent on temperature and pressure through the PT dependence of the shear modulus and the possible change in Burgers vector with temperature.

5.3 SAMPLES AND EXPERIMENTAL METHOD

For present purposes, use was made of calcite single crystals compressed parallel to the [40$\bar{4}$1] direction (refer chapter 2). Details on sample composition, preparation and experimental method were given before (sections 2.2, 2.3). It is recalled here that the crystals were uniaxially deformed at temperatures in the range 400-800 °C, at constant strain rates in the range 3×10^{-4} to 3×10^{-8} sec^{-1}. At the end of each test, the samples were rapidly unloaded, with immediate quenching using a blast of cold CO_2 gas, directly followed by removing the sample from the experimental set-up.

Out of the series of calcite single crystals compressed in the [40$\bar{4}$1] direction, 22 crystals were selected for dislocation density measurement. The selection of 15 of these was based entirely on flow stress level, i.e. choosing reasonably well distributed stresses irrespective of parent crystal composition, test temperature and strain rate. Included in the selection were three samples (deformed in air at T= 650 °C) which tended to disintegrate after the experiment (see section 2.4.2). The characteristics of the stress-strain curves obtained for these samples showed no reason to withdraw them from analysis. Seven additional crystals, deformed to varying final strains under otherwise identical conditions, were used to study the influence of strain on the development of the dislocation microstructure.

All selected samples exhibited steady state flow at strains above 1-2%, at T≤600 °C irregularly interupted by load drops associated with twinning. Optical and Scanning Electron Microscopy study of the deformed samples (refer chapter 2) revealed numerous slip lines, glide bands and kink bands, proving intense slip activity. Twinning on e was found to be an important mechanism of deformation at relatively low temperatures (T≤600 °C), but slip on the r<$\bar{2}$021>$^+$ and particularly f<10$\bar{1}$1>$^+$ systems dominated at higher temperature. Though quite inhomogeneous on the scale of the sample, the deformation was relatively homogeneous on the scale of a TEM-specimen used for dislocation density measurements (see Fig. 5.1).
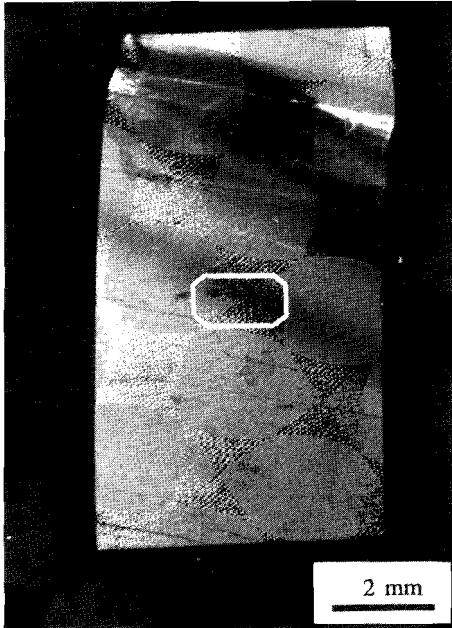
Figure 5.1
Transmission optical micrograph of a deformed calcite singe crystal (15sc20 - see Table 5.2), under crossed nicols. Vertical direction is parallel to the loading direction. Note the sample-scale undulose extinction (dark cross-cutting bands). Size of a TEM specimen is indicated.

All samples showed evidence of microcracking, but as stated earlier, these cracks were found to be introduced during the quench treatment.

5.4 TEM SAMPLE PREPARATION AND DISLOCATION DENSITY MEASUREMENT

TEM-specimens were prepared from the central region of the deformed crystals, following the method outlined in section 2.6.1. In addition, a few specimens were made by glueing thin cleavage fragments directly onto support grids. For study, a JEOL 200C electron microscope with a side-entry double tilt goniometer stage was used, operating at 200 kV. The microscope was equipped with an X-ray analytical system.

Dislocation density measurement was performed on areas which had a specimen thickness suitable for full plate images, generally using a magnification between 10000 and 30000 times, and paying no attention whatsoever to the dislocation structure. Images of dislocations were made in maximum contrast, under bright field, multi-beam conditions. An average of 14 plates was obtained for each specimen. The dislocation density was measured in terms of the number of dislocations occurring per unit area. This was done by counting the number of intersections of all dislocations with the series of linear traverses shown in the full plate network (29

lines) of Fig. 5.2a. The total dislocation density ρ_t was then determined using

$$\rho_t = 2N \ / \ \lambda t \qquad [cm^{-2}] \qquad (5.5)$$

in which N is the number of counted intersections, λ is the total length of linear traverse and t is the thickness of the specimen (after Schoeck 1962, see also Hirsch et al. 1965). This formula assumes a random distribution of dislocations, the factor 2 in equation 5.5 then correctly modifying the measured number-per-unit-area to the three-dimensional definition of dislocation density, i.e. line length per unit volume.

From equation 5.5 it is clear that an estimation of the sample thickness (t) is required to determine ρ_t. This thickness corresponds to the average vertical depth of the linear traverses through the selected area, which, in case the sample is tilted, is not necessarily equal to the shortest distance between top and bottom of the

a)

b)

c)   effective thickness [μm]
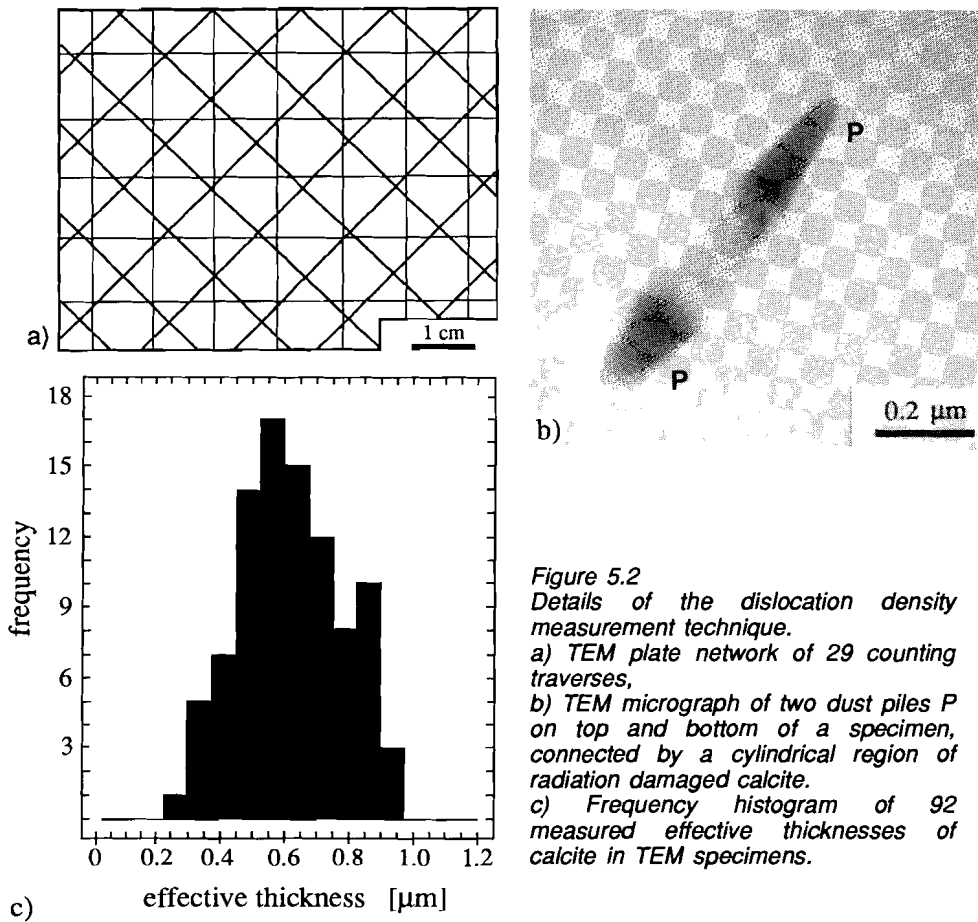
Figure 5.2
Details of the dislocation density measurement technique.
a) TEM plate network of 29 counting traverses,
b) TEM micrograph of two dust piles P on top and bottom of a specimen, connected by a cylindrical region of radiation damaged calcite.
c) Frequency histogram of 92 measured effective thicknesses of calcite in TEM specimens.

specimen in that area. For determining the effective thickness t, the electron beam was focussed onto the area under consideration. Deposits of contaminant 'dust' then accumulated on the top and bottom of the specimen, occasionally connected by a cylindrical region of radiation-damaged calcite (Fig. 5.2b). After rotating the specimen through a measured angle, the distance between the dustpiles, and thus the effective thickness t, could be determined from an exposed image, after correcting for the rotation angle. In this way, thickness estimates were made for every four plates (on average) containing dislocations. Obtained thicknesses varied between 0.27 and 0.97 μm, with a mean value of 0.62 μm (92 measurements, one standard deviation 0.17 μm). The results are given in the frequency histogram of Fig. 5.2c. The mean value of 0.62 μm agreed well with estimates based on projected widths of objects of known orientation, such as e-twin boundaries. The result for t also agrees favourably with the mean value of 0.34 μm found by Briegel and Goetze (1978) for limestone in TEM operating at 100 kV (i.e. half our operating voltage).

For every sample, the quoted dislocation density ρ_t is the arithmetic mean of the values per individual plate. In averaging, these values were linearly weighted for significant differences between plates, i.e. with repect to the size of the studied regions. Thus plates covering large areas were allocated more weight than those covering relatively small areas.

5.5 RESULTS

5.5.1 Dislocation microstructure

As described in chapter 2, the dislocation substructure of the deformed crystals can be characterized by both straight and curved, locally helical dislocations, and by isolated pseudo-hexagonal dislocation networks. Well defined tilt walls or subgrains were rare. The distribution of dislocations is moderately heterogeneous, though without visible concentration in localized bands. The dislocation lines showed only weak preferred orientations. Qualitatively, an increase in density of dislocations was observed with increasing flow stress, but the general nature of the microstructure did not vary substantially with temperature or strain rate. No evidence was found for any correlation between the quenching cracks reported previously and the observed dislocation substructure or density.

The typical dislocation microstructure is illustrated in Fig. 5.3. It shows a more or less random distribution of dislocations, as required for applying equation 5.5 in determining the dislocation density. Undeformed, annealed crystals (the starting material) showed only a few dispersed dislocations, with a density of $\sim10^6$ cm^{-2}.

a) ↓ increasing strain   1 µm   increasing stress ↓
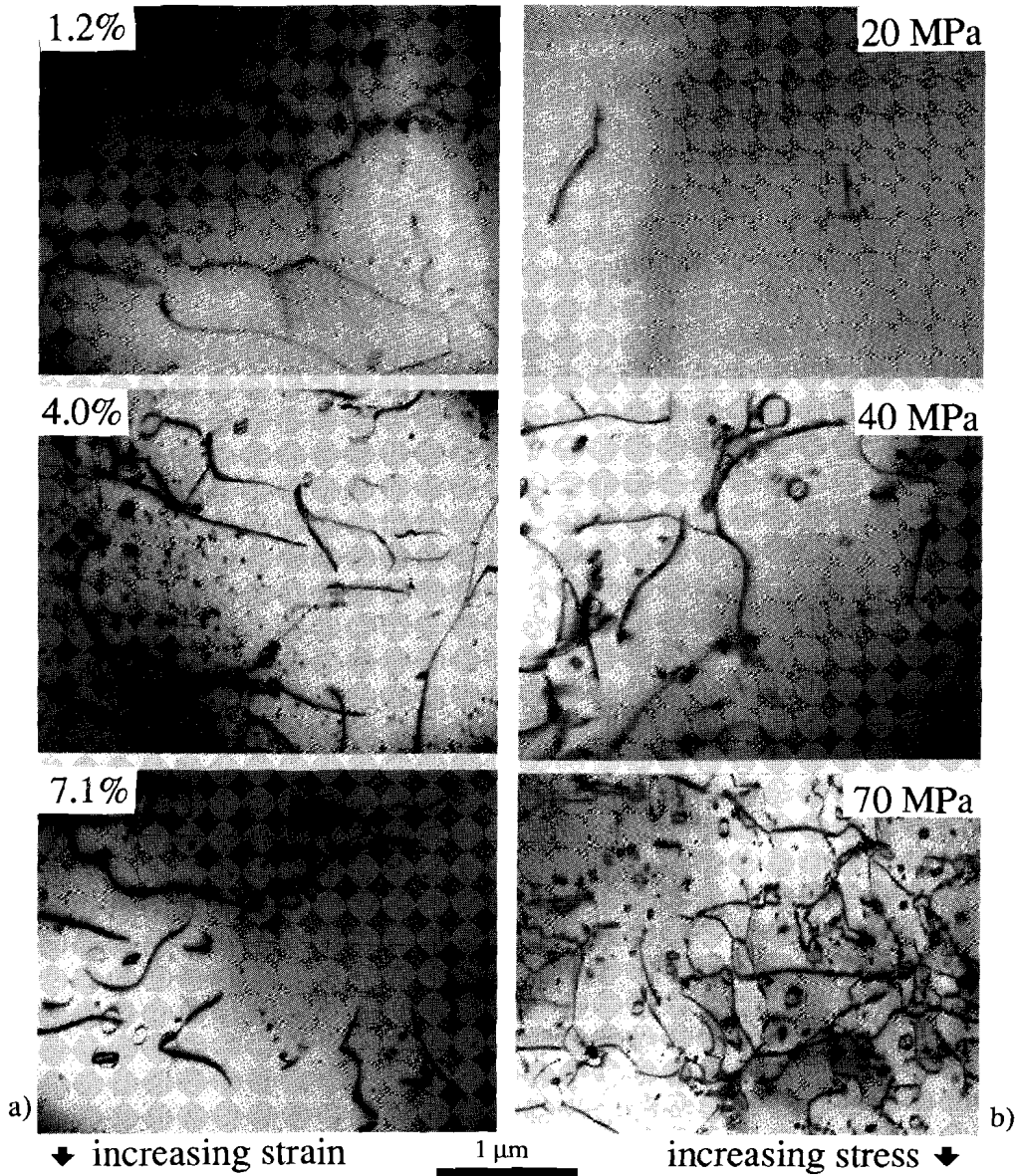
Figure 5.3
Bright field TEM micrographs of deformed calcite crystals illustrating the dependence of the dislocation density on strain (a) and on stress (b).
a) Steady state dislocation density developed at increasing strain, from 1.2% (sample 65sc94), via 4.0% (62sc91) to 7.1% (60sc89). Flow stress ~40 MPa, T=650, $\dot{\varepsilon}=3x10^{-5}$ sec^{-1}.
b) Increasing dislocation density at increasing flow stress, from 20 MPa (sample 28sc38), via 40 MPa (61sc90) to 70 MPa (01sc05).

5.5.2 Dependence of dislocation density on strain

Figure 5.4 shows the stress-strain curves for the seven single crystals taken from the same parent crystal and deformed to different strains at otherwise identical experimental conditions (Table 5.1, see also Fig. 5.3a). Closely reproducible steady state flow was achieved at strains of around 2%. The crystals were all found to deform by $f<10\bar{1}1>^{+}$ slip with minor $r<\bar{2}021>^{+}$ slip locally. Small inflections in the stress-strain curves at stresses around 6 MPa indicate the r^{+} yield point (refer chapter 4). The measured dislocation densities are given in Table 5.1 and are plotted as a function of strain in Fig. 5.5. From this, it is clear that the dislocation density vs. strain curve closely reflects the *stress*-strain curve (cf. Fig. 5.4). Most importantly, a constant dislocation density is established after ~2% strain, independently of further strain.

experiment	strain at end [%]	stress at end [MPa]	number of TEM plates	mean dislocation density [cm^{-2}]
60sc89	7.1	39.3	16	4.17($\pm$0.85) x10^{8}
61sc90	5.4	39.5	16	3.86($\pm$1.07) x10^{8}
62sc91	4.0	38.1	16	4.14($\pm$0.60) x10^{8}
63sc92	3.0	39.7	16	4.74($\pm$1.27) x10^{8}
64sc93	1.1	39.9	16	2.59($\pm$0.88) x10^{8}
65sc94	1.2	34.4	16	3.05($\pm$0.77) x10^{8}
66sc95	0.4	19.6	19	0.59($\pm$0.45) x10^{8}

Table 5.1
List of experiments and results for single crystals from one parent crystal (P3), deformed to different strains, at T=650 °C and $\dot{\varepsilon}$= 3x10^{-5} sec^{-1}. The given dislocation density is the mean value ($\pm$ one standard deviation) of the values per TEM plate.

5.5.3 Dislocation density vs. stress relation

Experimental conditions and results of dislocation density measurements for the 15 selected samples are given in Table 5.2. The densities are plotted against flow stress in Fig. 5.6, which includes the results from the samples deformed to different strains (Table 5.1). The dislocation density obviously increases with increasing stress. Densities measured in the thin cleavage fragments are not significantly different from those determined in conventional TEM specimens (cf. Table 5.2),
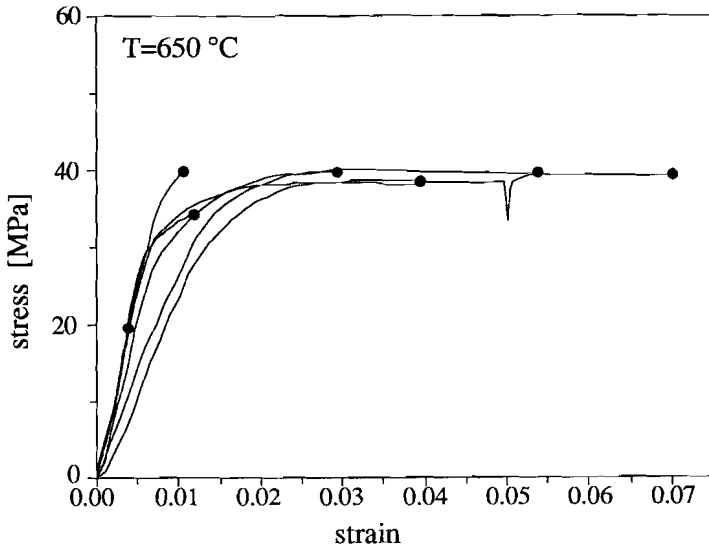
Figure 5.4
Stress-strain curves obtained for calcite single crystals from parent crystal P3 (see chapter 2). T=650 °C, $\dot{\varepsilon}=3x10^{-5}$ sec^{-1}. Dots indicate end points of curve. Figure is identical to Fig. 2.6.
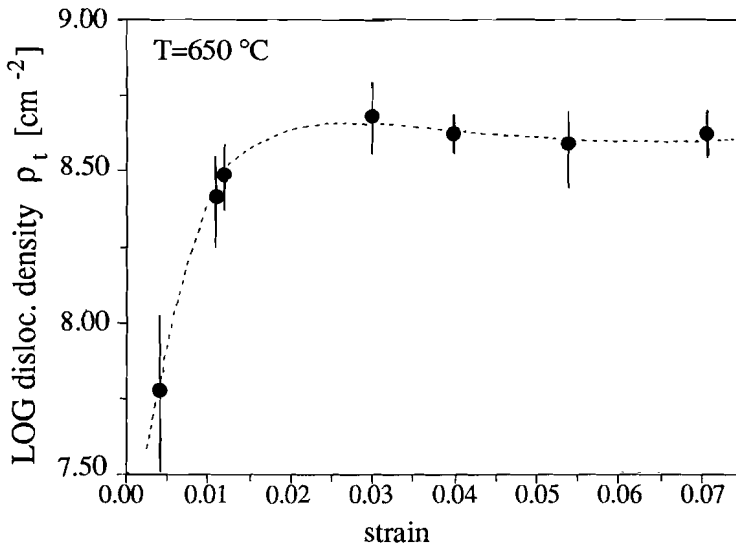
Figure 5.5
Relation between dislocation density and strain, as determined for the samples of Fig. 5.4 (see also Table 5.1). Error bars indicate one standard deviation from the mean value per sample.

demonstrating that influences of thin sectioning and ion-milling were negligible. Note that while most samples achieved a more or less steady state flow stress, the densities measured under *non-*steady state stress conditions (strains below 2-3%: Fig. 5.5) also fall on the general trend. Within the scatter of the data, no evidence was found for any significant influence of temperature, strain rate, strain rate history (i.e. the step-tests - Table 5.2) or composition of the starting material (Fig. 5.7).

The dependence of the total dislocation density (ρ_t) on stress (σ) was determined by a standard linear regression method (in log space). As input variables, the flow stess supported at the end of the experiment and the mean dislocation density per sample were used. Since in the present experiments, the flow stress *resulted* from the imposed experimental conditions, the stress cannot be considered as a true independent variable, Therefore, least-square regressions were performed using ρ_t as well as σ as dependent variables (including all 22 data points, Fig. 5.6). The results were averaged, yielding

$$\sigma = 10^{-3.20(\pm 0.53)} \cdot \rho_t^{0.56(\pm 0.06)} \qquad \text{corr.} = 0.897 \qquad (5.6)$$

where σ is in MPa, ρ_t in cm^{-2}, and where corr. indicates the correlation coefficient. If

experiment	P	temp. [°C]	strain rate [sec⁻¹]	strain at end [%]	stress at end [MPa]	number of TEM plates	mean dislocation density [cm⁻²]
07sc12	1	550	3×10^{-4}	6.8	112.6	15	$12.74(\pm 4.75) \times 10^8$
30sc52	2	550	3×10^{-5}	5.4	91.0	14	$10.54(\pm 2.21) \times 10^8$
01sc05	1	550	3×10^{-5}	5.7	69.8	23	$6.01 (\pm 2.01) \times 10^8$
19sc26	1	550	3×10^{-7} *	7.0	66.7	14	$10.57(\pm 3.65) \times 10^8$
10sc10 f	1	650	3×10^{-4}	6.9	63.1	11	$10.80(\pm 3.80) \times 10^8$
15sc20	1	600	3×10^{-6}	5.1	50.2	12	$4.24 (\pm 1.24) \times 10^8$
21sc45	2	700	3×10^{-5}	6.8	43.0	14	$7.94 (\pm 2.68) \times 10^8$
08sc09 f	1	650	3×10^{-5}	6.0	39.4	16	$4.12 (\pm 1.46) \times 10^8$
18sc24 f	1	600	3×10^{-8} *	6.0	37.4	9	$3.44 (\pm 1.65) \times 10^8$
22sc44	2	800	2×10^{-5}	5.9	30.2	13	$1.38 (\pm 0.34) \times 10^8$
09sc11 f	1	650	3×10^{-6}	5.7	28.9	6	$1.90 (\pm 0.74) \times 10^8$
24sc34	2	800	3×10^{-6}	5.2	25.4	16	$1.04 (\pm 0.38) \times 10^8$
37sc51	2	700	3×10^{-7}	5.2	22.5	14	$1.63 (\pm 1.03) \times 10^8$
23sc14	1	800	3×10^{-5}	8.1	20.7	10	$2.58 (\pm 0.96) \times 10^8$
28sc38	2	800	3×10^{-7}	4.7	19.6	16	$0.82 (\pm 0.30) \times 10^8$

Table 5.2
List of experiments and results for single crystals from two parent crystals (P1 and P2, second column), deformed at different flow stresses. The given dislocation density is the average value (± one standard deviation) of the values per indivudual TEM plate. Star (*) indicates strain rate stepped down from a higher rate (see chapter 2), 'f' denotes TEM specimen made from broken off fragment of a single crystal, without thin sectioning and ion milling.
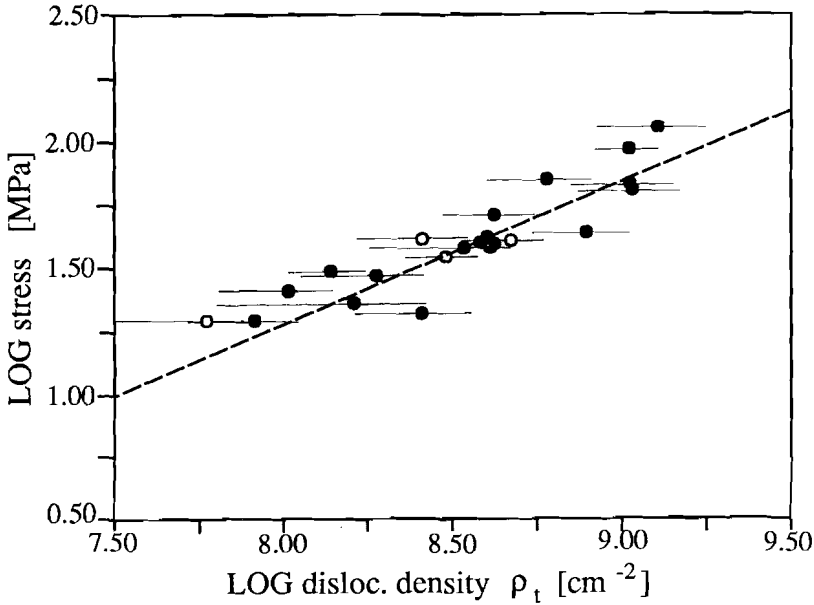
Figure 5.6
Relation between dislocation density and stress for 22 deformed calcite single crystals (Tables 5.1, 5.2). Half-open symbols denote dislocation densities obtained at non-steady state flow stresses (see Figs 5.4, 5.5). Error bars indicate one standard deviation from the mean value per sample. Best fit line after equation 5.6.
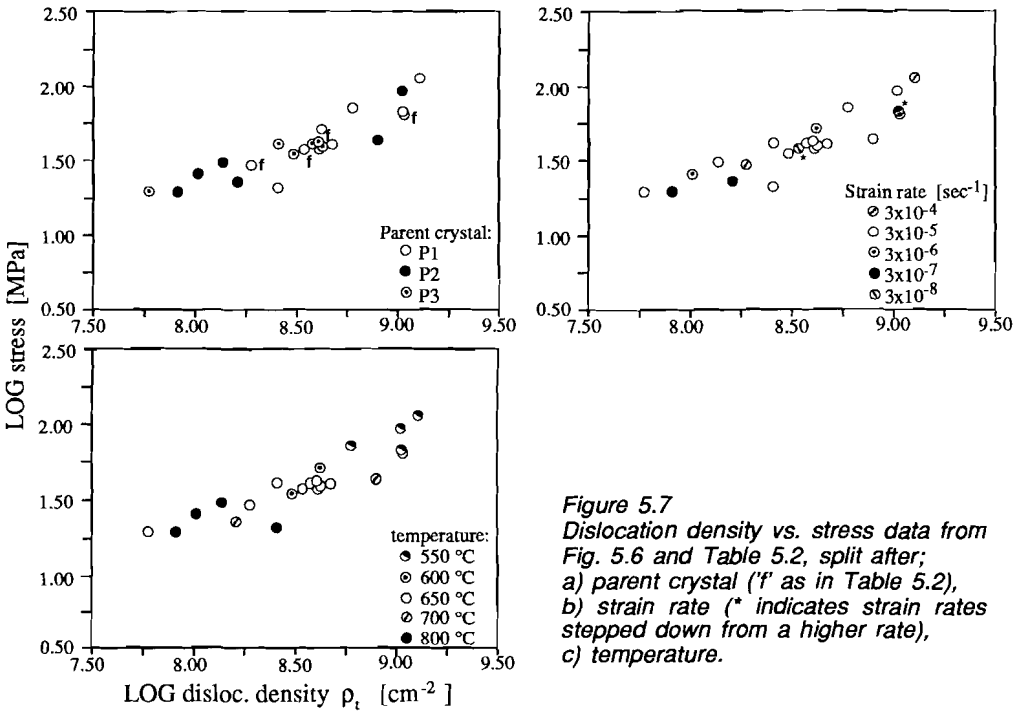
Figure 5.7
Dislocation density vs. stress data from Fig. 5.6 and Table 5.2, split after;
a) parent crystal ('f' as in Table 5.2),
b) strain rate (indicates strain rates stepped down from a higher rate),*
c) temperature.

the dislocation densities are considered only for samples deformed to strains above 5%, i.e. leaving out the densities measured in samples which did not achieve steady state conditions (see Figs 5.4-5.6), the best fit values for the density exponent and logarithm of the pre-exponential factor are 0.60 (±0.07) and -3.55 (±0.64) (corr.coef. 0.897) respectively. Note that equation (5.6) is an improved version of the preliminary equation presented by De Bresser (1988) and De Bresser and Spiers (1990).

5.5.4 Comparison of results with theory and previous single crystal data

The value of 0.56 (±0.06) obtained for the dislocation density exponent in equation 5.6 is in reasonably good agreement with the theoretically predicted value of 0.5 (eq. 5.4). However, in order to accurately fit the data to the theoretical equation 5.4, an estimate of the shear modulus μ and its temperature dependence must be made. For that purpose, the Hill averaging technique for isotropic elastic moduli (e.g. Carmichael 1984: p.40) was applied to the temperature dependent elastic constants of calcite single crystals determined by Dandekar (1968). This resulted in:

$$\mu = 34830 - (10.34 \cdot T) \tag{5.7}$$

with μ im MPa and T being the absolute temperature (i.e. in K). Best fitting of the stress-dislocation density data to equation 5.4, including equation 5.7 for the shear modulus μ and using a non-linear regression method (Marquardt 1963), yielded

$$\sigma = 10^{-7.07(\pm0.02)} \cdot \mu(T) \cdot \rho_t^{0.5} \quad corr.=0.896 \tag{5.8}$$

Taking a Burgers vector length of 6.37 Å (i.e. that of $\bar{b}$ for f<10$\bar{1}$1>[+] slip - chapters 2 and 4), a value of 1.34 was obtained for α (cf. eq. 5.4). This value is close to the expected value of ~1 (section 5.2) and falls in the range of 0.8 to 5.2 reported in the literature (Takeuchi and Argon 1976, Kohlstedt and Weathers 1980, Beeman and Kohlstedt 1988).

The experimental data presented above are plotted together with data from experimentally deformed single crystals of quartz and olivine in Fig. 5.8. The results for these three important rock forming minerals correspond very well with each other.
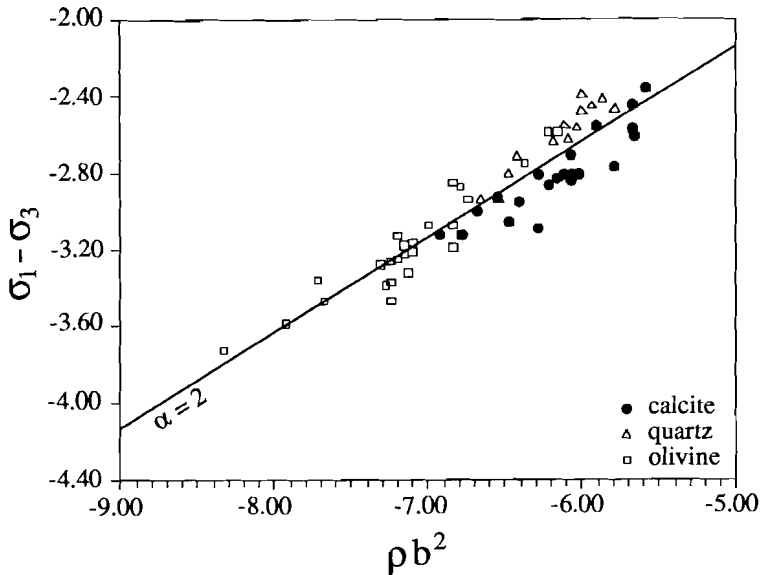
Figure 5.8
Normalised dislocation density (ρb²) vs. normalised differential stress (σ₁ - σ₃ / μ)
for experimentally deformed single crystals of calcite (this study), quartz (McCormick
1977) and olivine (Kohlstedt and Goetze 1974, Durham et al. 1977). Figure
compiled after Fig. 2 of Kohlstedt and Weathers (1980). Used shear moduli: for
calcite 25 GPa (T=700 °C, eq. 5.7), for quartz 44 GPa and for olivine 60 GPa.
Used Burgers vector lengths: for calcite 6.37 Å, for quartz 5 Å and for olivine
5.34 Å.

5.6 COMPARISON WITH PREVIOUS AND NEW DATA ON POLYCRYSTALLINE CALCITE

5.6.1 Dislocation densities measured in calcite rocks

Dislocation densities have been previously measured as a function of applied stress in various experimentally deformed *polycrystalline* calcite materials, see Fig. 5.9. At the higher stresses (>40 MPa) the results for the different calcite rocks match the single crystal data well, but do not correspond with these at low stresses, nor with each other. At low stresses, the dislocation density vs. stress data for polycrystalline calcite thus deviate from the theoretical model (eq. 5.4).

TEM specimens were made from new experimentally deformed samples of Carrara marble. The samples were deformed by J. Urai at ANU, Canberra, using the Paterson gas apparatus. Details of the experiments are given in Table 5.3 (for
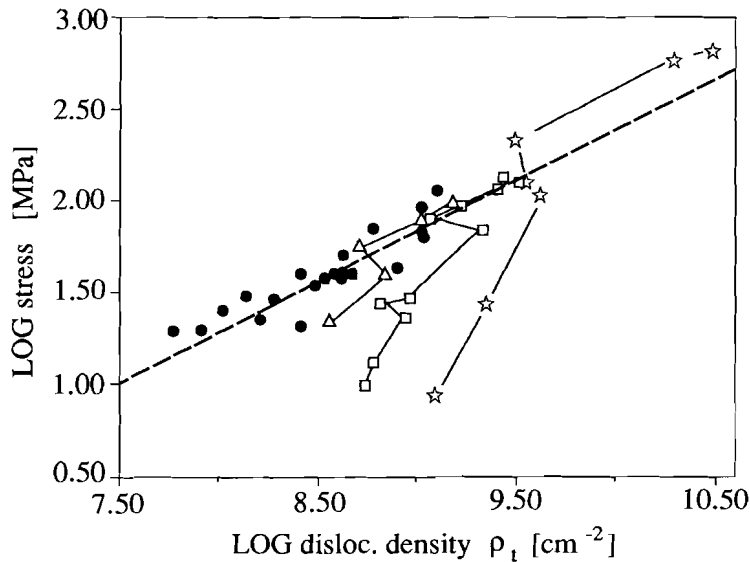
Figure 5.9
Dislocation density vs. (differential) stress for various experimentally deformed calcite materials:

- *1) single crystals (this study),*
- △ *2) Yule marble (after Goetze and Kohlstedt 1977),*
- □ *3) Carrara marble (after Schmid et al. 1980),*
- ✮ *4) Solnhofen limestone (after Schmid et al. 1977, two high stress data points after Briegel and Goetze 1978)*

Original dislocation densities given by Goetze and Kohlstedt (1977, Yule marble) and Briegel and Goetze (1978, Solnhofen limestone) were multiplied by a factor two, in order to obtain values of ρ_t in agreement with equation 5.5. Dashed lines after equation 5.4, using $\mu=25.5$ GPa and $b=6.37\text{Å}$.

preliminary results, see Urai 1989). The selected samples were compressed dry, in constant strain rate mode, at temperatures in the range 600 to 1000 °C. They were found to exhibit similar mechanical behaviour to the samples of Carrara marble deformed by Schmid et al. (1980). At relatively low temperature (600 °C), all grains showed heavy twinning, whereas towards the higher temperatures recrystallization by subgrain rotation and grain boundary migration became increasingly important. Dislocation densities were measured using the method outlined earlier, ignoring the type of grain (old vs. recrystallized), but not counting dislocations in well-ordered low angle tilt walls (conforming to the method applied by Goetze and Kohlstedt 1977, and Schmid et al. 1980). The results are shown in Fig. 5.10, together with the data for Carrara marble from Schmid et al. (1980). The new data match the previous quite well, confirming the deviation from theory.

exper. no.	temperature [°C]	final strain [%]	final stress [MPa]	number of TEM plates	mean dislocation density [cm^{-2}]
5349	600	13.4	204.3	12	20.84(±5.25) x10^8
5348	800	19.7	63.9	15	10.22(±3.44) x10^8
5336	900	8.5	44.2	10	5.69(±1.06) x10^8
5347	1000	20.5	27.5	16	9.28(±3.46) x10^8

Table 3
List of experiments and results for samples of Carrara marble, deformed by J.Urai at ANU-Canberra (see Urai 1980). Strain rate 10^{-5} sec^{-1}. Mean dislocation density (this study) as in tables 5.1 and 5.2.
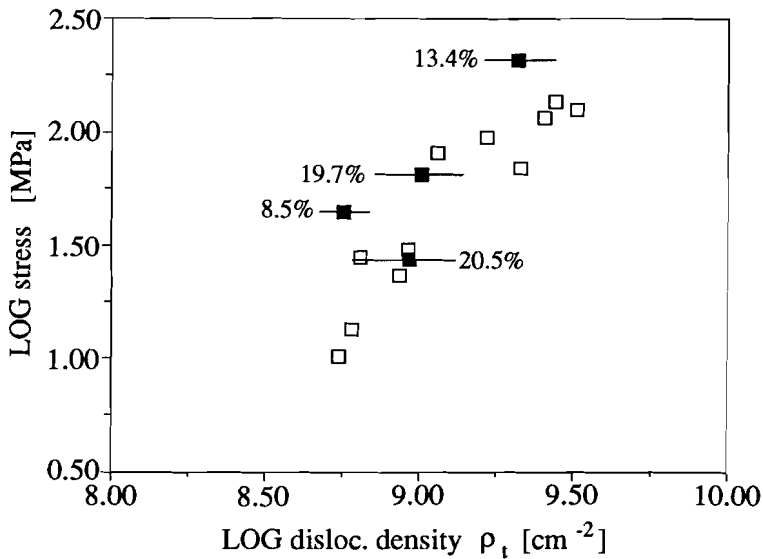
Figure 5.10
Dislocation density vs. differential stress for experimentally deformed Carrara marble. Open symbols after Schmid et al. (1980), closed symbols this study, after experiments done by J.L Urai at ANU, Canberra. Error bars indicate one standard deviation of the mean value per sample. Percentages final strain are indicated.

5.6.2 Possible explanations for the unexpectedly high dislocation densities

All dislocation densities given in Fig. 5.9 were measured in samples deformed in dislocation creep dominated flow regimes (refer section 1.4), with the exception of the two values obtained for Solnhofen limestone at the lowest stresses. The latter densities, were determined in samples deformed in the regime inferred to be controlled by grain boundary sliding (Schmid et al. 1977). However, little or no dislocation substructure is then expected inside the grains (Poirier 1985). Hence, ρ_t in these samples is unexpectedly high, as are the dislocation densities obtained at low stress ($\sigma < 40$ MPa, Fig. 5.9) for other calcite polycrystals.

Basically, three explanations can be brought forward to account for the anomalously high dislocation densities in calcite rocks at low stresses (Figs. 5.9 and 5.10). These concern the equilibration mechanism, the experimental procedure and the appropriateness of the theoretical relation for the case of polycrystals at low stress.

Firstly, equilibration to low dislocation densities may not have been possible because of inadequate recovery rates. This is suggested by the fact that the dislocation densities at low stresses for Yule and Carrara marble were in the range of the starting density (see Fig. 5.9). Thus, the dislocation density had to drop in order to equilibrate, in which case recovery would have been the rate limiting process. This may have been too slow within the time span of the experiments (Goetze and Kohlstedt 1977, Briegel and Goetze 1978), resulting in the high densities. However, annealing experiments performed by Schmid et al. (1980) showed that re-equilibration is rapid in calcite. This is confirmed by the fact that the single crystal results from strain rate down-stepping tests agree closely with the remaining data (cf. Table 5.2 and Fig. 5.7). The 'equilibration' argument can thus be eliminated.

Secondly, the experimental procedure of unloading and cooling may have influenced the dislocation configuration. During the cooling of jacketed polycrystalline specimens under pressure (see Schmid et al. 1980), small strains and associated new dislocations may be introduced as a result of the anisotropic thermal contraction (Nye 1976) of calcite. However, it appears virtually impossible to suppress microcracking in calcite polycrystals during a temperature change (Walsh 1973). The internal stresses build up during cooling can be relieved by this type of cracking, and dislocations, if created at all, are expected to be locally concentrated (especially near crack-tips) rather than uniformly distributed. Extremely local concentrations of dislocations were indeed observed in the Carrara marble samples of Schmid et al. (1980). Given a random selection of areas in TEM, however, it seems unlikely that such local concentrations can significantly influence the measurement of the total dislocation density.

Thirdly, the simple theory describing the relation between dislocation density and

flow stress (eq. 5.4) may not hold at low stresses for polycrystals. Noting that the grain size decreases from Yule marble (~300-350 μm), via Carrara marble (50-200 μm) to Solnhofen limestone (4-8 μm), the stress vs. dislocation density data seem to show a systematic influence of grain size, suggesting a grain size dependence of ρ_t at low stress.

Having ruled out the earlier two explanations, discussion is now concentrated on the third of the above possibilities.

5.6.3 Influence of grain size on dislocation density

Twiss (1986) re-evaluated previous quantitative data relating differential stress and dislocation substructure for a number of metals and for quartz and olivine. He concluded that for many materials the sensitivity of dislocation density to the differential stress decreases with decreasing stress, as seen in the present data for the various calcite rocks. The following *empirical* relation was proposed as fitting the experimental data better (Twiss 1986):

$$\sigma = \alpha \mu b \rho^k - \sigma_0 \qquad (5.9)$$

In this relation, k and α are constants expected to be 0.5 and around 1, as in equation 5.4, and σ_0 is an empirical material constant, called the stress constant. The calcite data have been fitted to equation 5.9, treating α and σ_0 as fitting parameters, i.e. setting k=0.5 and neglecting the weak temperature dependence (across the temperature range investigated) of the shear modulus. The results are given in Table 5.4 and Fig. 5.11. For all polycrystals, the results show a slightly better fit to equation 5.9 than to an equation of the type (see Table 5.4)

$$\sigma = 10^K \cdot \rho_t^{\,k} \qquad (5.10)$$

which is a modified version of equation 5.4, with the density exponent now being a free parameter (Table 5.4, Fig. 5.11). The values obtained for σ_0 differ with the type of calcite rock, and show a striking increase with decreasing grainsize.

Twiss (1986) stated that there is yet no theoretical justification for equation 5.9, and hence for the stress constant σ_0. In the following, some theoretical explanation will be sought for the observed correlation between σ_0 and grain size.

In general, a polycrystalline materially deforms plastically in a non-homogeneous way, because of strain incompatibility problems at grain boundaries. Gradients of deformation thus build up within grains, requiring dislocations to accomodate them. These are called *geometrically necessary dislocations* (Ashby 1970, 1971), in

	D [μm]	N	K	k	corr.	K'	σ_o	corr.
Single Crystals:	10000	22	- 3.20	0.56	0.897	-2.59	8.1	0.888
Polycrystals:								
-Yule Marble	300-350	5	- 7.65	1.06	0.892	-2.35	63.5	0.910
-Carrara Marble	50-200	15	-11.66	1.47	0.862	-2.28	120.3	0.861
-Solnhofen lmst.	4-8	7	-11.13	1.36	0.896	-2.26	204.4	0.961

$$\sigma = 10^K \cdot \rho_t{}^k \qquad \sigma = 10^{K'} \cdot \rho_t{}^{0.5} - \sigma_o$$
$$\text{(eq. 5.8)} \qquad\qquad\qquad \text{(eq. 5.9)}$$

Table 5.4
Dislocation density-stress relations and results of regression analyses obtained for various experimentally deformed calcite materials. Single crystal data from this study, for polycrystal data see Fig. 5.9 and references therewith. N is number of data points, D is the average grain size. New data on Carrara marble are included. The quality of fit is measured by the correlation coefficient (corr.), note the slightly better fit of the polycrystal data in the equation on the right, compared with that on the left.
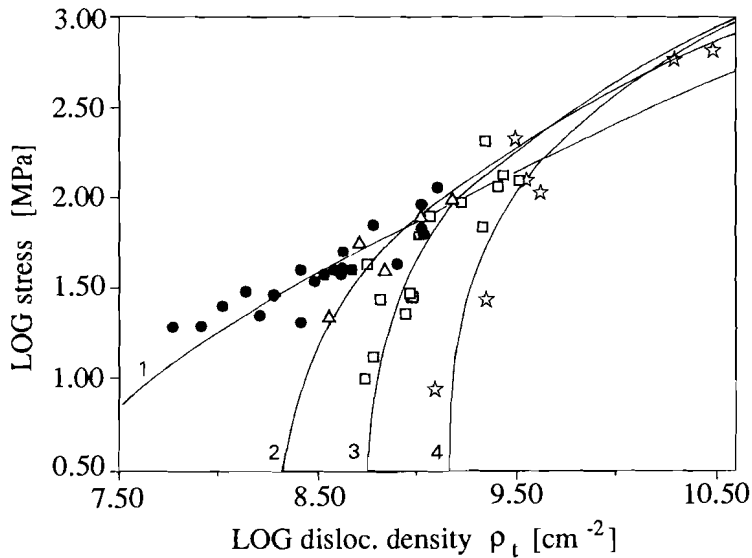
Figure 5.11
Dislocation density vs. (differential) stress plot showing data points from 5.9, as well as best fit lines after equation 5.8 and Table 5.4. (1) to (4) represent single crystals, Yule marble, Carrara marble and Solnhofen limestone respectively. Note that the dislocation density becomes increasingly stress-insensitive with decreasing grain size (1 to 4) at low stresses (cf. Table 5.4).

contrast to *statistically stored dislocations,* which achieve the general strain, but are not geometrically needed. Both types of dislocations, which are physically indistinguishable, contribute to the internal stress in the material and consequently to the applied stress required for deformation. However, the *way* they contribute need not be the same, and this may be reflected in the values for α in equation 5.4 (e.g. Lavrentev et al. 1980). As mentioned before, the character of the dislocations dominantly contributing to the total population (e.g. screw vs. edge), and the way the dislocations are arranged may play a role here.

Let the total dislocation density be simply the sum of the densities of the geometrically necessary dislocations and that of the statistically stored dislocations, i.e. $\rho_t = \rho_G + \rho_s$ (Ashby 1970, 1971). From equation 5.4, it follows that

$$\text{if } \rho_s = 0, \text{ then } \rho_G = \rho_t: \quad \sigma = \alpha_G \mu b \cdot \rho_t^{0.5} \tag{5.11}$$

$$\text{if } \rho_G = 0, \text{ then } \rho_s = \rho_t: \quad \sigma = \alpha_s \mu b \cdot \rho_t^{0.5} \tag{5.12}$$

where α_G and α_s are constants. However, if both geometrically necessary and statistically stored dislocations are present, the two types of dislocations are likely to influence each other, hence affect the overall arrangement of the dislocations. The constants α_G and α_s cannot then simply be linearly averaged in order to get one value for α (cf. eq. 5.4). Rather, α may become a non-linear function of the contribution of ρ_G to ρ_t, i.e. $\alpha = f(\rho_G/\rho_t)$, changing from $\alpha = \alpha_s$ if $\rho_G = 0$ to $\alpha = \alpha_G$ if $\rho_G = \rho_t$. Assume now, as a first approxiamtion, that α changes according to a monotonic power function

$$\alpha = \alpha_s - \left\{ (\alpha_s - \alpha_G)(\rho_G/\rho_t)^n \right\} \tag{5.13}$$

where n is a constant. Equation 5.4 then can be rewritten as:

$$\sigma = \left[\alpha_s - \left\{ (\alpha_s - \alpha_G)(\rho_G/\rho_t)^n \right\} \right] \cdot \mu b \cdot \rho_t^{0.5} \tag{5.14}$$

which is equivalent to

$$\sigma = \left(\alpha_s \mu b \cdot \rho_t^{0.5} \right) - \left((\alpha_s - \alpha_G)\mu b \cdot \rho_G^n \cdot \rho_t^{0.5-n} \right) \tag{5.15}$$

The second term in equation 5.15 is now equivalent to the stress factor σ_0 in equation 5.9, though it cannot be regared as a constant.

Based on an analysis of a three-dimensional pattern of non-deforming plates in a deforming matrix, Ashby (1970, 1971) derives a relationship between the density of

geometrically necessary dislocations, the shear strain on the single slip system assumed active in each cell and the size of the cells in the three-dimensional pattern. Generalized to a three-dimensional array of grains in tensile deformation, this yielded:

$$\rho_G \propto \varepsilon \,/\, 4bD \qquad\qquad\qquad (5.16)$$

in which ε is the (tensile) strain, b the length of the Burgers vector and D the grain size. Starting from the concept that dislocation behaviour in grain centers may be different from that in grain boundary regions, Thompson et al. (1973) came to the conclusion that the strain dependence of ρ_G (eq. 5.16) only holds at low strains (below a few percent), since increasing strain should not require a proportionate increase in accomodation at grain boundaries. This statement is in agreement with the fact that during *steady state* deformation, the value of ρ_G is not expected to indefinitely increase with increasing strain. Equation 5.16 then can be simplified to

$$\rho_G = A \cdot D^{-1} \qquad\qquad\qquad (5.17)$$

for strains above a few percent, A being a constant.

Incorporating equation 5.17 into equation 5.15, a formulation with three variables (σ, ρ_t and D) and three unknowns (α_s, n and (α_s-α_G)A) results:

$$\sigma = \left(\alpha_s\mu b \cdot \rho_t^{0.5}\right) - \left((\alpha_s\text{-}\alpha_G)\mu b A^n D^{-n} \cdot \rho_t^{0.5-n}\right) \qquad\qquad (5.18)$$

The data for the various calcite materials (given in Fig. 5.11 and Table 5.4) have been fitted to equation 5.18, using average grain sizes for the partly to completely recrystallized Solnhofen limestone and Carrara marble, taking the length of the samples (~1 cm) as the D-value for the single crystals, and applying a non-linear regression method based on a search algorithm (Marquardt 1963). Unfortunately, the values obtained for the fitting parameters (i.e. the unknowns) had standard errors too large to attribute any firm significance to them, presumably due to the large scatter in data (Fig. 5.11). Therefore, a more simple version of equation 5.18 was fitted, in which n=0.5:

$$\sigma = \left(\alpha_s\mu b \cdot \rho_t^{0.5}\right) - A^{\bullet}D^{-0.5} \qquad\qquad\qquad (5.19)$$

where $A^{\bullet}$ is a constant equal to $A^{0.5}(\alpha_s\text{-}\alpha_G)\mu b$. In comparison with equation 5.9, the empirical stress constant σ_0 is now replaced by a grain size dependent factor (i.e. $\sigma_0 \propto D^{-0.5}$). As justification for taking n=0.5, reference is made to Fig. 5.12, where the values independently obtained for σ_0 (Table 5.4) for the single- and polycrystalline calcite are plotted against Log D. The resulting best fit line has a slope of 0.44(±0.09), which thus offers some constraint on n. Fitting the available σ-

ρ_t -D data to equation 5.19 (using the non-linear regression method mentioned above, N=49), the following equation resulted:

$$\sigma = \left(10^{-2.59\pm0.03} \cdot \rho_t^{0.5}\right) - 2.97(\pm0.61)\cdot D^{-0.5} \qquad (5.20)$$

with σ in MPa, ρ_t in cm^{-2} and D in cm, and with a correlation coefficient of 0.858. Taking μ=25 GPa and b=6.37x10^{-8} cm (see section 5.4.4), a value of 1.61 for α_s results from equation 5.20 (cf. 5.19).

In Fig. 5.13, stress vs. dislocation density relations as calculated on the basis of equation 5.20 are given, with the corresponding σ-ρ_t data for the various calcite materials (compare with Fig. 5.11). Clearly, the fit is less good than that of the best fit lines determined individually for each calcite material using equation 5.9 (Fig. 5.11). Nevertheless, equation 5.20 predicts a stress vs. dislocation density relation for single crystals (i.e. for large D) which is in close agreement with the theoretical equation 5.4, and offers a description of the observed deviation from eq. 5.4 with decreasing grain size (in particular at low stresses). On the basis of strain compatibility arguments, this effect seems likely to be due to an increase in density of geometrically necessary dislocations with decreasing grain size.

Although considered in detail here for calcite, the observations of Twiss (1986) on quartz and olivine suggest that the approach is likely to apply to these materials as well: for both quartz and olivine, single crystals show linear σ-ρ_t trends in logarithmic space (refer Fig. 5.8), while deviations occur at low stress in polycrystals.
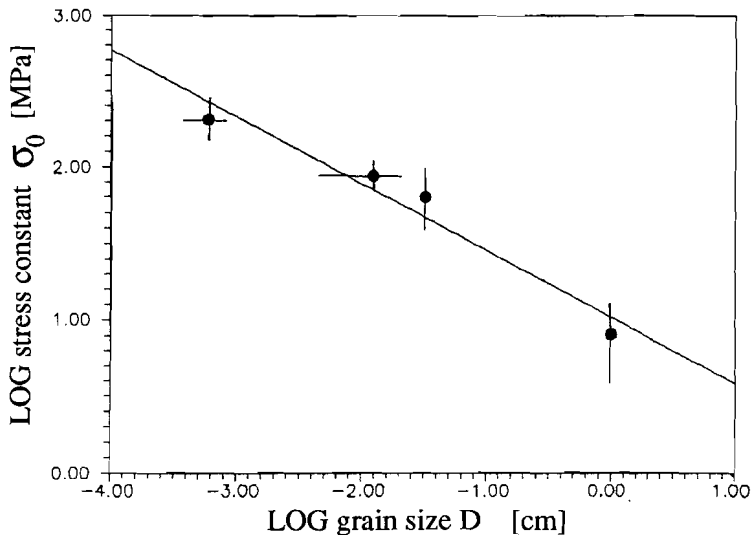
Figure 5.12
Log-log plot of the stress constant σ_0 (Table 5.4) vs. grain size D, showing a $\sigma_0 \propto D^{-0.44}$ relationship. Standard errors in σ^0 are indicated, error bars in D show variation grain size. See text.

dislocation density vs. stress
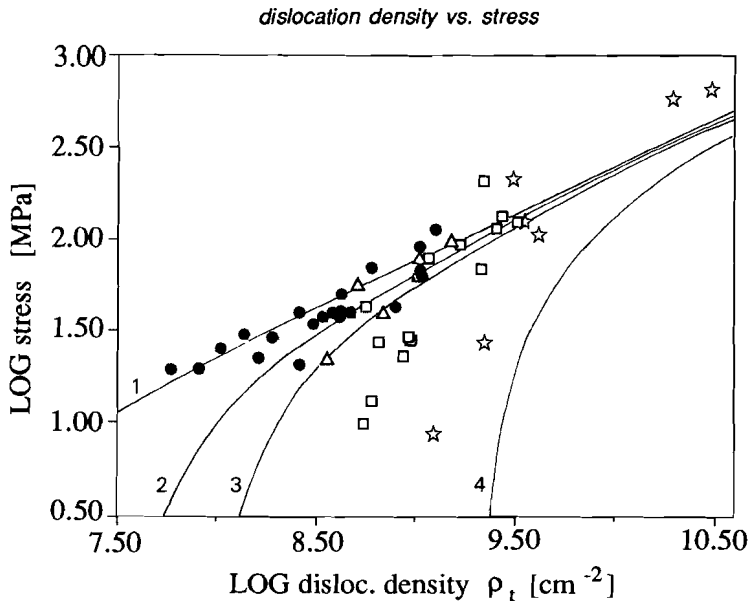
Figure 5.13
Dislocation density vs. flow stress plot showing data points from Fig. 5.9 and best fit lines after equation 5.20, for single crystals (1), Yule marble (2), Carrara marble (3) and Solnhofen limestone (4). Compare with Fig. 5.11.

5.6.4 Comparison with the Hall-Petch relationship

Studies on the influence of grain size on dislocation density have been published before, but were invariably directed to explain work hardening behaviour (e.g. Hirth 1972, Thompson et al. 1973, Nix et al. 1982, Van den Beukel 1978, Mayer et al. 1980). Based on models of dislocation pile up, these studies proposed relationships of the type

$$\sigma = \alpha\mu b \cdot \rho^{0.5} + \sigma_0 \qquad (5.21)$$

which, using $\rho \propto D^{-1}$ (cf. eq. 5.15), led to the so-called Hall-Petch relation

$$\sigma = KD^{-0.5} + \sigma_0 \qquad (5.22)$$

where K is a constante. Equations 5.21 and 5.22 fundamentally differ from equation 5.19, mainly because the models were derived focussing on the geometrically necessary dislocations only. A relationship of the type of 5.21 predicts a dislocation density which becomes *more* sensitive to stress toward low flow stresses, in contrast to the present findings. It is noteworthy in this respect that, in compiling stress vs dislocation density relations for a number of materials, Takeuchi and Argon (1976)

refer to the Hall-Petch relation (5.21), but present several *negative* values for σ_0, thus *resembling* equations 5.9 and 5.19 rather than 5.21.

5.6 SUMMARY/CONCLUSIONS

Dislocation densities have been measured in experimentally deformed single crystals of calcite, using transmission electron microscopy. The crystals exhibited steady state flow behaviour, with flow stresses in the range 20 to 115 MPa. A steady state dislocation density is established after ~2% strain. The total density ρ_t was found to depend on the flow stress σ according to the empirical equation:

$$\sigma = 10^{-3.20(\pm 0.53)} \cdot \rho_t^{0.56(\pm 0.06)}.$$

Within the range of conditions investigated, no significant influence of strain rate, deformation history, temperature or starting composition was observed.

The experimentally obtained relationship is in close agreement with the theoretical relation $\sigma \propto \rho^{0.5}$, based on elastic interaction of dislocations. This agreement between experiment and theory helps justify comparison of single crystal creep data with microphysical models derived using the theoretical relation $\sigma \propto \rho^{0.5}$.

In addition, dislocation densities measured in experimentally deformed calcite polycrystals (previous and new studies) appear to match the single crystal results at high stresses, but progressively deviate from them towards low stresses. The data fit the empirical relation:

$$\sigma = K \cdot \rho_t^{0.5} - \sigma_0,$$

K and σ_0 being constants (after Twiss 1986). The values obtained for σ_0 (the 'stress constant') differ with the type of calcite material, and increase with decreasing grain size. Using theory of non-homogeneous deformation, which accounts for the density contribution of geometrically necessary dislocations (after Ahsby 1970, 1971), σ_0 was related to the grain size (D) via a relation of the form $\sigma_0 \propto D^{-0.5}$. On the basis of this, the following tentative relationship between dislocation density, stress and grain size was derived

$$\sigma = \left(10^{-2.59 \pm 0.03} \cdot \rho_t^{0.5} \right) - 2.97(\pm 0.61) \cdot D^{-0.5}$$

The latter equation predicts a relation between dislocation density and stress which is close to the theoretical relation $\sigma \propto \rho_t^{0.5}$ for single crystals (no grain boundaries), with a progressive deviation from this at low stresses for polycrystalline material, as observed.

CHAPTER 6

CREEP MECHANISMS IN THE SLIP REGIME

6.1 INTRODUCTION

In the preceding chapters, mechanical and microstructural data were reported for calcite single crystals deformed experimentally at temperatures in the range 400 to 800 °C. In the present chapter, the mechanism controlling the *rate* of deformation will be discussed. The discussion is focussed on the 'steady state' creep behaviour observed in samples compressed parallel to [40$\bar{4}$1] under conditions favouring r<$\bar{2}$021>$^+$ and particularly f<10$\bar{1}$1>$^+$ slip, i.e. at T$\geq$600 °C (chapter 2). The creep data obtained under other conditions were considered to be too limited to include them in the analysis.

First, the principal microphysical creep models for intracrystalline deformation by dislocation mechanisms are reviewed, with emphasis on the route by which the corresponding constitutive creep equations are derived. The experimental data obtained for the calcite crystals are then compared with the various models. This is done by fitting the mechanical data to the theoretical creep equations, thus yielding values for the microphysical parameters characterising the models. The results obtained are then considered in relation to microstructure and constraints on the various microphysical (constitutive) parameters. Finally, the results for the single crystals are compared with the mechanical behaviour and microstructures reported in the literature for experimentally deformed calcite rocks under comparable experimental conditions. It will be argued that cross slip of (screw) dislocations is likely to be the rate controlling mechanism governing the dislocation creep behaviour of calcite (crystals and rocks) at intermediate to high temperatures (0.5-0.7 T$_m$).

6.2 MICROPHYSICAL CREEP MODELS

6.2.1 General background

The starting point of almost all dislocation creep and/or glide models is Orowan's equation (Orowan 1940). This relates the strain rate caused by dislocation motion to the density (ρ_m), the length of the Burgers vector (b) and the average velocity ($\bar{v}$) of mobile dislocations as follows

$$\dot{\varepsilon} = \rho \cdot b \cdot \bar{v} \qquad\qquad (6.1)$$

In most formulations, the mobile dislocation density ρ_m is subsequently linked to the applied stress σ using the relation $\rho \propto \sigma^2$ (refer section 5.2), leaving $\bar{v}$ to be expressed as a function of macroscopic (e.g. stress, temperature) and microscopic variables (e.g. type of dislocation, concentration of vacancies) in order to obtain a constitutive creep equation. The nature of barriers to dislocation motion and the way they are overcome form the governing factors taken into account in deriving such expressions. Notably, it follows from the Orowan equation (6.1) that for *steady state* creep, the dislocation density ρ_m *and* average velocity $\bar{v}$ of the mobile dislocations must remain constant during deformation, or that the rates of change of ρ_m and $\bar{v}$ perfectly balance each other. Whether or not creep actually occurs in steady state depends on the potential for recovery (dislocation annihilation) of the mechanism by which barriers to dislocation slip are overcome.

For present purposes, three broad classes of dislocation creep models are distinguished (after Frost and Ashby 1982, Weertman and Weertman 1983b, Langdon 1985, Poirier 1985), namely climb controlled creep, cross slip controlled creep and barrier controlled dislocation glide. These classes are characterised by particular functional descriptions for the average dislocation velocity $\bar{v}$, depending on the precise basic mechanism involved. An outline review of the main models is given below.

6.2.2. Climb controlled creep

At temperatures high enough to support significant solid state diffusion, edge dislocations can climb out of their glide plane by emission or absorption of vacancies at jogs in the dislocation line (e.g. Hirth 1983). Dislocations can thus overcome obstacles in their glide plane, and by climbing towards dislocations of opposite signs can recover the dislocation substructure by mutual annihilation. The glide component of dislocation motion is the strain accumulating mechanism. However, if glide is fast, the strain *rate* is controlled by the time necessary for dislocations to overcome

obstacles in the glide plane, i.e. the time (t_c) to climb the height (d) of the barrier. The ratio d/t_c thus represents the climb velocity $\bar{v}_c$. Approximating the average dislocation velocity ($\bar{v}$) by L/t_c, where L is the average glide distance between dislocation sources and obstacles, yields $\bar{v}=L\bar{v}_c/d$. Now, assuming diffusion control, $\bar{v}_c$ can be expressed as a linear function of stress (σ) (after Weertman 1955, Poirier 1985):

$$\bar{v}_c \propto (D_{SD} \cdot \sigma) \; / \; (kT) \qquad\qquad (6.2)$$

where D_{SD} is the self-diffusion coefficient, k is Boltzmann's constant and T the absolute temperature. Inserting equation 6.2 into the Orowan equation, and using the conventional relation between dislocation density and stress ($\rho \propto \sigma^2$, eq. 5.4), the following diffusion (climb) controlled creep model results:

$$\dot{\varepsilon} = A \cdot L/d \cdot (D_{SD} \cdot b \cdot \sigma^3) \; / \; (kT) \qquad\qquad (6.3)$$

where A ($\approx$constant) includes the Burgers vector length (b) and the shear modulus $\mu(T)$, and L/d may be either a constant (special case) or stress dependent (general case).

Weertman (1955, 1957a, 1968) presented a modified version of the above approach. In his model (Fig. 6.1), edge segments of dislocation loops in neighbouring planes become mutually interlocked in attractive junctions, forming long-range barriers to dislocation motion. Dislocation sources (density M) cease to produce new dislocation loops when the back stress caused by dislocations piling-up against these barriers becomes too high. Deformation can then continue only if the leading dislocation in the pile up climbs and annihilates with a counterpart of opposite sign (see Fig. 6.1). The average dislocation velocity $\bar{v}$ resulting from this process is $L\bar{v}_c/d$ (see above), where d is the climb distance for annihilation (i.e. half the spacing between parallel slip planes). Note that L equals half the diameter of the dislocation loop emitted from the source. In Weertman's model, the density of sources M is assumed constant and proportional to $1/dL^2$, so that $L \propto (dM)^{-0.5}$. Now, the spacing between parallel slip planes (2d) is roughly equivalent to the spacing between dislocations on neighbouring planes. Since the stress around a dislocation varies inversely with the distance from the dislocation line (eq. 5.1 - chapter 5), it thus follows that d must be proportional to $1/\sigma$. The ratio L/d in equation 6.3 can then be rewritten proportional to $\sigma^{1.5}/M^{0.5}$. The following, frequently quoted, 'Weertman' rate equation results:

$$\dot{\varepsilon} = (A \cdot D_{SD} \cdot M^{-0.5} \cdot \sigma^{4.5}) \; / \; (kT) \qquad\qquad (6.4)$$
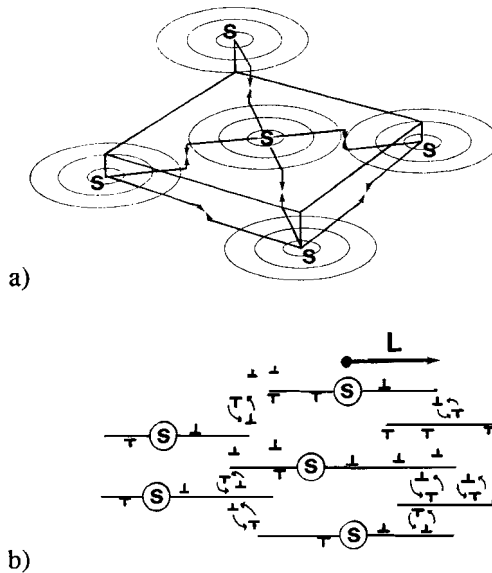
Figure 6.1
The Weertman model for climb
controlled dislocation creep.
(drawn after Weertman 1968)
a) creation of dislocation loops from
sources S and subsequent annihil-
ation by climb,
b) cross section of Fig. 6.1a: edge
dislocations of opposite signs.
produced by sources S on neigh-
bouring planes, become mutually
trapped after moving a distance L.
They annihilate after climbing a
distance d towards each other.

where A ($\approx$constant) is again proportional to the Burgers vector length b and the shear modulus $\mu(T)$. Note the difference in stress exponent between equations 6.3 and 6.4.

Numerous similar approaches have been followed in the literature, but all lead to a creep equation resembling eq. 6.3 (e.g. Weertman 1972, Mukherjee 1975, Lagneborg 1979). They differ from one another in the vacancy diffusion path (hence diffusivity D) that is considered (e.g. pipe diffusion along dislocation cores versus bulk diffusion), and in the assumed dislocation interactions, climb path and configuration. As an example of the latter, special attention is drawn here to creep models which involve the arrangement of dislocations in three-dimensional networks (Lagneborg 1979, Burton 1982). In these models, the formation of local dislocation junctions (leading to strain hardening) and their simultaneous destruction elsewhere (recovery) is controlled by the mobility of climbing dislocations, hence the diffusivity of vacancies. The resulting creep equations do not differ substantially from those given above (eqs. 6.3, 6.4), other than in their stress exponents (being 4 following Lagneborg 1979, and 3 after Burton 1983).

The close similarity of the various creep models involving diffusion controlled dislocation climb as the rate controlling process allows a generalised creep equation to be written for this type of mechanism (after Frost and Ashby 1982):

$$\dot{\varepsilon} = (A \cdot D \cdot \sigma^n) / (kT) \qquad\qquad (6.5)$$

This is a *power law* rate equation in which A is roughly constant (function of μ and b), n is the stress exponent which, dependent on the basic mechanism involved, varies between 3 and 6.5, and D is the 'effective' diffusivity, determined by the relative contributions of lattice diffusion and dislocation core (pipe) diffusion (i.e. $D = a \cdot D_{SD} + b \cdot D_{CORE}$, Frost and Ahsby 1982). When the contribution of pipe diffusion to transport of matter is negligible, D equals the coefficient of self-diffusion D_{SD}, and since diffusion is a thermally activated process, D can be rewritten following an Arrhenius type law (e.g. Cannon and Langdon 1988)

$$D_{SD} = D_0 \cdot \exp[-Q/kT] \qquad (6.6)$$

In equation 6.6, D_0 is a constant and Q is the stress independent activation energy (per atom) for the lattice diffusion process. For mixed contributions of pipe and lattice diffusion, D takes a similar form with D_0 and Q then assuming hybrid significance. Combining equation 6.6 with 6.5 (cf. Weertman 1955) gives:

$$\dot{\varepsilon} = A'/kT \cdot \sigma^n \cdot \exp[-Q/kT] \qquad (6.7)$$

When the temperature dependence of A'/k in equation 6.7 is negligible with respect to the influence of T in the exponential part, the general power law ('Dorn' equation) commonly used in describing plastic flow at relatively high homologous temperature ($T > 0.5\ T_m$) is obtained. This is written

$$\dot{\varepsilon} = A'' \cdot \sigma^n \cdot \exp[-Q/RT] \qquad (6.8)$$

where R is the gas constant and Q is now expressed in J/mole. It is commonplace in the literature to fit experimentally obtained creep data to this equation. If the n-values obtained fall between 3.5 and 6 and the apparent activation energy matches that determined independently for self-diffusion of the least mobile species, a climb-controlled creep mechanism is frequently inferred (e.g. Takeuchi and Argon 1976). As indicated by Poirier (1972), however, such conclusions are not necessarily justified since other mechanisms may produce similar results. Microstructural confirmation and a detailed consideration of the microphysical parameters is needed to draw firm conclusions on creep mechanisms.

6.2.3. Cross slip controlled creep

In cross slip, screw dislocations (or screw components of dislocation loops) change direction of propagation by gliding onto a plane oriented oblique to the original slip
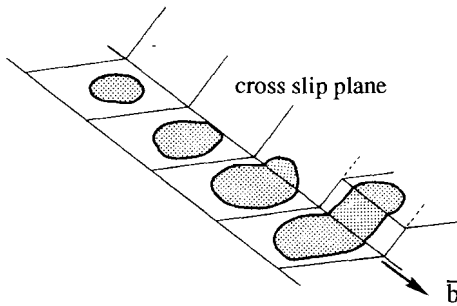
Figure 6.2
Successive stages in cross slip
of a dislocation (loop). Last stage
shows double cross slip, i.e.
back onto a plane parallel to the
original glide plane (after Hull
and Bacon 1984). $\bar{b}$ is Burgers
vector.

plane but sharing the same Burgers vector (Fig. 6.2). They can thus overcome obstacles and by cross slipping towards each other, screws of opposite sign can recover the dislocation substructure by mutual annihilation. Cross slip is a thermally activated process (Poirier 1976) in which, unlike in climb, the activation barrier is reduced by the applied stress. Thus, cross slip controlled creep models contain a stress dependent activation energy $Q(\sigma)$. The average velocity of dislocation cross slip $(\bar{v}_{cs})$ over obstacles controls the strain rate and, since thermally activated, can be expressed by an Arrhenius equation (cf. eq. 6.6) of the form:

$$\bar{v}_{cs} = v_0 \cdot \exp[-Q(\sigma)/RT] \tag{6.9}$$

where v_0 is a constant. Combining equation 6.9 with the usual dislocation density vs. stress relation (eq. 5.4) and the Orowan equation (6.1), the creep rate can thus be written

$$\dot{\varepsilon} = B \cdot \sigma^2 \cdot \exp[-Q(\sigma)/RT] \tag{6.10}$$

where B is a constant.

Theories to describe the stress dependence of the activation energy $Q(\sigma)$ for cross slip all start from the notion that in many materials (notably metals) dislocations are dissociated, forming stacking faults. These must be *constricted* (i.e. locally recombine) to allow the cross slip step. This will be followed by a re-*dissociation* and continued movement in the cross slip plane (Escaig and Bonneville 1980, Siethoff and Schröter 1984 - see Fig. 6.3). If constriction before cross slip is rate controlling, then the activation energy is usually expressed (Wolf 1960, Skrotzki and Liu 1982) as

$$Q(\sigma) = Q_{cs}(\ln \sigma_0/\mu_0 - \ln \sigma/\mu) \tag{6.11}$$

where μ is the shear modulus (at temperature T), μ_0 and σ_0 are the shear modulus and flow stress at T=0 K, and Q_{cs} is a proportionality constant (often, improperly,

a) dissociated dislocation
b) constriction
c) dissociation on the cross slip plane
d) movement on the cross slip plane
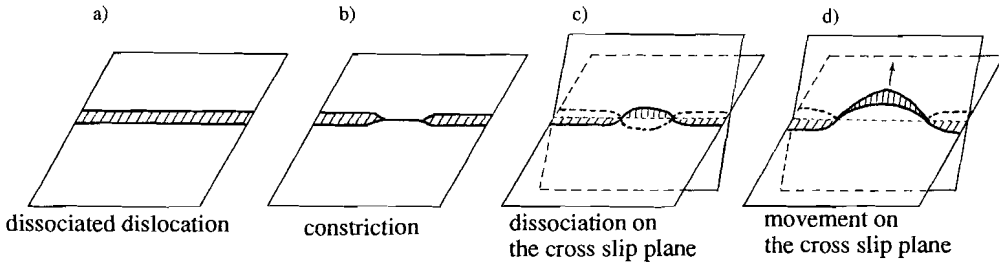
Figure 6.3
Successive stages in cross slip of a dissociated dislocation:
(after Schoeck and Seeger 1955)
a) dissociated dislocation (stacking fault) on the primary glide plane,
b) constriction of a dissociated dislocation,
c) cross slip of the constricted dislocation on a secondary glide plane and subsequent renewed dissociation,
d) motion of the dissociated dislocation on the cross slip plane.

called the apparent activation energy for cross slip) related to the stacking fault energy γ. According to Wolf (1960), Q_{cs} for large γ can be approximated by the relation

$$Q_{cs} = [\, \mu b^3 \, / \, 157(\gamma/\mu b) \,] \cdot (\beta - \gamma/\mu b)^{0.5} \qquad (6.12)$$

in which β depends on the elastic anisotropy of the material ($\beta = 2C_{44}/(2\pi\sqrt{3}(C_{11}-C_{12}))$ for FCC materials, see Seeger 1956). It can be seen from equation 6.11 that the activation energy $Q(\sigma)$ becomes zero at T=0 K, indicating that constriction of dislocations can occur without the help of thermal energy, i.e. under shear stress alone. On the other hand, if the applied stress σ approaches zero, $Q(\sigma)$ approaches infinity, implying that cross slip is not possible without the assistence of stress. The latter is best understood realizing that at zero applied stress, only the thermal vibration of a dislocation can bring about a successful constriction of split dislocations. The probability of this is finite only if the stacking fault associated with the split dislocation is about one lattice unit wide, falling rapidly to zero for wider faults.

If dissociation of the dislocation on the *new* plane is rate controlling (Fig. 6.3c), rather than the constriction step, the activation energy is generally expressed as linearly dependent on stress (Escaig 1968, Poirier 1976) by the function

$$Q(\sigma) = Q_{cs} \cdot (1 - K \cdot \sigma) \qquad (6.13)$$

Both constants Q_{cs} and K in equation 6.13 depend, in a complex way, on the stacking fault energy γ. Q_{cs} represents the activation barrier at zero applied stress,

reflecting the concept that dissociation of dislocations on the cross slip plane is possible without the aid of stress, i.e. at $\sigma=0$ there is still a finite probability of a successful dissociation jump (contrary to the constriction-model above).

According to Skrotzki and Liu (1982), the constriction-model leading to equation 6.11 offers the best description for results on ionic crystals, while the dissociation-model (eq. 6.13) agrees better with results on metals. For present purposes (i.e. in relation to calcite), the first model (eq. 6.11) is adopted here. Combining equation 6.11 with 6.10 then leads to the cross slip controlled creep equation

$$\dot{\varepsilon} = B \cdot \sigma^2 \cdot \exp[-Q_{cs}/RT \cdot (\ln \sigma_0/\mu_0 - \ln \sigma/\mu)] \qquad (6.14)$$

which is equivalent to

$$\dot{\varepsilon} = B \cdot \sigma^{(2 + Q_{cs}/RT)} \cdot \exp[-Q_{cs}/RT \cdot (\ln \sigma_0/\mu_0 + \ln \mu)] \qquad (6.15)$$

The form of equation 6.15 differs from the climb-controlled power law (eqs 6.7-6.8) mainly in its stress exponent. This is *temperature dependent.*

Skrotzki and Liu (1982) derive a constriction-controlled cross slip equation which is slightly different from the one above. Stating that cross slip is thermally activated, they directly write the *strain rate* in the Arrhenius form

$$\dot{\varepsilon} = \dot{\varepsilon}_0 \cdot \exp[-Q(\sigma)/RT] \qquad (6.16)$$

where $\dot{\varepsilon}_0$ is proposed to be a constant, which includes the slip distance and density of cross slip events (both unkown) and a fundamental jump frequency factor. Inserting the stress dependence of the activation energy Q for ionic crystals (eq. 6.11) into this equation, Skrotzki and Liu (1982) obtain

$$\dot{\varepsilon} = \dot{\varepsilon}_0 \cdot \exp[-Q_{cs}/RT \cdot (\ln \sigma_0/\mu_0 - \ln \sigma/\mu)] \qquad (6.17)$$

equivalent to

$$\dot{\varepsilon} = \dot{\varepsilon}_0 \cdot \sigma^{(Q_{cs}/RT)} \cdot \exp[-Q_{cs}/RT \cdot (\ln \sigma_0/\mu_0 + \ln \mu)] \qquad (6.18)$$

(see also Wawersik and Zeuch 1986, Wawersik 1988 and Skrotzki and Haasen). In the derivation of equations 6.17 and 6.18, Skrotzki and Liu (1982) replace the stress dependent dislocation density term required by the Orowan equation (which introduces the extra factor 2 in the stress exponent of eq. 6.15 with respect to that of eq. 6.18) by a stress *in*-dependent constant contained within $\dot{\varepsilon}_0$. They thus assume that the density of dislocations has no significant influence on the slip

distance and density of cross slip events. This assumption does not seem to be strictly correct, though it will be approximately valid when $Q_{cs} >> 2$.

6.2.4. Barrier controlled dislocation glide

Under conditions where dislocation climb and cross slip are relatively slow, dislocations are constrained to their glide plane. The rate of dislocation motion is then limited by the rate of overcoming barriers in the glide plane, which itself is determined by the nature of the barriers and by the dislocation core scale mechanisms by which they are overcome (Frost and Ashby 1982, Langdon 1983). In all glide models, whatever the type of barrier or core scale mechanism, the activation energy necessary to overcome the barrier is assumed to be reduced by the applied stress. An expression for the average dislocation velocity $\bar{v}$, analogous to the equation (6.9) for cross slip, can thus be obtained by applying reaction rate theory (e.g. Poirier 1985) to determine the successful jump frequency of dislocations over barriers, and hence the dislocation velocity $\bar{v}$. This results in

$$\bar{v} = v_0 \cdot \exp[-Q(\sigma)/RT] \qquad (6.19)$$

where v_0 is a constant. Following the derivation for cross slip control, the creep rate then becomes

$$\dot{\varepsilon} = C \cdot \sigma^2 \cdot \exp[-Q(\sigma)/RT] \qquad (6.20)$$

in which C is a constant.

The form of the stress dependent activation energy function $Q(\sigma)$ depends on the characteristics of the barriers to glide. Two types of barriers can be distinguished: discrete obstacles, such as other ('forest') dislocations or impurities, and intrinsic lattice friction resistance (Peierls stress), related to the nature of the inter-atomic bonds.

When *discrete obstacles* are met, dislocations bow out between the obstacles (Fig. 6.4a) and eventually will overcome the barrier by cutting through it (for example in case of forest dislocations), or by by-passing it leaving loops (e.g. around impurities - see examples in Hull and Bacon 1984). In these cases, the quantity $Q(\sigma)$ can be described (after Frost and Ashby 1982) as

$$Q(\sigma) = Q_0 \cdot \left[1 - (\sigma/\sigma_0)^p \right]^q \qquad (6.21)$$

in which Q_0 is the activation energy needed to overcome the obstacles in the
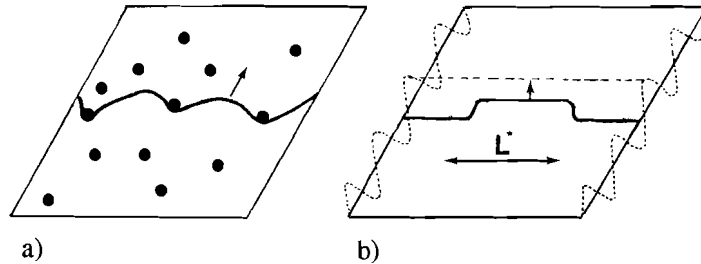
Figure 6.4
Dislocation glide controlled by:
a) dispersed discrete obstacles: Under an applied stress, the dislocation bows out between the obstacles until the line tension is high enough to break away,
b) lattice friction resistances: to get across the energy (Peierls) hills caused by the strength of the atom bonds to be broken for continued motion, the dislocation forms double kinks which are forced up the hill by the applied stress and laterally spread out.

absence of external stress, σ_0 is the flow stress at 0 K (no help of thermal energy) and p and q are constants determined by the distribution and specific shape of the obstacles. For regularly spaced discrete obstacles, p=1 and q=1 are considered reasonable approximations (see Frost and Ahsby 1982). Combining equations 6.20 and 6.21, it then follows that

$$\dot{\varepsilon} = C \cdot \sigma^2 \cdot \exp[-Q_0/RT \cdot (1 - \sigma/\sigma_0)] \qquad (6.22)$$

For high values of Q_0, the stress dependence of the exponential part of eq. 6.22 is much more important than that present in the pre-exponential factor. Thus, $C \cdot \sigma^2$ can be treated as about constant. This simplifies equation 6.22 to

$$\dot{\varepsilon} = C' \cdot \exp[-Q_0/RT \cdot (1 - \sigma/\sigma_0)] \qquad (6.23)$$

This rate equation represents one extreme in a range of slightly varying equations for *discrete obstacle controlled glide*. Note that the expression used for Q(σ) (eq. 6.21, setting p=q=1) is similar to that derived for dissociation-controlled cross slip of screw dislocations (eq. 6.13), implying that these models are indistinguishable from each other in form. This is due to the fact that both models are based on a consideration of succesfull core-scale dislocation jump phenomena.

The interaction of moving dislocations with the atomic bonds in a material leads to an *intrinsic resistance* of the crystal lattice to dislocation motion (Weertman 1957b, Guyot and Dorn 1967, Poirier 1985). The strength and separation of bonds produce harmonic variations of dislocation line energies, with long straight valleys of low energy (with close-packed atoms) lying between parallel energy barriers (the 'Peierls hills'). For continued motion, a dislocation has to overcome these energy barriers. This occurs with help of both thermal energy and applied stress in the following manner. A double-kinked segment of a dislocation line (Fig. 6.4b) is forced over the barrier. After this 'nucleation barrier' is overcome, the kinks propagate unstably until the whole dislocation has moved one atomic distance forward. The activation energy for the kink nucleation process can be written in the same way as for discrete obstacles (eq. 6.21). Analyzing various data, Frost and Ashby (1982) propose (empirical) values for p and q in equation 6.21, respectively 3/4 and 4/3 (see also Ashby and Verrall 1978). This leads (analogous to eq. 6.22) to a rate equation for lattice resistance controlled dislocation glide (with constant K) given

$$\dot{\varepsilon} = K \cdot \sigma^2 \cdot \exp[-Q_0/RT \cdot \left(1 - (\sigma/\sigma_0)^{3/4}\right)^{4/3}] \qquad (6.24)$$

At this stage, it is important to realize that the mechanisms for overcoming barriers which form the basis for rate equations 6.23 and 6.24, contrary to the climb and cross slip models, are incapable of recovering the dislocation substructure (no annihilation). Therefore, these glide-controlled models are not considered capable of producing true steady state behaviour (Stocker and Ashby 1973). However, recovery processes *may operate* while not being rate controlling. Based on this latter notion, Weertman (1957b) derived an expression for lattice friction (Peierls stress) controlled dislocation glide in which climb was included as recovery mechanism, but was not rate controlling. As in other lattice-resistance-limited models, Weertman assumed double kinks to form in the dislocation line, spreading out unstably over the energy (Peierls) barriers. The length L^* of the kinked segment (refer Fig. 6.4b) can be related to the radius of a dislocation loop, which in turn can be related to the stress by analyzing how far dislocations from one source could travel before being stopped by dislocations created from a source on a neighbouring slip plane (cf. Fig 6.1). Annihilation by climb then 'releaves' the blocked dislocations, as in the analysis of climb-controlled creep (Weertman 1955, 1957a - section 6.2.2), but is now so rapid that it is not rate controlling. Following this model, the average dislocation velocity can be expressed

$$\bar{v} = v_0 \cdot L^* \cdot \exp[-Q(\sigma)/RT] \qquad (6.25)$$

where v_0 is a constant and $Q(\sigma)$ is the stress-dependent activation energy for the

gliding process. Note that it is the parameter L^* which distinguishes the form of equation 6.25 from 6.19. In Weertman's model, L^* is found proportional to $(\sigma/M)^{1/2}$, where M is the density of dislocation sources (Weertman 1957a,b - section 6.2.2). $Q(\sigma)$ is expressed in a manner analogous to equation 6.21, namely

$$Q(\sigma) = Q_0 \cdot \left[1 - (\pi/2P) \cdot \sigma \right] \qquad (6.26)$$

In this equation, Q_0 is again the activation energy at zero applied stress, and P is the flow stress (Peierls stress) at T=0 K. Taking the density of dislocation sources M to be constant and $L^* \propto \sigma^{1/2}$ (see above), the following rate equation for *Peierls stress limited glide* is derived from the Orowan equation (6.1) and eqs. 6.25-6.26

$$\dot{\varepsilon} = K \cdot \sigma^{2.5} \cdot \exp[-Q_0/RT \cdot [1 - (\pi/2P) \cdot \sigma]] \qquad (6.27).$$

This is often referred to as the Weertman model for Peierls stress limited glide.

6.3 COMPARISON OF EXPERIMENTAL RESULTS WITH MICROPHYSICAL MODELS

6.3.1 Used data and aims

From the set of mechanical data obtained for calcite single crystals, the results for the slip regime for samples cleaved from parent crystal P2 and compressed parallel to $[40\bar{4}1]$ (Table 2.4, Figs 2.10 and 2.19b) were fitted to the creep models given in the previous section. This particular set of data was chosen because it comprises the most complete description of the mechanical behaviour in the range of experimental conditions investigated (T=600-800 °C, σ=20-75 MPa). The samples exhibited more or less steady state flow and were deformed by slip on the $r[\bar{2}021]^+$ and $f[10\bar{1}1]^+$ systems, the f-system dominating.

The fitting procedure yielded values for the microphysical parameters characterizing the various models. The values obtained were considered in relation to microstructural evidence for the active processes, and in relation to independent constraints on the parameters. The objective was to gain insight into the rate controlling mechanism in the slip regime.

6.3.2 Approach

The data have been fitted to the rate equations derived for climb-controlled creep (generalized power law, eq. 6.8), cross slip-controlled creep (constriction type, eqs. 6.15 and 6.18), and barrier-controlled dislocation glide for both the discrete-obstacle-limited (eq. 6.23) and Peierls-stress-limited (eq. 6.27) cases. As described previously, these models (with the exception of eq. 6.18) incorporate the theoretical relation $\sigma \propto \rho_m^{0.5}$, which links the density ρ_m of mobile dislocations to the applied stress σ. It was shown in chapter 5 that the dependence of the *total* dislocation density ρ_t on stress in calcite single crystals compressed parallel to [40$\overline{4}$1] is well described by this relation (refer eq. 5.4). This helps justify comparison of the present creep data with the various microphysical models. The initial density (i.e. before deformation) of potentially immobile (grown-in) dislocations was low, and the total dislocation density exhibited a steady state character suggesting that an increase in density of immobile (tangled) dislocations was unlikely.

The fitting procedure involved the non-linear regression method mentioned earlier (Marquardt 1963), in which a single dependent variable (stress) was related to two independent variables (strain rate and temperature). All of the constitutive parameters characterizing the theoretical equations were treated as 'free' fitting parameters. Estimates of these parameters were obtained by minimizing the sum of the squared deviations of the data points from the function under consideration, making use of a search algorithm. The temperature dependence of the shear modulus of calcite is weak in the temperature range investigated here (Dandekar 1968, see eq. 5.7) and was neglected in the fitting procedure. The shear modulus at absolute zero (μ_o) was taken as 34830 MPa (eq. 5.7).

6.3.3 Fitting results

The results obtained are presented in Table 6.1 and Fig 6.5. On the basis of the correlation coefficients, the power law and cross slip equations show a slightly better fit than the models for barrier-controlled dislocation glide. However, the differences are small and provide no indication of the rate controlling mechanism.

6.3.4. Microstructures and constraints on fitting parameters

The above models are now considered in relation to the available microstructural data for samples compressed parallel to [40$\overline{4}$1] and to (independent) constraints on the various constitutive parameters obtained from the fitting procedure.

-- generalized *POWER LAW CREEP* equation (eq. 6.8):

$$\dot{\varepsilon} = A' \cdot \sigma^n \cdot \exp[-Q/RT]$$

results of regression analysis:
LOG(A') = -3.81(±1.22), n = 11.5(±0.9) and Q = 362(±35) kJ/mole
corr.=0.972

-- *CROSS SLIP* equations:

$$\dot{\varepsilon} = B \cdot \sigma^{2+Qcs/RT} \cdot \exp[-Q_{cs}/RT \cdot (\ln \sigma_0/\mu_0 + \ln \mu)] \qquad \text{(eq. 6.15)}$$

results of regression analysis:
LOG(B) = 10.41(±1.97), Q_{cs} = 74(±8) kJ/mole and σ_0 = ~6100 MPa
corr.:0.967

$$\dot{\varepsilon} = B \cdot \sigma^{Qcs/RT} \cdot \exp[-Q_{cs}/RT \cdot (\ln \sigma_0/\mu_0 + \ln \mu)] \qquad \text{(eq. 6.18)}$$

results of regression analysis:
LOG(B) = 13.51(±2.01), Q_{cs} = 90(±8) kJ/mole and σ_0 = ~2600 MPa
corr.:0.966

-- *BARRIER CONTROLLED DISLOCATION GLIDE* equation

>> *DISCRETE OBSTACLE LIMITED* (eq. 6.23)

$$\dot{\varepsilon} = C' \cdot \exp[-Q/RT \cdot (1 - \sigma/\sigma_0)]$$

results of regression analysis:
LOG(C') = 13.05(±2.72), Q = 432(±32) kJ/mole and σ_0 = 202(±15) MPa
corr.: 0.937

>> *PEIERLS STRESS LIMITED* (eq. 6.27)

$$\dot{\varepsilon} = K \cdot \sigma^{2.5} \cdot \exp[-Q/RT \cdot (1 - (\pi/2p) \cdot \sigma)]$$

results of regression analysis:
LOG(K) = 5.98(±1.95), Q = 329(±41) kJ/mole and p = 443(±38) MPa
corr.: 0.899

list of symbols: $\dot{\varepsilon}$ = strain rate
                   σ = flow stress
                   Q   = apparent activation energy
                   A',B,C',K and n = constants
                   R   = gas constant
                   μ = shear modulus
                   μ_0 = shear modulus at absolute zero
                   σ_0 = flow stress at absolute zero
                   p   = Peierls stress
                   (ln = natural logarithm, LOG = ^{10}logarithm)

Table 6.1 (previous page)
Creep models and regression results obtained by best fitting of the present single crystal data (parent crystal P2, compressed parallel to [40̄41]) for the slip dominated regime. Temperature dependence of the shear modulus μ is neglected over the temperature range investigated (μ taken constant: 25 GPa at T=700 °C, μ_0 =34.8 GPa, see eq. 5.7). The quality of fit is measured by the correlation coefficient (corr.).

Firstly, the slip band shift features associated with f_t^+ slip (refer Fig. 2.20) are potentially explicable in terms of long range climb of edge dislocations from one slip band to another (compare with Fig. 6.1). In addition, considerable TEM evidence was found for dislocation climb (section 2.6). Furthermore, the general power law fit (Table 6.1) yields an activation energy of 362(±35) kJ/mole, which compares favourably with the values obtained for self-diffusion of carbon and oxygen in calcite, 370 and 420 kJ/mole respectively (Anderson 1969). However, the high stress exponent of 11.5(±0.9) contrasts strongly with the values of 3-6.5 predicted by existing climb-controlled creep models (section 6.2.2).

The slip band shift features mentioned above in relation to climb, can be equally well explained by cross slip of screw dislocations from one level to another, either on a highly oblique cross slip plane or homogeneously distributed in the 'shift zone'
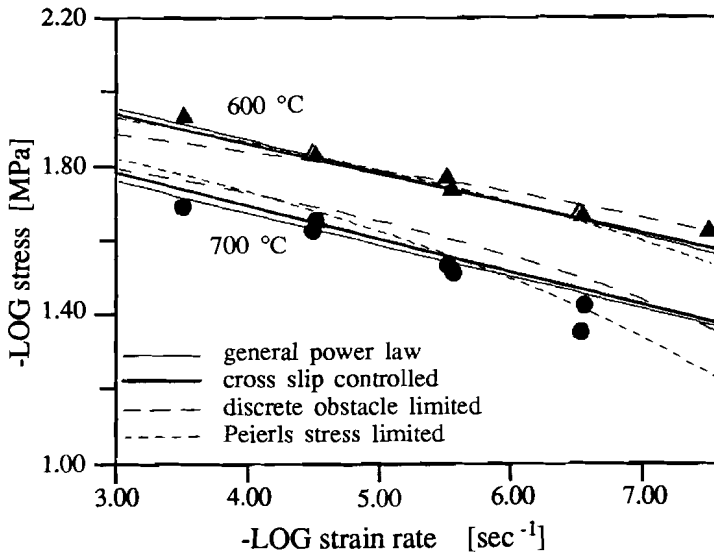

Figure 6.5
Log-log plot of strain rate vs. flow stress showing data points obtained at 600 and 700 °C (refer Fig. 2.10). Best fit lines correspond to the models listed in Table 6.1. The results for the two cross slip controlled equations overlap.

between the overlapping slip bands (refer Figs 2.20 and 6.2). Cross slip could also control recovery without contributing to the creep strain (Poirier 1976), thus producing no clear slip markings (Poirier 1976). The observed slip band shift microstructures are very similar indeed to cross slip related structures seen in copper and alumina (Honeycombe 1968; p.100), and in Ni-Co alloys (Haasen 1983). They also resemble the broad and wavy slip traces reported for involvement of cross slip in creep of salt (Wawersik 1988). Many of the loose, irregular dislocation networks observed in TEM (section 2.6.4) were suggested to be related to the shift features, forming twist boundaries interconnecting separate slip bands (see section 2.7.3). The main dislocation networks were found oriented oblique to the **r** and **f** slip systems, parallel to $(0\bar{1}11)$, and the model proposed to explain their development involved dislocation cross slip (refer Fig. 2.28).

In addition to the above, the change from $n \approx 13$ at 600 °C to $n \approx 9.5$ at 800 °C seen in the empirical power law fits presented in Fig. 2.10, shows that n is temperature dependent - one of the principle characteristics of cross slip-controlled creep (Table 6.1). The apparent 'activation energies' Q_{cs} obtained by fitting the data to the constriction controlled cross slip models (Table 6.1) are 74($\pm$8) and 90($\pm$8) kJ/mole respectively. These values are 0.2-0.25 times those for self-diffusion of carbon and oxygen in calcite. Estimates of the activation area (the area swept out by an individual dislocation event) obtained following the method of Skrotzki and Haasen (1988), yield values of $7b^2$ to $30b^2$, where b is the length of the Burgers vector (taken as 6.37 Å, i.e. $\bar{b}$ for $f<10\bar{1}1>$ slip). The above values for activation energy and area are broadly comparable with data for salt, which show an apparent activation energy for cross slip of 0.1 times that for self-diffusion (Wawersik 1988) and an activation area of $20\text{-}400b^2$ (Skrotzki and Haasen 1988). However, no theoretical constraints on these quantities are presently available for calcite. The value of activation area expected for climb-controlled creep is of the order of $1b^2$ (Argon 1966), i.e. about an order of magnitude lower than found here.

The apparent activation energy for cross slip can be theoretically related to the stacking fault energy γ (see section 6.2.3). Inserting the two values obtained for Q_{cs} into equation 6.12, using a value of 0.058 for the elastic parameter β (calculated for calcite at T=700 °C from data given by Dandekar 1968 and assuming that the definition of β for fcc-materials can be used for the distorted fcc-structure of calcite), stacking fault energies of 0.66 and 0.61 J/m^2 respectively were obtained. These values are 2-3 times the value for salt (0.2-0.3 J/m^2, after Wawersik 1988) and 2 to 60 times higher than published stacking fault energies for metals such as Ni, Mg and Cu (resp. 0.3, 0.1 and 0.04 J/m^2, Sestak 1980) and austenitic steels (Ni-Cr-Si-Co alloys: 0.01-0.08 J/m^2, Hornbogen 1983). Thus, the stacking fault energies obtained here for calcite are rather high. This raises the question of whether or not stacking faults would be observed in calcite if a conventional (constriction controlled) cross slip mechanism is rate controlling. This is answered as follows. The

approximate equilibrium spacing (d) of dissociated dislocations forming stacking faults is related to the stacking fault energy γ (e.g. Hull and Bacon 1984) by the equation

$$d = \mu b^2/4\pi\gamma \tag{6.28}$$

On this basis, the f<10$\overline{1}$1> dislocations in calcite can be expected to be separated by only 12-13 Å, i.e. about 2b. Practically, this implies that with conventional TEM-techniques at relatively low operating voltages (as in the present study), it would be virtually impossible to observe f-related stacking faults in calcite. The lack of observations on dissociated dislocations in calcite in the present study does not then rule out constriction controlled cross slip as the rate controlling creep mechanism.

Lastly, let us consider the evidence that dislocation glide mechanisms might have been rate controlling. The numerous slip bands seen in the samples can certainly be viewed as consistent with the dislocation glide models presented in section 6.2.4. Furthermore, while the dislocation structures observed using TEM are indicative of climb, they do not rule out glide as being rate controlling. On the other hand, glide control is generally expected at lower homologous temperature (0.2-0.4 T_m, Langdon 1985) than the present tests, and only the Peierls stress limited model of Weertman (1957b) includes a recovery mechanism capable of producing steady state behaviour of the type observed rather than continuous work hardening (see Stocker and Ashby 1973). Furthermore, when glide is rate controlling at least some TEM evidence would be expected for straight dislocations lying between Peierls hills (Guyot and Dorn 1967). No such evidence was found. As regards to microphysical parameters, no constraints seem to be available to compare with the values of the fitting parameters obtained for the obstacle limited glide model. However, by fitting our data to the Weertman (1957b) model for the Peierls mechanism (Table 6.1), a Peierls stress of 443(±38) MPa was obtained, which is ~0.02 times the shear modulus μ (at T=700 °C) of calcite. This is a high ratio compared with most metals and ionic materials (Guyot and Dorn 1967, Haasen 1985), but is nonetheless of the same order of magnitude as that found for zinc (Weertman 1957), iron (Arsenault 1975) and iron-alloys (Guyot and Dorn 1967, Christian 1971).

6.3.5. Discussion: cross slip as rate controlling mechanism?

Based on the above considerations, the climb controlled creep model (n=3-6.5) is rejected because of the very high stress exponent obtained from the power law fit to the present data (n~11.5). Dislocation climb was clearly active in the tests, but was

not a significant strain accumulating mechanism itself (as evidenced by morphological observation), and was apparently too fast to be rate controlling. By contrast, the cross slip and glide models cannot be rejected. They show comparable quality of fit, the values obtained for the various material constants are reasonable (as far as can be assessed), and the observed microstructures are not inconsistent with these models. However, several aspects favour cross slip as the rate controlling mechanism: a) the cross slip model fits the experimental data slightly better than the glide models (refer Table 6.1), b) cross slip can, contrary to most glide mechanisms, be viewed as a recovery mechanism (Poirier 1976) and is therefore capable of producing the observed steady state behaviour of the calcite single crystals, and c) the involvement of cross slip rather than glide alone explains the characteristics of the dislocation substructure, notably the development of $(0\bar{1}11)$ dislocation networks with segments oriented oblique to the main glide planes (refer section 2.7.3).

Discussion is now focussed on this latter point, i.e. on the role of cross slip in the development and recovery of the dislocation substructure. As demonstrated in chapter 5, the steady state flow of the crystals compressed parallel to $[40\bar{4}1]$ corresponds with a steady state dislocation density and structure. Local development of dislocation network segments must therefore be balanced by their annihilation elsewhere. Analyzing dislocation configurations in deformed single crystals of various metals, Myshlyaev (1976, see also Myshlyaev and Khodos 1980) argued that a dynamic equilibrium of network creation and destruction is possible. This concept was further elaborated by Friedel (1977) who, assuming dissociated dislocations, brought forward the idea that constriction of a dislocation due to interaction with a forest dislocation facilitates cross slip (refer section 6.2.3) thus facilitating network *formation*. At the same time, Friedel proposed that the constricted node within an existing network is a likely initiation point for cross slip, allowing dislocations to be released, thus *destroying* the network. In *in situ* experiments on aluminium inside a high-voltage electron microscope, Caillard and Martin (1982a, 1982b, 1983) directly observed the formation, migration and progressive destruction of hexagonal dislocation networks with cross slip as the rate controlling process, thus proving the importance of the cross slip mechanism in attaining a steady state dislocation network configuration (given the right conditions). Cross slip has also been directly observed in *in situ* TEM work on semiconductor materials such as Si and Ge (Möller et al. 1979). The stress-strain behaviour of these materials shows various stages of hardening and recovery (Brion et al. 1981), and it is widely accepted that cross slip is the controlling recovery mechanism up to relatively high temperatures (Siethoff and Schröter 1983, Schröter and Siethoff 1984, Siethoff et al. 1986). Dislocation structures in deformed Si and Ge crystals are found to consist mainly of hexagonal screw dislocation networks (Brion and Haasen 1985, Haasen et al. 1986), which initially harden the crystal but at higher stresses are dismantled (recovered) by cross slip. Thus aluminium and semiconductor materials appear to furnish examples of

cross slip controlled creep involving formation and destruction of (hexagonal) dislocation networks, as proposed theoretically by Friedel (1977).

On the basis of the quality of fit obtained for cross slip controlled creep models, the consistency of the observed microstructures (notably the shift features) with cross slip mechanisms, and the resemblance of the present data for calcite with theoretical and experimental analyses on other materials given in the literature, it seems likeley that the deformation rate of calcite single crystals under the conditions investigated is dominantly cross slip controlled. However, a cross slip model alone cannot adequately explain the curvature observed in a log stress versus 1/T plot (Fig. 6.6). This suggests a changing apparent activation energy with temperature. The slight concave curvature might, at first glance, be associated with the disappearance of r-slip towards lower flow stresses (refer Fig. 2.19). However, it is also clearly apparent in the regime of pure f-slip. In this regime, dislocation networks are less conspicuous towards the higher stresses (section 2.6.2), and having discussed above the role of cross slip in network formation and destruction, this might be interpreted as indicating diminishing cross slip control at those high stress conditions. Dislocation glide may then become an additional mechanism controlling the rate of deformation. Glide and cross slip are serial processes which cannot act independently, so that the slower process limits the creep rate. Though speculative,
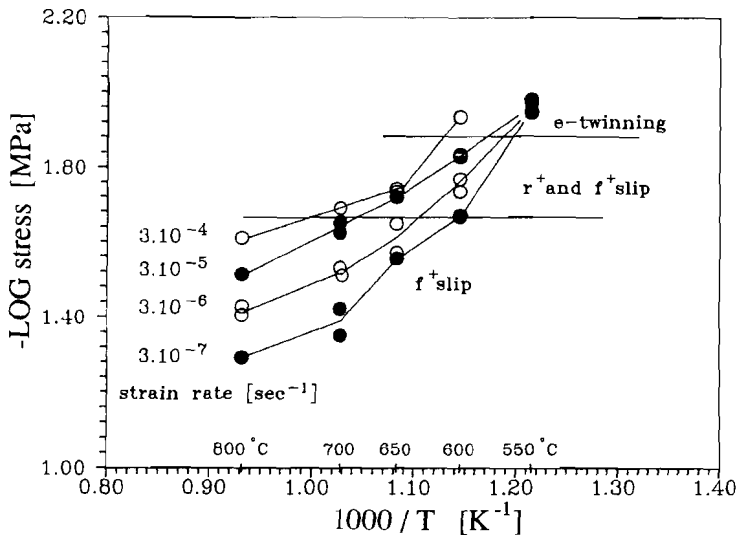
Figure 6.6
Log flow stress vs. reciprocal temperature for samples from parent crystal P2. Twinning and slip regimes after Fig. 2.19b. Figure identical to Fig. 2.13.

it therefore seems conceivable that under the range of experimental conditions investigated, cross slip is the slowest process overall, with dislocation glide becoming comparably significant in limiting the creep rate towards high stresses, thereby co-controlling the deformation rate.

6.4 SINGLE CRYSTAL BEHAVIOUR vs. CREEP IN POLYCRYSTALLINE CALCITE

6.4.1 Comparison of experimental conditions and mechanical data

In Fig. 6.7 the mechanical behaviour of the single crystals is compared with that of calcite rocks deformed experimentally at similar temperature (700 °C). The single crystal data best resemble the results for the coarse-grained Carrara and Yule marbles, both of which are known to deform by intracrystalline mechanisms under the temperature conditions considered (see section 1.4). Schmid et al. (1977) and Schmid and Paterson (1977) have demonstrated that in their experiments on the
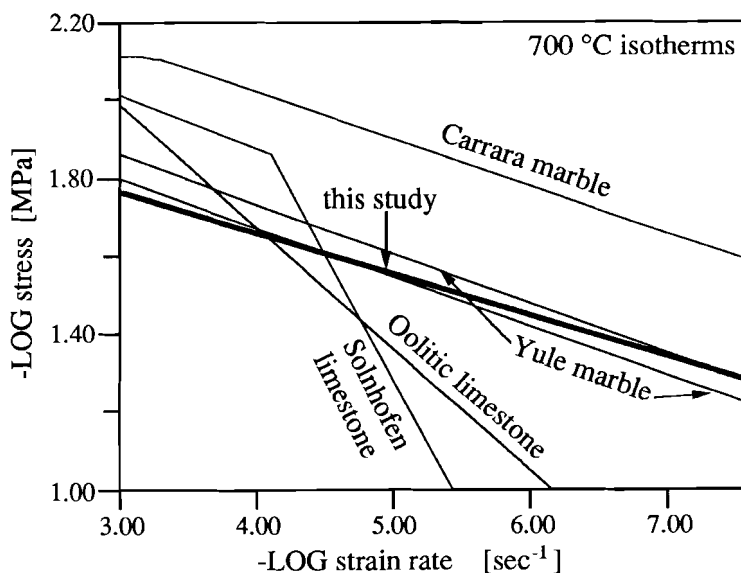
Figure 6.7
Log-Log plot of strain rate vs. differential stress showing 700 °C isotherms plotted using best fit creep laws for various calcite materials (see Tables 1.3 and 6.2). Carrara marble isotherm after Schmid et al. (1980), Yule marble after Heard and Raleigh (1972), Solnhofen limestone after Schmid et al (1977), Oolitic limestone after Schmid and Paterson (1977). Single crystal isotherm taken from Fig. 2.10 (parent crystal P2). See also section 1.4

much finer-grained oolitic and Solnhofen limestones, deformation was likely to be governed by grain boundary related processes, namely grain boundary sliding and associated diffusion ('superplastic' behaviour). For this reason, attention is focussed here on a comparison of the present single crystal data with the data available on Yule and Carrara marble.

The experimental conditions and mechanical data obtained for the single crystals and for Carrara (regime 2) and Yule marble are compared in Table 6.2. In this Table, the mechanical data are represented in terms of the empirical power law fits derived by the respective authors. The ranges of temperature, strain rate and flow stress investigated in the experiments on the single crystals and marbles were roughly comparable, but whereas the single crystals were deformed at near-atmospheric pressure, the Carrara and Yule marbles were tested at 300 and 500 MPa confining pressure respectively. The constitutive parameters appearing in the various power laws show the following features:

a) a reasonable agreement in the pre-exponential term for Yule marble and the single crystals, but a considerably higher value for Carrara marble;

b) similarly high values for the stress exponent n for both the marbles and the single crystals;

c) variability by a factor of ~2 in the apparent activation energy for creep (Q).

Heard and Raleigh (1972) reported a constant n-value over the range of conditions investigated for Yule marble, but Schmid et al. (1980) on Carrara marble found evidence for a temperature-dependent stress exponent (see Table 1.3). They attributed this to a change in deformation mechanism and subdivided the flow behaviour into deformation regimes with their own characteristic microstructure and

	experimental conditions				power law fitting results		
	T [°C]	σ-range [MPa]	$\dot{\epsilon}$-range [sec^{-1}]	pressure [MPa]	LOG(A')	n	Q [kJ/mole]
single crystals	600-800	20-75	3×10^{-4}-3×10^{-8}	0.25 (CO_2)	-3.8(±1.2)	11.5(±0.9)	362(±35)
Yule -I -T	500-800 id.	16-140 id.	10^{-3}-10^{-7} id.	500 id.	-3.9(±0.7) -3.6(±0.9)	8.3(±0.4) 7.7(±0.5)	260(±12) 255(±12)
Carrara (regime 2)	700-1000	20-100	10^{-2}-10^{-6}	300	3.1(±0.4)	7.6(±0.8)	420(±42)

Table 6.2
Comparison of experimental conditions and mechanical results for single crystals (this study), Yule marble (after Heard and Raleigh 1972; I=normal to foliation, T=parallel to foliation) and Carrara marble (Schmid et al. 1980). See also Table 1.3. Fitting results given for general power law (eq. 6.8).
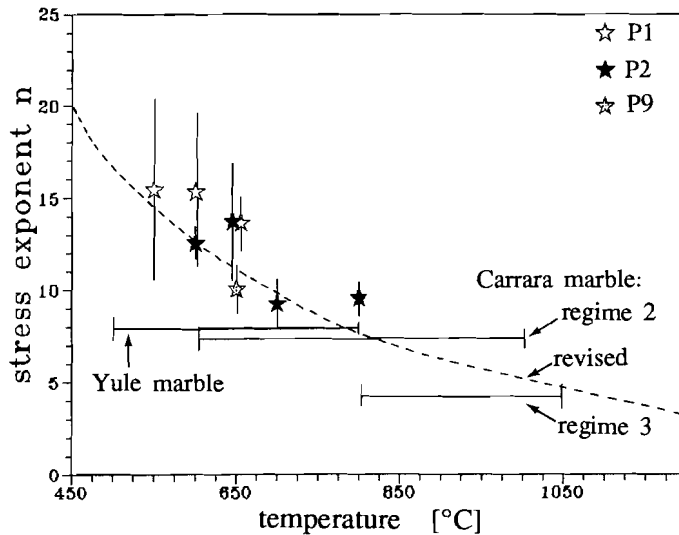
Figure 6.8
Power law stress exponent n vs. temperature for various calcite materials. Single crystal data after Table 2.7, marble data after Tables 1.3 and 6.2. Revised trend for Carrara marble after preliminary data from Chopra et al. (1988). Note the good correspondence of the present single crystal stress exponents with the latter.

power law creep equation with constant n (their second regime is included in Table 6.2). Recently however, Chopra et al. (1988) revised Schmid's work on Carrara marble with new experiments. They came to the conclusion that no real grounds exist for establishing strict deformation regimes. Instead, they infer a gradual change of the stress exponent with temperature, from n~20 at 450 °C to n~3 at 1200 °C. The n-values of Chopra et al. (1988; preliminary results!) and the values obtained for calcite single crystals compressed parallel to [40$\overline{4}$1] (Table 2.7) are plotted in Fig. 6.8. They show a reasonably good correspondence, both in magnitude and in dependence on temperature.

6.4.2 Microstructural observations

The microstructural observations on experimentally deformed Yule and Carrara marble, and on single crystals are summarized in Table 6.3. The presence of subgrain development and recrystallization phenomena in the marbles is in sharp contrast to the single crystal microstructures. However, the occurrence of slip bands and a dislocation structure consisting of irregular (helical) free dislocations,

	optical microstructures	TEM microstructures
single crystals	slip lines, shift features (chapter 2)	straight and curved, locally helical dislocations, irregular pseudo hexagonal dislocation networks, kinks, jogs loops, dipoles, debris, no subgrain walls
Yule marble	slip bands, limited twin bands, minor grain boundary sliding	free dislocations of irregular direction, dislocation loops, three-fold dislocation nodes (reactions), dislocation networks, forming well-defined subboundaries
Carrara marble	deformation bands, undulatory extinction, subgrain-development core and mantle - structures, paucity of twinning, minor grain-boundary sliding	non-uniformly distributed free dislocations, dipoles, loops, dislocation reactions (nodal points), subboundary networks

Table 6.3
Comparison of optical and transmission electron microscopy observations on experimentally deformed single crystals (this study), Yule marble (after Goetze and

dislocation loops, dipoles, and dislocation networks and nodes are closely comparable.

6.4.3 Discussion: cross slip-controlled creep in marbles?

As in the case of the single crystals (section 6.3.3), climb control for creep of marbles under the present conditions of intermediate stresses and temperatures can be rejected because of the relatively high stress exponents (~8 compared with 3-6.5 predicted by microphysical models). Dislocation climb obviously was active in both Yule (Goetze and Kohlstedt 1977) and Carrara marble (Schmid et al. 1980), but apparently too fast to be rate controlling. That climb is *not* the creep rate controlling process is further supported for Yule marble by the low value obtained for Q, i.e. 260 kJ/mole (cf. 370 and 420 kJ/mole for self diffusion carbon and oxygen in calcite respectively - Anderson 1969). Taking into account the fact that steady state deformation (requiring recovery) is achieved in the marbles under the conditions of present interest (Heard and Raleigh 1972, Schmid et al. 1980), glide control seems

an unlikely candidate for the rate controlling mechanism (though a Weertman-type Peierls-stress limited model cannot be excluded). For this reason, attention is now restricted to a discussion of cross slip control for creep in the marbles, as seen in the single crystals.

Firstly, it is recalled that a characteristic element of the constriction-controlled cross slip rate equation (eq. 6.18) is formed by the temperature dependent stress exponent (n). Such a temperature dependence was indeed concluded from new experiments on Carrara marble (Chopra et al. 1988), although not reported earlier for marbles (Heard and Raleigh 1972, Schmid et al. 1980). Both the magnitude of the stress exponents obtained and the relative change with temperature (Fig. 6.8) are broadly consistent with the behaviour of the single crystals inferred to be controlled by cross slip.

Secondly, the repeated observations in Yule and Carrara marble of three-fold dislocation nodes forming loose to dense networks (Table 6.3) is of particular interest and similarity to the single crystal microstructures. These features were interpreted to be intimately associated with cross slip controlled recovery in the single crystals (sections 2.7.3 and 6.3.3), and it is inferred here that they probably reflect the same process occurring in the marbles. The frequent subboundaries reported in the optical and TEM studies of the marbles (Goetze and Kohlstedt 1977, Schmid et al. 1980) are not clearly distinguishable from the dislocation network arrays seen in the single crystals. It therefore seems possible that the reported subgrains may reflect the network formation seen in single crystals, modified by additional arrays of 'geometrically necessary' dislocations (see chapter 5) expressing the influence of multiple slip in the polycrystalline material.

Finally, in proposing cross slip as the creep controlling process in the marble as well as in the single crystals, some points require special consideration. These are treated seperately in the following sections.

6.4.4 Taylor factor

In comparing the intracrystalline plastic behaviour of single crystals with polycrystals, it is necessary to account for the fact that in polycrystals multiple slip (ideally on 5 systems) occurs in the individual grains, in accordance with the Von Mises criterion for homogeneous deformation. Even if the strengths of the individual slip systems are known, this poses a problem for calculating the aggregate flow strength (e.g. Takeshita et al. 1987). Commonly, the strength of the grains (and hence of the polycrystal), considering all slip systems to be of about equal strength τ, is related to τ using an orientation averaging factor, known as the Taylor factor M (e.g. Van Houtte and Wagner 1985). Thus, the aggregate flow stress is given

$$\sigma = M \cdot \tau \qquad\qquad (6.29)$$

where M can be regarded as an average reciprocal Schmid factor. The single crystal flow data under consideration here, represent axial stresses - not resolved shear stresses. Taking $f[10\bar{1}1]^+$ as the main active slip system in the single crystal tests, the Schmid factor (~0.5) allows the measured flow stresses to be converted into flow stresses on f. No attempt is made here to calculate a precise Taylor factor for calcite. However, by analogy with fcc- and bcc-metals (e.g. Reed-Hill 1973), it is reasonable to take M≈3. Applying this value for M to the calcite crystal data and using the Schmid factor for f^+ slip (~0.5), all stress data must be multiplied by 3/2 to estimate the corresponding polycrystal flow stress, assuming that the Von Mises condition is largely fulfilled by f-slip alone. In the constriction controlled cross slip equation (eq. 6.18) with stress constant $Q_{cs}/RT≈11$ (at T=700 °C, see Table 6.1) representing the single crystal behaviour, this results in a decrease in strain rate by a factor $(3/2)^{11}$, i.e. about two orders of magnitude. This positions the single crystal 700 °C isotherm in Fig. 6.7 between those of Yule and Carrara marble, implying reasonable agreement with the average behaviour of marbles.

6.4.5 Influence of confining pressure

The single crystals and marbles under consideration were deformed under different confining pressure conditions (Table 6.2). Confining pressure is well known to influence the flow strength of marbles under low PT conditions where intergranular microcracking mechanisms are active (Fredrich et al. 1989). In contrast, little is known regarding the effect of pressure on *intra*crystalline flow processes in calcite materials. However, on the basis of experiments on NaCl crystals and from theoretical considerations regarding lattice dilatation associated with stacking faults, dissociation of screw dislocations is thought to be more difficult at high pressure (Poirier 1985), thus facilitating constriction and consequently cross slip under such conditions. When constriction is rate controlling, this would imply lower flow strengths towards higher confining pressures, which might account for the difference in flow strength (Fig. 6.7) between Yule and Carrara marble (500 and 300 MPa confining pressure respectively). However, the flow strength of the present single crystals, corrected for the Taylor factor, would then be expected to lie *above* that of Carrara marble (0.25 and 300 MPa confining pressure respectively), which it does not (at T=700 °C). Thus, other factors such as composition must be involved in controlling the creep strength. In this respect, attention is drawn to the discussion in section 2.7.1 on possible solid solution softening effects in the calcite single crystals.

6.4.6 Influence of grain size

Analysis of dislocation density (ρ) versus stress in experimentally deformed calcite polycrystals has shown that the commonly obtained and theoretically expected relationship $\sigma \propto \rho^{0.5}$ does not hold at low stresses (i.e. below about 40 MPa for the marbles - refer Fig. 5.11). In chapter 5, this was explained as being possibly related to the influence of grain size. If true, it follows that flow data below these stress levels cannot directly compared with microphysical creep models which do not account for such a grain size effect (as is the case for *all* intracrystalline mechanisms presented above, section 6.2). A further evaluation of the influence of grain size on the rate of creep by intracrystalline mechanisms is clearly needed.

In the analysis presented in chapter 5 (section 5.6.3), a distinction was made between geometrically necessary dislocations and statistically stored dislocations (after Ashby 1970). The former of these are required to accomodate gradients of deformation in grains and above a few percent strain are thought to have a constant density (ρ_G) inverse propotional to the grain size (eq. 5.17). It is the population of statistically stored dislocations (with density ρ_s) which achieve the increasing strain during deformation, and thus ρ_s is of importance in terms of the Orowan equation (eq. 6.1). Now, given equation 5.15

$$\sigma = \left(\alpha_s \mu b \cdot \rho_t^{0.5}\right) - \left((\alpha_s - \alpha_G)\mu b \cdot \rho_G^{n} \cdot \rho_t^{0.5-n}\right) \tag{6.29}$$

where α_s, α_G en n are constants, μ is the shear modulus, b is the Burgers vector magnitude and ρ_t is the total dislocation density equal to $\rho_s + \rho_G$, the following expression for ρ_s is obtained taking n=0.5 (see section 5.6.3)

$$\rho_s = \left(\sigma/(\alpha_s \mu b)\right)^2 + \left(2\sigma(\alpha_s - \alpha_G)\rho_G^{0.5}\right)/(\alpha_s^2 \mu b) + \left[((\alpha_s - \alpha_G)/\alpha_s)^2 - 1\right]\rho_G \tag{6.30}$$

Incorporating $\rho_G = AD^{-1}$ from equation 5.17, equation 6.30 can be rewritten

$$\rho_s = U \cdot \sigma^2 + V \cdot \sigma \cdot D^{-0.5} + W \cdot D^{-1} \tag{6.31}$$

where $U = (\alpha_s \mu b)^{-2}$, $V = (2(\alpha_s - \alpha_G)A^{0.5}/\alpha_s^2 \mu b)$ and $W = A[((\alpha_s - \alpha_G)/\alpha_s)^2 - 1]$. Note that if D is very large (i.e in case of single crystals), equation 6.31 boils down to the usual $\rho \propto \sigma^2$ relationship (section 5.2). Using the Orowan equation (eq. 6.1), the following grain size dependent equation for constriction controlled cross slip is obtained from equations 6.14 and 6.15 (refer section 6.2.3 for details on the equations)

$$\dot{\varepsilon} = B/U \cdot [U \cdot \sigma^2 + V \cdot \sigma \cdot D^{-0.5} + W \cdot D^{-1}] \cdot \sigma^{(Qcs/RT)} \cdot \exp[-Q_{cs}/RT \cdot (\ln \sigma_0/\mu_0 + \ln \mu)] \tag{6.32}$$

Since both α_S and α_G are positive values, and since $\alpha_S > \alpha_G$ (that is, as determined for calcite materials, see section 5.6.3), parameter W in equations 6.31 and 6.32 will always be negative. This implies that with changing grain size, the effect on ρ_S, hence on $\dot{\varepsilon}$ (i.e. increase or decrease), is very sensitive to the magnitudes of the parameters U, V and W, and on the level of flow stress. Using available dislocation density vs. stress data for various calcite materials, values for α_S and for the composite parameter $(\alpha_S - \alpha_G)\mu bA^{0.5}$ (denoted A^*) could be obtained ($\alpha_S = 1.61$ and $A^* = 2.97$ respectively, eqs. 5.19, 5.20), but quantitatively, the results were not fully satisfactory (refer Fig. 5.13). Also, A and α_G remained unknown, and thus no well-constrained values for U, V and W can be obtained. However, on the basis of equation 5.17 ($\rho_G = A \cdot D^{-1}$), a maximum value of $\sim 10^7$ cm^{-1} can be estimated for A, since ρ_G in a given rock type must be less than the minimum dislocation density measured (refer Fig. 5.9). From A^* (see above) a maximumum value of -1 then follows for α_G. These values imply that with decreasing grain size (D) at a given stress, the strain rate ($\dot{\varepsilon}$) will decrease, i.e. the material will harden.

6.4.7 Interpretation

The flow behaviour of Yule and Carrara marble at temperatures between 500 and 1000 °C and flow stresses above 20 MPa was attributed by their investigators to diffusion controlled dislocation creep, presumably with dislocation climb being rate limiting. Difficulties in relating single crystal plasticity with that of polycrystals (Taylor factor), effects of confining pressure, and possible influences of grain size on dislocation density presently hamper a fully satisfactory comparison of the single crystal behaviour vs. Yule and Carrara marble. Nonetheless, the above discussion on both mechanical and microstructural aspects of deformation in these materials clearly suggests cross slip controlled creep as a better explanation for the observed behaviour, not only in single crystals but also in marbles.

6.5 SUMMARY/CONCLUSIONS

Flow data reported in chapter 2 for calcite single crystals experimentally compressed in the [40$\bar{4}$1] orientation have been fitted to microphysical models for climb-controlled creep, cross slip-controlled creep and barrier-controlled dislocation glide. After an evaluation of the fitting results, a consideration of the microstructural observations in relation to the models, and a comparison of the microstructures and

microphysical constitutive parameters obtained from this fitting procedure with existing data on metals and semiconductors, it was concluded that the deformation of the single crystals is best explained by cross slip-controlled creep models. The mechanical behaviour and dislocation-microstructural characteristics of experimentally deformed marbles under intermediate conditions of temperature and stress (T=500-1000°C, σ=20-100 MPa) correspond reasonably well with those reported for the single crystals ([40$\bar{4}$1] orientation), suggesting that under these conditions, creep of marbles may be controlled by the same mechanism, i.e. by cross slip.

N.B. Parts of this chapter were published in special publication no. 54 of the Geological Society of London (De Bresser and Spiers 1990).

CHAPTER 7

INTRACRYSTALLINE DEFORMATION IN A NATURAL CALCITE TECTONITE: the Tutt shear zone, South-Wales

7.1 INTRODUCTION

In this chapter, an attempt is made to gain insight into the deformation behaviour of a natural calcite tectonite, using experimental data reported in the literature and in the preceding chapters. The tectonite studied occurs in a small-scale shear zone developed in limestones of low metamorphic grade, outcropping on the coast of South Wales. It was chosen since intracrystalline deformation mechanisms were clearly important in its development, and since the maximum temperatures attained in the shear zone were too low to allow significant deformation by solid state diffusion (T<0.4Tm, Langdon 1985).

The tectonite was studied using optical and electron microscopy, placing emphasis on paleopiezometric aspects of the microstructure, such as dislocation density, recrystallized grain size and twinning frequency. The results obtained are combined with previous experimentally derived calibrations in order to estimate the syn-kinematic flow stress. Further constraints on the flow stress result from considerations relating to brittle failure. In addition, the stresses developed during deformation are estimated using both empirical and microphysically-based 'dislocation creep' equations for various calcite materials. The stress estimates obtained using the various microstructural paleopiezometers and brittle failure criteria fall in the range 70-500 MPa, with some evidence for a narrower range of 70-200 MPa. Stress estimates calculated using the cross slip controlled creep law determined for single crystals in chapter 6 are consistent with these figures. It is suggested that cross slip controlled creep may be the most important mechanism of intracrystalline deformation in calcite rocks at low temperatures and that the corresponding flow law offers a possible method of estimating minimum flow stress when the deformation rate is constrained.

7.2 THE TUTT SHEAR ZONE: Geological setting and field observations

7.2.1 Geological setting

The tectonite under study occurs in a small-scale shear zone developed in the Lower Carboniferous limestones at Tutt on the Gower peninsula near Swansea, South Wales, U.K. (Fig. 7.1). The shear zone (referred to henceforth as the Tutt shear zone) represents a lateral thrust ramp linking two intraformational detachment horizons developed within a kilometer-scale, EW-trending anticline (Hyett 1990). The anticline forms part of the Variscan fold and thrust belt (e.g. Owen and Weaver 1983) affecting Devonian Old Red Sandstones, Lower-Carboniferous limestones and Upper-Carboniferous terrigenous sediments rich in coal (the 'Coal Measures').

The thickness of the overburden during development of the Tutt shear zone was of the order of 5 km. This figure is based on stratigraphic records (Owen 1973, Anderson and Owen 1980, Dunne 1983) and on estimated maximum depths of burial estimated, for the Coal Measures, using coal rank data (Gill et al. 1979). On the basis of illite crystallinity, an upper anchizone degree of metamorphism can be inferred for the limestones hosting the Tutt shear zone (Gill et al. 1977, 1979, see also Parker et al. 1983). This grade of metamorphism correlates with a temperature of about 200 °C (Winkler 1979, Kisch 1987), in agreement with the value of 175-250 °C suggested for Variscan events by Hancock et al. (1983). Taking into account the calculated thickness of the overburden (~5 km), these temperatures are also fully
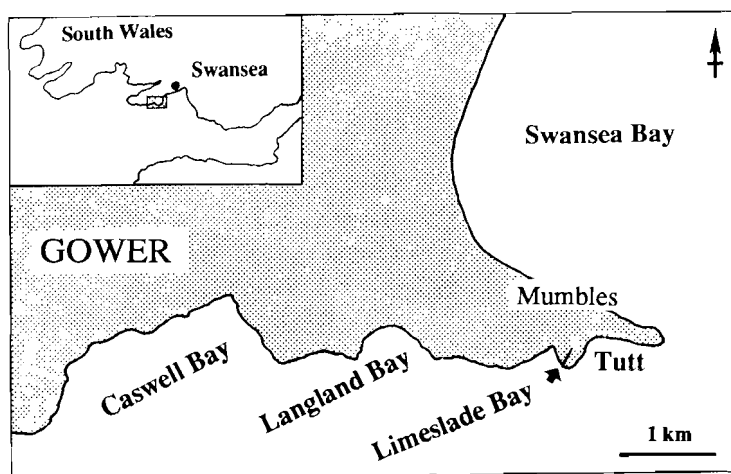
Fig. 7.1
Location of the Tutt shear zone, eastern side of Limeslade Bay, Gower peninsula, South Wales.

consistent with the geothermal gradient of 33-50 °C/km believed to apply to the thermal history of the Coal Measures (Gill et al. 1979). Thus, the pressure-temperature conditions prevailing during development of the Tutt shear zone are estimated at approximately 130 MPa and 200 °C respectively.

7.2.2 Field observations

The shear zone (Figs 7.2 and 7.3) is exposed in a coastal section at Limeslade Bay (refer Fig. 7.1). It consists of a narrow, thrust-type shear zone of about 0.5 m in width. Parts of the zone show cataclastic deformation. However, the bulk of the zone is characterized by progressive rotation of a newly formed cleavage into the shear plane, indicating coherent ductile deformation (Fig. 7.3). A planar discontinuity in the centre of the zone points to late stage fracturing of the zone, with fibrous calcite coating this plane indicating a movement direction consistent with that implied by the cleavage. The maximum displacement accomodated along the thrust plane is ~3.5 m.

Figure 7.2
Field appearance of the Tutt shear zone. Note the planar discontinuity.
Box indicates Fig. 7.3. Note geological hammers for scale.
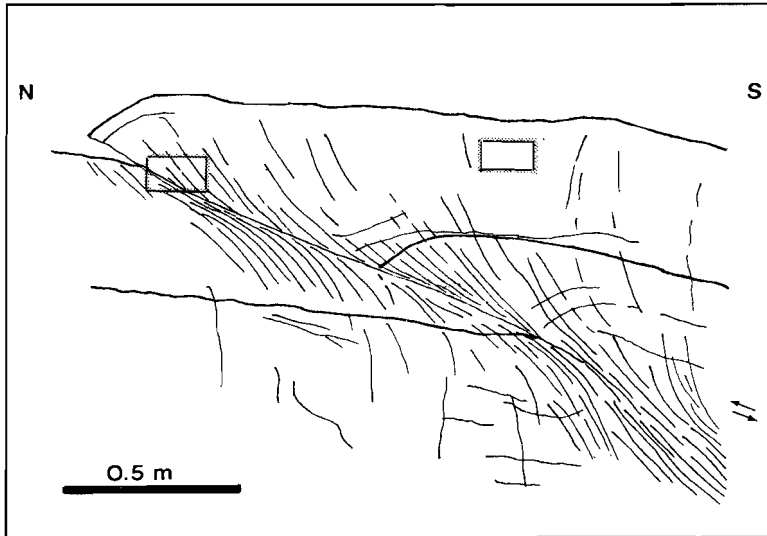
Figure 7.3
Tip of the Tutt shear zone, drawn after Fig. 6 from Hyett (1990). Boxes indicate
sample locations for deformed and undeformed material.

7.3 MICROSTRUCTURAL OBSERVATIONS AND INTERPRETATIONS

For the purpose of the present study, only coherently sheared limestone tectonite samples were selected for microstructural investigation. In particular, attention was focussed on samples taken near the tip of the shear zone (Fig. 7.3), i.e. at the upper end of the ramp where relatively high stresses can be expected because of compatibility problems and associated stress intensification (Elliot 1976, Hyett 1990). Undeformed 'control material' was sampled from the same sedimentary horizon at a position outside the shear zone (Fig. 7.3).

7.3.1 Optical and SEM microstructures

The undeformed limestones sampled outside the Tutt shear zone consist of calcareous grainstones (Fig. 7.4a), containing ooids, pelloids and fossil fragments of various sizes, held together by sparry interparticle calcite cement (of grain size 20-700 μm). Within the shear zone, the ooids, the biogenic particles, the fossil fragments (such as single crystal crinoid fragments) and the sparry calcite grains all become progressively flattened (Fig. 7.4b), defining a penetrative foliation developed oblique to the shear plane. The elongated sparry calcite grains and single crystal fossil fragments contain numerous twins and show widespread undulose extinction in
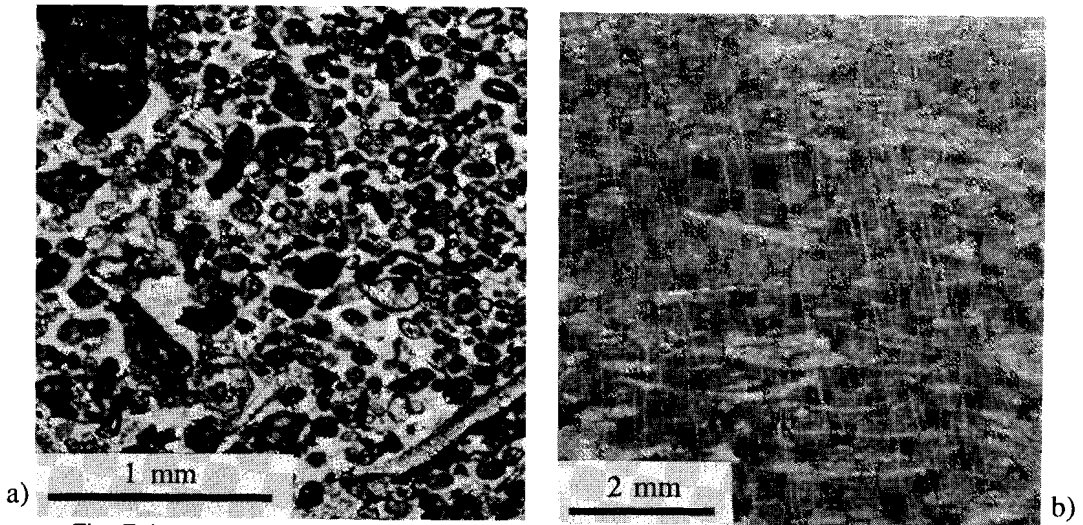
Fig. 7.4
Microstructure of undeformed Tutt limestone (a) and deformed Tutt limestone (b). In (b), note the strong flattening of the various types of grains and of interparticle cement, resulting in development of a penetrative foliation (horizontal in picture). Note also the numerous (subvertical) microcracks.

plane polarized light, indicative of considerable intracrystalline straining. Similar undulose extinction features are present in the oolitic and fine biogenic calcite. Pervasive recrystallization of the coarse calcite resulted in strong grain size reduction, producing an overall mylonitic microstructure with old grain porphyroclasts (of widely varying grain sizes ~10-500 µm) surrounded by fine (1-2 µm) recrystallized grains (Fig. 7.5). New grains have relatively equidimensional shapes (Fig. 7.6), but show undulose extinction as do the old grain relics, implying a syn-deformational origin. Close inspection of the flattened calcite cement, using ultra-thin sections (<5 µm), revealed the presence of numerous subgrains, with sizes similar to those of the recrystallized grains (Fig. 7.5). Presumably, progressive rotation of subgrains (e.g. Urai et al. 1986) was the main recrystallization mechanism. However, new grains may have developed locally from grain- and twin boundary bulges, by migration recrystallization (refer Fig. 7.5). The average size of the recrystallized grains was found to be 1.3 µm (± one standard deviation of 0.7 µm) - Fig. 7.7. This was determined by measuring grain diameters directly from SEM-micrographs (e.g. Fig. 7.6).

Locally, mm-scale shear bands cross-cut and destroy the intense foliation developed in the sheared material (see also White et al. 1980), without markedly changing the recrystallized grain size. These small shear bands are oriented more or
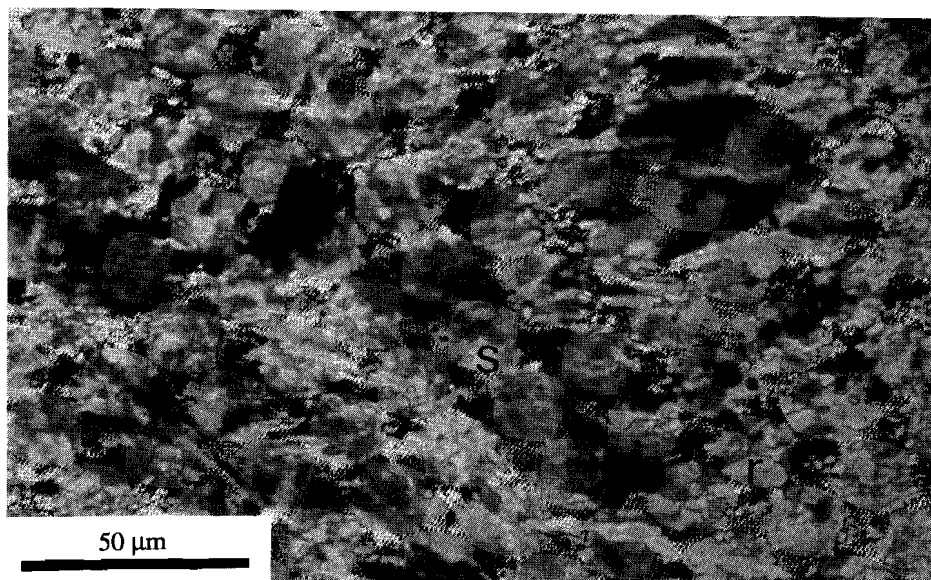
Fig. 7.5
Micrograph of ultra-thin section of limestone tectonite from the Tutt shear zone,
showing subgrains (s) and recrystallized (r) grains of approximately the same
size. This suggest recrystallization by a subgrain rotation mechanism. Locally,
bulging of twin boundaries evidences subordinate migration recrystallization. Old
grain porphyroclasts are relics of sparry calcite.
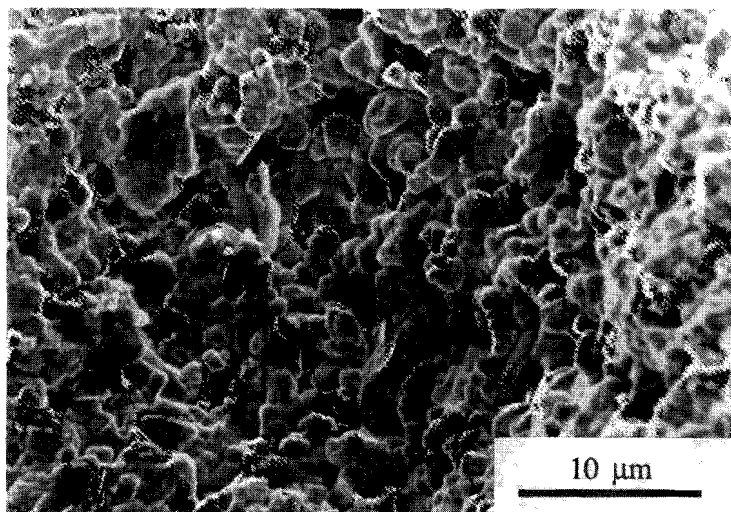
Fig 7.6
SEM micrograph (secondary electrons) of recrystallized grains in a deformed
sample from the Tutt shear zone.

less parallel to the conspicuous failure plane in the centre of the Tutt zone (refer Fig. 7.2). Estimates of strain in the rocks near the tip of the shear zone (Hyett 1990) yielded strain ellipse axial ratios of 2.5-4.2 for the plane containing the shear direction and shear plane normal (i.e. the xz-plane).

In addition to the abundant evidence for crystal plastic deformation described above, samples from the shear zone often show evidence for microcracking and veining (e.g. Fig. 7.3b). The cracks are generally oriented at a high angle to the foliation. Occassionally, bubble traces in relatively large (flattened) grains provide evidence for healing of transgranular fractures. Usually, however, such cracks are filled with calcite grains of the same size as the recrystallized grains in the host rock and show comparable undulose extinction. It follows that the cracks must have developed before or contemporaneously with the intracrystalline deformation phenomena. Despite a careful search, no offsets have been found in the sealed cracks, indicating that grain boundary sliding ('superplastic flow'; e.g. Schmid et al. 1977) was not a significant deformation mechanism, at least not after microcracking occurred.
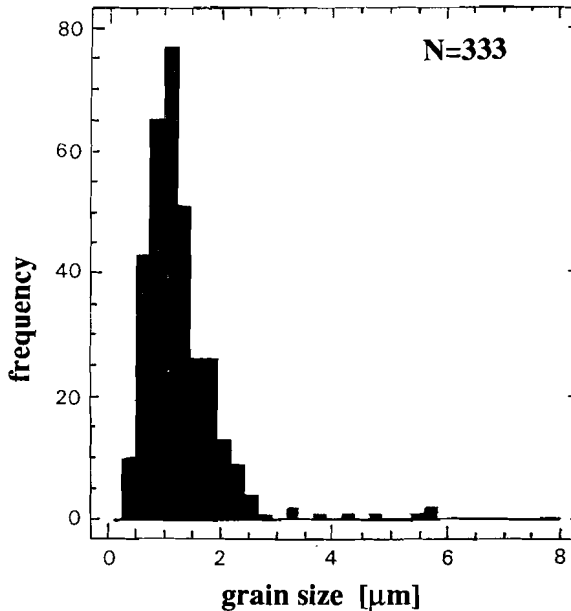
Figure 7.7
Histogram showing the distribution of recrystallised grain sizes in deformed limestone from the Tutt shear zone. The mean of the distribution lies at 1.3 μm.

7.3.2 Crystallographic preferred orientations

The orientation distributions of calcite a-axes in a deformed sample from the Tutt shear zone were been measured using X-ray diffraction method by H.-G. Brokmeier (Clausthal). Typical results (Fig. 7.8a) show a weak but clear a-axis girdle of developed at ~40° to the shear plane (i.e. to the shear bands). This bulk texture includes contributions from large old grains and from the fine recrystallized grains which are volumetrically dominant. C-axis traces measured optically in old grains alone (Fig. 7.8b), in a section containing the shear direction and shear plane normal, yield a preferred orientation which matches very well with the a-axes texture obtained using X-rays (n.b.: c is perpendicular to a). Qualitatively speaking, the fine recrystallized grains show a similar optical preferred orientation (revealed using a gypsum plate), and it is therefore inferred that the X-ray texture of Fig. 7.8a characterises both the old and recrystallized grains.

The observed crystallographic preferred orientations are consistent with the various pieces of microstructural evidence for intracrystalline deformation in both the old and recrystallized grains. The a-axis girdle distribution and corresponding c-axis

X-ray: poles on a-planes   optical: c-axes traces
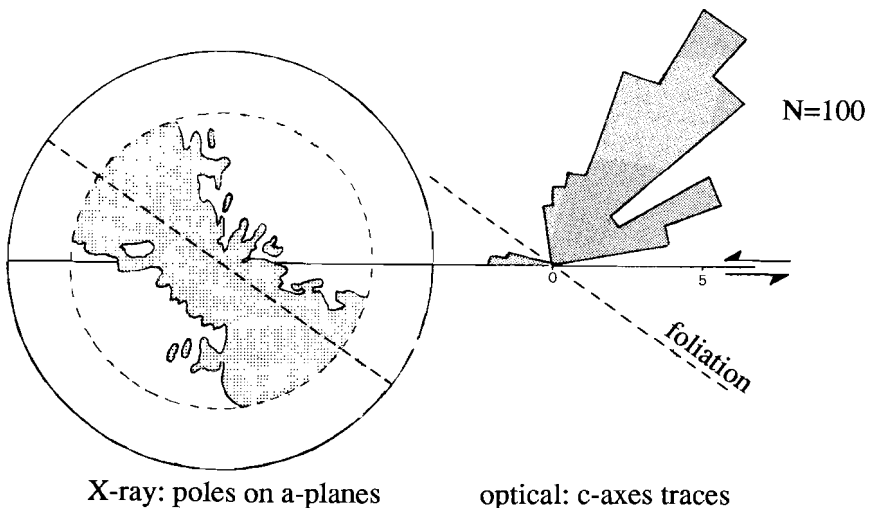
Figure 7.8
Measured crystallographic preferred orientations in a limestone sample from the Tutt shear zone.
a) a-axis distribution measured by X-ray diffraction (equal area projection, outer rim not measured). Sample volumetrically dominated by recrystallized grains.
b) rose diagram illustrating preffered orientation of c-axis traces in old, generally twinned sparry calcite grains.

maximum are also consistent with calculated and experimentally produced low-temperature shear textures (compare with Fig. 1.5), as regards both pattern and sense of asymmetry.

7.3.3 TEM observations

Transmission Electron Microscopy was carried out on the Tutt mylonite using a JEOL 200C microscope, operating at 200 kV.

At the TEM scale, irregular, twinned porphyroclasts were commonly observed, but the microstructure of the samples was found to be dominated by the presence of the recrystallized grains of ~1 μm diameter (Fig. 7.9a). Up to 10% of these show thin twin lamellae, but the twinned volume per grain never exceeds 10%. The recrystallized grains exhibit a near polygonal fabric, with straight grain boundaries occasionally being oriented parallel to low-index crystallographic planes, notably r-planes. Triangular voids are commonly developed at grain boundary triple junctions (Fig. 7.9b). Most grains (small as well as relatively large grains) show zones of high contrast (Fig. 7.9c), often yielding streaky diffraction patterns, i.e. showing elongated spots indicative of strong local lattice bending. These high contrast zones appear to represent volumes of very high dislocation density. Where resolved, dislocations are straight or slightly curved and sometimes show interactions. The high density prevents detailed characterization. Locally however, the density of dislocations (ρ_t) could be quantitatively determined using the method outlined in chapter 5. In general, this was in areas of low contrast in grains with sizes larger than 1-5 μm. Assuming a mean thickness of the electron transparant areas of 0.62 μm (i.e. identical to that for the single crystals - Fig. 5.2), and averaging the results of 13 plates, a value ρ_t of 2.47×10^9 cm^{-2} (± one standard deviation of 0.97×10^9 cm^{-2}) was obtained. Note however that this value of ρ_t represents a *minimum* for the deformed rock since only areas of relatively low contrast, where individual dislocations could be resolved, were studied.

7.3.4 Interpretation/conclusion

On the basis of the microstructural observations and texture data reported above, it can now be firmly concluded that deformation within the Tutt shear zone occurred principally by intracrystalline plastic mechanisms accompanied by extensive dynamic recrystallization and minor cataclasis. The Tutt tectonite can thus be viewed as a true calcite mylonite.
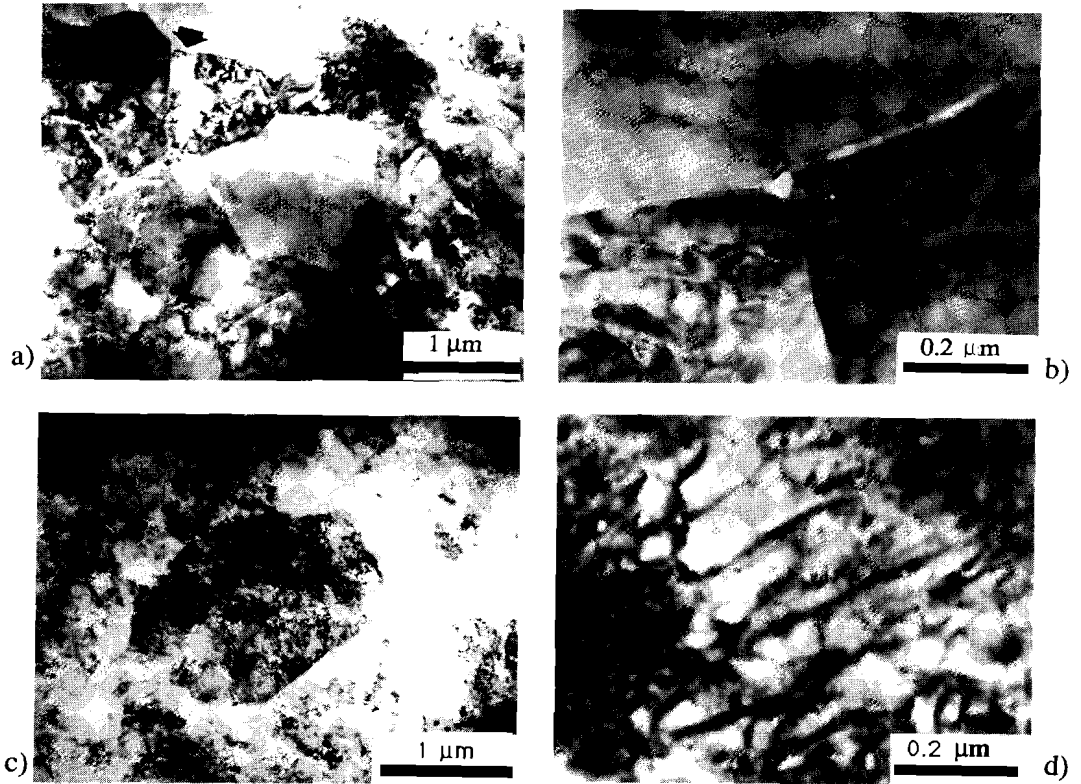
Figure 7.9
TEM micrographs showing characteristic substructures in tectonite material from the
Tutt shear zone.
a) polygonal fabric of fine recrystallized grains. Note the occasional thin twins
(arrow),
b) triangular void on grain boundary triple junction,
c) recrystallized grain with zone of high contrast (multibeam conditions), interpreted
as due to a high density of dislocations.
d) individual dislocations resolved in a zone of high contrast (refer Fig. 7.9c).

7.4 ESTIMATION OF PALEOSTRESS

7.4.1 Starting remarks

While fully recognising the problems and limitations inherent to the various methods of estimating paleostresses from deformd rocks (e.g. Nicolas and Poirier 1976, White 1979, Schmid 1982, Paterson 1987, Carter and Tsenn 1987), an attempt is now made to apply these methods to place at least some constraints on the flow stresses asociated with the development of the Tutt mylonite. Firstly, conventional methods of microstructural paleopiezometry will be applied, namely the dislocation density and recrystallized grain size methods (e.g. Twiss 1977). Calcite twinning paleopiezometry (Rowe and Rutter 1990) will then be considered. This is followed by an analysis of physically realizable stress states as defined by brittle failure criteria for the Tutt limestone. Lastly, the flow strength of the Tutt mylonite is estimated by extrapolating 'dislocation creep laws' for various calcite materials to the appropriate temperature and strain rate conditions. Both empirical and microphysically based creep equations are used.

7.4.2 Conventional paleopiezometry

1) *Dislocation Density Method*

From theory, flow stresses during plastic deformation of crystalline materials are expected to be related to dislocation density via expressions of the form $\sigma \propto \rho^{0.5}$ (refer chapter 5). When experimentally calibrated, such relations offer a means of estimating σ from ρ, provided that ρ is preserved.

In chapter 5, a series of stress vs. dislocation density relations were obtained for calcite single crystals and rocks, on the basis of experimental data. The single crystal data were closely consistent with expectations from theory ($\sigma \propto \rho^{0.5}$). However, the polycrystal data appeared to show an effect of grain size. The main stress vs. dislocation density relations obtained are summarized in Table 7.1 where they are applied, using the dislocation density measured in the Tutt material, to calculate the corresponding flow stress. Note that an empirical relation for Solnhofen limestone is included in Table 7.1 since this is of roughly similar grain size to the Tutt mylonite (~6 vs 1 μm).

The flow stresses calculated from the first three equations (Table 7.1) fall in the range 69-127 MPa. Since the dislocation density measured in the Tutt mylonite is thought to represent a lower bound (section 7.3.3), these flow stresses are also thought to constitute lower bounds. In Table 7.1, the grain size dependent σ-ρ relationship is also included. In applying this relation to the Tutt mylonite, the

question arises which value for the grain size should be used. Presumed old grains (porphyroclasts now) have widely varying grain sizes (~10-500 μm), while the recrystallized grains on average have D=1.3 μm. Although certainly above 1-5 μm, unfortunately, the exact sizes of the grains in which dislocation densities were measured are not known. Using D=1.3 μm, a meaningless (negative) stress value of -107 MPa results from equation 4 in Table 7.1, but inserting an average porphyroclast size of ~100 μm (e.g. Fig. 7.5), a (positive) paleostress of ~124 MPa follows from the equation. However, because of the uncertainties involved, no significance can be attributed to these stress estimations.

	stress (σ) vs. dislocation density (ρ_t) relation	measured ρ_t for Tutt mylonite [cm^{-2}] (lower bound)	estimated flow stress [MPa] (lower bound)
(1)	$\sigma = 10^{-3.20} \cdot \rho_t^{0.56}$ (empirical single crystal equation, 5.6)	$(2.47 \pm 0.97) \times 10^9$	115 ±26
(2)	$\sigma = 10^{-7.07} \cdot \mu(T) \cdot \rho_t^{0.5}$ (theoretically constrained single crystal equation, 5.8)	"	127 ±25
(3)	$\sigma = 10^{-2.26} \cdot \rho_t^{0.5} - 204.4$ (empirical equation for Solnhofen limestone, Table 5.4)	"	69 ±55
(4)	$\sigma = (10^{-2.51} \cdot \rho_t^{0.5}) - (2.97 \cdot D^{-0.5})$ (empirical polycrystal equation including effect of grain size, after eq. 5.20)	" D = 1.3 μm (new grains) D = 100 μm (old grains)	87 ±31 - 107 ±30 124 ±31

Table 7.1
Stress determination on the basis of experimentally determined relationships between stress and dislocation density (refer chapter 5). Shearmodulus μ at T=200 °C is 30 GPa, after eq. 5.7. The shear modulus at T=200 °C is also included in equation (4) (cf. eq. 5.20).

2) Recrystallized Grainsize Method

It is well established from experimental work on a wide variety of materials (eg. Takeuchi and Argon 1976) that the average diameter (D) of either subgrains or recrystallized grains developed during intracrystalline creep tends to be inversely related to the flow stress (σ). Some theoretical basis for this has been provided by

Twiss (1977), who obtained the relation

$$\sigma = A \cdot \mu b/(1-v) \cdot D^{-m} \tag{7.1}$$

where A and m are constants, μ represents the shear modulus, b is the Burgers vector magnitude and v is Poisson's ratio. According to Twiss' theory, m is expected to be 1 for subgrains or rotation recrystallized grains, while m=–0.7 for migration recrystallized grains. Testing equation 7.1 for data on quartz, olivine and a variety of metals, Twiss (1977) found that his theory was in good agreement with the experimental data. An empirical value of 8.13 was obtained for the parameter A. Despite controversy regarding Twiss' model, empirical σ-D relations have been widely applied to estimate paleostresses. In the case of calcite rocks, the following empirical relations have been determined (cf. eq. 7.1)

$$\sigma = 10^{-1.38} \cdot D^{-1.01 \pm 0.05} \tag{7.2}$$

$$\sigma = 10^{-0.89} \cdot D^{-0.70} \tag{7.3}$$

with grain diameter D in cm and σ in MPa. These equations were respectively obtained for rotation recrystallized grains in Carrara marble (by Schmid et al. 1980) and for migration recrystallized grains in calcite fault gauge (by Friedman and Higgs 1981).

In the deformed Tutt limestone, the average size of the recrystallized grains, formed by progressive rotation of subgrains, is 1.3 µm. Taking reasonable values for Poisson's ratio v (0.31, after Twiss 1977), the shear modulus μ (30 GPa, calculated at T=200 °C using eq. 5.6) and Burgers vector length b (6.37×10^{-8} cm, see section 2.6.4), a paleostress of 170 MPa follows from the theoretically based eq. 7.1. Using the empirical relation for rotation recrystallization given by equation 7.2 (after Schmid et al. 1980), a paleostress of 390 MPa results. At this stage, the implied discrepancy between the two relations cannot be explained.

7.4.3 Twinning paleopiezometry

The use of e-twinning as an indicator of paleostress magnitude in plastically deformed calcite rocks has been suggested by Jamison and Spang (1976), Spiers (1982) and Schmid (1982). Spiers (1982) (see also Schmid 1982) reports experimental results for calcite rocks which clearly show that the importance of twinning (relative to slip) increases with increasing flow stress and decreases with decreasing grain size. Twinning appears to become more difficult in finer grained

material, since grain boundaries tend to impede the spreading and widening of twins.

Recently, Rowe and Rutter (1990) performed a series of high temperature deformation experiments on calcite rocks of different grain sizes, aiming to establish relationships between flow stress, grain size and various measures of the importance of twinning. They report the following empirical relations

$$\sigma = -293 + 2.13 \cdot lt\% - 204 \cdot LOG(D) \qquad (7.4)$$

$$\text{and } LOG(\sigma) = 1.12 + 0.40 \cdot [LOG(V\%) - LOG(D)] \qquad (7.5)$$

where σ is the flow stress in MPa, D is the grain size in cm, lt% is the percentage of grains in a given grain size class interval which contain twin lamellae, and V% is the maximum twinned volume in a grain size class. Both twinning incidence and volume percentage seem to be independent of temperature and strain rate, though they almost certainly increase significantly with strain when this exceeds moderate laboratory values (Spiers 1982).

The fine-grained nature of the Tutt mylonite does not permit an extensive study to obtain values for lt% and V%. However, it was found that not more than 10% of the recrystallized grains contain twin lamellae, the twinned volume within the grains not exceeding 10%. This sets upper limits to lt% and V% of 10 and 1 respectively. Putting D=1.3 μm, equations 7.4 and 7.5 now yield upper bound paleostresses of 520 and 470 MPa respectively.

7.4.4 Failure-related constraints on flow stress

The planar discontinuity in the centre of the Tutt shear zone evidences a (late) stage of brittle behaviour in the deformation history. Assuming that this fault plane indicates compressional shear failure, failure strength data can be used to determine the upper bound stress which was eventually reached in the Tutt shear zone.

With this aim, a limited number of fracture tests were carried out on cylinders of undeformed Tutt limestone sampled near the shear zone. Firstly, four cylindrical limestone samples of 65 mm length were loaded to failure in a fluid medium, triaxial testing machine (the 'Heard' apparatus, described by Spiers et al. 1986). The tests were carried out at room temperature, a strain rate of 2×10^{-4} sec^{-1} and confining pressures in the range 0.1-10 MPa. In addition, one cylindrical plate of 40 mm diameter was tested using the so-called Brazilian method, allowing determination of the tensile strength of the rock (e.g. Hoek and Brown 1980). The results are presented in Table 7.2 and in the Mohr diagram of Fig. 7.10. A preliminary Mohr envelope is drawn in Fig. 7.10 describing the failure criterion for the Tutt limestone.

It corresponds well with results published for other limestones. At the same time, it almost certainly delineates upper bound strengths for the strongly foliated Tutt mylonite under syn-deformational PT-conditions.

During development of the Tutt shear zone, the lithostatic confining pressure was of the order of 130 MPa (section 7.2). Due to the presence of fluids, evidenced by the presence of bubble traces and veins, the *effective* confining pressure P_e was presumably lower. Assuming that the pore pressure was at least equal to the pressure exterted by a column water of identical height to the overburden (e.g. Handy 1989), one can write $P_e \leq 80$ MPa. From Fig. 7.10, the maximum differential stress during shear failure then can be determined by setting the least principal stress σ_3 equal to P_e and increasing the size of the Mohr-circle until the failure-envelope is reached. This yields a differential stress of 410 MPa, which therefore represents a reasonably reliable upper limit for the flow stress during development of the Tutt shear zone.

The above approach focusses on compressional shear fracture within the centre of the Tutt zone rather than on the micro-scale veins (refer section 7.2.3). The latter can be interpreted as indicating *extensional* failure during deformation, and as such suggest a state of stress lying on the strongly curved portion of the failure envelope drawn in Fig. 7.10. This in turn suggests that differential (flow) stresses did not exceed 200 MPa in the Tutt zone (see Fig. 7.10).

test	P_{CONF}	failure	notes
TH01	10 MPa	not reached	no failure up to 225 MPa
TH01a	5 MPa	227 MPa	shear fracture normal makes 62° with σ_1
TH02	2.5 MPa	not reached	no failure up to 226 MPa
TH02b	-	179 MPa	dominantly axial splitting
TH03	-	5.6 Mpa	tensile strength, Brazilian method

Table 7.2
Results of fracture tests on undeformed samples of Tutt limestone, temperature 22 °C, strain rate 2×10^{-4} sec^{-1}, various confining pressures (P_{CONF}). All tests were triaxial compression tests, except TH03 which was a Brazilian failure test.
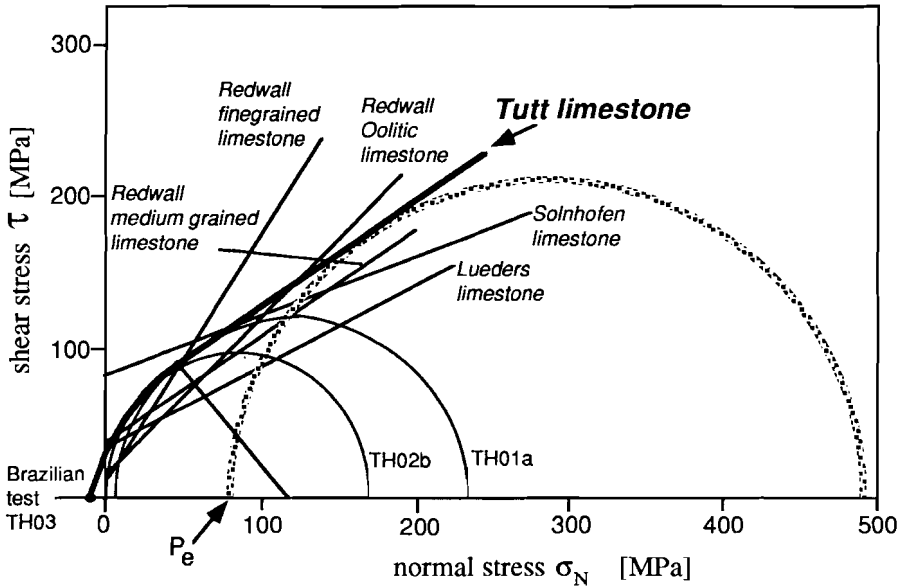
Figure 7.10
Normal stress (σ_N) vs. shear stress (τ) diagram with Mohr circles at failure for Tutt limestone sampled outside the shear zone. TH01a, TH02b and TH03 were tested in the laboratory (Table 7.2). The thick solid line represents the Mohr envelope drawn taking the orientation of the shear fracture in TH01a into account. In comparison, failure envelopes are given for fine-grained, oolitic and medium grained Redwall limestone (after Clark 1966), Lueders limestone (after Stearns et al. 1981), and Solnhofen limestone (averaged after Jaeger and Cook 1979 and Carmichael 1984). Using the effective confining pressure P_e (≈ 80 MPa) as least principal stress σ_3, the failure strength in the natural Tutt shear zone follows from the dashed Mohr circle.

7.4.5 Stress estimates from flow laws

Various experimentally determined flow laws for calcite materials have already been presented in earlier chapters. These include empirical descriptions of the flow behaviour of polycrystals (refer Table 1.3) as well as fits to microphysically-based creep laws for calcite single crystals (Table 6.1). On the basis of these flow equations, the stresses required for deformation, under the conditions prevailing in the Tutt shear zone, can be calculated. As indicated previously, the temperature during deformation was estimated to be ~200 °C, while a reasonable value for the natural strain rate in a shear zone is $\dot{\varepsilon} = 10^{-11} - 10^{-13}$ (Pfiffner and Ramsay 1983). The

results of the calculations are given in Table 7.3 and Fig. 7.11. Notably, the stresses obtained mostly fall in the range 90-500 MPa, though several of the polycrystal power laws give much higher values.

Now, the results of Table 7.3 are only meaningful with respect to the Tutt material if they concern the natural mechanism of deformation. Since the Tutt mylonite appears to be dominantly deformed by dislocation mechanisms, flow laws describing grain boundary controlled deformation are inappropriate for stress estimation. In the present set of calcite flow equations this excludes the relation given for the mechanical behaviour of Solnhofen limestone in its regime 3, i.e. the ('superplastic') grain boundary sliding regime (GBS, see section 1.4). In the view of the present author (see also Walker et al. 1990), insufficient data exist on the grain size dependence of creep rate in the GBS field to meaningfully compute whether or not this mechanism may have played a role in the Tutt mylonite.

paleostress σ (MPa) at strain rate $\dot{\varepsilon}$:

material	$\dot{\varepsilon}=10^{-11}$	$\dot{\varepsilon}=10^{-13}$ sec^{-1}		
single crystals	710	476	power law	Table 6.1
	190	155	cross slip eq.	this study
	100	91	obstacle limited eq.	
	111	96	Peierls limited eq.	
Yule marble	402	231	power law, I-orientation	Table 1.3
	208	166	expon. law, I-orientation	after Heard and
	544	299	power law, T-orientation	Raleigh 1972
	267	203	expon. law, T-orientation	
Carrara marble	313	260	expon. law, regime 1	Table 1.3
	17697	9653	power law, regime 2	after Schmid
	5×10^6	2×10^6	power law, regime 3	et al. 1980
Solnhofen lmst.	401	327	expon. law, regime 1	Table 1.3
	8678	3257	power law, regime 2	after Schmid
	70000	4640	power law, regime 3	et al. 1977

Table 7.3
Flow stresses calculated at T=200 °C on the basis of experimentally determined flow laws for a number of calcite materials. (Refer Tables 6.1 resp. 1.3 for details).
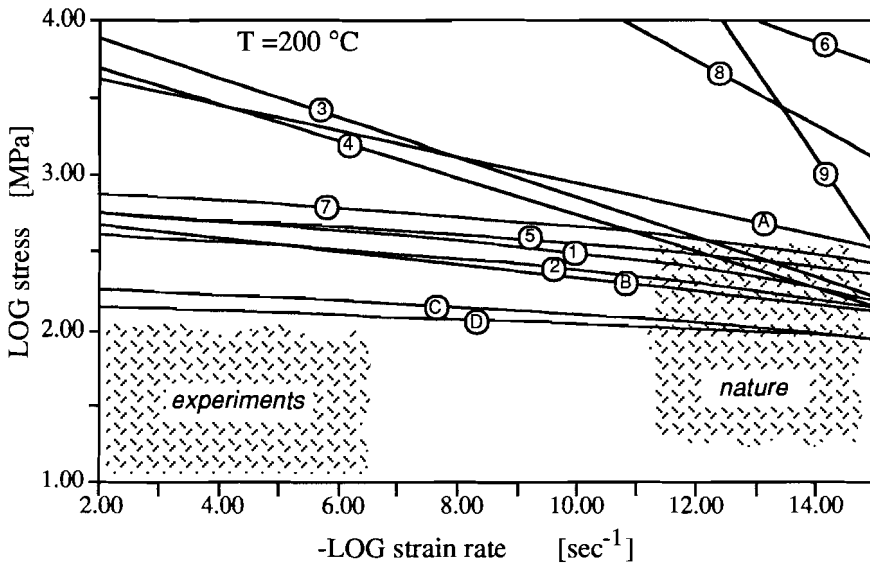
Figure 7.11
Log-log plot of strain rate vs. flow stress showing 200 °C isotherms for various calcite materials. The isotherms are based on experimentally established flow equations, extrapolated to lower temperature and strain rate (i.e. natural conditions). Single crystal flow equations after Table 6.1: A) power law, B) cross slip model, C) Peierls stress limited model, and D) discrete obstacle limited model. Flow equations for polycrystals after Table 1.3. Yule marble: 1) exponential flow regime - T-orientation, 2) exponential flow regime - I-orientation, 3) power law flow regime - T-orientation, and 4) power law flow regime - I-orientation. Carrara marble: 5) flow regime 1, 6) flow regime 2. Solnhofen limestone: 7) flow regime 1, 8) flow regime 2, and 9) flow regime 3.

7.4 DISCUSSION

In Fig 7.12, a summary is given of the stresses estimated for the Tutt shear zone on the basis of the paleopiezometers, the brittle failure envelope and extrapolated flow laws of the various calcite materials. From this figure, it is clear that the paleostresses determined from dislocation density, recrystallized grain size, twinning and failure criteria do not fall in a particularly narrow range. As argued previously however, the dislocation density measured in the Tutt mylonite is a minimum value, hence the derived stresses form lower bounds for the shear zone paleostress. On the other end, the strength at failure (~410 MPa) provides a relatively firm upper bound to the differential stress. This is reasonably consistent with the (upper bound) twinning values of ~500 MPa. The stresses estimated on the basis of recrystallized

grain size fall within the 70-410 Mpa range. However, the extensional failure features may suggest a maximum value of only 200 MPa. Notwithstanding the rather poorly constrained nature of the estimated stress, the range 70-410 MPa is similar to the ranges found for paleostresses in other deformation zones (in carbonates and other rock types, see Fig. 7.12). It is also similar to values calculated from geophysical considerations, though a little higher (e.g. Hanks and Raleigh 1980, Lambeck 1980, Sibson 1982, Etheridge 1983, Carter and Tsenn 1987, Ranalli 1987, Ord and Hobbs 1989). The stress values inferred for the Tutt shear zone thus can be regarded as of reasonable magnitude, particularly if the intensification of stress around the thrust tip is taken into account (Elliot 1976).

The experimentally determined flow laws used here to calulate stresses in the Tutt shear zone can be divided in two types; power laws (eq. 6.5) and otherwise. Stresses calculated from power laws for Yule marble (partly) fall within the range 70-410 MPa established for the Tutt shear zone, but the results obtained by extrapolating power laws for the other calcite materials to the relevant geological conditions, rise above the upper limit set by failure criteria (Fig. 7.12). Thus, currently available power laws for calcite materials seem unable to predict realistic paleostresses for low temperature geological deformation. Since power laws are most commonly associated with diffusion (climb) controlled dislocation creep (e.g. Heard and Raleigh 1972, Schmid et al. 1977, 1980), deformation in the Tutt shear zone appears to have been controlled by other dislocation mechanisms, such as glide or cross slip (refer chapter 6).

In contrast to the above, stresses resulting from extrapolation of experimentally determined *exponential* flow laws for calcite polycrystals fall within the range 70-410 MPa (see Fig. 7.12). Hence, flow laws of exponential type cannot be rejected as suited for estimating flow stresses in low grade deformation zones in limestones. Unfortunately, however, exponential flow equations are not microphysically based. Occassionally, dislocation glide is put forward to explain an exponential dependence of strain rate upon stress (see Tsenn and Carter 1987), but further evaluation of the constraints on the fitting parameters is not commonplace, hence the rate controlling mechanism cannot be substantiated with confidence.

In chapter 6, the mechanical behaviour of calcite *single crystals* was found to be best explained by glide or cross slip controlled creep equations. Extrapolated to T=200 °C and $\dot{\varepsilon}=10^{-11}$-$10^{-13}$ sec^{-1}, these flow equations predict stresses between 90 and 190 MPa (Table 7.3, Fig. 7.12). This is well inside the range 70-410 MPa established for the Tutt shear zone, even if the former stress values are corrected by a factor of ~1.5 to account for the differences in characteristics between single crystals and polycrystals ('Taylor' factor, see section 6.4). In the particular case of the Tutt shear zone, the low temperatures implied that solid state diffusion (i.e. dislocation climb) should not have been of significant importance. This may be supported by the inability of (climb controlled) power law creep equations to predict

stress [MPa]

| 0 | 200 | 400 | 600 | 800 |

I
Dislocation density: Table 7.1 eq. 1
"   Table 7.1 eq. 2
"   Table 7.1 eq. 3
Recrystallized grain size   eq. 7.1
"   eq. 7.2
Twinning It% , eq. 7.4
Twinning V%, eq. 7.5
Failure strength, Fig. 7.10

II
Single crystal power law, Table 6.1
"   , cross slip equation, Table 6.1
"   , obstacle limited eq., Table 6.1
"   , Peierls stress limited eq., Table 6.1

III
Yule marble 1 - regime 1
"   - regime 2
Yule marble T - regime 1
"   - regime 2
Carrara marble - regime 1
"   - regime 2
"   - regime 3
Solnhofen limestone - regime 1
"   - regime 2
"   - regime 3

out of scale
out of scale
out of scale
out of scale

IV
Quartzite Moine thrust   a)
"   b)
"   c)
Granodiorite Massif Central   d)
limestone Helvetic Alps   e)
"   Cantabrian Mountains   f)

Tutt range

◄■ *upper bound*
■► *lower bound*

Figure 7.12
Summary of stresses estimated for the Tutt shear zone on the basis of paleopiezometers and failure criteria (I), and extrapolated flow laws for calcite single crystals (II) and polycrystals (III). Refer section 7.4. Also given are stresses presented in the literature for other, upper crustal deformation zones (IV), after a) Kohlstedt and Weathers (1980), b) Ord and Christie (1984), c) Etheridge and Wilkie (1981), d) Kohlstedt and Weathers (1980), e) Pfiffner (1982) and f) Rowe and Rutter (1990).

realistic flow stress magnitudes for the deformation zone (refer section 6.2.2 and Fig. 7.12). However, observations on grain shape, textures, subgrain- and recrystallisation phenomena indicated that dislocation mechanisms including recovery must have been active in the Tutt mylonite. Referring to the discussion in chapter 6 (section 6.3.3), a cross slip controlled deformation process then is preferred to barrier limited glide. From the above considerations on stress magnitudes, it thus appears that the cross slip controlled creep equation (Table 6.1), with constraints on its fitting parameters set by single crystal experiments, can be used (neglecting hardening by grain boundaries) to infer a minimum value for the flow stress in natural, low temperature (upper crustal) shear zones.

In addition to the above, in chapter 6 (section 6.4.6), a cross slip creep equation was presented which takes into account the observed grain size dependence of the dislocation density (refer section 5.4.2). It was inferred that, for cross slip controlled creep at relatively low flow stresses, fine grained calcite material is stronger than coarse grained or single crystal calcite. Unfortunately, the values obtained for the various fitting parameters of the grain size dependent cross slip equation (eq. 6.32) are not well enough constrained to allow calculation of an accurate flow stress at conditions having prevailed in the Tutt mylonite. However, some idea about the order of magnitude can be obtained from the grain size term in the cross slip equation, $U \cdot \sigma^2 + V \cdot \sigma \cdot D^{-0.5} + W \cdot D^{-1}$, where U, V and W are constants (see eq. 6.32). From considerations discussed in section 6.4.6, values for U, V and W (upper bound) can be calculated, respectively 1.5×10^5, 9×10^5 and -6.1×10^6. With an average grain size of, for example, 20 μm (cf. range 1-100 μm, section 7.4.2) flow stress of *at least* 150 MPa is required to yield a positive value for the above term, hence a realistic strain rate. Considering only the recrystallized grains (D=1.3 μm), the stress must be as high as 350 MPa. Although very rough estimates, these values are consistent with the stress values obtained above using other methods.

7.6 SUMMARY/CONCLUSIONS

Deformed limestones from a small scale shear zone in South Wales, U.K. (PT conditions ~130 MPa resp. 200 °C), have been studied by light-optical and electron microscopy. The limestones show a) strongly flattened/strained calcite grains with numerous twins and subgrains, b) widespread development of recrystallised grains of roughly equidimensional shape but packed with dislocations (i.e. heavily strained), and c) a weak but distinct crystallographic preferred orientation. These observations were interpreted as indicating significant deformation by intracrystalline dislocation mechanisms, with contemporaneous dynamic recrystallization by progressive rotation of subgrains. Using densities of dislocations, recrystallized grain size, twinning

activity and failure criteria, a paleostress within the range 70-410 MPa was inferred to be linked with the development of the shear zone. Although rather wide, this estimated range of stresses was found to be of realistic magnitude in comparison with stress values obtained for other upper crustal deformation zones.

The stresses were also compared with values computed by extrapolating various experimentally determined flow equations to the relevant geological conditions (T=200 °C, $\dot{\varepsilon}=10^{-11}-10^{-13}$ sec^{-1}). It was found that power laws ($\dot{\varepsilon} \propto \sigma^n$) are unsuccesful in reliably predicting paleostresses in deformed calcite rocks at the given conditions. On the other hand, creep equations of exponential type ($\dot{\varepsilon} \propto \exp[\sigma]$) yield magnitudes of stress in good agreement with those resulting from microstructural parameters and failure considerations. However, they generally lack a microphysical base. From the current results on behaviour of calcite single crystals, a cross slip controlled creep equation seems the most likely alternative for the power and exponential laws. Such a creep law is attractive since a) the theoretical basis justifies extrapolation outside the experimental range, and b) cross slip is a potential recovery mechanism at relatively low temperature, thus allowing steady state deformation in upper crustal deformation zones. Flow stresses predicted on the basis of the cross slip creep equation are found to be in good agreement with magnitudes determined from microstructural parameters, even when the strenthening effect of reduced grain size is taken into account. It is concluded that the constitutive creep law describing dislocation cross slip controlled flow in calcite single crystals may offer a method of estimating minimum differential stresses in limestones deforming at relatively low temperature.

APPENDIX: SUGGESTIONS FOR FUTURE RESEARCH

The ressearch documented in this thesis can be grouped under four main headings:

1) new data on the calcite glide systems,

2) quantification of the stress dependence of dislocation density in calcite single crystals,

3) identification of the rate controlling mechanism for deformation of single crystals at intermediate to high temperatures, and

4) applicability of the experimental results obtained for single crystals to natural calcite tectonites.

These are briefly discussed below, indicating scope for future research.

[1] New data on the calcite glide systems.

In the present study, important new systems were identified (i.e. $f<10\bar{1}1>^{\pm}$), and the strengths of new as well as of previously known glide systems ($r<\bar{2}021>^{\pm}$, $c<a>$) were determined as a function of temperature and strain rate. Now, the relatively easy $f<10\bar{1}1>^{\pm}$ and $c<a>$ systems have not previously been taken into account in texture modelling (Taylor-Bishop-Hill modelling of Lister 1978, Wenk et al. 1986, Takeshita et al. 1987). Furthermore, the symmetrical strengths of the $r<\bar{2}021>^{+}$ and $r<\bar{2}021>^{-}$ systems found in the present study differ from the asymmetric values used in recent texture simulation work (e.g Wenk et al. 1987). Therefore, previous simulations must be regarded with caution and it is recommmended to perform new modelling work on texture development in calcite rocks. Notably, for the high temperature situation where, in the present tests, $f<10\bar{1}1>^{\pm}$ and $c<a>$ slip dominated, such modelling might yield better agreement between predicted textures and natural textures than currently established. In addition, further systematic study (slip lines, TEM) of calcite single crystals compressed in various orientations to various strains would be useful in elucidating slip system interactions and the effects of mutual strain hardening on relative strengths. Such information would aid in the comparison of calculated and measured textures (natural or experimental) and would facilitate highly sophisticated texture modelling. Additional tests in the [22$\bar{4}$3] orientation would be of particular value in this, since, at T>600 °C, crystals deformed parallel to [22$\bar{4}$3] show clearly identifiable multistage stress-strain behaviour, with all three important glide systems in calcite (r, f and c) being activated.

[2] The relation between stress and dislocation density

The experimentally determined relationship between flow stress and dislocation density for single crystals was found to be in good agreement with existing theory. However, data on calcite polycrystals deviate from it. Based on theory of non-

homogeneous deformation (after Ashby 1970), a simple model was presented explaining this effect in terms of the influence of grain size. This model needs to be refined taking the effects of the relative densities of geometrically necessary and statistically stored dislocations into full account. The resulting theory would form a firm basis for a 'paleopiezometer' relating flow stress to dislocation density and grain size, valid for any plastically deformable material. The same relationship would also provide a means of building the effect of grain size into theoretical models for dislocation creep. With regard to paleopiezometry in calcite rocks, it is suggested to perform compression experiments on calcite polycrystals of various but controlled grain sizes in order to experimentally test and calibrate the proposed model. In this respect, *synthethic* calcite rocks of different controlled grain sizes, prepared from crushed calcite single crystals (eg. Walker et al. 1990), would appear to be suitable materials.

[3] Identification of the rate controlling process.

Crystals compressed parallel to $[40\overline{4}1]$ were found to deform in near-steady state at T≥550 °C. Comparing the mechanical data with microstructural observations and microphysical models for creep, the deformation rate was inferred to be controlled by a dislocation cross slip process associated with dislocation network recovery. The behaviour and microstructures of experimentally deformed calcite polycrystals show various similarities with the single crystals, and might well be explained by the same rate controlling mechanism. Future research related to this is suggested to primarily concentrate on the following:

a) Additional TEM study of dislocations in single crystals deformed in the $[40\overline{4}1]$ orientation. These are needed to critically test the proposed rate controlling mechanism. In samples with a low dislocation density (i.e. deformed at relatively high temperatures, T=700-800 °C), an extensive and detailed characterization of the geometry and orientation distribution of the dislocation configuration should reveal various stages ('snapshots') of the recovery process, notably the formation and destruction of dislocation networks and the possible role of cross slip therein.

b) Additional compression experiments in the $[40\overline{4}1]$ orientation at a range of strain rates, at temperatures higher than imposed in the present study (i.e. T>800 °C). Such experiments might uncover a transition from the currently observed flow 'regime', probably controlled by cross slip, to a climb-controlled regime in which flow stresses are more sensitive to the strain rate. Note that for experiments at temperatures above 800 °C the presently used confining pressure of 0.25 MPa is not sufficient to suppress decomposition of calcite.

c) Independent determination of activation quantities. The apparent activation energy and activation area presented for the cross slip controlled creep of single crystals were obtained by fitting the mechanical data to the constriction-controlled creep equation. No independent check of the values of these parameters is presently

available, but might be obtained by means of sophisticated stress-relaxation or temperature change experiments using the [40$\bar{4}$1] orientation (e.g. Poirier 1985).

d) In order to confirm whether or not the proposed cross slip/network recovery mechanism controls creep in polycrystalline calcite rocks as well as single crystals, new experiments on polycrystals are needed. These need to be more systematic than previous work, using well controlled synthethic material and independently varying temperature, strain rate and grain size from test to test. The results should be compared with the cross slip and other models used in the present work, building in the effect of grain size if possible (see point 2 above). The final results should be compared with previous experimental data for calcite rocks to form an integrated picture of creep behaviour.

[4] Natural calcite tectonites.

The experimental results obtained for the single crystals as well as results on polycrystals published previously were used to set constraints on the flow stresses having prevailed in a natural calcite tectonite (the Tutt shear zone). The particular shear zone was chosen since maximum temperatures attained during its development were such that deformation was not likely to be controlled by dislocation climb. However, the inhomogeneous and very fine grained nature of the deformed limestone complicated microstructural study, both on optical and on TEM scale. Flow stresses thus were less constrained than desired. Therefore, it is suggested to perform a comparable study on somewhat coarser grained calcite rock. Deformed marbles of low to medium metamorphic grade of the island of Naxos (e.g. Urai et al. 1990) appear suitable for this.

Finally, one last aspect of intracrystalline deformation of calcite not mentioned under the above headings (since not focussed upon in the present study) needs further investigation, namely the observed correlation between increasing impurity content and decreasing flow strength in calcite single crystals compressed parallel to [40$\bar{4}$1]. In order to better understand deformation behaviour of calcite rocks in metamorphic terrains, where fluid circulation, and hence compositional changes are common, a systematic and more detailed study of this effect is required. Chemical analysis of calcite mylonites and their host rocks, and deformation experiments on single crystals of various compositions are proposed as possible routes to obtaining such information. The basic mechanism of the 'solid solution softening' is also of fundamental interest.

180

REFERENCES

Alexander, H. & Haasen, P. 1968. Dislocations and plastic flow in the diamond structure. Solid State Physics Vol. 22, 28-158

Anderson, T.F. 1969. Self-diffusion of carbon and oxygen in calcite by isotope exchange with carbon dioxide. Journal of Geophysical Research 74, 3918-393

Anderson, J.G.C. & Owen, T.R. 1980. The structure of the British Isles (sec. edition). Pergamon Press LTD., pp 251

Argon, A.S. 1966. Plastic deformation in crystalline materials. In: McClintock, F.A. & Argon, A.S. (eds) Mechanical behavior of materials. Addison-Wesley Publ. Company, 152-211

Arsenault, R.J. 1975. Low temperature of deformation of bcc metals and their solid-solution alloys. In: Arsenault, R.J. (ed) Treatise on materials science and technology (Volume 6); Plastic deformation of materials, Academic Press, 1-99

Ashby, M.F. 1970. The deformation of plastically non-homogeneous materials. Philosophical Magazine 21, 399-42

Ashby, M.F. 1971. The deformation of plastically non-homogeneous alloys. In: Kelly, A. & Nicholson, R.B. (eds) Strenghtening methods in crystals. Applied Science Publishers Ltd. London, 137-192

Ashby, M.F. & Verrall, R.A. 1978. Micromechanisms of flow and fracture, and their relevance to the rheology of the upper mantle. Philosophical Transactions of the Royal Society of London (A) 288, 59-95

Barber, D.J. & Wenk, H.-R. 1973. The microstructure of experimentally deformed limestone. Journal of Materials Science 8, 500-508

Barber, D.J. & Wenk, H.-R. 1976. Defects in deformed calcite and carbonate rocks. In: Wenk, H.-R. (ed.) Electron microscopy in mineralogy. Springer Verlag, 428-442

Barber, D.J. & Wenk, H.-R. 1979a. On geological aspects of calcite microstructure. Tectonophysics 54, 45-60

Barber, D.J. & Wenk, H.-R. 1979b. Deformation twinning in calcite, dolomite, and other rhombohedral carbonates. Physics and Chemistry of Minerals 5, 141-165

Baumhauer, H. 1879. Über künstliche Kalkspath-Zwillinge nach $1/2$R. Zeitschrift fur Kristallografie 3, 588-591

Beeman, M.L. & Kohlstedt, D.L. 1988. Dislocation density: stress relationships in natural and synthetic sodium chloride. Tectonophysics 149, 147-161

Behrmann, J.H. 1983. Microstructure and fabric transitions in calcite tectonites from the Sierra Alhamilla (Spain). Geologische Rundschau 72, 605-618

Bishop, J.F.W. & Hill, R. 1951a. A theory of plastic distortion of a polycrystalline aggregate under combined stresses. Philosophical Magazine 42, 414-427

Bishop, J.F.W. & Hill, R. 1951b. A theoretical derivation of the plastic properties of a polycrystalline face-centered metal. Philosophical Magazine 42, 1298-1307

Borg, I. & Handin, J. 1967. Torsion of calcite single crystals. Journal of Geophysical Research 72, 641-669

Braillon, P., Kubin, L. & Serughetti, J. 1978. Plastic deformation of calcite single crystals deformed in compression parallel to [111]. Physica Status Solidi (a) 45, 453-462

Braillon, P., Mugnier, J. & Serughetti, J. 1972. Deformation plastique de mono-cristaux de calcite, en compression suivant [111]. Comptes rendus de l'Academie des Sciences, Paris (B), t.275, 605-608

Braillon, P., Mugnier, J. & Serughetti, J. 1974. Transmission electron microscope observations of the dislocations in calcite single crystals. Crystal Lattice Defects 5, 73-78

Braillon, P. & Serughetti, J. 1976a. Mechanical twinning in calcite - observation of twinning dislocations and planar defects by Transmission electron microscopy. Physica Status Solidi (a) 33, 405-413

Braillon, P. & Serughetti, J. 1976b. Déformation plastique de monocristaux de calcite en compression suivant <001>. Physica Status Solidi (a) 36, 637-646

Briegel, U. & Goetze C. 1978. Estimates of differential stress recorded in the dislocation structure of Lochseiten limestone (Switzerland). Tectonophysics 48, 61-76

Brion, H.G. & Haasen, P. 1985. Screw dislocation networks generated in Ge and Si by stage IV compression. Philosophical Magazine A 51, 679-891

Brion, H.G., Siethoff, H. and Schröter, W. 1981. New stages in stress-strain curves of germanium at high temperatures. Philosophical Magazine A 43, 1505-1513

Burton, B. 1982. The dislocation network theory of creep. Philosophical Magazine A 45, 657-675

Caillard, D. & Martin, J.L. 1982a. Microstructure of aluminium during creep at intermediate temperature - I. Dislocation networks after creep. Acta Metallurgica 30, 437-445

Caillard, D. & Martin, J.L. 1982b. Microstructure of aluminium during creep at intermediate temperature - II. In Situ study of subboundary propperties. Acta Metallurgica 30, 791-798

Caillard, D. & Martin, J.L. 1983. Microstructure of aluminium during creep at intermediate temperature - III. The rate controlling process. Acta Metallurgica 31, 813-825

Calnan, E.A. & Clews, C.J.B. 1950. Deformation textures of face-centered cubic metals. Philosophical Magazine 41, 1085-1100

Cannon, W.R. & Langdon T.G. 1988. Review: Creep of ceramics, Part 2. An examination of flow mechanisms. Journal of Materials Science 23, 1-20

Carmichael, R.S. (ed.) 1984. Handbook of physical properties of rocks. CRC Press Inc.

Carter, N.L. & Tsenn, M.C. 1987. Flow properties of continental lithosphere. Tectonophysics 136 (1987) 27-63

Casey, M, Rutter, E.H., Schmid, S.M., Siddans, A.W.B. & Whalley, J.S. 1978. Texture development in experimentally deformed calcite rocks. Proceedings 5th International Conference on textures of materials, Aachen. Springer (Berlin), 231-240

Chopra, P.N., Olgaard, D.L. & Paterson, M.S. 1988. High temperature flow of Carrara marble: revisited. EOS 69, 1417

Christian, J.W. 1971. The strength of martensite. In: Kelly, A. & Nicholson, R.B. (eds) Strengthening methods in crystals, Applied Science Publishers Ltd. London, 261-329

Christie, J.M. & Ardell, A.J. 1976. Deformation structures in minerals. In: Wenk, H.-R. (ed.) Electron Microscopy in mineralogy, Springer Verlag, 374-403

Clark, S.P. (ed.) 1966. Handbook of physical constants (revised edition). Geological Society of America Memoir 97

Cox, S.F. 1986. High temperature creep of single crystal galena (PbS). A.G.U. Geophysical Monograph 36, 73-98

Dandekar, D.P. 1968. Variation in the elastic constants of calcite with temperature. Journal of Applied Physics 39, 3694-3699

Davidge, R.W. & Pratt, P.L. 1964. Plastic deformation and work-hardening in NaCl. Physica Status Solidi 6, 759-776

De Bresser, J.H.P. 1988. Deformation of calcite crystals by r^+ and f^+ slip: mechanical behaviour and dislocation density vs. stress relation. EOS 69, 1418

De Bresser, J.H.P. 1989. Calcite c-axis textures along the Gavarnie thrust zone, central Pyrenees. Geologie en Mijnbouw 68, 367-375

De Bresser, J.H.P. & Spiers, C.J. 1990. High temperature deformation of calcite single crystals by r^+ and f^+ slip. In: Knipe, R.J. and Rutter, E.H. (eds) Deformation mechanisms, rheology and tectonics. Geological Society of London Special Publication No. 54, 285-298

Deer, W.A., Howie, R.A. & Zussman, J. 1962. Rock-Forming minerals - Vol. 5, non-silicates. Longmans, Green and co Ltd.: pp 301

Dietrich, D. 1986. Calcite fabrics around folds as indicators of deformation history. Journal of Structural Geology 8, 655-668

Dietrich, D. & Song, H. 1984. Calcite fabrics in a natural shear environment, the Helvetic nappes of western Switzerland. Journal of Structural Geology 6, 19-32

Dunne, W.M. 1983. Tectonic evolution of SW Wales during the Upper Paleozoic. Journal of the Geological Society of London 140, 257-265

Durham, W.B., Goetze, C. & Blake, B. 1977. Plastic flow of oriented single crystals of olivine: 2. Observations and interpretations of the dislocation structures. Journal of Geophysical Research 82, 5755-5770

Edington, J.W. 1975. Interpretation of transmission electron micrographs - Practical electron microscopy in materials science monograph 3, Macmillan Press Ltd: pp 112

Edward, G.H., Etheridge, M.A. & Hobbs, B.E. 1982. On the stress dependence of subgrain size. Textures and Microstructures 5, 127-152

Elliot, D. 1976. The motion of thrust sheets. Journal of Geophysical Research 81, 949-963

Escaig, B. 1968. Sur le glissement dévié des dislocations dans la structure cubique à faces centrées. Journal de Physique 29, 225-239

Escaig, B. & Bonneville, J. 1980. A new technique to study cross-slip in FCC crystals. In: Haasen, P., Gerold, V. & Kostorz, G. (eds.) 1980. Strength of metals and alloys. Proceedings 5th International Conference, Aachen (1979). Pergamon Press, 3-8

Etheridge, M.A. 1983. Differential stress magnitudes during regional deformation and metamorphism: Upper bound imposed by tensile fracturing. Geology 11, 231-234

Etheridge, M.A. & Wilkie, J.C. 1981. An assessment of dynamically recrystallized grainsize as a palaeopiezometer in quartzbearing mylonite zones. Tectonophysics 78, 475-508

Fredrich, J.T., Evans, B. & Wong, T.F. 1989. Micromechanics of the brittle to plastid transition in Carrara marble. Journal of Geophysical Research (B) 94, 4129-4145

Friedel, J. 1977. Sur le fluage par déviation. Revue de Physique Appliquée 12, 1649-1654

Frost, H.J. & Ashby, M.F. 1982. Deformation-mechanism maps, the plasticity and creep of metals and ceramics. Pergamon Press

Gill, W.D., F.I. Khalaf & Massoud, M.S. 1977. Clay minerals as an index of the degree of metamorphism of the carbonate and terrigenous rocks in the South Wales coalfield. Sedimentology 24, 675-691

Gill, W.D., F.I. Khalaf & Massoud, M.S. 1979. Organic matter as indicator of the degree of metamorphism of the Carboniferous rocks in the South Wales coalfields. Journal of Petroleum Geology 1, 4, 39-62

Goetze, C. & Kohlstedt, D.L. 1977. The dislocation structure of experimentally deformed marble. Contributions to Mineralogy and Petrology 59, 293-306

Griggs, D.T. & Miller, W.B. 1951. Deformation of Yule marble: Part 1. Compression an extension experiments on dry Yule marble at 10,000 atmospheres confining pressure, room temperature. Geological Society of America Bulletin 62, 843-862

Griggs, D.T., Turner, F.J., Borg, I. & Sosoka, J. 1951. Deformation of Yule marble: Part IV. Effects at 150 °C, Geological Society of America Bulletin 62, 1385-1406

Griggs, D.T., Turner, F.J., Borg, I. & Sosoka, J. 1953. Deformation of Yule marble: Part V. Effects at 300 °C, Geological Society of America Bulletin 64, 1327-1352

Griggs, D.T., Turner, F.J. & Heard, H.C. 1960. Deformation of rocks at 500 to 800 °C. Geological Society of America Memoir 79, 39-105

Guyot, P. & Dorn, J.E. 1967. A critical review of the Peierls mechanism. Canadien Journal of Physics 45, 983-1016

Haasen, P. 1983. Mechanical properties of solid solutions and intermetallic compounds. In: Cahn, R.W. & Haasen, P. (eds) Physical metallurgy; third, revised and enlarged edition, North Holland Physics Publishing, 1341-1403

Haasen, P. 1985. Dislocations and the plasticity of ionic crystals. In: Dislocations and properties of real materials. The Institute of Metals, London, 312-332

Haasen, P., Gerold, V. & Kostorz, G. (eds.) 1980. Strength of metals and alloys. Proceedings 5th International Conference, Aachen (1979). Pergamon Press, pp 1594

Haasen, P., Messerschmidt, U. & Skrotzki, W. 1986. Low energy dislocation structures in ionic crystals and semiconductors. Materials Science and Engineering 81, 493-507

Hancock P.L., Dunne, W.M. & Tringham, M.E. 1983. Variscan deformation in Southwest Wales. In: Hancock, P.L. (ed.) The Variscan fold belt in the British Isles. Adam Hilger LTD. Bristol, 47-63

Handy, M.R. 1989. Deformation regimes and the rheological evolution of fault zones in the lithosphere: the effect of pressure, temperature, grainsize and time. Tectonophysics 163, 119-152

Hanks, T.C. & Raleigh, C.B. 1980. The conference on magnitude of deviatoric stresses in the earth's crust and uppermost mantle. Journal of Geophysical Research (B) 85, 6083-6085

Head, A.K., Humble, P., Clarebrough, L.M., Morton, A.J. & Forwood, C.T. 1973. Computed electron micrographs and defect identification. North Holland Publishing Company, pp 400

Heard, H.C. 1963. Effect of large changes in strain rate in the experimental deformation of Yule marble. Journal of Geology 71, 162-195

Heard, H.C. & Raleigh, C.B. 1972. Steady-state flow in marble at 500 to 800 °C. Geological Society of America Bulletin 83, 935-956

Heard, H.C. & Ryerson, F.J. 1986. Effect of cation impurities on steady-state flow of salt. A.G.U. Geophysical Monograph 36, 99-115

Heinisch, H.L., Sines, G. & Goodman, J.W. 1975. Elastic stresses and self-energies of dislocations of arbitrary orientation in anisotropic media: olivine, orthopyroxene, calcite and quartz. Journal of Geophysical Research 80, 1885-1896

Heitzmann P. 1987. Calcite mylonites in the central Alpine 'root zone'. Tectonophysics 135, 207-215

Hirsch, P.B., Howie, A., Nicholson, R.B. and Pashley, D.W. 1965. Electron microscopy of thin crystals. Butterworths London

Hirth, J.P. 1972. The influence of grain boundaries on mechanical properties. Metallurgical Transactions 3, 3047-3067

Hirth, J.P. 1983. Dislocations. In: Cahn, R.W. & Haasen P. (eds) Physical metallurgy; third, revised and enlarged edition. North Holland Physics Publishing, 1223-1258

Hirth, J.P. & Lothe, J. 1968. Theory of dislocations, McGraw-Hill NY

Hoek, E. & Brown, E.T. 1980. Underground excavations in rock. The Institution of Mining and Metallurgy, London.

Honeycombe, R.W.K. 1968. The plastic deformation of metals. Edward Arnold Publishers LTD., pp 477

Hornbogen, E. 1983. Physical metallurgy of steels. In: Cahn, R.W. & Haasen P. (eds) Physical metallurgy; third, revised and enlarged edition. North Holland Physics Publishing, 1223-1258

Hull, D. & Bacon, D.J. 1983 Introduction to dislocations (3rd edition). International series on materials science and technology, Vol. 37. Pergamon Press, pp 257

Hyett, A.J. 1990. Deformation around a thrust tip in Carboniferous limestone at Tutt head, near Swansea, South Wales. Journal of Structural Geology 12, 47-58

Jaeger, J.C. & Cook, N.G.W., 1979. Fundamentals of rock mechanics. Chapman and Hall, London

Jamison, W.R. & Spang, J.H. 1976. Use of calcite twin lamellae to infer differential stress. Geological Society of America Bulletin 87, 868-872

Keith, R.E. & Gilman, J.J. 1960. Dislocation etch pits and plastic deformation in calcite. Acta Metallurgica 8, 1-10

Kern, H. & Wenk, H.-R. 1983. Calcite texture development in experimentally induced ductile shear zones. Contributions to Mineralogy and Petrology 83, 231-236

Kisch, H.J. 1987. Correlation between indicators of very low-grade metamorphism. In: Frey, M. (ed.) Low temperature metamorphism. Blackie & Son, Glasgow, 227-300

Kohlstedt, D.L. & Goetze, C. 1974. Low-stress high-temperature creep in olivine single crystals. Journal of Geophysical Research 79, 2045-2051

Kohlstedt, D.L. & Weathers, M.S. 1980. Deformation-induced microstructures, paleopiezometers, and differential stresses in deeply eroded fault zones. Journal of Geophysical Research (B) 85, 6269-6285

Lagneborg, R. 1979. Creep deformation mechanisms. In: Bernasconi, G. & Piatti, G. (eds) Creep of engineering materials and structures. Applied Science Publishers London, 7-34

Lambeck K. 1980. Estimates of stress differences in the crust from isostatic considerations. Journal of Geophysical Research (B) 85, 6397-6402

Langdon, T.G. 1985. Regimes of plastic deformation. In: Wenk, H.-R. (ed) Preferred orientation in deformed metals and rocks, an introduction to modern texture analysis, Academic Press, 219-232

Lavrentev, F.F., Salita, O.P. & Shutyaev, P.D. 1980. Basal dislocation density dependence of the deforming stress in Zn crystals in the temperature range from 1.5 to 300 K. In: Haasen, P., Gerold, V. & Kostorz, G. (eds) Strength of metals and alloys - Proceedings 5th International Conference, Aachen 1979. Pergamon press, 157-162

Lister, G.S. 1978. Texture transitions in plastically deformed calcite rocks. Proceedings 5th International Conference on textures of materials, Aachen. Springer (Berlin), 199-210

Marquardt, D.W. 1963. An algorithm for least squares estimation of non-linear parameters. Journal of the Society of Industrial and Applied Mathematics 11, 431-441

Mayer, M., Vöhringer, D. & Macherauch, E. 1980. The grain size dependence of mobile dislocation density in copper alloys at the onset of the Portevin-le Chatelier effect. In: Haasen, P., Gerold, V. & Kostorz, G. (eds) Strength of metals and alloys - Proceedings 5th International Conference, Aachen 1979. Pergamon press, 807-812

McCormick, J.W. 1977. Transmission electron microscopy study of experimentally deformed synthetic quartz. Ph.D. thesis, University of California, Los Angeles, pp 171

McKie, D. & McKie, C. 1986. Essentials of Crystallography, Blackwell Scientific Publications: pp 437

McLaren, A.C., Cook, R.F., Hyde, S.T. & Tobin, R.C. 1983. The mechanisms of the formation and growth of water bubbles and associated dislocation loops in synthetic quartz. Physics and Chemistry of Minerals 9, 79-94

McLaren, A.C., Fitz Gerald, J.D. & Gerretsen, J. 1989. Dislocation nucleation and multiplication in synthetic quartz: relevance to water weakening. Physics and Chemistry of Minerals 16, 465-482

Möller, H.-J., Ewaldt, H. & Haasen, P. 1979. Cross slip of single dissociated screw dislocations in silicon and germanium. Physica Status Solidi (a) 55, 469-478

Morrison-Smith, D.J., Paterson, M.S. & Hobbs, B.E. 1976. An electron microscope study of plastic deformation in single crystals of synthetic quartz. Tectonophysics 33, 43-79

Motohashi, Y., Braillon, P. & Serughetti, J. 1976. Elastic energy, stress field of dislocations, and dislocation parameters in calcite crystals. Physica Status Solidi (a) 37, 263-270

Myshlyaev, M.M. 1976. Creep and dislocation structure of crystals at moderate temperature. Conference Proceedings 4th International Conference on the strength of metals and alloys, 1037-1091

Myshlyaev, M.M. & Khodos, I.I. 1980. High-temperature creep and dislocation structure of BCC single crystals. In: Haasen, P., Gerold, V. & Kostorz, G. (eds.) 1980. Strength of metals and alloys. Proceedings 5th International Conference, Aachen (1979). Pergamon Press, 3-8

Nabarro, F.R.N. 1985. Solution hardening. In: Dislocations and properties of real materials. The Institute of metals, London, 152-169

Nicolas, A. & Poirier, J.P. 1976. Crystalline plasticity and solid state flow in metamorphic rocks. Wiley London, pp 444

Nix, W.D., Gibeling, J.C. & Fuchs, K.P. 1982. The role of long-range internal back stresses in creep of metals. In: Rohde, R.W. & Swearengen, J.C. (eds) Mechanical testing for deformation model development. American Society for Testing and Materials (STP 765), 301-321

Nye, J.F. 1976. Physical properties of crystals. Oxford University Press, pp 322

Olgaard, D.L. 1985. Grain growth and mechanical processes in two-phased synthetic marbles and natural fault gauges. Ph.D. thesis, M.I.T. Cambridge, Massachusetts, pp 204

Ord, A. & Christie, J.M. 1984. Flow stresses from microstructures in mylonite quartzites of the Moine thrust zone, Assynt area, Scotland. Journal of Structural Geology 6, 639-654

Ord, A. & Hobbs, B.E. 1989. The strength of the continental crust, detachment zones and the development of plastic instabilities. Tectonophysics 158, 269-289

Orowan, E. 1940. Problems of plastic gliding. Proceedings of the Physical Society 52, 8-22

Owen, T.R. 1973. Geology explained in South Wales. David & Charles LTD., pp 211

Owen, T.R. & Weaver, J.D. 1983. The structure of the main South Wales coalfield and its margins. In: Hancock, P.L. (ed.) The Variscan fold belt in the British Isles. Adam Hilger LTD. Bristol, 47-63

Parker, A., Allen, J.R.L. & Williams, B.P.J. 1983. Clay mineral assemblages of the Townsend Tuff Bed (Lower Old Red Sandstone), South Wales and the Welsh borders. Journal of the Geological Society of London 140, 769-779

Paterson, M.S. 1979. Deformation mechanisms in carbonate crystals. In: Borland, D.W., Clarebrough, L.M. & Moore, A.J.W. (eds), Physics of materials (A festschrift for Dr. Walter Boas). CSIRO and University of Melbourne, 199-208

Paterson, M.S. 1985. Dislocations and geological deformation. In: Dislocations and Properties of Real Materials. The Institute of Metals, London, 359-377

Paterson, M.S. 1987. Problems in the extrapolation of laboratory rheological data. Tectonophysics 133, 33-43

Paterson, M.S. & Turner, F.J. 1970. Experimental deformation of constrained crystals of calcite in extension. In: Paulitsch, P. (ed.) Experimental and natural rock deformation. Proceedings International Symposium, Darmstadt febr. 1969, Springer Verlag, 109-141

Pfiffner, O.A. 1982. Deformation mechanisms and flow regimes in limestones from the Helvetic zone of the Swiss Alps. Journal of Structural Geology 4, 429-442

Pfiffner, O.A. & Ramsay, J.G. 1982. Constraints on geological strain rates: arguments from finite strain states of naturally deformed rocks. Journal of Geophysical Research (B) 87, 311-321

Phillips, F.C. 1962. An introduction to crystallography. Longmans, Green and co Ltd.: pp 340

Poirier, J.P. 1978. Is power-law creep diffusion-controlled? Acta Metallurgica 26, 629-637

Poirier, J.P. 1976. On the symmetrical role of cross-slip of screw dislocations and climb of edge dislocations as recovery processes controlling high-temperature creep. Revue de Physique Appliquee 11, 731-738

Poirier, J.P. 1985. Creep of crystals. Cambridge University press, pp 260

Ranalli, G. 1987. Rheology of the earth. Allen & Unwin, Boston. pp 366

Reed-Hill, R.E. 1973. Physical Metallurgy Principles. D. van Nostrand Company, pp 920

Reed-Hill, R.E., Hirth, J.P. & Rogers, H.C. (eds.) 1964. Deformation twinning. Gordon and Breach, New York

Rowe, K.J. & Rutter, E.H. 1990. Paleostress measurement using calcite twinning: experimental calibration and application to nature. Journal of Structural Geology 12: 1-17

Rutter, E.H. 1974. The influence of temperature, strain rate and interstitial water in the experimental deformation of calcite rocks. Tectonophysics 22, 311-334

Rutter, E.H., Atkinson, B.K. & Mainprice, D.H. 1978. On the use of the stress relaxation testing method in studies of the mechanical behaviour of geological materials. Geophysical Journal of the Royal Astronomic Society 55, 155-170

Schmid, S.M. 1976. Rheological evidence for changes in the deformation mechanism of Solnhofen limestone towards low stresses. Tectonophysics 31, T21-T28

Schmid, S.M. 1982. Laboratory experiments on rheology and deformation mechanisms in calcite rocks and their application to studies in the field. Mitteilungen aus dem Geologischen Institut der ETH und der Universitat Zürich 241, 1-62

Schmid, S.M., Boland, J.N. & Paterson, M.S. 1977. Superplastic flow in finegrained limestone. Tectonophysics 43, 257-291

Schmid, S.M., Casey, M. & Starkey, J. 1981. The microfabric of calcite tectonites from the Helvetic Nappes (Swiss Alps). Geological Society of London Special Publication 9, 151-158

Schmid, S.M., Panozzo, R. & Bauer, S. 1987. Simple shear experiments on calcite rocks: rheology and microfabric. Journal of Structural Geology 9, 747-778

Schmid, S.M. & Paterson, M.S. 1977. Strain analysis in an experimentally deformed oolitic limestone. In: Saxena, K. & Battachanji, S. (eds) Energetics of geological processes. Springer N.Y.: 67-93

Schmid, S.M., Paterson, M.S. & Boland, J.N. 1980. High temperature flow and dynamic recrystallization in Carrara marble. Tectonophysics 65, 245-280

Schoeck, G. 1962. Correlation between dislocation length and density. Journal of Applied Physics 33, 1745-1747

Schoeck, G. & Seeger, A. 1955. Defects in Crystalline solids. The Physical Society, London, pp 340

Schröter, W. & Siethoff, H. 1984. New phenomena in the plasticity of semiconductors and FCC metals at high temperatures - part II: Analysis of experimental data. Zeitschrift für Metallkunde 75, 482-491

Seeger, A. 1956. The mechanism of glide and work hardening in face-centered cubic and hexagonal close-packed metals. In: Fisher, J.C., Johnston, W.G., Thomson, R., & Vreeland. T.jr. (eds) Dislocations and mechanical properties of crystals. John Wiley NY, 243-329

Sestak, B. 1980. Plasticity and Crystal structure. In: Haasen, P., Gerold, V. & Kostorz, G. (eds.) 1980. Strength of metals and alloys. Proceedings 5th International Conference, Aachen (1979). Pergamon Press, 3-8

Sibson, R.H. 1982. Fault zone models, heat flow, and the depth distribution of earthquakes in the continental crust of the United States. Bulletin of the Seismological Society of America 72, 151-163

Siethoff, H., Brion, H.G., Ahlborn, K. & Schröter, W. 1986. Dynamical recovery of <111> germanium. Physica Status Solidi (a) 97, 153-162

Siethoff, H. & Schröter, W. 1983. Work hardening and dynamical recovery in silicon and germanium at high temperatures and comparison with FCC metals. Scripta Metallurgica 17, 393-398

Siethoff, H. & Schröter, W. 1984. New phenomena in the plasticity of semiconductors and FCC metals at high temperatures - part I: Theoretical models. Zeitschrift für Metallkunde 75, 475-481

Skrotzki, W. & Haasen, P. 1988. The role of cross slip in the steady state creep of salt. Proceedings second Conference on the Mechanical Behaviour of Salt. Trans Tech Publications, Clausthal-Zellerfeld, 69-81

Skrotzki, W. & Liu, Z.G. 1982. Analysis of the cross slip process in alkali halides. Physica Status Solidi (a) 73, k225-k229

Spiers, C.J. 1979. Fabric development in calcite polycrystals deformed at 400 °C. Bulletin de Mineralogie 102, 282-289

Spiers, C.J. 1982. The development of deformation textures in calcite rocks. Ph.D. thesis, Imperial College of Science and Technology London, pp 251

Spiers, C.J., Urai, J.L., Lister, G.S., Boland, J.N. & Zwart, H.J. 1986. The influence of fluid-rock interaction on the rheology of salt rock. Final report. Nuclear Science and Technology, CEC Volume EUR 10399 EN, pp 13.

Spiers, C.J. & Wenk, H.-R. 1980. Evidence for slip on r and f in the positive sense in deformed calcite single crystals. EOS 61, 1128

Stearns, D.W., Couples, G.D. Jamison, W.R. & Morse, J.D. 1981. Understanding faulting in the shallow crust: Contributions of selected experimental and theoretical studies. In: Carter, N., Friedman, M., Logan, J. & Stearns, D. (eds) Mechanical behaviour of crustal rocks. Geophysical Monograph AGU 24, 215-229

Stocker, R.L. & Ashby, M.F. 1973. On the rheology of the upper mantle. Reviews of Geophysics and Space Physics 11, 391-426

Takeshita, T., Tomé, C., Wenk, H.-R. & Kocks, U.F. 1987. Single-Crystal Yield Surface for trigonal lattices: application to texture transitions in calcite polycrystals. Journal of Geophysical Research 92, 12917-12930

Takeuchi, S. & Argon, A.S. 1976. Steady-state creep of single-phase crystalline matter at high temperature. Journal of Materials Science 11, 1542-1566

Taylor, G.I. 1934. The mechanism of plastic deformation of crystals, part I and II. Proceedings Royals Society London (A) Vol. 145, 362-404

Taylor, G.I. 1938. Plastic strain in metals. Journal of the Institute of Metals 62, 307-324

Thomas, J.M. & Renshaw, G.D. 1967. Influence of dislocations on the thermal decomposition of calcium carbonate. Journal of the Chemical Society (A), 2058-2061

Thompson, A.W., Baskes, M.I. & Flanagan, W.F. 1973. The dependence of polycrystal work hardening on grain size. Acta Metallurgica 21, 1017-1028

Trommsdorff, V. 1964. Gefügestudien an Calcitmarmor aus Val Prato (Tessin). Schweizerische Mineralogische und Petrografische Mitteilungen 44, 595-611

Tsenn, M.C. & Carter, N.L. 1987. Upper limits of power law creep in rocks. Tectonophysics 136, 1-26

Turner, F.J., Griggs, D.T., Clark, R.H. & Dixon, R.H. 1956 Deformation of Yule marble. Part VII: Development of oriented fabrics at 300-500 °C. Geological Society of America Bulletin 67, 1259-1294

Turner, F.J., Griggs, D.T. & Heard, H.C. 1954, Experimental deformation of calcite crystals. Geological Society of America Bulletin 65, 883-934

Turner, F.J. & Heard, H.C. 1965a. Deformation in calcite crystals at different strain rates. University of California Publications on Geological Sciences 46, 103-126

Turner, F.J. & Heard, H.C. 1965b. Experimentally induced extrusion fabrics in calcite and marble. University of California Publications on Geological Sciences 46, 127-152

Turner, F.J. & Orozco, M. 1976. Crystal bending in metamorphic calcite, and its relations to associated twinning. Contributions to Mineralogy and Petrology 57, 83-97

Turner, F.J. & Weiss, L.E. 1963. Structural analysis of metamorphic tectonites. McGraw Hill New York: pp 545

Twiss, R.J. 1977. Theory and applicability of a recrystallized grain size paleopiezometer. Pageophysics 115, 227-244

Twiss, R.J. 1986. Variable sensitivity piezometric equations for dislocation density and subgrain diameter and their relevance to olivine and quartz. A.G.U. Geophysical Monograph 36, 247-261

Urai, J.L. 1989. High temperature deformation of wet and dry Carrara marble. EOS 70, 1380

Urai, J.L., Means, W.D. & Lister, G.S. 1986. Dynamic recrystallization of minerals. Geophysical Monograph AGU 36, 161-199

Urai, J.L., Schuiling, R.D. & Jansen, J.B.H. 1990. Alpine deformation on Naxos (Greece). In: Knipe, R.J. and Rutter, E.H. (eds) Deformation mechanisms, rheology and tectonics. Geological Society of London Special Publication No. 54, 509-522

Van den Beukel, A. 1978. Grain size dependence of the dislocation density in cold worked metals. Scripta Metallurgica 12, 809-813

Van Houtte, P. & Wagner, F. 1985. Development of textures by slip and twinning. In: Wenk, H.-R. (ed.) Preferred Orientation in deformed metals and rocks, an introduction to modern texture analysis. Academic Press, 233-258

Vernon, R. 1981. Optical microstructure of partly recrystallized calcite in some naturally deformed marbles. Tectonophysics 78, 601-612

Wagner, F., Wenk, H.-R., Kern, H., Van Houtte, P. & Esling, C. 1982. Development of preferred orientation in plane strain deformed limestone, experiment and theory. Contributions to Mineralogy and Petrology 80, 132-139

Walker, A.N. Rutter, E.H. & Brodie, K.H. 1990. Experimental study of grain-size sensitive flow of synthethic hot-pressed calcite rocks. In: Knipe, R.J. and Rutter, E.H. (eds) Deformation mechanisms, rheology and tectonics. Geological Society of London Special Publication No. 54, 259-284

Walsh, J.B. 1973. Theoretical bounds for thermal expansion, specific heat, and strain energy due to internal stress. Journal of Geophysical Research 78, 7637-7646

Wawersik, W.R. 1988. Alternatives to a power-law creep model for rock salt at temperatures

below 160 °C. Proceedings second Conference on the Mechanical Behaviour of Salt. Trans Tech publications, Clausthal-Zellerfeld, 103-128

Wawersik, W.R. & Zeuch, D.H. 1986. Modelling and mechanistic interpretation of creep of rock salt below 200 °C. Tectonophysics 121, 125-152

Weertman, J. 1955. Theory of steady-state creep based on dislocation climb. Journal of Applied Physics 26, 1213-1217

Weertman, J. 1957a. Steady-state creep through dislocation climb. Journal of Applied Physics 28, 362-364

Weertman, J. 1957b. Steady-state creep of crystals. Journal of Applied Physics 28, 1185-1189

Weertman, J. 1968. Dislocation climb theory of steady-state creep. Transactions of the American Society of Metals 61, 681-694

Weertman, J. 1972. High temperature creep produced by dislocation motion. In: J.E. Dorn Memorial Symposium, Cleveland, Ohio (1972)

Weertman, J. & Weertman, J.R. 1983a. Mechanical properties, mildly temperature-dependent. In: Cahn, R.W. & Haasen, P. (eds) Physical metallurgy; third, revised and enlarged edition, North Holland Physics Publishing, 1259-1307

Weertman, J. & Weertman, J.R. 1983b. Mechanical properties, strongly temperature-dependent. In: Cahn, R.W. & Haasen, P. (eds) Physical metallurgy; third, revised and enlarged edition, North Holland Physics Publishing, 1309-1340

Weiss, L.E. & Turner, F.J. 1972. Some observations on translation gliding and kinking in experimentally deformed calcite and dolomite. A.G.U. Geophysical Monograph 16, 95-107

Wenk, H.-R. 1985. Carbonates. In: Wenk, H.-R. (ed) Preferred orientation in deformed metals and rocks. An introduction to modern texture analysis, Academic Press: 361-384

Wenk, H.-R., Barber, D.J. & Reeder, R.J. 1983. Microstructures in Carbonates. In: Reeder, R.J. (ed.) Carbonates: mineralogy and chemistry, Reviews in Mineralogy Vol. 11, 301-367

Wenk, H.-R., Takeshita, T., Bechler, E., Erskine, B.G. & Matthies, S. 1987. Pure shear and simple shear calcite textures. Comparison of experimental, theoretical and natural data. Journal of Structural Geology 9, 731-745

Wenk, H.-R., Takeshita, T., Van Houtte, P. & Wagner, F. 1986. Plastic anisotropy and texture development in calcite polycrystals. Journal of Geophysical Research (B) 91, 3861-3869

Wenk, H.-R., Venkitasubramanyan, C.S. & Baker, D.W. 1973. Preferred orientation in experimentally deformed limestone. Contributions to Mineralogy and Petrology 38, 81-114

White, S.H. 1979. Difficulties associated with paleo-stress estimates. Bulletin de Minéralogie 102, 210-215

White, S.H., Burrows, S.E., Carreras, J., Shaw, N.D. & Humphreys, F.J. 1980. On mylonites in ductile shear zones. Journal of Structural Geology 2, 175-187

Winkler, H.G. 1979. Petrogenesis of metamorphic rocks (fifth edition). Springer Verlag, pp 348

Wolf, H. 1960. Die Aktivierungsenergie für die Quergleitung aufgespaltener Schrauben versetzungen. Zeitschrift für Naturforschung 15A, 180-193

Wyllie, P.J. & Tuttle, O.F. 1960. The system $CaO-CO_2-H_2O$ and the origin of carbonatites. Journal of Petrology 1, 1-17

CURRICULUM VITAE

21-05-1959   Geboren te Boxtel

20-06-1977   Diploma VWO-B, Jacob Roelandslyceum Boxtel
26-01-1980   Kandidaatsexamen Geologie, richting G3, Rijksuniversiteit
                  Utrecht (RUU)
15-04-1985   Doktoraal examen (cum laude) Strukturele Geologie met Petrologie
                  en Economische Geologie

15-05-1985 tot 01-09-1985   Toegevoegd docent RUU
01-11-1985 tot 01-11-1989   Wetenschappelijk assistent RUU
01-03-1990 tot 31-05-1990   Toegevoegd onderzoeker (part time) RUU
vanaf 17-08-1990   In dienst by Shell Internationale Petroleum Mij.,
                              afdeling 'Global Geology and Special Studies',
                              Den Haag

The research described in this thesis
was carried out at the
HPT laboratory, Dept. of Geology,
Institute of Earth Sciences
P.O.Box 80.021
3508 TA Utrecht
the Netherlands

ERRATA:

1) The label of the y-axis of figures
   1.4 (p. 9), 2.19 (p. 39), 6.5 (p.141), 6.6 (p. 145)
   and 6.7 (p. 146)
   should be "LOG stress" in stead of "-LOG stress"

2) Fig. 5.8: the labels of the x- and y-axis should be
   $LOG[\rho b^2]$ and $LOG[(\sigma_1 - \sigma_3)/\mu]$ respectively.

3) Table 6.3 caption: add "...Kohlstedt (1977) and
   Carrara marble after Schmid et al. (1980)."

4) Table 7.1: delete 87±31

5) equation 7.3 (p. 167) should be $\sigma = 10^{0.43} \cdot D^{-0.70}$

   [with D in cm and σ in MPa]